University of Southampton

Faculty of Engineering and the Environment

Contributions to the Management of Shallow Failures in Transportation Cuttings

by

Miguel Angel Vivas Mefle

Thesis for the Degree of Doctor of Engineering

March 2021

University of Southampton

Abstract

Faculty of Engineering and the Environment

Thesis for the Degree of Doctor of Engineering

Contributions to the Management of Shallow Failures in Transportation Cuttings

by Miguel Angel Vivas Mefle

Shallow cutting failures are the main cause of derailments on the UK railway lines. These failures are triggered by intense rainfall and occur fast, with no previous warning. Frequently the first person to notice them is the train driver. The derailment that took place at Watford on 16 September 2016 is a clear example of the risks that shallow cutting failures pose to the railway passengers.

Network Rail uses a classification system to obtain a history record of cutting failures by type. A statistical analysis of these records was used in the past to calculate the probability of failure in cuttings accounting for the type of failure. If the classification system is prone to ambiguities, and the type of failures are difficult to allocate using only visual inspections, the estimation of the likelihood of failure will be inaccurate under these premises.

Shallow cutting failures are in some cases triggered by runoff flowing along the face of cuttings. At present, there is not a recognised analytical method for the calculation of the stability of cuttings subject to runoff. Traditional limit equilibrium methods do not capture this type of failures since hydrodynamic forces are not considered.

This thesis proposes the introduction of two measures that will help to improve the management of cuttings: A new classification system for shallow cutting failures, and a novel method to assess the stability of cuttings subject to runoff.

It is expected that the new classification system will help to improve the accuracy of classifying cutting failures and to have a better understanding of the factors involved in each type of failure. A better knowledge of past failures will help to prevent future failures.

The novel method to analyse the stability of runoff triggered cutting failures has been designed to account for runoff hydrodynamic forces by coupling computational fluid

dynamics and the discrete element method in combination with the theory of sedimentology for the initiation of movement in particles.

The resulting method establishes a relationship between the angle of the cutting and the critical shear stress that initiates the mass failure of the cutting. A design chart version of this method has also been introduced where the assessment of stability is carried out knowing the catchment area, the rainfall intensity and the angle of the cutting. The method has been validated using 17 cases and was successful in the assessment of the stability in all of them.

Declaration of Authorship

Print name:	Miguel Angel Vivas Mefle
Title of thesis:	Contributions to the Management of Shallow Cutting Failures

I declare that this thesis and the work presented in it are my own and has been generated by me as the result of my own original research.

I confirm that:

1. This work was done wholly or mainly while in candidature for a research degree at this University;
2. Where any part of this thesis has previously been submitted for a degree or any other qualification at this University or any other institution, this has been clearly stated;
3. Where I have consulted the published work of others, this is always clearly attributed;
4. Where I have quoted from the work of others, the source is always given. With the exception of such quotations, this thesis is entirely my own work;
5. I have acknowledged all main sources of help;
6. Where the thesis is based on work done by myself jointly with others, I have made clear exactly what was done by others and what I have contributed myself;
7. None of this work has been published before submission

Signature: Date:

Acknowledgements

My supervisors, Professor William Powrie and Dr Fleur Loveridge have been both an inspiration and a pleasure to work with. I would like to thank my sponsors Network Rail, EPSRC and Amey for funding this research. I wish to thank the University of Southampton for giving me the opportunity to produce this research. I thank my parents Pepe and Elo for their constant support throughout my life and my brothers Jose and Carlos.

Po, for her encouragement and support and Alan for his advice.

Contents

Table of Figures

Table of Tables

Definitions and Abbreviations

$A =$ area of the catchment

$A_i =$ Inverse of the relative humidity of the soil surface

$A_p =$projected area of the particle

AE = Actual evaporation rate

$ARU =$ actual root water uptake

B = Inverse of relative humidity in the air

$c' =$ soil cohesion

$c_p =$ specific heat of dry air at constant pressure

$c_r =$ root cohesion

$C =$ Courant Number

$C_D =$ drag coefficient

$C_{LS} =$shear lift coefficient

$C_n =$ contact damping in the normal direction

$C_{n\,rest} =$ normal coefficient of restitution

$C_t =$ contact damping in the tangential direction

$C_{t\,rest} =$tangential coefficient of restitution

$d =$zero plane displacement

d_*= dimensionless particle diameter

$d_n =$ overlap in the normal direction at the contact point

$d_p =$diameter of a particle

$d_t =$overlap in the tangential direction at the contact point

$D_p =$median diameter of surface particles

$e_a =$vapour pressure in the air above the surface

e_s =vapour pressure at the surface

E = Evaporation and evapotranspiration

E' = modified turbulent wall function coefficient

$\bar{E}$ =interslice force in horizontal direction

E^* =turbulent wall function coefficient for smooth walls

E_a= vapour removal parameter

E_{eq} =equivalent Young's modulus

E_o = evaporation rate for open water

f = roughness function

f_0 = starting infiltration rate

f_c = constant or equilibrium infiltration rate

f_t = infiltration rate at time t

F_n^d = viscous normal force between particles

F_n^e = elastic normal force between particles

F_t^d = viscous tangential force between particles

F_t^e = elastic tangential force between particles

$\boldsymbol{F}_{DI}$ =drag force vector

$\boldsymbol{F}_{LR}$ =spin lift force (Magnus force) vector

$\boldsymbol{F}_{LS}$ =particle shear lift force vector

$\boldsymbol{F}_p$ =buoyant force vector

$\overrightarrow{\boldsymbol{f_c}}$ = force between two particles

$\vec{\boldsymbol{f}}_{\boldsymbol{fluid}}$ = resulting force exerted by the fluid over the particle

$\vec{\boldsymbol{f}}_{\boldsymbol{g}}$ = gravitational vector

$\vec{\boldsymbol{f}}_{\boldsymbol{n}}$ = normal component of the particle-particle contact force

$\vec{\boldsymbol{f}}_{\boldsymbol{t}}$ = tangential component of the particle-particle contact force

G =Soil heat flux density at the soil surface

G_{eq} =equivalent shear modulus

G_k = generation of turbulence kinetic energy

G_p =particle shear modulus

h =hydraulic head

h_b = bed elevation

h_{gw} = height of the ground water level

h_s =relative humidity at the soil surface

h_w = soil water potential

H =flux density of sensible heat into the air

H_d = local vertical depth of water

I = Infiltration

I_i = moment of inertia about the centroid of a particle

k_e = turbulent kinetic energy

k_s = equivalent sand-grain roughness or Nikuradse roughness

K =hydraulic conductivity

K_n =normal spring stiffness

K_s^+ = roughness Reynolds number

K_{sat} = saturated hydraulic conductivity

K_t =tangential spring stiffness

l = length of each slice

LAI = leaf area index

m_i = mass of a discrete particle

M_{eq} =equivalent particle mass

$\overrightarrow{\boldsymbol{M_r}}$ = rolling resistant moment over a particle

N = the total normal force on the base of the slice

NWD = normalised water uptake distribution

N_n =normal damping

N_{ndamp} = normal damping coefficient

N_t =tangential damping

N_{tdamp} = tangential damping coefficient

P = Precipitation

PE = potential evapotranspiration

PLF = plant moisture limiting function

PRU = potential root water uptake

PT = potential transpiration

q_x = flow rate of water per m^2 section in the x direction

Q =runoff flow rate

Q_n = flow rate per unit width

r= albedo, or canopy reflection coefficient

r_a = aerodynamic resistance

r_p =radius of the particle

r_s =bulk surface resistance

$\overrightarrow{\boldsymbol{r_c}}$ = vector from the particle centroid to the contact point

R = Surface runoff

R_* = particle Reynolds number

R_a= solar radiation

R_c = shortwave radiation measured at the site

R_{eq} = equivalent radius

R_i = distance of the contact point from the particle centroid

R_n = Net radiation or Net all-wave radiation

R_{ns}= R_n reaching the soil surface

S = source/sink term

SCF = soil cover fraction

S_b = bed slope

S_f = slope of the energy grade line

S_{fx} = friction term in the x direction

S_{fy} = friction term in the y direction

S_{ox} =slope in the x direction

S_{oy} = slope in the y direction

$\bar{\boldsymbol{s}}_{\boldsymbol{d}}$ = streamwise depth-averaged velocity vector

$\bar{\boldsymbol{s}}$ = streamwise mean velocity vector

$\mathbf{S_t}$ = mean rate-of-strain tensor

T = mobilized shear force at the base of a slice

T_N = root tensile stress

T_R = root tensile strength

T_a= air temperature

T_p = pull-out resistance

T_s = tensile strength of the root material

u =actual velocity component in the x direction

$\bar{u}$ =mean velocity component in the x direction

u' = fluctuating velocity component in the x direction

u^+ =dimensionless velocity

u^* = shear velocity or friction velocity

u_2 = wind speed

u_a = pore air pressure

$\bar{u}_d$ = depth-average velocity in the x direction

u_w =pore water pressure

U = depth-average velocity in the streamwise direction

$\overline{\boldsymbol{u}}$ = mean velocity vector

$\boldsymbol{U}$ =average fluid velocity vector

v =actual velocity component in the y direction

$\bar{v}$ = mean velocity component in the y direction

v' = fluctuating velocity component in the y direction

$\bar{v}_d$ = depth-average velocity in the y direction

V_{cell} = volume of a cell

V_p = volume of a particle

$\bar{\mathbf{v}}$ = mean velocity vector

$\mathbf{v}'$ = fluctuating velocity vector

$\boldsymbol{V}$ = particle velocity vector

w = actual velocity component in the z direction

$\overline{w}$ =mean velocity component in the z direction

w' = fluctuating velocity component in the z direction

W = weight of a single slice

$\overrightarrow{\boldsymbol{\omega}}$ =fluid rotation velocity

$\overrightarrow{\boldsymbol{\omega_\iota}}$ = angular velocity of a particle

x = streamwise direction

$\bar{X}$ = interslice force in vertical direction

$\overrightarrow{\boldsymbol{x_\iota}}$ = centroid position of a discrete particle

y^+ =dimensionless distance y from the wall

z =elevation head

z_0 = roughness length

z_h = thickness of translational mass movement

z_r = root system depth

$\boldsymbol{\tau}^{\mathbf{R}}$ = Reynolds stress tensor

$\boldsymbol{\tau}^{\mathbf{t}}$ = total shear stress tensor

γ_{sat} = saturated unit weight

γ_t = total unit weight

γ_w =specific weight of liquid water

ε_i =void fraction around a particle

θ_r =residual volumetric water content

θ_s = saturation volumetric water content

μ_p = angle of static friction

μ_r = coefficient of rolling resistance

μ_t = eddy or turbulent viscosity

ν_t =tangential relative velocity between particles

ρ_a = mean air density at constant pressure

ρ_p =density of a particle

ρ_s =density of soil granules

σ' = effective stress

σ_n = total normal stress

τ^* = dimensionless shear stress

τ_0 = critical shear stress at horizontal bed

τ_S = shear strength of the soil

τ_T = mobilised shear strength to maintain the slice in equilibrium

τ_b = bed shear stress

τ_c = critical shear stress

τ_c^* = dimensionless critical shear stress

τ_d= design critical shear stress

τ_{sb}= Stefan-Boltzman costant

τ_w = wall shear stress

τ_β = critical shear stress at a tilted bed with an angle β

ϕ^b = matric suction angle of internal friction

$\bar{\boldsymbol{\tau}}$ = viscous stress tensor

$\boldsymbol{\tau_w}$ = shear stress vector

Δ = Slope of the saturation vapour pressure versus temperature chart at the mean air temperature

α'= porosity near the particle

Θ = degree of saturation

ι = decay constant

a, n, m = curve fitting parameters

β =slope angle

γ = psychrometric constant

ε = turbulence dissipation rate

θ = volumetric water content

κ =von Karman's constant

λ =latent heat of vaporization of water

μ =dynamic viscosity

ν = Poisson's ratio

ρ =density of the fluid

ς = extinction coefficient

χ= Bishop's effective stress factor

ψ =matric suction

ϕ'= angle of internal friction

Chapter1: Introduction

The UK rail network has more than 70,000 discrete cutting assets, most of them constructed more than 100 years ago during the Victorian era, where empiricism and trial and error techniques were utilised during their construction (Skempton 1996). As a result, there is a legacy of cuttings built at considerably steeper angles and by much less robust construction methods than would occur today (Power et al., 2016). Nowadays, several factors like ageing, the lack of engineering knowledge at the time of their construction and the more frequent extreme weather events due to climate change, make these cuttings more vulnerable to failure than those constructed more recently (Nelder et al., 2006; ORR, 2017).

1.1 The importance of washout failures and their disproportionate involvement in train derailments

NR currently classify the type of earthwork failures in three main categories: Soil cutting failures, rock cutting failures and embankment failures. Among them, shallow slope failures and rock cutting failures pose the highest risk to passengers safety since they can move fast and travel large distances with the potential to overtop the railway tracks and cause derailments (Network Rail, 2018).

Network Rail (NR), who own and maintain the UK rail infrastructure, maintain a database of earthwork failures. Analysis of this data shows that from 2012 to 2018, 47% of the recorded failures were of the type shallow slope failures. These have been the cause of all of the soil cutting failures that ended up in derailments since the year 2007 according to Rail Accident Investigation Branch (RAIB) reports.

Considering the failures recorded in the database, 'washout' is the second most common type of failure in NR cuttings accounting for the 29% of soil cutting failures from 2012 to 2018. In addition, washout represented 5 out of the 9 accidents leading to derailment since 2007 according to RAIB reports.

1.2 The need of a revised hazard index algorithm and classification system

During the last two decades, efforts have been made by NR to implement a system to identify and prevent earthwork failures. In 2003, NR commissioned Babtie Group to develop a system to facilitate routinely railway cuttings inspections and allow independent assessment of their condition. In result, an algorithm upon which an index related to the likelihood of failure called the Soil Slope Hazard Index (SSHI) was derived (MAINLINE Project, 2013).

The system was modified in 2014 with the inclusion of a new algorithm and the Soil Cutting Hazard Index (SHCI).

Inspected parameters such as the angle and height of the cuttings, the existence of retaining walls, the area of the adjacent catchment, or the application of loads on top of the cutting seems likely to contribute differently to the failure of cuttings depending on the mode of failure. The SSHI accounted for it and the logic underlying this approach was recognised by the Rail Accident Investigation Branch (RAIB, 2008c) who considered it as 'technically sound'.

According to the NR soil cutting failures database and the Rail Accident Investigation Branch, the introduction of the SCHI has not resulted in a reduction of the number of soil cutting failures with respect to the old SSHI algorithm. The SCHI has also failed in recognising the risk of washout failures in some of the most recent derailments. Therefore, it is possible that the SCHI could be further improved with the introduction of a statistical algorithm accounting for the type of failures. However, an investigation of the NR classification system of cutting failures carried out during this thesis , shows that the current NR classification system presents at some degree overlapping of categories and a lack of detail description (Network Rail, 2015a) that may potentially affect the robustness of the classification system and the performance of any type of proposed failure-type related hazard index.

1.3 Proposal of a revised classification system

The first contribution of this thesis is the proposal for a new classification system focused on shallow cutting failures that meet the recognised criteria of good classification systems (i.e. conservatism, uniqueness, simplicity, flexibility and universality) (Hungr et al., 2001;Hungr et al., 2014). The new classification system has been designed to classify cutting failures in a consistent manner based only on visual inspections so that the classification can be carried out objectively by a trained operative. This could be the first step in the development of a proposed hazard index where historical failures were to be classified and introduced in a statistical algorithm to assess the vulnerability of cuttings for the possible modes of failure (Chapter 3).

1.4 The Watford incident to test the hypothesis that washouts may be unidentified

A prominent example of a recent washout failure is the washout failure that took place at Watford on 16 September 2016 that led to the derailment of a train and the collision with a second train circulating in the opposite direction.

While the failure at Watford was mainly attributed to 'washout' by the Rail Accident Investigation Branch (RAIB, 2017), the real cause of failure is still uncertain since a thorough investigation of the stability of the cutting at the time of failure has not been carried out so far to the knowledge of this author.

The Watford cutting failure had a great repercussion in the UK and was profusely aired in the media (e.g. BBC NEWS, 2016; Independent, 2016; The Guardian, 2016) damaging the reputation of NR. RAIB attributed the failure to the limitations of the NR system to identify and prevent washouts and recommended an improvement in the identification of cuttings vulnerable to this type of failure (RAIB, 2017).

The second contribution of this thesis is the stability analysis of the Watford cutting at the time of failure using continuum numerical methods of analysis. The analysis has been carried out by coupling limit equilibrium analysis and transient pore water pressures using the finite element method (Chapter 7). The effect of precipitations and evapotranspiration was considered with the inclusion of the Wilson-Penman equation for the soil-climate interaction.

The analysis was carried out to dismiss other possible triggering mechanisms other than washouts at Watford (i.e. rising of ground water levels or dissipation of matric suctions) and to further proof that washout was the real cause of failure using the novel method against washouts.

The Watford case study set an example of how the application of the novel method introduced in this thesis can be used to predict washouts that previously could have not been detected using the NR system or continuum methods of analysis.

1.5 A new approach for assessing vulnerability to washouts

A deterministic approach to assess the vulnerability of cuttings against 'washouts' is still lacking.

The initiation of soil particles movement due to runoff (soil erosion) has been largely studied in the field of sedimentology since the work of Shields, (1936) to estimate the threshold surface shear stress that initiate the movement of particles. At higher surface shear stresses, the hydrodynamic forces can lead to a different process involving the dislodgement of soil peds with the potential to initiate the mass failure of a cutting (i.e. runoff generated debris flow).

Recent work and associated advances regarding runoff-generated mass failures have been carried out in the last two decades for river channels where the majority of debris

flows are initiated (e.g. Gregoretti, 2000; Tognacca et al., 2000; Armanini and Gregoretti, 2005), but not for infrastructure slopes.

Previous investigations introduced semiempirical equations to obtain the critical shear stress initiating the mass failure in channels under deposits of sands and gravels typical of river bed conditions (e.g. Gregoretti, 2000; Tognacca et al., 2000; Armanini and Gregoretti, 2005). However, these equations were developed for slopes less steep than that encountered in transportation cuttings and introduce varying non-physical parameters, required for the calculation of the critical shear stress in such cuttings. This presents an opportunity to learn lessons from the advances in calculation of channelized debris flow initiation and to apply them to cuttings.

The third and final contribution of this thesis is the introduction for the first time of a method for the assessment of the stability of transportation cuttings against runoff (Chapter 8). The novel method has been developed to be used in two of the most common soils in the UK: clayey soils (i.e. head deposits, cohesive glacial tills, clay with flints, cohesive alluvium) and chalk where Watford failure took place.

The novel method has been designed by coupling computational fluid dynamics (CFD) with the discrete element method (DEM). This approach allows the inclusion of hydrodynamic effects of surface runoff over the face of the cuttings that cannot be addressed using continuum methods of analysis.

The use of CFD-DEM allows the numerical simulation of flume experiments for all possible combinations of angle of cuttings and properties of chalk and clayey soils present in the UK railway cuttings.

The use of CFD-DEM supposes a significant contribution to the analysis of transportation cuttings offering advantages over traditional flume tests. The installation of flume tests in transportation cuttings in the field would be affected by access restrictions and the large number of experiments corresponding to the different combinations of soil properties and slope angles would make research extremely cumbersome. CFD-DEM allows the analysis of multitude of parameters combinations by only changing gravity components and particle parameters. The critical shear stress initiating debris flows can be readily obtained using CDF-DEM whereas in flume tests, and specially in steep cuttings, the accuracy is reduced when the depth of runoff is in the order of millimetres.

Previous research using CFD-DEM has concentrated in the investigation of seepage (Kawano et al., 2017;Suzuki et al., 2007; Chen, (2009), consolidation (Chen et al., 2011),

fluidisation in granular beds (Liu et al., 2015), internal erosion in granular soils (Kawano et al., 2018; Kawano et al., 2017) and the analyses of granular mass movements in water (Zhao, 2014;Shan and Zhao, 2014; Li Zhao, 2016).

This is the first time that CFD-DEM is applied to the initiation of cutting failures triggered by runoff and the research will help to expand the possibilities of CFD-DEM.

The method consists in the identification of the threshold shear stress that initiates the mass movement of soil peds at different slope angles using CFD-DEM. For the assessment of the stability of a cutting against runoff, the actual bottom shear stress over the cutting face during a rainfall event is obtained using the shallow water equations where precipitation parameters, the digital terrain model of the cutting and the catchment area are integrated. Then, the threshold and the actual shear stress for the cutting analysed are compared and the vulnerability of the cutting is assessed.

The application of the novel method only requires limited computation provided by the simplifications inherent to the shallow water equations and can be applied to extensive catchments adjacent to transportation cuttings in a reasonable amount of time.

In addition, a variant of the method has been developed to be used without the need of carrying out numerical methods of analysis. The assessment of the stability of cuttings is here obtained from three easily to obtain parameters: the catchment area, the slope angle and the rainfall intensity.

This variant of the method has been proved to be useful as a feasible initial estimation of the stability of the cuttings against runoff.

1.6 Testing of the method with reference to real cases

The novel method has been used to assess the main factor that initiated the failure at Watford cutting and has also been validated against other real cases of failures caused by washout that led to derailments: 2 of them at St Bees and another 2 in a road cutting at Beaminster where failure resulted in the killing of two people who were engulfed by failure deposits.

The method has also been validated against cuttings that were subject to runoff but remained stable (4 of them at Watford, 3 at St bees, 2 at Beaminster and one at Loch Treig where failure took place but was not attributed to runoff.

The novel method proved to be successful in the identification of those cuttings at risk of failure. In particular, the Watford case was identified as extremely vulnerable to runoff,

proving that the implementation of the novel method in the NR management system will likely help in the identification and prevention of similar events.

1.7 Aim and Objectives

The aim of this work is to facilitate more proactive management of fast moving failures in railway cuttings through improved understanding of their occurrence and appropriate analysis of their mechanisms. Objectives are:

1. To review the NR's earthworks management system particularly, how failure classification is defined and applied.
2. To propose a new shallow slope failure classification system to better reflect actual mechanisms of failure and keeping with current state of the art systems
3. To propose a new method for determining the vulnerability of slopes to erosion drive 'washout' type failures based on CFD-DEM coupling that can assess the slope stability accounting for the hydrodynamic effect of runoff
4. To assess the capability of the novel method to detect cutting failures triggered by superficial runoff that otherwise would have remained inconclusive after assessment using continuum models to analyse slope stability.

1.8 Layout of the thesis

Chapter 2 presents the particular characteristics of railway cuttings in the UK that makes them especially vulnerable to failures.

It covers the evolution of the NR management system of railway cuttings and the current system used. An introduction to the NR classification system of slope failures is set out as a base to the analysis of the most frequent and disruptive type of earthwork failures identified. Finally, the performance of the current hazard index for slope failures is discussed.

Chapter 3 analyses the limitations of the NR's classification system. Then, a new classification system for railway slope failures is proposed. Finally, a guide to classify slope failures by a trained operative under the new system is introduced, together with a proposal for a new hazard index algorithm based on the new classification system.

Chapter 4 introduces the theoretical background for continuum methods of slope stability analysis. This included the equations describing the movement of water within the soil, the processes of infiltration, evaporation and transpiration and limit equilibrium methods for the assessment of slope stability under continuum approach.

Chapter 5 presents the theoretical background behind the novel method for the stability assessment of transportation cuttings against washouts. This includes the equations describing the movement of surface runoff, the equations describing the discrete element method (DEM) and the coupling of computation fluid dynamics with the discrete element method (CFD-DEM).

Chapter 6 introduces the range of geotechnical parameters for clayey soils and chalk in the UK that will be subsequently for analysis. Following this, an overview of the case studies that will be analysed using continuum methods and the novel method against washouts is introduced.

Chapter 7 focuses on the stability assessment of Watford cutting using continuum methods of analysis.

Chapter 8 introduces the novel method for the stability assessment of transportation cuttings against washouts

Chapter 9 analyses the vulnerability of the cases presented in chapter 6 (i.e. real case transportation cuttings against washouts) using the novel method proposed.

Chapter 10 details the main conclusions drawn from the case studies presented

Table 1-1 below further clarifies the structure of the research. The flow of the structure can be summarised as:

(i) The importance of washout failures and their disproportionate involvement in train derailments (Chapter 2).

(ii) Presentation of evidence of the need of a revised classification system and hazard index algorithm (Chapter 2)

(iii) Development of a revised classification system and proposal of a new algorithm approach (Chapter 3)

(iv) Theoretical background (Chapters 4 and 5)

(v) Introduction to case studies to test the novel method

(vi) The Watford incident as a case study to test the hypothesis that washouts may go unidentified and unreported and set out the requirements of an analysis method to identify washouts (Chapter 7)

(vii) The development of a proposed method to identify washout type of failures (Chapter 8)

(viii) Testing the method (Chapter 9).

Table 1-1 Layout of the thesis

(i) **The importance of washout failures and their disproportionate involvement in train derailments (Chapter 2)** Description of the NR management system of cuttings (2.1 and 2.2) Description of the NR classification system of soil cutting failures (2.3) Investigation of the most frequent and disrupting types of failures (2.4and 2.5) ***(ii)*** **Presentation of evidence of the need of a revised hazard index algorithm and classification system (Chapter 2)** Performance of the system before and after the introduction of the SCHI (2.6) Discussion (2.7) ***(iii)*** **Development of a revised classification system and proposal of a new algorithm approach** **(Chapter 3)** Identification of the areas of improvement in the NR classification system (3.1) Introduction of a new classification system (3.2)	Guide to classifying cutting failures (3.3) Proposal of a new hazard index algorithm (3.4) Conclusion (3.5) ***(iv)*** ***Theoretical background for continuum methods of stability analysis*** ***(Chapter 4)*** Water movement within the soils (4.1) Infiltration, evaporation and transpiration (4.2) Analysis of mass movement using the continuum approach (4.3) Conclusion (4.4) ***Theoretical background behind the novel method of washout assessment*** ***(Chapter 5)*** Surface runoff movement (5.1) The discrete element method (5.2) CFD-DEM coupling (5.3) Conclusion (5.4)	***(v)*** ***Introduction of case studies*** ***(Chapter 6)*** Geotechnical parameters for chalk and clayey soils (6.1) Case Studies (6.2-6.6) ***(vi)*** **The Watford incident as a case study to test the hypothesis that washouts may be unidentified (Chapter 7)** Model setup (7.1) Input parameters (7.2) Results (7.3) Discussion (7.4)	***(vii)*** ***The development of a proposed method for the assessment of washouts (Chapter 8)*** Previous Research (8.1) Novel method overall approach (8.2) Input parameters (8.3) Bottom shear stress (8.4-8.5) Critical shear stress: Method, validation, sensitivity analysis and design chart (8.6) Discussion (8.7) Conclusion (8.8)	***(viii)*** ***Testing of the method with reference to real cases (Chapter 9)*** Watford Case Study (9.1) St Bees Case Study (9.2) Beaminster Tunnel Case Study (9.3) Loch Treig Case Study (9.4) Discussion (9.5) Conclusion (9.6) ***Conclusions and Recommendations*** ***(Chapter 10)*** *Overall conclusions (10.1)* *Recommendations for practice (10.2)* *Recommendations for future work (10.3)*

Chapter2: Failures in cuttings and asset management systems

The majority of the railway network currently in use in the UK were built in the second half of the 19th century, known as the Victorian era. Between 1834 and 1841, nine main railway lines were constructed totalling 660 miles in length, including complex engineering constructions such as tunnels, bridges, viaducts and stations, requiring an enormous magnitude of earthworks construction (Skempton, 1996).

Organisations such as the Institution of Civil Engineers and the Geological Society of London arranged forums for knowledge share to establish 'best practice procedures' in construction. These guidelines were primarily based on findings of the behaviour of cuttings and embankments already constructed (Nelder et al., 2006).

Since transport contracts were assigned to private investors owning railway lines, they focused on the rate of construction at expenses of the quality. This tendency became the norm during the whole 19th century, resulting in overstep cuttings compared to modern practises (Power et al., 2016).

More recently, rail infrastructure has been characterised by underinvestment in renewals (Network Rail, 2014a). Ageing, that has led to a reduction of the strength of the cuttings (Nelder et al., 2006), traffic loadings well in excess of those they were originally designed for (Nelder et al., 2006) and the growing rate of high intensity rainfall events as a consequence of the climate change have all led to the highest observed levels of deterioration in railway cuttings (Power et al., 2016).

To address this issue, an increase in investment has been seen more recently in railway infrastructure, to ensure that adequate safety and operating standards are maintained, as well as implementing more efficient strategies for the asset management (Network Rail, 2014a).

In 2014, the introduction of the SCHI in the NR's asset management system as a tool to assess the likelihood of cutting failures through visual inspections was envisioned as an improvement over the former SSHI. However, while the SCHI is recognised as giving a much better indication of the relative risk of failure for different earthworks types, its application has not resulted in a reduction in the number of failures according to the NR failure database records from 2008 to 2018.

2.1 Historical review of railway asset management for cuttings

In the past, earthworks asset management occurred in a reactive manner, with repairs being carried out when needed. (Network Rail, 2015a). During the period post privatisation of the UK railway network, some earthworks failures occurred which were considered to be avoidable should an efficient system of earthworks inspection and stability assessment had been in place (RAIB, 2008c).

At the time the infrastructure maintainer was Rail Track, they recognised the need to stablish a methodology for inspection and assessment of earthworks. It resulted in the issue of the company procedure RT/CE/P/030 'Management of embankments and cuttings' in 1997 which required that earthworks and their associated drainage were to be physically inspected and then evaluated for condition in accordance with a prearranged marking procedure, and with the intention to offer a means of readily comparable results. However, the application of the company procedure was varied and inconsistent (RAIB, 2008c).

In 2003, Network Rail commissioned Babtie Group to develop a system to facilitate routinely railway earthworks inspections (both soil cuttings and embankments) to enable independent assessment of their condition (Babtie Group, 2003). In result, an algorithm for soil cuttings upon which an index related to the likelihood of failure called the Soil Slope Hazard Index (SSHI) was derived (MAINLINE Project, 2013).

The Soil Slope Hazard Index was included in RT/CE/S/065 'Examination of Earthworks' In June 2005 (now designated NR/L3/CIV/065) (RAIB, 2008c).

To determine the SSHI, cyclic site inspections were required to be undertaken by NR trained operatives, to visually report over 30 separate parameters indicating some form of degradation. The observed parameters were then fed into the algorithm.

The algorithm behind the SSHI took account of the failure mechanism, which was classified as one of rotational, translational, earthflow, washout or burrowing (Doherty et al., 2013). The 30 observable parameters reported during the inspections were weighted differently for each possible mode of failure based on engineering judgement (Network Rail, 2017a). 4

The algorithm then generated the SSHI for each cutting inspected indicating relative risk based upon possible failure modes. Then, the highest SSHI score was used to assess the risk of failure (Crapper et al., 2014).

The SSHI was shown to predict the likelihood of soil cutting failure fairly well (Network Rail, 2017a)

Although the SSHI had proven an acceptable performance (Network Rail, 2017a) in the assessment of the conditions of cuttings, the drive for continuous improvement and the availability of ten years of examination data and failure records prompted NR to introduce a statistical algorithm for the assessment of cuttings to remove engineering judgement from the weighting of parameters (Power et al., 2016).

The new Hazard Index was called the Soil Cutting Hazard Index (SHCI) currently in use, and was included in 2014 in issues 4 and 5 of NR/L3/CIV/065.

In contrast to the SSHI, the SCHI was derived by a largely statistical assessment of historical failure data (Power et al., 2016).

Unlike the old SSHI, the algorithm behind the SHCI was developed without considering the different types of failures in the weighting of parameters. However, the classification of failures into rotational, translational, earthflow, washout and burrowing remained in the failure reporting system (Network Rail, 2017a).

Analysis suggested that this approach gather a more accurate representation of the relative risk of failure for each cutting compared to the older SSHI system.

2.2 Current NR asset management system: Cuttings

NR maintains on-site cyclic inspections as the procedure to assess the probability of failure in soil cuttings. All the cuttings in the railway network are visually inspected and checked against a number of established parameters that indicates some form of degradation in accordance with the procedure set out in NR/L3/CIV/065 ‘Examination of Earthworks’ (Standards, 2017).

Unlike the SSHI, the SHCI algorithm was developed without considering the different categories of failures but was derived from a largely statistical assessment of historical failure data, and therefore removing the ‘engineering judgement’ element from the weighting of parameters (Figure 2-1) (Power et al., 2016). For each parameter, an assessment of the data available was carried out for the entire population of soil cuttings and the inspection records made prior to a logged failure (Power et al., 2016).

The more prevalent parameters observed during the visual inspection of failed cuttings were given a positive weighting in the new algorithm.

Those more prevalent in the whole population were negatively weighted. The sum of the parameter weightings for a specific cutting results in the Soil Cutting Hazard Index (SCHI) and is obtained for all cuttings within the boundary of the NR infrastructure as well as nearby assets that may have an impact (Power et al., 2016).

The SCHI score provides a measurement of the degradation (or improvement following an intervention) of soil cuttings to enable decisions to be made on how to control risks of failure. The SCHI does not account for the types of failures, as the SSHI did, and therefore the failure classification is currently assessed independently from the SCHI.

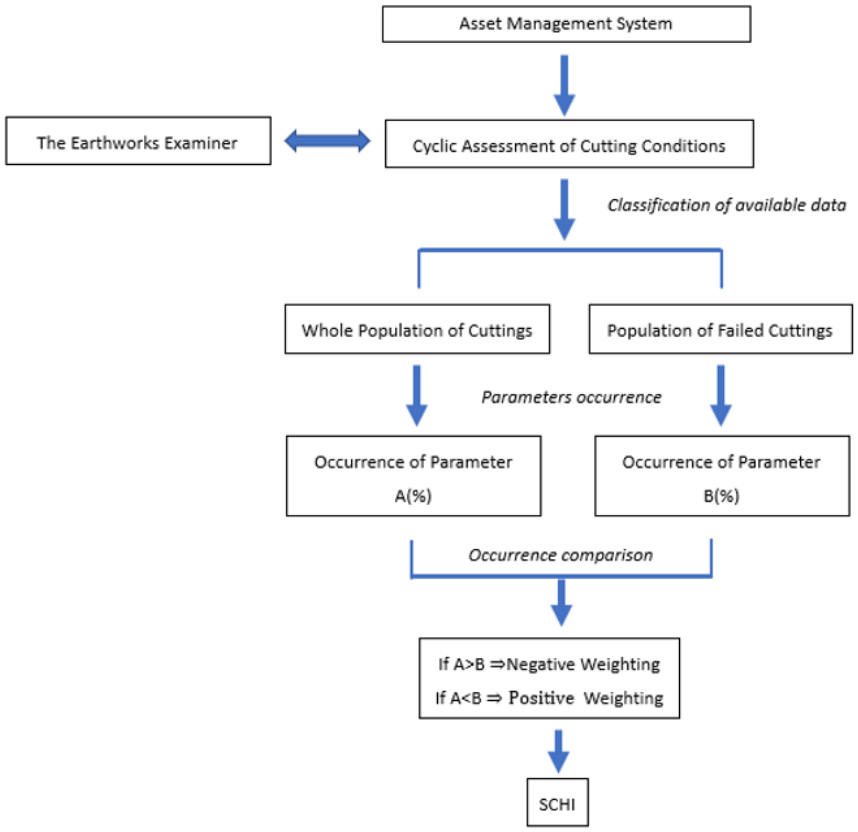

Figure 2-1 SCHI algorithm

2.2.1 The railway cuttings examination process: The role of the earthworks examiner

The examinations are performed by an Earthwork Examiner (EE) who is a competent person independent of the examination contractor and meets the requirements stablished in the specification NR/SP/CTM/017 'Competence and Training in Civil Engineering'. The EE is trained and certified in the assessment of the hazard Index and the use of the Civils Strategic Asset Management Solution (CSAMS). The CSAMS is the

software that calculates the hazard index for the cutting using the methodology included in the NR Standard NR/L3/CIV/065/Mod02 'Definition of Soil Cutting Hazard Index'.

Once the assessment has been completed, the EE submits the data for upload to CSAMS which generates a report to be submitted to the Earthwork Examining Engineer (EEE), a qualified trained Chartered Engineer or Geologist who reviews and approves the report and records the approval on CSAMS within 28 days of the examination date.

Finally, the approved report is issued to the Earthworks Manager (EM) who accepts or rejects the final issue of the report within three months of the examination date.

2.2.2 The assessment of cutting conditions

The NR system to identify mitigation measures and cutting interventions requirements is based on a safety risk matrix type, as shown in Figure 2-1. The magnitude of the safety risk of each asset can be represented by the asset's position on the matrix , for example, earthworks in cell A1 present the lowest safety risk to the network, whereas earthworks in cell E5 has the highest safety risk (Network Rail, 2015a).

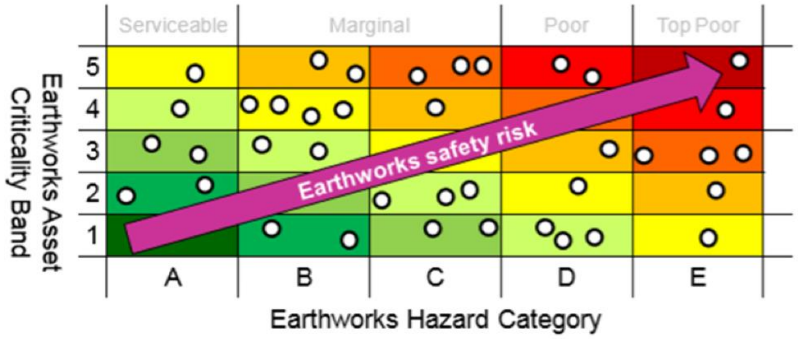

Figure 2-2 Earthworks safety risk matrix (Network Rail, 2015a)

Earthworks asset criticality is an assessment of the potential safety consequences of the failure of an earthworks asset (Network Rail, 2015a). The assessment assigns an Earthwork Asset Criticality Band (EACB) (y-axis of the matrix) to a given Earthwork asset, where values range from 1 (least critical) to 5 (most critical) (Network Rail, 2017c). An Asset Criticality score has been assigned to each earthworks type on the NR network.

SCHI scores are segmented into five Earthwork Hazard Categories (EHC), extending from A (lowest hazard indices, lowest likelihood of failure) to E (highest hazard indices, highest likelihood of failure) (Power et al., 2016). The EHC represents the x-axis of the earthworks safety risk matrix.

2.3 The current NR classification system of cutting failures

The cutting failure classification system adopted by NR, accounts for two main factors: 1) the type of Earthwork Asset (i.e. Soil Cutting, Rock Cutting and Embankments), and 2) the type of failure (Network Rail, 2015a).

Soil Cuttings are classified by NR in the CP5 Earthworks Asset Policy (Network Rail, 2015a) into five modes of failure: Translational Failure, Earthflow, Burrowing, Washout and Rotational Failure. CP5 describes each type of failure as follows:

1. Translational failures

Translational failures are defined as a slope failure that occurs parallel with a slope's surface and is usually limited to the sliding of superficial materials. This type of failures is mostly attributed to weathered superficial cohesive soils. Translational failures may also occur on granular soils where the granular materials form a discrete layer of soil mantling the cutting.

Translational failures are considered to be triggered by the following, such as:

1. Weathering of the shallow layer parallel to the slope surface
2. Surge in moisture content leading to a reduction in strength of the soil materials.
3. Heavy rainfall leading to a sudden increase in soil weight
4. Weakening due to other environmental factors, such as lack of vegetation or to animal burrowing.

No information regarding slide velocity and degree of deformation experienced is given in NR policy documents or standards (Network Rail, 2014, Network Rail, 2015a). A representative example is given in Figure 2-3 (Network Rail, 2015a).

Figure 2-3 Example of translational failure according to NR classification system. (Network Rail, 2015a)

2. Earthflows

Earthflow failures are plastic flows that occur when water, saturate and weaken the soils in a slope to the point where they no longer have the strength to stand at the slope angle. The surface layer slides and the materials beneath are converted to slurry, which flows down slope.

Earthflows may be the result of two triggering mechanisms:

1. A prolonged surface flow that saturates and weakens the weathered surface layer.
2. The presence of a low permeability surface layer that form a 'dam'. The failure occurs after a rise in ground water table when the pore water pressure exceeds the weight of the overlying soils

No information is given in policy documents or standards (Network Rail, 2014, 2015a) regarding the velocity of this type of failures. A representative example is given in (Figure 2-4) (Network Rail, 2015a).

Figure 2-4 Example of earthflow failure according to NR classification system. (Network Rail, 2015a)

3. Washout failures

Washouts are the washing away of soil particles by a concentrated flow of water (Figure 2-5). This commonly occurs where adjacent ground falls towards a vulnerable asset and the local conditions provide little obstruction to allow surface water to concentrate at a specific point

Figure 2-5 Example of washout according to NR classification system (Network Rail, 2015a)

4. Rotational failures

Rotational failures are defined by movement of a soil mass along a failure surface that is spherical or curved (Figure 2-6). Local ground conditions may further develop this failure surface so that it is non-circular, or there may be multiple rotational failures down a slope.

Rotational failures typically occur as a consequence of one or more of the following factors:

1) Variation in ground water conditions affecting the soil
2) Alteration of soil strength as a result of weathering effects and
3) Change in a slope's loading condition; typically either an increased load at the slope crest, or removal of material at the slope toe (Network Rail, 2015a).

Figure 2-6 Example of rotational failure according to NR classification system (Network Rail, 2015a)

5. Burrowing

Cutting failures can be triggered by animals excavating materials that acted as support (e.g. rabbits, foxes, badgers) (Figure 2-7). In addition, burrows become preferential paths for water that facilitates erosion. These types of failures are more common in granular soils since they are more prone to excavation by animals.

Figure 2-7 Example of burrowing according to NR classification system (Network Rail, 2015a)

In the next section, the occurrence of different types of earthwork failures will be analysed.

2.4 Failure recording

NR standards require the reporting of safety related events which include earthworks failures (Network Rail, 2015b,2017). The definition of an earthwork failure in this context is a 'slope in a state of collapse: e.g. rock fall or soil slip, slide or flow in an embankment, cutting or natural slope' (Network Rail, 2015a). As well as reportable failures, detail of 'incidents' are collected where unplanned or uncontrolled events may cause either an accident or an increased likelihood of an accident.

NR's database shows that 448 soil cutting, 102 rock cutting and 250 embankment failures took place in the UK from 2012 to 2018. These values are presented in Figure 2-8 where 56% of incidents and failures occurred in soil cuttings.

The data shows that **soil cutting failures are the most frequent type of earthwork failures in the NR network.**

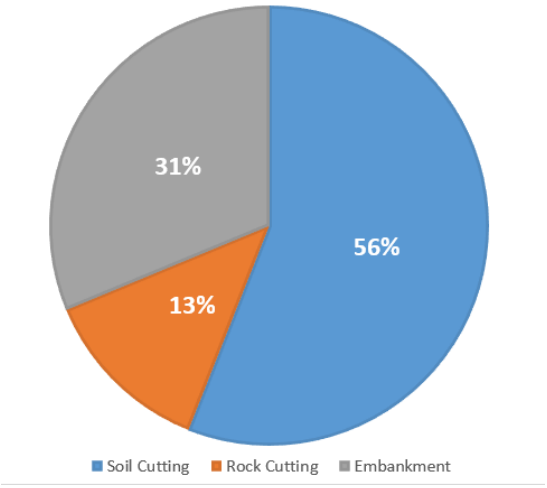

Figure 2-8 Distribution of Network Rail earthwork failures by type from 2012 to 2018

The distribution of soil cutting failures by type according to the NR classification system is shown in Figure 2-9.

Two types of failure in cuttings stand out from the rest: translational failures (54%) and washouts (29%) (Figure 2-9).

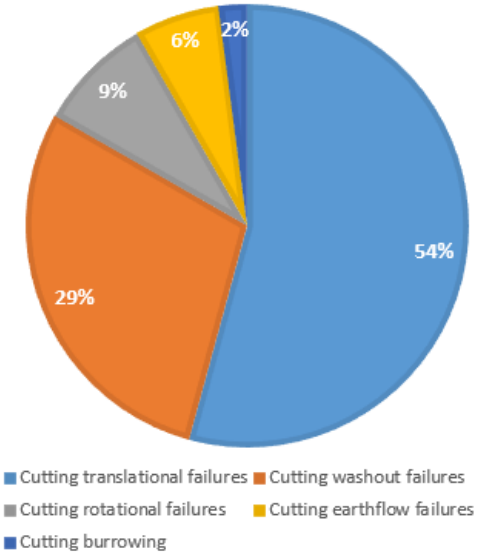

Figure 2-9 Distribution of Network Rail cutting failures by type from 2012 to 2018

In terms of the total number of earthwork failures by type, as shown in Figure 2-10, translational failures (31%) and washout cutting failures (16%) clearly stand out from the rest and above the 7% attributed to rotational failures.

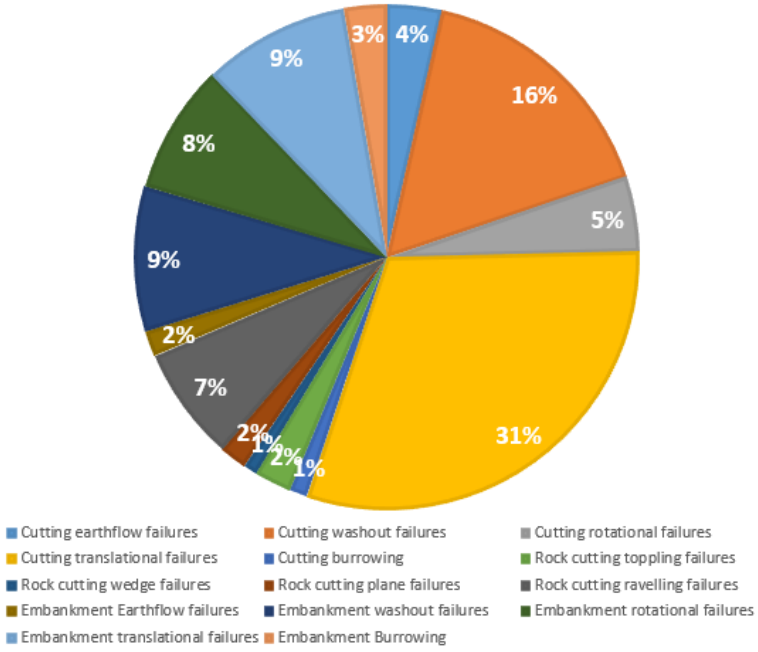

Figure 2-10 Distribution of Network Rail earthwork failures by categories from 2012 to 2018

From the above it can be inferred that translational and washout cutting failures are potentially fast-moving with long runout distances and pose the highest risk to the integrity of the railway lines.

Earthworks failure resulting in derailments from 1994/1995 to 2015/2016 is represented in Figure 2-11. It shows that 72% of derailments are attributed to soil cutting failures. This is also ratified by RAIB reports from 2007 to 2019, where translational and washout

failures were identified as the cause of all the soil cuttings-related derailments in the NR network.

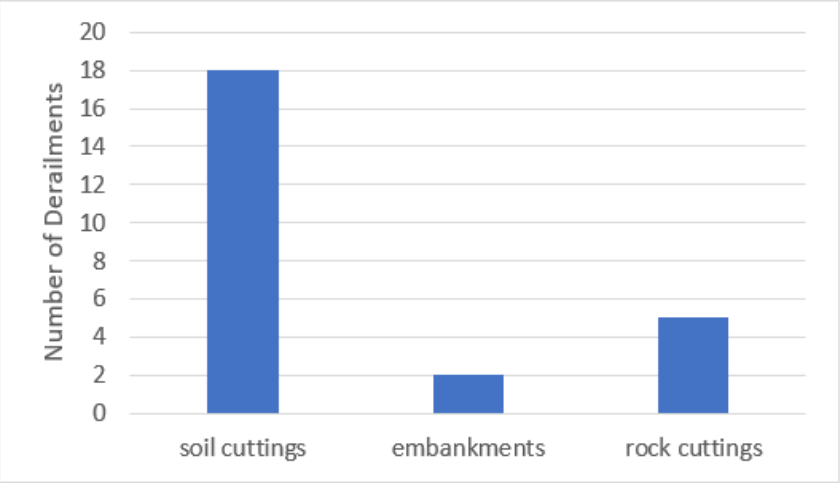

Figure 2-11 Number of derailments by type of earthwork from 1994/1995 to 2015/2016

From the above, it is recommended that the NR management system improvements are focused on the assessment of the likelihood of translational and washout failures. Improvements have been proposed in this thesis with the introduction of the new classification system for shallow cutting failures and the novel method for the assessment of the stability of cuttings against washouts.

In next section, the characteristics of the most recent soil cutting failures that resulted in derailments are discussed.

2.5 Failures leading to derailments

The location and type of soil cutting failures and natural slopes that resulted in derailments registered in the RAIB accident investigation reports from 2007 to 2019 is presented in Table 2-1.

Table 2-1 Soil cutting failures that resulted in derailments from 2007 to 2019

Date	Location	Type of NR failure
January 2007	Hooley	Translational Failure
January 2007	Kemble	Translational Failure
November 2009	Gillingham tunnel	Washout
April 2012	Clarborough	Washout
July 2012	Rosyth	Washout
June 2012	Loch Treig	Translational Failure

August 2012	St Bees	Washout
September 2016	Watford	Washout
January 2018	Lochailort	Translational failure

From the data presented in Table 2-1, it is important to remark the prevalence of the number of derailments attributed to washouts (5 out of the 9 failures). This validates the importance of the novel method presented in this thesis to predict and prevent this type of failures.

The locations of the failures presented in Table 2-1 and photographs obtained from RAIB reports are shown in Figure 2-12 and Figure 2-13. It can be observed that most recent soil cutting failures in the NR lines that resulted in derailments extends over the entire UK.

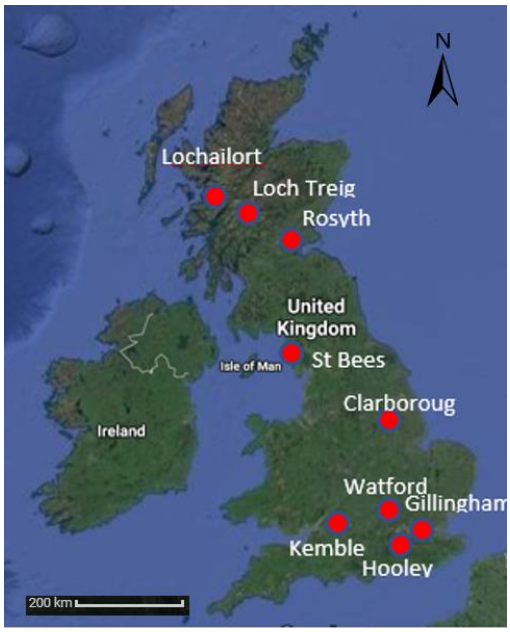

Figure 2-12 Recent cutting failures causing derailments (RAIB, 2008a; RAIB, 2008b; RAIB, 2010; RAIB, 2014; RAIB, 2017;.RAIB, 2018)

Hooley (January 2007)

Kemble (January 2007)

Gillingham (November 2009)

Clarborough (April 2012)

Loch Treig (June 2012)

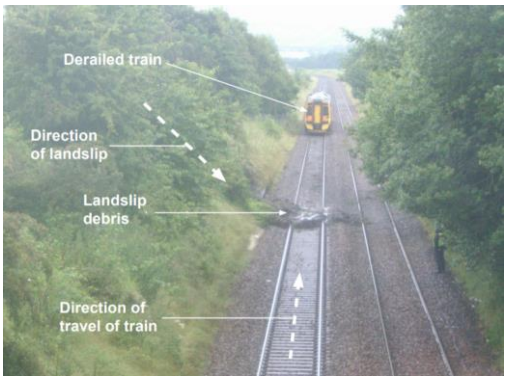

Rosyth (July 2012)

St Bees (August 2012)

Watford (September 2016)

Lochailort – Glenfinnan (January 2018)

Figure 2-13 Recent NR cutting failures resulting in derailments from 2007 to 2019

Rainfall has been a common factor in the majority of derailments. Rainfall at the time of failure was recorded at Gillingham tunnel (RAIB, 2010), Clarborough (RAIB, 2012), Rosyth (RAIB, 2014), Loch Treig (RAIB, 2018b), St Bees (RAIB, 2014), Watford (RAIB, 2017) and within one week prior to the failure at Kemble (RAIB, 2008b).

Failures that were not directly associated with rainfall are located at Lochailort and Hooley. The derailment at Lochailort was caused by washout due to a thaw period, immediately after a very cold spell of weather (RAIB, 2018a) and therefore is still related to either excessive infiltration or surface water runoff generated by ice/snow melt. The derailment at Hooley was attributed to an increment of the slope angle from 53 to 60 degrees (RAIB, 2008a).

In terms of soil type, 7 out of 9 failures occurred in cuttings made up of coarse particles embedded in a fine matrix of clay and/or silt (Cohesive Glacial till, Alluvium and Head deposits) and 2 of them in chalk (Table 2-2) according to RAIB reports and BGS geological maps.

Table 2-2 Geology of soil cuttings that resulted in derailments from 2007 to 2019

Kemble	Gillingham tunnel	Rosyth	Loch Treig	St Bees	Lochailort	Hooley Cutting	Watford	Clarborough
Alluvium (Clay, Silt, Sand and Gravel)		Cohesive Glacial till				Chalk		Head (Clay, Silt, Sand and Gravel)

In addition, data from the NR database of soil cutting failures classified by geology from April 2003 to April 2016 shows that the highest number of failures occurred in cuttings of cohesive glacial tills, head deposits and alluvium soils (Figure 2-14).

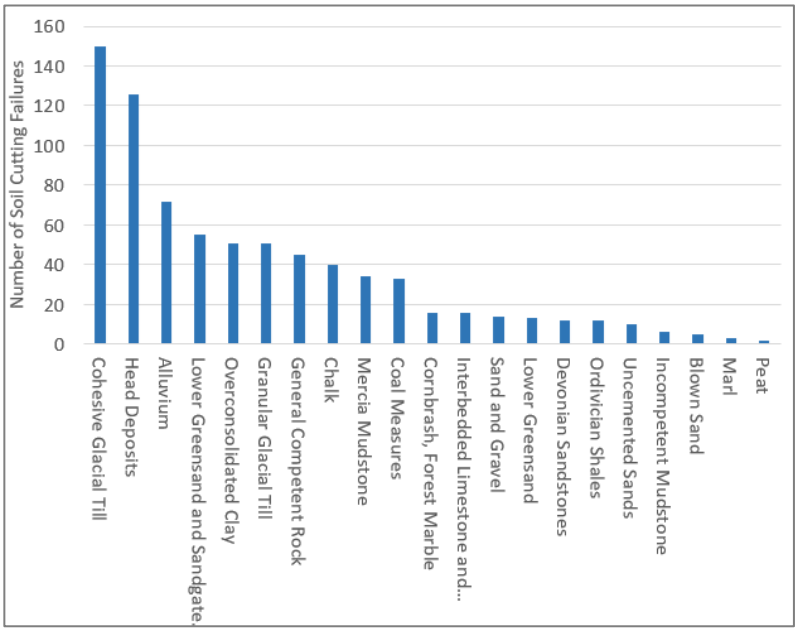

Figure 2-14 Number of soil cutting failures by geology April 2003 to April 2016

In this thesis, the novel method for the assessment of the vulnerability of cuttings against 'washouts' will be designed for chalk and for clayey soils. Chalk has been selected as it is required to assess the stability at Watford cutting, which is of special interest for NR. Clayey soils have also been assessed as they extends over a large part of the UK and is the type of material most vulnerable to failure.

2.6 Performance of the SCHI in practice

Since the SCHI was introduce in 2014, cutting failures that resulted in derailments from 2014 to 2018 (Watford and Loch Treig) were visually inspected prior to the failures taking place.

The derailment at Watford (September 2016), was visually inspected in August 2014. The resulting SCHI classified the cutting as category 'B' from ABCDE classification where 'A', represents the least and 'E' the most likelihood of failure (RAIB, 2017).

The derailment that took place at Lochailort was previously visually inspected just one month before the accident and the SCHI also failed to identify the risk of failure in the cutting, according to the RAIB report (RAIB, 2018a).

As such, while the current approach is on average better at identifying relative risk of failure within the cutting population, it is clear that is does not always give a good priori prediction. However, this only proves that cuttings can rapidly change condition, and clearly more rapidly than the frequency of inspections.

Looking at the total cutting failure population, data provided by NR from 2008 to 2018 is presented in Figure 2-15. The introduction of the SCHI in 2014 did not result in a reduction of the number of failures compared with the period 2008-2013 when the SSHI was applied, and the average number of failures remaining fairly constant over the years.

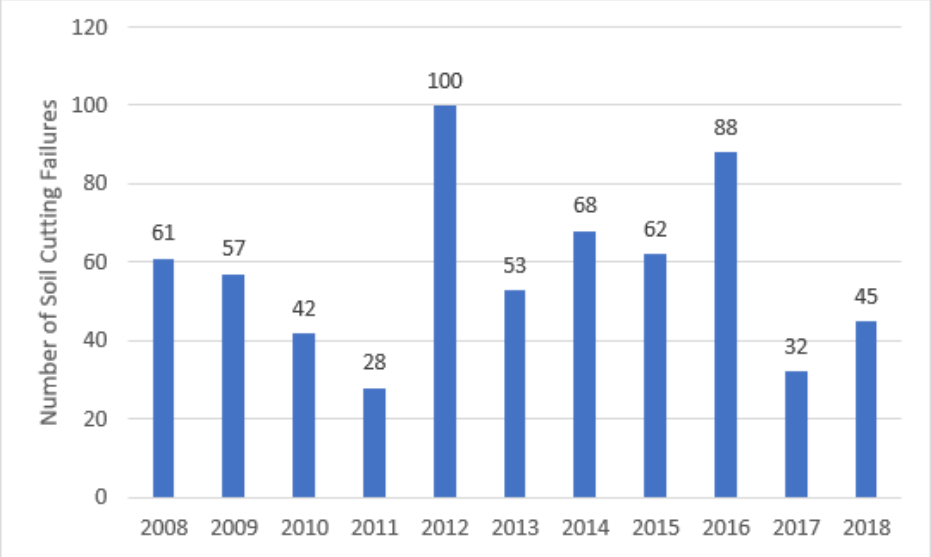

Figure 2-15 Number of soil cutting failures from 2008 to 2018

This shows that despite of the fact that the SCHI was derived from statistical analysis of all recorded date until its introduction, the system has failed to reduce the number of failures.

2.7 Discussion

The constant drive of NR to promote efficiency in their asset management system has been reflected with the inclusion of an improved hazard algorithm in 2014. However, it has not resulted in a reduction of the number of failures.

From the analysis carried out on NR's database for the number and type of cutting failures, it can be concluded that shallow failures are the most disruptive ones and cause the vast majority of derailments in the UK.

Given the fact that the number of failures still remain at levels recorded over 10 years ago, it is advocated that further work is required in this field to reduce future incidents and minimise failure and derailment risk. The analysis of recent failure data suggests that there are a number of approaches that could contribute to better understand failure prevention.

1. A revised classification system for shallow cutting failures that is easier to use and better reflects the causes and mechanisms of failure.

2. A revised hazard algorithm that considers susceptibility of different slope types to different failure mechanisms.
3. A better approach for determining the vulnerability of cutting slopes to rapid translation and washout failures that can rapidly change the hazard category, leading to failure without warning and ultimately train derailments.

It is important to remark that the classification of cutting failures does not take part in the current SCHI and therefore in the prevention of shallow cutting failures. Regardless of whether a new hazard index algorithm is implemented or not, the new classification system proposed in this thesis will contribute by itself to the improvement of the current NR system. Having an enhanced recognition system of the type of failures that took place in the past and the features associated to them, will help to understand the contribution of factors checked during visual inspections.

The next chapter will focus on the areas where the NR system is considered to be in need of improvement and the introduction of a proposed classification system for shallow cutting failures, as well as further guidance for the classification process.

Chapter3: Proposed system for classification of shallow failures in cuttings

Chapter 3 analyses and discusses the NR classification system for shallow cutting failures. A revised classification system is proposed, which addresses the limitations of the current system and should facilitate the process of failure classification by observation. A scoring system based only on visual features has been proposed to allow for a more objective approach to shallow failure classification. A diagram showing the proposed system process has been introduced at the end of this chapter in Table 3-1.

3.1 Limitations of the current classification system

An attempt has been made to classify failures using the existing 5 category system in 114 rapid response reports filed by Amey, NR's management service provider. These reports are populated following special earthworks examinations in response to incidents, and contain photographs and detailed descriptions of the events. The reports consulted referred to cuttings and natural slope failures between 31/01/2010 and 23/07/2017 which revealed limitations of the current approach in four broad areas:

1. The terms used in the system did not correspond with definitions used in previous classification systems, resulting in confusion when trying to convey and understand the nature of the failures..
2. Key information inherent in the definitions is not always available from visual inspection alone.
3. Some of the categories overlap, making it difficult to assign a particular failure in one category.
4. The lack of detailed descriptions for each category.

1) Lack of conservatism in the use of terms

The NR classification system includes terms that does not correspond with previous definitions given in the most popular classification systems to identify the same types of failure. The lack of backward compatibility with older literature is undesirable, as pointed out by Hungr et al., (2014).

Cutting inspectors may bring their own knowledge and experience to categorisation, and the lack of conservatism can lead to confusion and potentially incorrect classification.

This issue has been analysed by comparing the description of terms given by NR with the most generally accepted classification systems. The incorrect use of the terms such as

'translational failure', 'earthflow' and 'washout' is illustrated and analysed in the following paragraphs.

a. Translational failures

Despite translational sliding being an overall movement type in Varnes, (1978), the term 'translational failure' is not included in any of the major mass movement classification systems, breaking the principle of conservatism.

'Translational failure' might refer to any type of mass movement that moves with no significant rotation and therefore breaks the uniqueness criterion. The term could encompass a large variety of processes depending on the degree of deformation, the type of soil and the velocity of movement (e.g. Earth block slide, earth slide, debris slide, mudflow, debris flow).

As such, a different term that concisely defines the type of failure given in Figure 2-3, is advisable, where slide is the main mechanism of movement, with little degree of deformation and a well-defined slip surface.

b. Earthflows

In the example shown in Figure 2-4, the term 'earthflow' is considered as a rapid or extremely rapid mass movement that can be inferred with an extreme degree of deformation where the initial internal structure of the soil is completely lost. This definition does not match with the slow plastic movement adopted by the most widely adopted classification systems (e.g. Varnes, 1978; Cruden and Varnes, 1996; Hungr et al., 2001; Hungr et al., 2014), breaking again the principle of conservatism. Although the use of the terms 'earthflow' and 'rapid earthflow' was adopted to describe extremely rapid flows by Sharpe, (1938), and Varnes, (1958, 1978) respectively, in both cases the material involved were sensitive clays which are not encountered in the UK.

Therefore, considering that the term 'earthflow' is used in the major classification systems to describe a slow process, mainly occurring by sliding of the moving mass and with relatively little degree deformation, it is recommended that a different term to describe this type of failure is considered.

c. Washouts

Network Rail, (2015a) defines washout failure as an erosion process caused when surface water flows downslope on the face of the cutting, washing away particles along its path (Figure 2-5). However, the term 'washout' as a type of erosion process, is not

encountered in any relevant soil erosion classification system (e.g. Ayres, 1936; Bennett, 1939; Kohnke and Bertrand, 1959; Kozmenko, 1954; Sobolev, 1948; Fournier, 1956).

The term 'washout' is applied to surface and also underground erosion processes (Aberg, 1993; Israr and Indraratna, B. Rujikiatkamjorn, 2016). The term is also applied to the transport of contaminants in the atmosphere (Andersson, 1969) and in water (Lyubimova et al., 2016)

Due to the different processes historically associated with the term 'washout', it is advisable to use a revised term that concisely defines the type of process that is intended to describe.

2) Triggering factors

Another limitation of the NR system is that the classification is based on triggering factors that cannot be easily detected visually: weathering (translational failures and earthflow), increase in moisture content (translational failure), and increase in ground water level (earthflow) (Network Rail, 2015a).

Weathering can be extremely difficult to observe and quantify because it occurs internally, likewise, rising ground water levels and loss of matric suction cannot be always identified by visual inspections. Weathering has often been cited as the possible cause of failures when for whatever reason, the real cause has gone undetected or unrecognized (McColl, 2015).

As such, the use of weathering within the classification system could be of use when further investigations other than visual inspections have been carried out.

3) Overlapping of categories

Overlapping occurs when a cutting failure can be assigned to two different categories. Overlapping is present in the NR classification system (Network Rail, 2015a), in that, animal burrowing is both a possible triggering factor for a translational failure and also, a category on its own.

4) Lack of detailed descriptions

The lack of detailed descriptions of the different modes of failure in the CP5 Earthworks Asset Policy weakens the robustness of the classification system. The classification is based mainly on triggering factors and features representative of each type of failure are not described. Visual features that could help in the identification of the type of failure might include the degree of deformation, deformation features, depositional form,

fragmentation of the falling layer, characteristics of the sliding surface, presence of distinct scars, etc)

In Section 3.2, a revised classification system for shallow failures is proposed which aims to address some of the limitations of the current NR classification system discussed above.

3.2 A proposed classification system for shallow failures in transportation cuttings

Shallow failures have catastrophic consequences when they occur requiring railway lines to be closed to carry out remedial works. They result in great disruption and also present the highest risk to derailments. As such, the proposed classification system, presented in Table 3-1, is focused on shallow failures.

The classification system has been designed as a tool aiming to improve the NR system of recording failures, to enhance current and future understanding and ultimately, to contribute towards the prevention of accidents. The proposed system also allows its implementation in any future changes to the hazard index algorithm where the types of failures are considered.

3.2.1 Characteristics of the proposed classification system

The new system has been designed to embody the five main characteristics of a good classification system: conservatism, uniqueness, simplicity, flexibility and universality (Hungr et al., 2001;Hungr et al., 2014).

* Conservatism: The categories of the new system have been selected so that they are consistent with previous usage and adopt established terms to the greatest extent possible.
* Uniqueness: The categories are clearly defined and mutually exclusive
* Simplicity: The number of categories is reasonably small, to make the system simple and easy to use and review
* Flexibility: The system is sufficiently flexible to allow application both in cases where only meagre preliminary data exist, as well as those where data are detailed and abundant
* Universality: Each category is supported by a concise, but comprehensive formal definition

The new classification system follows a typological structure that corresponds to the historical preferred option to classify landslides (e.g. Varnes, 1958; Varnes, 1978; Cruden and Varnes, 1996). The terms adopted for each category are compounds of two descriptors: the type of material and type of movement. In the case of flow-like type of failures, subcategories have been introduced based on previous terms adopted (i.e. hillslope debris flow) or adding a new descriptor based on the primary trigger mechanism (i.e. runoff generated debris flow and man-made debris flow).

An extended use of 'debris' has been used in the proposed classification system for the flow-type mass movement to allow for the inclusion of fine material forming aggregations of soil peds.

The degree of deformation of the failing mass represents the distribution and continuity of relative movements of particles within the moving mass itself during and after the failure. A low degree of deformation is attributed to failures where the soil maintains its initial structure, whereas a high degree of deformation is attributed to failures where the initial structure of the soil is lost and the soil particles or aggregates can move apart from each other (Varnes, 1978).

The new classification system of shallow slope failures is divided in two main categories based on the different types of movements: Slides and flows, and is presented in Table 3-1 . Within each category, the failures are classified according to the degree of deformation and the type of material. Visual features associated with each type of movement are presented so that failures can be consistently classified by visual inspections.

There is a gradual transition between slides and flows. Translational slides in some cases, continue deforming as they move and slides transition into flows as a result of further disintegration, increase in water content or increase in pore water pressures (Varnes, 1978).

Table 3-1 Classification system for shallow slope failures

<table>
<tr><th>Type of movement</th><th colspan="2">Primary trigger factor</th><th>Degree of deformation</th><th>Principal Type of material</th><th colspan="2">Proposed terms</th><th>Network Rail existing terms</th></tr>
<tr><td rowspan="3">Slide</td><td colspan="2" rowspan="4">Gravity</td><td>Low or non-existent degree of deformation of the slide mass</td><td>Weak mudstones & siltstones, over consolidated clay)</td><td rowspan="3">Translational slides
(Varnes, 1978; Hutchinson, 1988; Cruden and Varnes, 1996; Hungr et al., 2014)</td><td>Earth block slide (Hugget, 1997)</td><td rowspan="3">Translational failure</td></tr>
<tr><td rowspan="2">Greatly deformed</td><td>80 percent or more of the particles smaller than 2 mm (Cruden and Varnes, 1996)</td><td>Earth slide (Cruden and Varnes, 1996)</td></tr>
<tr><td>Significant proportion of coarse material; 20 to 80 percent of the particles larger than 2 mm, and the remainder are less than 2 mm. (Cruden and Varnes, 1996)</td><td>Debris slide (Cruden and Varnes, 1996)</td></tr>
<tr><td rowspan="4">Flow</td><td rowspan="3">Water</td><td rowspan="2">Rainfall</td><td rowspan="3">Extremely deformed</td><td>Plastic material with at least 50 percent sand, silt, and clay size particles (Varnes, 1958;Varnes, 1978)</td><td colspan="2">Mudflow (Varnes, 1958;Varnes, 1978)</td><td rowspan="2">Earthflow</td></tr>
<tr><td rowspan="2">Non-plastic material from clay to boulders (plasticity index <5% in sand and finer fractions) (Hungr et al., 2001)</td><td rowspan="2">Debris flow</td><td>Hillslope debris flow</td></tr>
<tr><td>Failed drainage/Broken pipes</td><td>Runoff generated debris flow</td><td>Washout</td></tr>
<tr><td colspan="2"></td><td></td><td>Man-Made debris flow</td><td></td></tr>
</table>

3.2.2 The proposed classification system: Method

To develop a new system it was first necessary to study in detail the nature of failures that are currently affecting the railway network.

Reports filed by Amey between 31/01/2010 and 23/07/2017 as part of their asset management system of the network have been reviewed.

These reports are populated following special earthworks examinations in response to incidents. They are produced regardless of whether any particular incident is subsequently classified as a reportable failure.. Of these reports, 114 were related to shallow soil failures in cuttings which would be classified as either earthflow, translational failure or washout.

The value of assessing the smaller subset of data related to the rapid response reports, rather than the full database of failures and incidents, is in the availability of photographs of the events within the original reports. The reports can also contain images and a more detailed descriptions than the database which typically covers the failure classification and very limited additional information. These reports have been used to assess the modes of failure and their fit with the existing classification scheme. Insights drawn from the limitations identified in Section 3.1 where then used when proposing the new classification system.

The new system is described in detail in the following sections.

3.2.3 Definition of categories

In this section, a detailed description of the different categories proposed is presented.

The classification system consists of two main categories for shallow translational failures: Slides and flows. The motivation to separate Slides from Flows stems from the different degree of deformation and subsequent runout of deposits presented, which are paramount in the preservation of the railway track. For each category, three subsections are included: 1) the reasoning for the selection of the terms chosen, 2) the possible triggering mechanisms and 3) the visual features associated with each or several categories.

1. Slides

Slides would be the equivalent movement type for the NR term translational failure. Slides may occur in a range of different materials, the more competent the material the

less degree of deformation. For example, the case shown in Figure 2-3 appears to show little internal deformation, however, the rapid response report shows that slides with significant deformation actually occur commonly within rail cuttings. Consequently, three sub-terms are proposed based on the material type and deformation: Earth block slide, Earth slides and Debris slides.

a) Earth block slide

Reasoning for the selection of the term:

The terms Block slide, Slab slide, and Earth block slide were initially considered for the new classification. Earth block slide was selected over block slide or slab slide in order to maintain backward compatibility with older literature.

A block slide is a failure where a mass consisting of unweathered, fairly hard and jointed material progresses out, or down and out, as a single or few units along a more or less planar surface. This is a type of failure where the mass is essentially undeformed, and the moving mass may even slide out on the original ground surface (Varnes, 1978, Skempton and Hutchinson, 1969).

Although the definition of block slide proposed by Varnes, (1978) and Skempton and Hutchinson, (1969) can still be valid for cohesive soils, block slide is a term mostly associated with rocks.

The term ‘slab slide’ was introduced by Skempton and Hutchinson, (1969) and Hutchinson, (1988) and defined as a variety of block glides in slopes consisting of coherent, fine soils or coarser debris with a fine matrix. The term ‘slab slide’ avoid the common association with rocks presented by ‘block slide’. However, the term ‘slab slide’ breaks the principle imposed in the proposed system where terms consists of type of material followed by type of failure.

The term earth block slide has been used by Hugget, (1997) and (Keefer, 1999) as an equivalent of the term slab slide. The use of this term which is specific of clayey slopes better represents most of the block type of failures occurring in the NR cuttings and maintain consistency with the other terms proposed in the new classification system where categories are introduced by the type of material.

Triggering mechanisms:

* Weathering on a shear zone close to a surface of unweathered or lightly weathered bedrock (Ritchie, 1958).

* Raising of groundwater levels (Skempton and Hutchinson, 1969)
* Loading at the head or unloading at the toe (Ritchie, 1958).

Visual Features:

* The movement is characterised by sliding along a roughly planar surface with little rotation or backward tilting (USGS, 2016).
* Some degree of deformation is permitted although the material fails predominantly as a unit (Varnes, 1978, Skempton and Hutchinson, 1969).
* Presence of a few major breaks in the upper part of the failure (Ritchie, 1958).
* The head of the slide mass separates from stable soil along a deep vertical tension crack (Hungr et al., 2014)
* Differentiated slickensided slip and lateral surfaces (Ritchie, 1958).
* Competent cohesive soil (e.g. weak mudstones & siltstones, over consolidated clays)
* Toe may have steep front (Ritchie, 1958).
* Short runout distance

Based on the above the following definition for Earth Block Slide is proposed:

Earth block slide: '*a translational mass movement consisting of unweathered, fairly hard material that slides as a single or a few units along a more or less planar surface with little deformation and a small runout distance*'.

A representative example of an Earth block slide is illustrated in Figure 3-1.

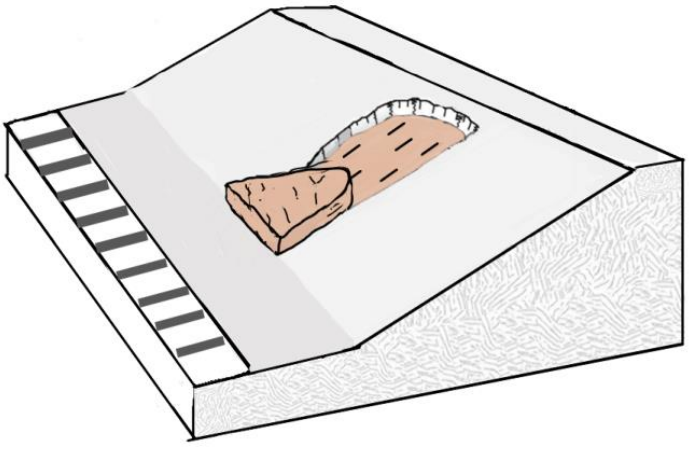

Figure 3-1 Representative illustration of 'earth block slide'

b) Earth Slides and Debris Slides

Reasoning for the selection of the term:

In all translational slides, the soil mass will move along a planar or slightly undulating surface before sliding out on top of the original ground surface. While deeper seated rotational slides may come to a natural stabilisation, translational slides may continue to move, with material breaking up if the velocity of movement increases (Cruden and Varnes, 1996). Shallower translational slides with higher degrees of deformation than earth block slides are often referred to as debris slides (e.g. Sharpe, 1939, Varnes, 1958).

Different terms used in relevant classification systems to refer to debris slide and earth slide are presented in Table 3-2.

Table 3-2 Summary of the terms used to define slides with high degrees of deformation

	Sharpe, (1938)	**Varnes, (1958)**	**Varnes, (1978)**	**Hutchinson (1988)**	**Cruden and Varnes, (1996)**	**Hungr et al., (2014)**
Coarse grained soil	Debris slide	Debris slide	Broken or disrupted debris slide	Debris slide	Debris slide	Gravel/sand/debris slide
Clayey Soil	Debris slide	Debris slide	Broken or disrupted earth slides	Not defined	Earth slide	Clay/silt/planar slide

The terms debris slides and earth slides have been used indistinctly by Sharpe, (1938) and Varnes, (1958). However, the two-fold division by Cruden and Varnes, (1996) is proposed to distinguish between earth slides, which are principally low sensitivity clay-rich materials of intermediate consistency and debris slides, which contain a significant proportion of coarse materials (Cruden and Varnes, 1996)

Triggering mechanisms:

* Increase in ground water within the slide due to intense rainfall (Baum et al., 2003; Ng and Shi, 1998; Rahardjo et al., 2007)
* Rainfall infiltration causing progression of a wetting front and a reduction of shear resistance due to the decrease of matrix suction in the unsaturated soils (Fredlund and Rahardjo, 1993; Rahardjo et al., 1995).
* In clays, a reduction in undrained shear strength due to increasing water content (Cruden and Varnes, 1996)

* Internal seepage leading to a destabilising rise in pore water pressure (Iverson and Reid, 1992)
* Loading at the head or unloading at the toe cutting (Ritchie, 1958).

Visual Features

* The movement is represented by sliding along a roughly planar surface with little rotation or backward tilting (USGS, 2016).
* The main body of the slide mass may be greatly deformed and quite blocky (Hungr et al., 2014;Kojan et al., 1972), although commonly breaks up into many more or less independent units (Sharpe, 1938;Varnes, 1958).
* The deformation of the soil is characterised by undulating surface with ripple like structures (Varnes, 1958).
* Ground cracking in brittle material and a lobate toe when the displaced soil reaches the foot of the slope may be present (Borgomeo et al., 2014).
* Slicken-sided lateral margins and a distinct slicken-sided surface where the translational movement takes place (Hungr et al., 2001)
* A steep main scarp that separates the undisturbed ground at the upper edge with the head of the failure(Hungr et al., 2014; Turner & Schuster, 1996)
* The material is mostly coarse grained in debris slides and clay-like in earth slides. As a reference, for earth slide 80 percent or more of the particles are smaller than 2 mm (Cruden and Varnes, 1996) and for debris slide, 20 to 80 percent of the particles larger than 2 mm, and the remainder are less than 2 mm. (Cruden and Varnes, 1996)

As such, the following definitions are proposed:

Earth Slides: *'a translational mass movement consisting of low sensitivity clay-rich materials that slides along a more or less planar surface with a significant degree of deformation but maintaining some of the initial internal structure of the soil'*

Debris slides: *'a translational mass movement consisting of soils containing a significant proportion of coarse materials that slides along a more or less planar surface with a significant degree of deformation but maintaining some of the initial internal structure of the soil'*

Representative examples of debris slide and earth slide are illustrated in Figure 3-2 and Figure 3-3.

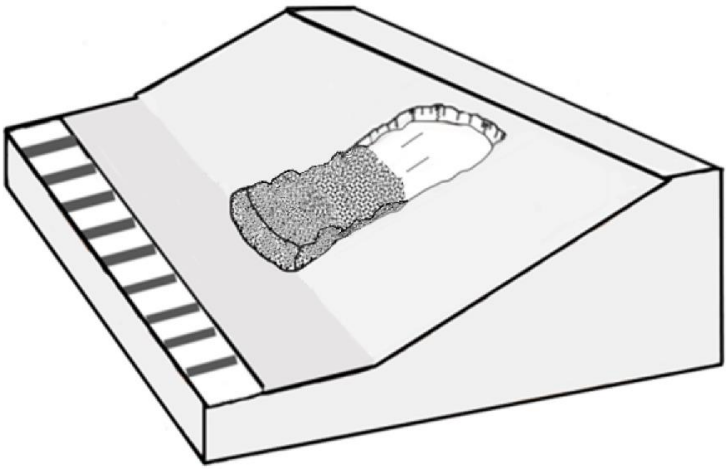

Figure 3-2 Representative illustration of Debris Slide

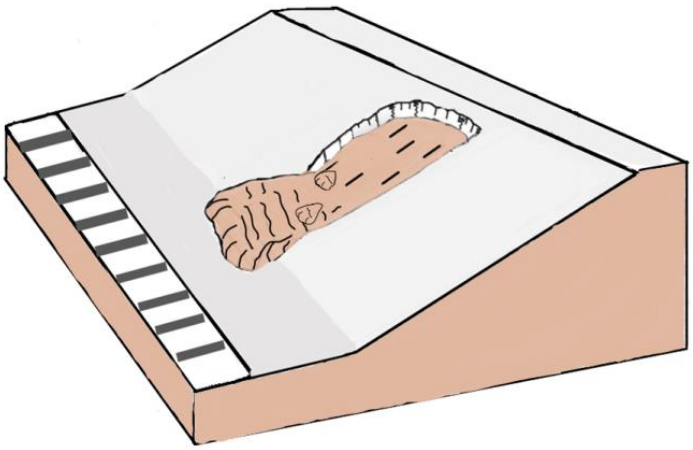

Figure 3-3 Representative illustration of Earth Slide

2. Flows

Flows are a type of failure where the movement is essentially by flowing of the soil material rather than by sliding (Hansen, 1973) and individual particles move separately (Goudie, 2004) rather than as a soil mass. Frequently, there is a progression from slides to flows, depending on the water content, mobility, and evolution of the movement (Highland and Bobrowsky, 2008).

For flows, different terms have been adopted to refer to this process in some of the major mass movement classification systems: mudflows, debris avalanches and debris flows.

The terms mudflow and debris flow are adopted in the proposed classification system depending on the materials being transported and the failure triggering mechanism.

a) Mudflows

Reasoning for the selection of the term:

Mudflow is a very rapid to extremely rapid flow of saturated plastic material. This broad description of mudflows has been adopted by Sharpe, (1938), Varnes, (1958) Varnes, (1978), Hungr et al., (2001) and Hungr et al., (2014). It may be considered as a large scale channelised failure (Sharpe, 1938, Hungr et al., 2001, Hungr et al., 2014) or without specification in that respect (Varnes, 1958, Varnes, 1978).

In the context of this thesis, infrastructure cuttings, the definition of Varnes, (1958) and Varnes, (1978) is adopted for mudflow, a flow containing material that is sufficiently wet to flow rapidly (commonly as a result of unusually heavy precipitations) with at least 50 percent sand, silt, and clay-sized particles.

Triggering mechanisms

* Thin soils overlying bed rocks, especially on steep slopes, get saturated very fast after heavy rains. Rapid mixing of the originally stiff or dry clayey matrix with surface water, raise the water content to or above the liquid limit.(Hungr et al., 2001)
* Freeze-thaw action may also cause mudflow. During summer, the frozen soil thaws and turns into saturated mud that flows downhill (Kimei and Khabongo, 2004).
* When the velocity of an earth slide increases, destruction of cohesive bonds and undrained loading from the headward part decreases its viscosity resulting in a mudflow (Goudie, 2004).

Visual features

* Mudflows are very mobile and can flow downslope quickly. They tend to spread out into a flat fan or a thin sheet (Goudie, 2004).
* The mass movement has the appearance of a low viscosity flow, lower viscosity than debris flows and with greater water content (Hungr et al., 2014).

* Soil is mostly clay-like. As a reference: material with at least 50 percent sand, silt, and clay size particles (Varnes, 1958; Varnes, 1978)
* Long runout distances usually overtopping the railway track.
* As in the case of debris flows the original block units are disintegrated into small fragments to the point that features such as undulating surface with ripple like structures, ground cracking and a lobate toe are removed (Ritchie, 1958).
* Lack of blocky units and minor scarps (Ritchie, 1958).
* Main scar and slickensided slip surfaces may be present when mudflows form as a result of gradation from earthslides.

As such, the following definition is proposed:

Mudflow: *'a rapid to extremely rapid shallow translational mass movement consisting of saturated mud that moves as a flow. The soil presents an extreme degree of deformation completely losing any degree of particle aggregation and tend to spread out into a flat fan or a thin sheet'*

A representative example of mudflow is illustrated in Figure 3-4.

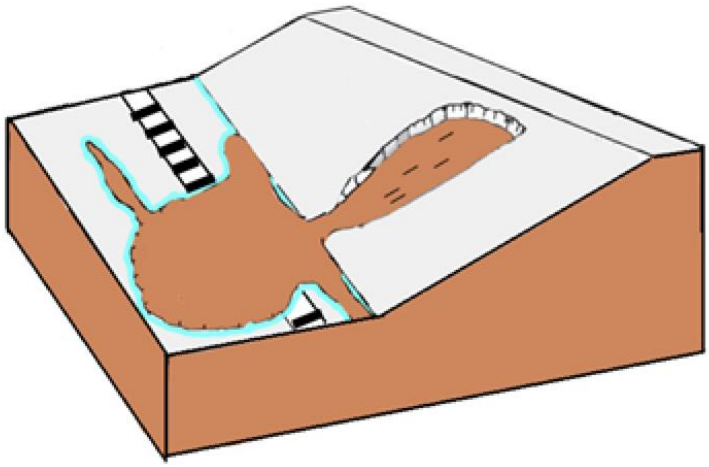

Figure 3-4 Representative illustration of mudflow

b) Debris flow

Reasoning for the selection of the term:

Sharpe, (1938), Varnes, (1958), Varnes, (1978), Cruden and Varnes, (1996), Hungr et al., (2001) and Hungr et al., (2014) referred to 'debris avalanches' as a gradation from 'debris slides' and as a result of an increase in water content, velocity or the steepness of the slope. Debris avalanches are defined by Cruden and Varnes, (1996) as extremely rapid

open-slope flows and originated when a debris slide mass accelerates, disintegrates, and enlarges through entrainment (Hungr et al., 2014).

Rapp, (1963) and Temple and Rapp, (1972) recommended that the term avalanche should be used only in connection with mass movements of snow, either pure or mixed with other debris.

Debris avalanche was considered as a type of debris flow by Varnes, (1978) and Hutchinson, (1988) and the same approach has been followed in the proposed classification.

Although the use of the term 'debris avalanche' for the type of failure normally occurring in transportation cuttings is widely used by different authors, it is commonly associated with an image that would be quite different to the case here intended, leading to unnecessary confusion, therefore the term debris avalanche has been discarded for the classification and debris flow is proposed instead.

Debris flow is a very rapid to extremely rapid flow of saturated non-plastic debris (Plasticity Index <5% in sand and finer fraction) in a steep slope.

Debris flows can be triggered by different factors, giving raise to two terminologies as follows, adopted for the proposed classification:

1) *Hillslope debris flow* is defined by Hutchinson, (1988) as a very rapid to extremely rapid unconfined flow that originates by shallow failures in unconsolidated material at steep slopes. As translational sliding continues, the displaced mass breaks up, gains velocity and then flows, becoming a debris flow rather than a slide (Varnes, 1978). Hillslope debris flows in clays, differentiate from mudflow by the lower plasticity, higher viscosity and the aggregation of clay particles in the form of soil peds.

2) Channelised debris flows is a very rapid to extremely rapid flow of saturated non-plastic debris in an stablished steep channel (Hungr et al., 2001). Channelised debris flows initiate by mobilization of the channel bed (Takahashi, 1991). Water flowing over the ground surface apply a shear stress that if high enough leads to mobilisation of the surface layer (Takahashi, 1991; Gregoretti et al., 2016; Berti and Simoni, 2005).
   However, the term '*runoff generated debris flow'* has been used indistinctively to define channelised debris flow by some authors (e.g. Tognacca et al., 2000;

Degetto et al., 2015; Berti et al., 2020). This term better represents the mechanism of failure and avoids the use of 'channelised' that is not a necessary characteristic in transportation cuttings.

In relation to the type of material, the term debris indicates the presence of a relatively high percentage of coarse fragments (Varnes, 1978). However, for the purpose of an engineering-geological mass movement classification, the grain-size criteria has been avoided in debris flows since it has little significance (Hungr et al., 2001) due to the fact that the percentage of coarse materials, when embedded in a clay matrix, have little effect on the mechanical behaviour of the flowing mass.

Although the term runoff generated debris flows is applied to soils containing a significant proportion of coarse materials, there is enough evidence that this type of failure can also occur in clayey soils where fines are aggregated in soil peds behaving as a granular material (Mehta et al., 1989; Foster, 2010; Jain and Kothyari, 2009). As such, the term 'debris' has been maintained based on this premisses.

A third type of debris flow, *man-made debris flow*, specific of transportation cuttings occurs as a result of water originating from a failure of the drainage system that can lead to hillslope debris flow or runoff generated debris flow. This type of failure is not necessarily associated with extreme weather events, although in practice this is likely to still be the case.

Triggering mechanisms

1) Hillslope debris flows:

* When a slope become unstable, such as during the downfall of weathered slopes in steep topography (Highland and Bobrowsky, 2008)
* Rainfall-induced mass movement along the sliding surface leads to crushing of aggregates, resulting in the liquefaction along this surface and leads to rapid movement and long runout distance (Sassa, 1998).
* Static liquefaction where a sudden increase in pore water pressure is experienced above the impermeable bed under high intensity rainfall (Reid et al., 1997).
* When the movement of debris slides is constrained, the soil (if loose) experiences a contraction in the lower portion of the mass movement. Contraction produces momentary excess pore pressures that contributes to the weakening of the mass and enhance the transformation from

localised failure to generalised flow (Bishop, 1973; Iverson and Major, 1986a; Eckersley, 1990;Iverson et al., 1997; Iverson, 1997)

2) Runoff generated debris flow:

The triggering mechanisms is the shear stress that overland flow (runoff) applies over the ground surface.

Rainfall first saturates soil deposit laying over a slope and then, when the rate of rainfall exceed the rate of infiltration, overland flow develops over the face of the cutting. (Gregoretti, 2000). Overland flows first initiate the movement of small particles, then when the rate of overland flow reaches a threshold, a sudden scour is first observed to takes place at some location that rapidly cascades to other parts of the slope (Gregoretti, 2000).

3) Man-made debris flow:

Water leaking from a pipe or drainage can lead to instability of the cutting in several ways.

* Saturation of the soil layers, seepage, mounding of the water table and accelerated weathering can initiate failure by sliding that in turn can progress into flows.
* Hydrodynamic forces applied by overland flow over the ground surface

Visual Features

* As a consequence of the more rapid movement, debris flows can be differentiated from debris slides by their larger run-out and an extreme degree of deformation. The original block units are disintegrated into small fragments to the point that features of debris slides such as undulating surface with ripple like structures, and lobate toe are removed (Coussot and Meunier, 1996).
* The component velocities in the displacing mass of a flow mimic those in a viscous liquid (Highland and Bobrowsky, 2008).
* The depositional form constructed by debris flows is a laterally unconstrained apron. The mass movement has the appearance of a low viscosity flow with long runout distances usually overtopping the railway track.

* Lack of blocky units and minor scarps (Ritchie, 1958).
* Main scar and slickensided slip surfaces may be present when debris flows form as a result of gradation from debris slides (only applicable to hillslope debris flow and some man-made debris flows).
* High water content in runoff generated debris flow but no necessary in hillslope debris flows (Hungr et al., 2001).
* Low points at the crest of the cutting where overland flows accumulate (only applicable to runoff generated debris flow)
* Water leaking from a pipe or drainage (only applicable to man-made debris flow)
* Non-existence or poor working conditions of the crest drainage

Therefore, the following definition is proposed:

Debris Flow: *'a very rapid to extremely rapid shallow translational mass movement of saturated non-plastic debris (Plasticity Index <5% in sand and finer fraction) in a steep slope that moves as a flow rather than sliding. The soil presents an extreme degree of deformation completely losing the initial internal structure with individual particles moving separately'.*

Hillslope debris flow: *'A debris flow triggered by shallow failures that break up, gain velocity and then flow.*

Runoff generated debris flow: *'A debris flow triggered by rainfall runoff shear stresses applied over the ground surface'.*

Man-made debris flow: *'A debris flow triggered by the effect of water leaking from a damaged drainage system'.*

A representative example of debris flow is illustrated in Figure 3-5.

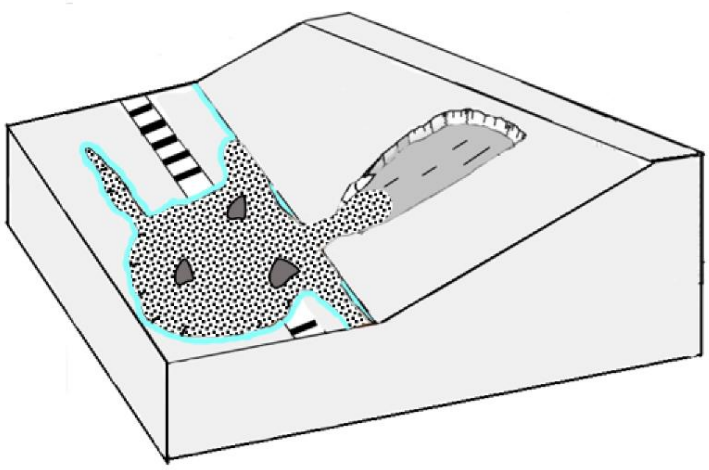

Figure 3-5 Representative illustration of debris flow

3.3 Guide to classifying cutting failures

The new classification system is based on visual features of the cutting failures. The visual features are classified in six groups: **Degree of deformation, Degree of Partition, Deformation Features, Runout Distances, Presence of water and Type of Soil.**

The description of the visual features is presented in Table 3-3 **and some of the features are presented in** Figure 3-6**.**

Table 3-3 Description of visual features associated to the classification system

Visual Features	Parameters	Description
Degree of deformation	**Low deformation**	The soil fails with none or little degree of deformation behaving as a block.
	Greatly deformed	The soil experiences significant degree of deformation but the internal initial structure of the soil is not completely lost. Transition between block and flow.
	Extremely deformed	The internal initial structure of the soil is completely lost. The soil behaves as a flow.
Degree of Partition	**Material fails predominantly as a unit or independent units**	Independently of the degree of deformation, the soil remains as a unit or is broken down into independent units that move apart from each other
	Material fails as a flow	Material deposits in different areas with particles/aggregates moving apart from each other
Deformation Features	**Undulating surface with ripple like structures**	The soil present certain plasticity and compressive forces lead to visible undulating surface deformation
	Distinct Lobate toe	Bulging of the toe
	Slicken-sided surfaces	Polished surface at the sliding surface or lateral margins
Runout Distances	**Short runout distances**	The soil can move over the sliding plane and the toe can reach the foot of the slope
	Long runout distances	When the toe or deposits reach the ballast but do not overtop the railway track
	Extreme runout distances	When the deposits overtop the railway track
Presence of water	**Presence of abundant water**	Presence of water is detected on the soil surface, ballast and drainage at the time of failure
Type of soil	**Grain size**	Determine fine vs coarse visually in the field

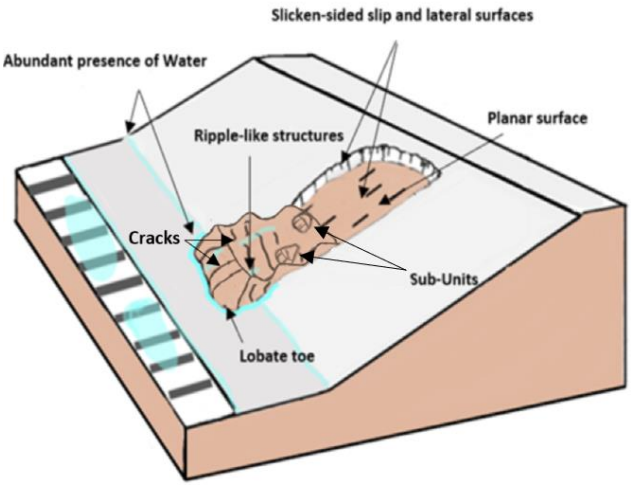

Figure 3-6 Visual features associated to the classification system

To help with the classification of railway cutting failures, a check list table with the visual features associated to each category has been produced. To determine which category a cutting failure should be associated, the check list table will be used with a system of scores in order to make the classification procedure as much objective as possible.

The proposed check list table and the classification of five types of cutting failures in the Network Rail network using the system have been included in Appendix A.

Since the subcategories of debris flows may present the same visual features, a flow chart step-by-step type has been designed to aid with the classification of shallow failures where the novel method can be used to differentiate hillslope debris flows from runoff generated debris flows (Figure A 1).

3.4 Proposal for a new hazard index algorithm

A revised classification system has been presented in an attempt to improve the robustness of the current NR classification system.

The proposed classification system could be implemented in future statistical algorithms as it account for the occurrence of historical failures by type.

A future statistical algorithm could include the two most valuable components of the former algorithms: the sounded approach of the SSHI based on the classification of historical failures by type and the SCHI approach where the weighting of parameters is based on a statistical analysis removing engineering judgement.

Once historical failures are classified by categories in accordance with the new classification system, for every type of failure the algorithm would analyse parameters more or less prevalent in the pre-failure examination of failed cuttings than the whole population of cuttings. Parameters more prevalent in the failed cuttings within each category, would be given a positive weighting in the future algorithm, the higher the prevalence the higher would be the weighting. Those more prevalent in the entire population would be negatively weighted. The parameter weightings would then be summed up for each category, and the highest hazard index score included in the corresponding Hazard Category.

A description of the principal characteristics of the NR soil cutting hazard indexes and the proposed hazard index is presented in Table 3-4.

Table 3-4 Characteristics of hazard index por application into the NR management system

Hazard Index	Characteristics of the Hazard Index
SSHI (2006-2014)	The algorithm is not statistical. It accounts for the type of failure and the weighting of parameters based on engineering judgement
SCHI (2014-Present)	The algorithm is fully statistical. It does not account for the types of failures in the weighting of parameters
Proposed Hazard Index	* The algorithm would be fully statistical and would account for the types of failures in the weighting of parameters *Same recognised sounded approach of the SSHI * Not based on subjectivity associated to engineering judgement * **Classification of historical failures by type using the new classification system**

3.5 Conclusions

Classifying historical failures accurately poses great benefits towards gaining a better understanding of the occurrence of different failure types and using this knowledge will help reduce future incidents.

The analysis of the NR classification system evidence the need for an improvement. Lack of conservatism in the use of terms, classification based on triggering factors, overlapping of categories, lack of detailed descriptions and guidance to classify cutting failures have been identified in the current classification system weakening the robustness of the process.

A new classification system for cutting failures has been proposed in an attempt to improve the current NR classification system. More appropriate terms and detailed descriptions have been introduced and overlapping of categories has been eliminated. A guide to classify cutting failures has also been introduced and the process of classification has been 'automatised' using a system of scores so that only visual features are required.

The proposed system has been used to classify five real cases of railway cuttings. Using the score system all the cases have been successfully classified as intended in an objective manner.

With the introduction of the proposed classification system, it is expected that cuttings in the NR network may now be classified more consistently and contribute to a better performance of possible future algorithms.

Chapter4: Continuum methods for slope stability analysis

Continuum methods for slope stability analysis involve soils considered as a continuum and porous medium where the water movement within the pores can be calculated using the Richards equations.

In this thesis, the slope stability at Watford has been assessed considering the distribution of pore water pressures over time to account for climatic conditions and coupling it with stability analysis using the limit equilibrium method.

In cold rainy seasons, rising of pore water pressures takes place from the addition of rainfall water to the soil via infiltration. As a result, the effective shear stresses within the soil are reduced and the cuttings become more vulnerable to failure. In warm dry seasons, precipitations are less frequent and root water uptake is increased resulting in the net loose of water via evaporation and transpiration. This reduction in moisture content leads to the development of negative pore water pressures within the soil that contribute to the stability of the slopes.

The effect of climatic parameters is assessed by adding sources of water (infiltration) to the Richards equations to simulate precipitation and sinks to simulate evaporation and transpiration.

The equations behind the movement of water within the soil, into the soil (rainfall infiltration) and out of the soil due to thermodynamic principles (evaporation) and out of the soil due to root water uptake (transpiration), are solved using continuum numerical methods (e.g. the finite element method) via numerical software such as SEEP/W for specified time steps. From these equations, the pore water pressures can be obtained at any time and location of the model.

The stability of the slope is assessed at each time step by the application of equilibrium equations to the sliding soil mass (limit equilibrium methods) or to discrete elements of soils (continuum numerical methods) accounting for the distribution of pore water pressures (coupled transient seepage-limit equilibrium).

In this chapter, the equations used by SEEP/W (the software used for transient seepage at Watford), to describe the movement of water within the soil and between the soil and the atmosphere are described. The principles behind the limit equilibrium methods of slope stability analysis and in particular the Spencer method used in SLOPE/W for the stability assessment at Watford are also introduced.

4.1 Water movement within the soil

Water movement within the soils is driven by water energy gradients (Fredlund and Rahardjo, 1993). Water moves from locations with higher energy to locations with lower energy and this property is reflected in the governing equations of all types of fluid motion.

Water energy is normally expressed as energy per unit weight. The total energy of water is presented as the hydraulic head (h) and depends on three parameters: Pressure head, elevation or gravitational head, and velocity head.

In geotechnical engineering, velocity head is normally neglected in groundwater flow since the velocity of water within the soil is very low. The hydraulic head is then described as (4.1):

$$h = \frac{u_w}{\gamma_w} + z \tag{4.1}$$

Where,

h =hydraulic head (m);

$\mathrm{u_w}$ =pore water pressure (Pa);

γ_w =specific weight of liquid water $\left(\frac{\mathrm{N}}{\mathrm{m^3}}\right)$;

z =elevation head (m);

$\frac{\mathrm{u_w}}{\gamma_\mathrm{w}}$ =pressure head. When negative it is called matric suction (ψ) (m);

The movement of water within the soil depends on the permeability of the soil (K) and the soil moisture content (θ). When all the pores in the soil are filled with water, the soil is saturated, and the equations of movement are known as the Darcy's flow equations. When the soil is unsaturated, more parameters are involved in the equations governing the flow movement and they are known as the Richards equations (Bear and Corapcioglu, 2012).

4.1.1 Saturated flow

The flow of water in saturated soils is calculated using Darcy's law. It is based on the principle that the flow rate through the soil is proportional to the hydraulic head gradient

and the hydraulic conductivity in the direction of the flow. Considering that the principal directions of anisotropy coincide with the x, y, and z coordinates, assumption usually valid for soils, the three-components constituting the Darcy's law equations are expressed as:

$$q_y = -K_y \frac{\partial h}{\partial y} \tag{4.2}$$

$$q_x = -K_x \frac{\partial h}{\partial x} \tag{4.3}$$

$$q_z = -K_z \frac{\partial h}{\partial z} \tag{4.4}$$

Where,

q_x, q_y and q_z are the flow rate of water per m^2 section in the x, y and z directions.

K_x and K_y and K_z are the hydraulic conductivities in the x, y and z directions.

Equations (4.2), (4.3) and (4.4) are the momentum conservation equations in the x, y and z directions respectively and describe the movement of water in saturated soils under steady conditions.

Darcy's equations for unsteady flows need corrections in terms of the time derivatives of the pressure gradients (Burcharth and Andersen, 1995; Hall et al., 1995; Gu and Wang, 1991). However, for the analysis of groundwater flows, steady-state conditions prevail, and transient groundwater flows can be approximated using Darcy's law (Mongan, 1985).

4.1.2 Unsaturated flow

Darcy's Law was derived from experiments conducted on saturated soils. Richards, (1931) extended Darcy's equations to be applied to unsaturated soils for steady and transient flows.

The hydraulic conductivity in homogeneous saturated soils is constant, whereas in unsaturated soils it depends on the soil moisture content. As the soil moisture content usually varies from one point to another in unsaturated soils, and so does the hydraulic conductivity.

In unsaturated soils, negative pore water pressures develops as the soil dries and air enters into the pores, known as the soil matric suctions (ψ) (Fredlund and Xing, 1994).

A high matric suction corresponds to lower water content and hydraulic conductivity than a low matric suction. Therefore, the relationship between the hydraulic conductivity and the soil water content (hydraulic conductivity functions) and between the soil water content and the matric suctions (soil water characteristic curves) are needed to describe the flow in unsaturated soils.

Richards equations actually refers to four equations in 3D analysis. One equation corresponds to the conservation of mass, and the other three equations correspond to the conservation of momentum in three perpendicular directions.

The transient term in Richards equations is given by the volumetric water content (θ). It defines the amount of water contained within the pores in the soil and is calculated as the volume of liquid water per volume of bulk soil.

$$\theta = \frac{V_W}{V_{WET}} \tag{4.5}$$

Where,

V_W =volume of water;

V_{WET} =total volume of the wet soil;

The conservation of mass is described mathematically in vectorial form as:

$$\frac{\partial \theta}{\partial t} + \nabla \cdot \vec{\boldsymbol{q}} = 0 \tag{4.6}$$

Introducing ψ into (4.2), (4.3) and (4.4), a valid expression for unsaturated soils is obtained

$$\vec{\boldsymbol{q}} = -K_x \frac{\partial \psi}{\partial x} \hat{\boldsymbol{\imath}} - K_y \frac{\partial \psi}{\partial y} \hat{\boldsymbol{\jmath}} - K_z \left(1 + \frac{\partial \psi}{\partial z}\right) \hat{\boldsymbol{k}} \tag{4.7}$$

In addition, for unsaturated flows, the hydraulic conductivity and matric suctions are expressed as functions of the volumetric water content θ.

$$K = K(\theta) \tag{4.8}$$

$$\psi = \psi(\theta) \tag{4.9}$$

Hence, substituting (4.7), (4.8) and (4.9) in (4.6), the general unsaturated-flow equation known as Richards equations for three-dimensional flows reads as follows

$$\frac{\partial \theta}{\partial t} = \frac{\partial}{\partial x}\left(K_x(\theta)\frac{\partial \psi(\theta)}{\partial x}\right) + \frac{\partial}{\partial y}\left(K_y(\theta)\frac{\partial \psi(\theta)}{\partial y}\right) + \frac{\partial}{\partial z}\left(K_z(\theta)\left(\frac{\partial \psi(\theta)}{\partial z} + 1\right)\right) \tag{4.10}$$

Richards equations are the equations universally applied for water movement within the soil in geotechnical engineering and are profusely applied in numerical methods for mass movements stability analyses (e.g. Berti and Simoni, 2005;Melchiorre and Frattini, 2012; Baum et al., 2008; Cho, 2014).

The Richards equations are also extensively applied to hillslope or catchment-scale subsurface flow problems. (e.g., Stephenson and Freeze, 1974; Nieber and Walter, 1981) as well as redistribution of infiltrated rainfall (e.g., Buchanan and Savigny, 1990; Iverson, 2000).

The relationships between matric suctions and volumetric water content $\psi = \psi(\theta)$ and between hydraulic conductivity and volumetric water content $K = K(\theta)$ are discussed in the next section.

4.1.3 The soil water characteristic curve

In unsaturated soils, the relationship between the soil moisture content, hydraulic conductivity and matric suctions need first to be obtained for the particular soil to be able to model the flow of water. These relationships are provided by the Soil Water Characteristic Curve (SWCC), that correlates the volumetric water content with the soil matric suction, and the hydraulic conductivity function, which correlates the hydraulic conductivity with the soil water content.

The SWCC is different for each soil and mainly depends on the particle size distribution and the characteristics of the pores. The SWCC can be determined experimentally but this approach requires numerous and laborious tests. To facilitate the process, empirical models are used instead where only a few values are obtained through experiments, and the rest of the values are interpolated using a series of fitting parameters.

A number of SWCC equations have been proposed in the literature (e.g. Williams et al., 1983; Brooks and Corey, 1964; McKee and Bumb, 1984; McKee and Bumb, 1987; van Genuchten, 1980; Fredlund and Xing, (1994).

Leong and Rahardjo, (1997) proved that the equations that give a sigmoid curve like the one presented in (Figure 4-1) better approximate to the actual SWCC. They also concluded that four-parameter equations are more flexible and better represent the real SWCC obtained from experimental data.

Based on this statement, they recommended the use of the equations proposed by van Genuchten, (1980) and Fredlund and Xing, (1994), over those proposed by Williams et al., (1983), Brooks and Corey, (1964), McKee and Bumb, (1984) and McKee and Bumb, (1987).

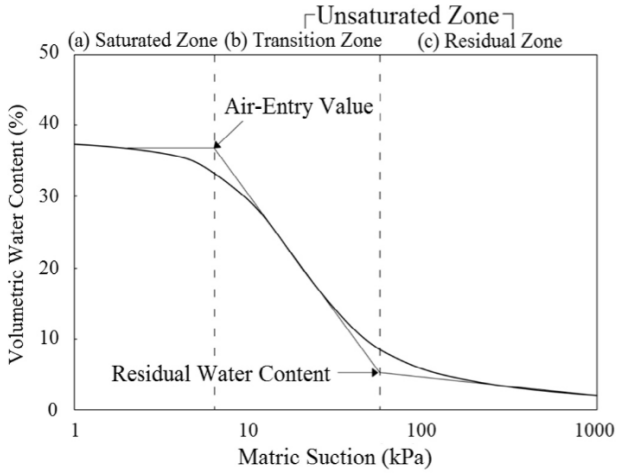

Figure 4-1 Typical sigmoidal soil water characteristic curve (SWCC) and its zones of desaturation (Kim et al., 2015)

Direct estimation of the hydraulic conductivity in unsaturated soils requires expensive equipment and a long time to conduct the experiments. As a consequence, the unsaturated hydraulic conductivity is preferably obtained indirectly through the calculation of the SWCC (van Genuchten, 1980).

The combined model using the SWCC proposed by van Genuchten, (1980) and the derivation from the SWCC of the hydraulic conductivity function proposed by Mualem, (1976) is currently the most used approach by researchers. Many authors have considered it as appropriate to a large range of soil, especially for fine soils (Bouchemella et al., 2016).

The mathematical expressions proposed by van Genuchten reads as follows:

$$\Theta = \left(\frac{1}{1 + (\lambda\psi)^n}\right)^m \tag{4.11}$$

Where λ, n and m are fitting parameters and Θ is the degree of saturation obtained as:

$$\Theta = \frac{\theta - \theta_r}{\theta_s - \theta_r} \tag{4.12}$$

Where θ_s =saturation volumetric water content and θ_r =residual volumetric water content.

When the three fitting parameters in van Genuchten, (1980) model are not available, an optimisation may be performed to obtain the most proximate fitting parameters of any given SWCC (e.g. SEEP/W, 2014). Using the derived fitting parameters, the hydraulic conductivity function can be obtained from Mualem's, (1976) model (4.13) that only requires the introduction of the saturated hydraulic conductivity (K_{sat}) (Schaap and van Genuchten, 2006).

$$k(\psi) = K_{sat} \frac{\left[1 - \left(a\psi^{(n-1)}\right)(1 + (a\psi^n)^{-m})\right]^2}{\left[((1 + a\psi)^n)^{\frac{m}{2}}\right]} \tag{4.13}$$

Where k_{sat} = saturated hydraulic conductivity, a, n, m = curve fitting parameters and $n = 1/(1 - m)$.

SWCC can be given by the chart gravimetric water content vs matric suction. The gravimetric water content w, is defined as the mass of water per mass of dry soil. The conversion between the gravimetric and the volumetric water content is given as:

$$\theta_v = \theta_g \frac{\gamma_{bulk}}{\gamma_{water}} \tag{4.14}$$

Once the equations describing the movement of water within the soil have been determined, the next step is the introduction of the equations that describe the movement of soil moisture at the interface soil-atmosphere through the processes of infiltration from rainfall, evaporation from thermodynamic processes and transpiration from vegetation.

They are modelled in finite element analysis as a boundary condition between the surface of the soil and the atmosphere. The equations describing these processes are introduced in the next section.

4.2 The soil surface boundary condition

The term ;evaporation' is referred to the moisture movement from a water surface or a soil surface towards the atmosphere due to radiation and aerodynamic processes, while the word 'transpiration' is referred to an upward moisture movement through plants roots within the soil (Fredlund et al., 2012). The sum of evaporation and transpiration is called evapotranspiration.

To assess the stability of cuttings along time, changes of soil moisture content caused by evapotranspiration and infiltration from rainfall are to be considered.

Interaction of the soil surface with the atmosphere is simulated by using a climatic boundary condition that accounts for infiltration, evaporation and transpiration.

4.2.1 Equations for infiltration

The equations governing the rate of rainfall infiltration into the soil are well stablished, and different equations are available depending on the degree of accuracy intended for the analyses (e.g. Richards, 1931; Green and Ampt, 1911; Horton, 1940).

The 1D Richards equation provides a more rigorous analysis of infiltration than the empirical equations proposed by Horton, (1940) or Green and Ampt, (1911), which are limited by the assumption of surface ponding (Briggs, 2011). 1D Richards equation describes infiltration processes without the assumption of surface ponding and accounts for changes in hydraulic conductivities with soil moisture content.

Applications of 1D Richards equation for infiltration processes are commonly used in the literature (e.g. Varado et al., 2006; Bah et al., 2009; Turkeltaub et al., 2014; Lai et al., 2016).

The 1D Richards equation is presented as:

$$\frac{\partial \theta}{\partial \psi}\frac{\partial \psi}{\partial t} = \frac{\partial}{\partial z}\left(K_z(\psi)\frac{\partial \psi}{\partial z}\right) + \frac{\partial}{\partial z}K_z(\psi) = \frac{\partial}{\partial z}\left(K_z(\psi)\left(\frac{\partial \psi}{\partial z} + 1\right)\right) \tag{4.15}$$

Where,

K_z =vertical hydraulic conductivity.

4.2.2 Equations for evapotranspiration

Evapotranspiration causes changes in soil moisture content and subsequently in hydraulic conductivities. These changes directly affect the distribution of rainfall into infiltration and surface water runoff and consequently the stability of the slopes.

Equations to describe evapotranspiration rates are based on thermodynamic principles and involve a considerable number of parameters, not familiar for geotechnical engineers. The equations aim to obtain the vapour flux density or evapotranspiration rate E at the soil surface.

Methods to obtain E based on climatic parameters are called micro-climatic methods. They are classified in three groups: a) the aerodynamic or mass transfer methods, b) the energy balance method and c) the combination methods. The combination method has become the most popular in geotechnical engineering problems and the most accurate method as they couple energy balance and aerodynamic equations (Wilson, 1990).

The first combination method is attributed to Penman, (1948) and further modifications of the method have taken place along the years (e.g. Penman and Schofield, 1951; Monteith, 1965; van de Griend and Owe, 1994; Shuttleworth and Wallace, 1985; Wallace et al., 1990; Camillo and Gurney, 1986; Aluwihare and Watanabe, 2003; Bittelli et al., 2008).

However, combination methods have a series of drawbacks:

a) The methods are based on the Philip and De Vries, (1957) formulation for the flow of water which assumes that water movement is driven by soil moisture gradients instead of hydraulic head gradients. Wilson, (1990) considered that this assumption was not acceptable in geotechnical engineering practice.

b) Properties of the soil such as hydraulic conductivity are not considered.

c) The methods include changing variables that depends on environmental conditions and plant growth.

It has been proved that these methods give good estimates of evapotranspiration, although only for full covered vegetated soils, and therefore can be considered reasonably valid only for dense canopies (Monteith, 1965; Allen et al., 1998). Below this value, these methods are not recommended (Feddes and Lenselink, 1994).

Wilson, (1990) developed a combination method known as the Wilson-Penman equation, based on assumptions where the flow of water is driven by a hydraulic-head gradient and the properties of the soil are taken into account (Wilson et al., 1994) what makes it ideal for use in geotechnical engineering problems.

4.2.3 The Wilson-Penman equation

Wilson, (1990) proposed a combination method based on the Penman equation to calculate evaporation for unsaturated soils that does not need the inclusion of changing variables with no direct physical meaning. The model was formulated using variables commonly used in geotechnical engineering practice.

Actual evaporation in the Wilson-Penman equation, is a function of climatic parameters (i.e. relative humidity, air temperature, solar radiation, and wind speed) and the matric suctions at the soil-atmosphere interface.

The Wilson-Penman equation is presented as:

$$AE = \frac{\frac{\Delta R_n}{\lambda} + \gamma E_a}{\Delta + \frac{\gamma}{h_s}} \tag{4.16}$$

Where,

AE = Actual evaporation rate;

Δ = Slope of the saturation vapour pressure versus temperature chart at the mean air temperature;

γ = Psychrometric constant;

h_s =relative humidity at the soil surface;

R_n = The net radiant energy (obtained from the empirical formula given by Penman, (1948).

And

$$E_a = f(u)e_a(B - A_i) \tag{4.17}$$

Where,

$f(u) = 0.35(1 + 0.146\mathrm{u}_2)$;

u_2 = wind speed;

e_a = actual water vapour pressure of the air above the soil surface (mm Hg);

A_i = Inverse of the relative humidity of the soil surface;

B = Inverse of relative humidity in the air.

The drawback of the Wilson-Penman equation is that it was designed for bare soils. Later, Tratch, (1995) proposed a methodology that allows the calculation of evapotranspiration for vegetated soils based on the evapotranspiration partition.

4.2.4 Evapotranspiration partition

The prediction of actual evaporation and actual transpiration from a plant population in unsaturated soils may be broken down into the five-step methodology proposed by Tratch, (1995).

1) The potential evapotranspiration (PE) is the rate of evaporation for bare saturated soils using the Penman's original formulation.

2) The potential transpiration (PT) is the rate of transpiration for saturated soils and determined based on PE and the vegetation coverage at the site using the Ritchie, (1972) equations.

$$PT = 0 \text{ when } LAI < 0.1 \quad (4.18)$$

$$PT = PE(-0.21 + 0.70LAI^{0.5}) \text{ when } 0.1 <= LAI < 2.7 \quad (4.19)$$

$$PT = PE \text{ when } 2.7 <= LAI \quad (4.20)$$

Where

LAI is the leaf area index. It is calculated as the leaf area (considering only one side of the leaves) per unit ground surface area (LAI = leaf area / ground area, m2 / m2)

The three equations are applied for the PT rate under bare soil (4.18), partial cover (4.19) and full vegetative cover (4.20) conditions respectively.

3) Distribution of the PT through the root's depth.

PT does not take place at the very soil surface. Instead, it takes place all along the roots and is distributed over their entire length. Therefore, PT flux must be distributed throughout the soil profile.

The potential root water uptake (PRU) is the profile of maximum root water uptake with depth which may occur in ideal soil conditions.

Once PT has been obtained, PRU is calculated using a normalised water uptake distribution (NWD) that represents the root water uptake distribution over depth.

$$PRU = \mathrm{NWD} \cdot PT \tag{4.21}$$

PRU is measured as water removal rate per unit volume of soil (L3 /t/ L3) and can be obtained at any specific depth from PT (4.21).

A number of NWD has been proposed (e.g. Molz and Remson, 1970; Hoogland et al., 1981; Rvard Hoffman and Van Genuchten, 1983; Feddes et al., 1978;Prasad, 1988).

Feddes et al., (1978) proposed a simple approach based on a uniform root water uptake distribution all over the entire depth (4.22).

$$NWD = \frac{1}{z_r} \tag{4.22}$$

Where z_r is the maximum depth of the root system.

Equation (4.22) represents a drastic simplification as the rate of extraction at the very tip of the root system can be expected to be zero, whereas near the surface, where root densities are maximum, the rate of extraction should be higher. However, Feddes' et al., (1978) approach can be relevant if the roots are located in a relatively thin soil layer such as the case of steep slopes (Novák, 2012).

Once PRU has been obtained, a further reduction of transpiration rate due to the ability of plant roots to absorb water at different matric suctions must be considered.

4) Adjustment of PRU to account for the moisture availability to obtain the actual root uptake profile.

The PRU is the maximum possible flux rate without considering the reduction of root uptake as the soil moisture decreases. To account for this reduction, the inclusion of a plant limiting function has been recommended by many authors (e.g. Radcliffe et al., 1980, Perrochet, 1987, Novak, 1987).

PRU fluxes must then be modified depending on the soil moisture availability to determine the actual root uptake flux (ARU). The moisture availability is a function of the matric suction existing at each depth. ARU is then calculated from PRU by introducing a reduction coefficient known as the plant moisture limiting factor (PLF) as presented in (4.23):

$$ARU = PRU \times PLF \tag{4.23}$$

Two types of PLF are fundamentally encountered in the literature Feddes et al., (1988) and Tratch et al., (1995) (Novák, 2012).

Tratch et al., (1995) suggested that the actual root water uptake is maintained at the PT values when soil suction is low. Once a specified limiting value is exceeded, the actual transpiration flux decreases exponentially (i.e. straight line on a semilog plot) until the wilting point is reached. Transpiration will be zero at soil suctions above the wilting point. Tratch et al., (1995) suggested defaults values for the limiting and the wilting point of 100 and 1500 kPa, respectively (Figure 4-2).

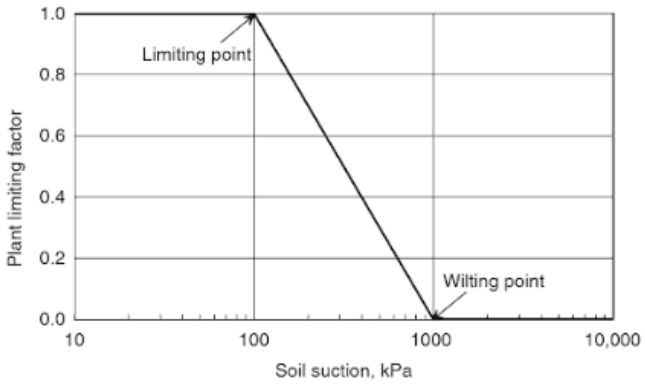

Figure 4-2 PLF model after Tratch et al. (1995)

PLF based on Feddes et al., (1988) and Tratch et al., (1995) are both extensively used by researchers (e.g. Nyambayo and Potts, 2010; Briggs et al., 2016; Soltani et al., 2016). Whether one of the methods outperform the other is still unclear (Skaggs et al., 2006).

The ARU then becomes a function of depth and soil moisture that constitute a sink term in the governing flow equations. The sink term is the volume of water extracted per unit time per unit bulk volume of soil, or in depth units, the rate of water extraction per unit depth (Prasad, 1988).

5) Calculation of the actual evaporation rate under vegetation cover

Considering R_{ns} as the part of net radiation (R_n) reaching the soil surface below the canopy, Ritchie, (1972) proposed a relationship to obtain R_{ns} as a function of R_n based on the interception of the solar radiation by the canopy effect.

$$R_{ns} = R_n \, e^{-ç(LAI)} \tag{4.24}$$

Where,

R_n= net radiation flux density (W/m^2);

R_{ns}= the part of R_n reaching the soil surface (W/m^2);

LAI= leaf area index (m^2 leaf area/ m^2 soil area);

ç= extinction coefficient between 0.5 and 0.75. A factor which may vary according to the geometrical properties of vegetation.

Considering the soil cover fraction (SCF) as

$$SCF = 1 - e^{-ç(LAI)} \tag{4.25}$$

Then

$$R_{ns} = R_n \, (1 - SCF) \tag{4.26}$$

The actual evaporation under the vegetation cover and water stress conditions is finally obtained by applying the Wilson-Penman equation using R_{ns} instead of R_n

$$AE = \frac{\frac{\Delta R_{ns}}{\lambda} + \gamma E_a}{\Delta + \frac{\gamma}{h_s}} \tag{4.27}$$

For the application of the Wilson-Penman equation, the introduction of climatic parameters is needed.

4.2.5 Climatic parameters

For the implementation of the Wilson-Penman equation, a series of climatic parameters are needed: Air temperature, relative humidity, wind speed, precipitation, solar radiation and albedo. All these parameters except albedo, can be obtained from meteorological stations.

Although wind speed can be obtained from meteorological stations, the lecture provided are measured at 10m height and therefore need to be extrapolated to 2m height in order to be included in the Wilson-Penman equation. This interpolation is performed using the log wind profile (Holmes, 2018).

$$u(z_2) = u(z_1)\frac{ln\big((z_2 - d)/z_0\big)}{ln\big((z_1 - d)/z_0\big)} \tag{4.28}$$

Where,

$u(z_2)$ =estimated wind speed at the height z_2;

$u(z_1)$ =known wind speed at the height z_1;

d =zero plane displacement;

z_0 =roughness length.

The zero plane displacement can be approximated from vegetation height (Holmes, 2018).

$$d \approx \frac{2}{3}(\text{vegetation height}) \tag{4.29}$$

An additional parameter 'Albedo' is needed in climatic boundary conditions. Albedo (r), is a parameter that depends on the characteristics of the ground surface to reflect solar radiation, indicating the proportion of the solar energy that is reflected back to the space. A surface that is very reflective like snow, will have a higher albedo coefficient that a less reflective surface. As such, evapotranspiration is expected to be higher in less reflective surfaces where more solar energy is absorbed than in more reflective surfaces such as tropical forests (Aktas et al., 2017).

The Wilson and Penman equation and the Tratch et al., (1995) method were used in the analysis of Watford cutting in chapter 7 to assess the stability of the cutting against rising pore water pressures. The analysis was carried out by coupling a seepage software (SEEP/W) that integrates the Wilson and Penman equation and the Tratch et al., (1995) method for evapotranspiration with a limit equilibrium software (SLOPE/W).

4.2.6 Implementation

The infiltration when rainfall takes place, the actual root water uptake and the actual evaporation (Wilson, 1990), are included in SEEP/W using the 1D Richards equation in (4.15) that govern the flow of water at the interface soil-atmosphere.

Rainfall is incorporated into the 1D Richards equation as a source term and evaporation and transpiration as a sink term. The 1D Richards equation constitute the upper boundary condition of the 2D Richards equations that govern the flow of water below the interface soil-atmosphere. Transient pore water pressures feed SLOPE/W for the calculation of the slope stability using the method of slices.

4.3 Analysis of mass movement using the method of slices

In the method of slices, the soil mass above a predetermined slip surface is discretised into a series of slices. The base of each slice is approximated to a straight line, and the factor of safety is defined as the ratio of the shear strength to the shear stress acting on the slip surface (Janbu, 1954).

The method of slices is one of a broader group called limit equilibrium methods. The limit equilibrium methods assume that soil at failure obeys the perfectly plastic Mohr-Coulomb criterion and the stability of the slope is calculated from the equilibrium of forces and/or moments considering the soil as a rigid perfectly plastic material. The limit equilibrium approach is fully static and the soil stress field is not determined as only global equilibrium conditions rather than equilibrium conditions at every point are fulfilled (Yu et al., 1998).

The method of slices introduced by Fellenius, (1926), is most typically applied to circular slip surfaces but can also be applied to more complex geometries. The soil mass over a predetermined slip surface is divided into slices and equilibrium conditions are imposed to each slice and the slices as a whole. A system of n equations is obtained where n is the number of equations and $n + (2n - 2)$ are the number of unknowns present in the equations. To equal the number of unknowns and the number of equations, assumptions are to be made regarding interslice forces (Boutrup, 1977).

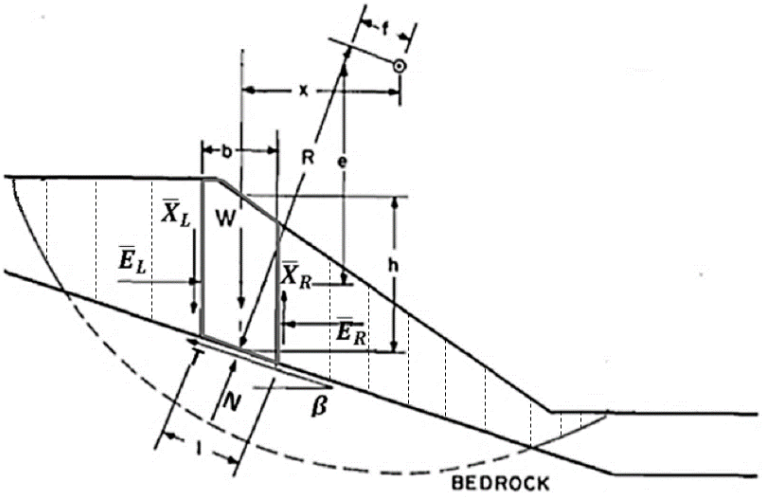

Figure 4-3 Method of slices: Division of sliding mass into slices and forces acting on a typical slice (Fredlund and Krahn, 1977)

Figure 4-3 shows the forces that must be defined for a general slope stability problem. The variables associated with each slice are defined as follows:

$W =$ total weight of the slice of width b and height h;

$N =$ total normal force on the base of the slice over a length l;

$T =$ shear force mobilized on the base of the slice;

$R =$ radius or the moment arm associated with the mobilized shear force T;

$f =$ perpendicular offset of the normal force from the centre of rotation;

$x =$ horizontal distance from the slice to the centre of rotation;

$\beta =$ angle between the tangent to the center of the base of each slice and the horizontal;

$\bar{E} =$ horizontal interslice force;

$L =$ subscript designating left side;

$R =$ subscript designating right side;

$\bar{X} =$ vertical interslice forces;

$e =$ vertical distance from the centroid of each slice to the centre of rotation.

Considering the equilibrium of each slice, the mobilised shear stress at the base of a slice (τ_T) can be written as (Lambe and Whitman, 1969)

$$\tau_T = \frac{\tau_S}{\text{FoS}} \tag{4.30}$$

Where

τ_S is the shear strength of the soil, and τ_T is the mobilised shear strength to maintain the slice in equilibrium.

$$\tau_S = c' + \sigma' tan\emptyset' \tag{4.31}$$

(4.30) can also be presented as:

$$T = \tau_T \cdot l = \frac{\tau_S \cdot l}{\text{FoS}} = \frac{S}{\text{FoS}} \tag{4.32}$$

Where

$$S = c'l + (Wcos\beta - u_w l)tan\emptyset' \tag{4.33}$$

Considering the shear strength of the material at the base of each slice (τ_S) given by (4.31) and imposing certain assumptions on the inter-slice boundary conditions, different versions of the method of slices are obtained.

Different methods of slices differentiate each other by the interslice normal ($\bar{E}$) and shear ($\bar{X}$) forces assumptions, by the equations of equilibrium imposed in the analysis and by considering the assumption of circular slip surfaces or not (e.g. Ordinary Fellenius, Bishop's simplified, Janbu's Simplified, Janbu's GPS, Lowe-Karafiath, Corps of Engineers, Sarma, Spencer, Morgenstern-Price)

Some of the versions are suitable only for circular slip surfaces (e.g. Ordinary Fellenius, Bishop's simplified) whereas other methods can be applied to different shapes as the one presented in Figure 4-4.(e.g. Spencer, Morgenstern-Price)

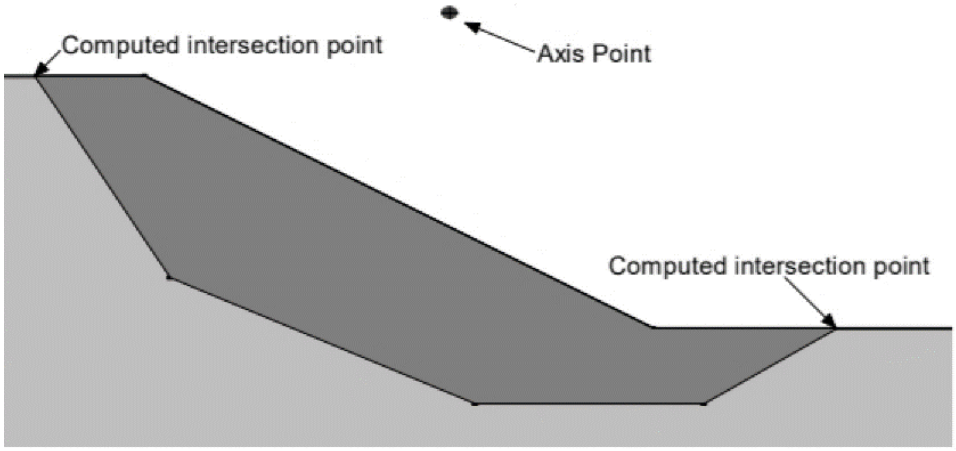

Figure 4-4 Composed slip surface (SLOPE/W, 2018)

Methods which satisfy all conditions of equilibrium (Sarma, Spencer, Morgenstern-Price) give essentially the same value of FoS. As stated by Duncan and Wright, (1980), for any practical slope stability problem, any method which satisfies all conditions of equilibrium will give a value of FoS which differs by no more than +5% from what may be considered the 'correct' answer.

One of the more popular versions that can be applied to non-circular slip surfaces is the Spencer's method. This method satisfies both force and moment equilibrium forces.

Spencer's, (1967) method assumes that there is a constant relationship between the magnitude of the interslice shear and normal forces.

$$tan\lambda = \frac{\bar{X}_L}{\bar{E}_L} = \frac{\bar{X}_R}{\bar{E}_R} \tag{4.34}$$

Where λ is the angle of the resultant interslice force from the horizontal.

Spencer,(1967) applied equilibrium forces in the vertical and horizontal directions for each slice.

$$\sum F_V = 0 \tag{4.35}$$

$$W - (\bar{X}_R - \bar{X}_L) - Ncos\beta - Tsin\beta = 0 \tag{4.36}$$

$$\sum F_H = 0 \tag{4.37}$$

$$-(\bar{E}_R - \bar{E}_L) + Nsin\beta - Tcos\beta = 0 \tag{4.38}$$

From (4.36) and (4.38), the equation (4.39) for N is obtained

$$N = \left[W - (\bar{E}_R - \bar{E}_L)tan\lambda - \frac{c'lsin\beta}{FoS} + \frac{ultan\phi'sin\beta}{FoS}\right]/m_\beta \quad (4.39)$$

Where

$$m_\beta = cos\beta + (sin\beta tan\phi')/F \quad (4.40)$$

Spencer, (1967) derived two FoS equations, one is based on the summation of moments about a common point and the other on the summation of forces in a direction parallel to the interslice forces.

The FoS equation for the summation of moments is presented as:

$$FoS = \frac{\sum[c'lR + (N - u_w l)Rtan\phi']}{\sum Wx - \sum Nf} \quad (4.41)$$

The FoS equation based on force equilibrium can be derived by summing forces in a horizontal direction from (4.37) and (4.38).

$$\sum(E_L - E_R) + \sum Nsin\,\beta - \sum Tcos\,\beta = 0 \quad (4.42)$$

The interslice forces $(E_L - E_R)$ must cancel out and the factor of safety equation with respect to force equilibrium reduces to:

$$FoS = \frac{\sum[c'lcos\beta + (N - u_w l)tan\phi'cos\beta]}{\sum Nsin\beta} \quad (4.43)$$

Spencer's method generate two FoS for each angle of side forces. The correct angle of interslice forces is achieved by iterations, when the two FoS are equal and both moment and force equilibrium are satisfied. The Spencer's method was applied for the stability analysis at Watford cutting in Chapter 7. The Spencer's equations for the FoS presented in this section are only valid for saturated soil conditions. In the case of unsaturated soils a correction must be done to account for the contribution of matric suctions.

4.3.1 Application of the method of slices to unsaturated conditions

Limit equilibrium methods can be applied to saturated or unsaturated soils with the inclusion of the shear strength at the slip surface accounting for the pore water pressures and matric suctions.

There are currently two widely recognised macroscale approaches for describing the state of stress in unsaturated soil (Lu and Likos, 2006) 1) The modified effective stress approach or Bishop's effective stress approach, and 2) the independent stress state variable approach or Fredlund and Morgenstern's approach.

Bishop's approach has been widely used by a lot of researchers, however, is not flawless. Jennings and Burland, (1962) argued that Bishop's approach failed to capture the collapse phenomenon in unsaturated soils. Moreover, the determination of effective stress factor (χ) in Bishop's approach requires nonconventional experimental procedures (Nuth and Laloui, 2008).

In the Fredlund and Morgenstern's approach, the net normal stress ($\sigma - u_a$) and matric suction ($u_a - u_w$), are treated independently. The shear strength for the Mohr–Coulomb failure criterion is:

$$\tau_S = c' + [(\sigma_n - u_a)tan\,\phi' + (u_a - u_w)]tan\,\phi^b \tag{4.44}$$

Where ϕ^b is introduced to account for the contribution of matric suction to the shear strength (Lu and Likos, 2006). The main drawback of Fredlund and Morgenstern's approach is that ϕ^b has a nonlinear evolution over wide ranges of suction and a single value of ϕ^b is therefore not representative.

Despite this, Fredlund and Rahardjo, (1993)suggested that a constant value for ϕ^b of about half the residual angle of internal friction yielded reasonable estimates (Heyerdahl, 2017).

Combining equations (4.44) with (4.41) and (4.43) gives the Spencer's FoS equations for unsaturated soils

$$FoS = \frac{\sum[(c'lcos\beta + Ntan\phi'cos\beta - u_w tan\phi^b cos\beta)]}{\sum Nsin\alpha} \tag{4.45}$$

$$FoS = \frac{\sum\left[c'lR + \left(NRtan\phi' - u_w lRtan\,\phi^b\right)\right]}{\sum Wx - \sum Nf} \tag{4.46}$$

The equations for transient seepage and slope stability have been introduced and will be applied in the stability assessment at Watford cutting. SEEP/W will be used for the calculation of transient pore water pressures and SLOPE/W for the calculation of stability analysis. Both software will work coupled where information from SEEP/W will feed SLOPE/W at each time step.

4.4 Conclusion

In this chapter, the equations used in the assessment of the stability of slopes using continuum methods of analysis have been introduced.

Changes in pore water pressures due to rainfall and evapotranspiration are described by infiltration and evapotranspiration equations. These equations are applied at the boundary between the soil surface and the atmosphere and result in a sink and a source term respectively in the Richards equations that governs the flow of water within the soil.

The Richards equations, describe the movement of water within the soil and variations in pore water pressures at specific locations of the model using numerical methods. The number of locations depends on the density of the mesh used in the numerical method. The Richards equations are transient equations and the pore water pressures are calculated for each time step that will be chosen depending on the time scale analysed.

For each time step, the distribution of pore water pressures is calculated and included in the limit equilibrium method where the shear strength of the soil is calculated at the base of each slice.

The equations described in this chapter, allows the assessment of the stability of slopes accounting for the effects of infiltration and evapotranspiration. The premises of all the equations included in this chapter is the treatment of the soil as a continuum. The dislodgment of particles due to hydrodynamic forces are beyond the capabilities of this approach.

The continuum approach is relevant in this thesis for the stability assessment of Watford cutting and the results of the analysis concluded whether the failure at Watford took place as a consequence of rising pore water pressures or it was triggered by a different factor not accounted in this approach.

Chapter5: Bases of slope stability analysis using the discrete approach

In this thesis, superficial water runoff is the principal factor used to analyse the vulnerability of cuttings against runoff generated debris flows. The movement of water was analysed by resolving shallow water equations and turbulence model equations using continuum numerical methods of analysis. The soil was simulated using the discrete element method (DEM) as a number of discrete spherical particles simulating soil peds. Then, interactions between superficial water runoff and soil surface was calculated by coupling the equations governing the movement of water with the spherical soil peds. This approach is known as coupled computational fluid dynamics and discrete element method (CFD-DEM).

In this chapter, the equations behind the movement of superficial water runoff (CFD) and the spherical particles (DEM) are introduced. Then, the interactions of water with soil spheres is described (CFD-DEM).

5.1 Overland flow

Flows above the soil surface behave differently to flows within the soil. Overland flows occur at a much higher speed than in soils and are normally turbulent whereas underground flows are mostly laminar and move at negligible velocities. As such, the mathematical representation of both types of flows is also different.

Overland flows can be modelled using the well-known 3D Navier-Stokes equations or any of its simplified variations called turbulence models (Thomasset, 2012). However, when the purpose is to model the flow at a catchment scale, the computational time required to model large extensions would be extremely high. For this purpose, the use of 2D shallow water equations is considered as the best approach when dealing with this kind of scales.

In this chapter, the equations behind the turbulence model derived from the 3D Navier-Stokes equations and the shallow water equations are introduced. These equations were used in the development of the novel method (chapter 8) for the simulation of surface water runoff.

5.1.1 3D Models: The Navier-Stokes equations and simplified form (RANS)

The Navier-Stokes equations (NS) are the core of overland flow models for laminar and turbulent flows. They can reproduce the flow field of any type of flows. The flow field is

resolved by coupling mass and momentum conservation equations. The pressure, stress and fluid velocity are obtained at a microscale level for any point in space and time given initial and boundary conditions.

The general NS equations for the movement of water are simplified based on the incompressibility of water. Under this hypothesis, they are presented for the conservation of momentum in the x, y, and z directions as (Dronkers, 1964):

$$\frac{\partial u}{\partial t}+u\frac{\partial u}{\partial x}+v\frac{\partial u}{\partial y}+w\frac{\partial u}{\partial z}=-\frac{1}{\rho}\frac{\partial u_w}{\partial x}+g_x+\frac{\mu}{\rho}\left[\frac{\partial^2 u}{\partial x^2}+\frac{\partial^2 u}{\partial y^2}+\frac{\partial^2 u}{\partial z^2}\right] \quad (5.\ 1)$$

$$\frac{\partial v}{\partial t}+u\frac{\partial v}{\partial x}+v\frac{\partial v}{\partial y}+w\frac{\partial v}{\partial z}=-\frac{1}{\rho}\frac{\partial u_w}{\partial y}+g_y+\frac{\mu}{\rho}\left[\frac{\partial^2 v}{\partial x^2}+\frac{\partial^2 v}{\partial y^2}+\frac{\partial^2 v}{\partial z^2}\right] \quad (5.\ 2)$$

$$\frac{\partial w}{\partial t}+u\frac{\partial w}{\partial x}+v\frac{\partial w}{\partial y}+w\frac{\partial w}{\partial z}=-\frac{1}{\rho}\frac{\partial u_w}{\partial z}+g_z+\frac{\mu}{\rho}\left[\frac{\partial^2 w}{\partial x^2}+\frac{\partial^2 w}{\partial y^2}+\frac{\partial^2 w}{\partial z^2}\right] \quad (5.\ 3)$$

Where

u, v, and w are the x, y, and z components of the velocity vector

u_w =water pressure

g =acceleration of gravity

μ =dynamic viscosity

The mass conservation equation is expressed as:

$$\frac{\partial u}{\partial x}+\frac{\partial v}{\partial y}+\frac{\partial w}{\partial z}=\frac{S}{\rho} \quad (5.\ 4)$$

Where S is a source or sink term such as precipitation or infiltration.

These general equations are meant here to include both laminar and turbulent flows. The NS equations are non-linear partial differential equations and as such the solution must be approximated using numerical methods. The direct calculation of the NS equations using numerical methods require extreme computational power and so, to facilitate the analyses, simplified models such as the Reynolds Averaged Navier Stokes equations (RANS) have been utilised based on assumptions and simplifications.

5.1.2 The Reynolds Averaged Navier Stokes equations

RANS is a simplified form of the NS equations. RANS solve the mass and momentum conservation equations decomposing pressures and velocities into a mean and a fluctuating part. This method only solves the mean variables making some assumptions and simplifications of the original NS equations, resulting in considerably reduction of computational costs.

RANS is the most popular method nowadays since the resolution of small scales eddies usually have not considerable effects in engineering applications and is currently considered as the most cost-efficient method that yields sufficiently accurate results for engineering applications (Bates et al., 2005; ANSYS Fluent, 2013).

Substituting u, v and w by their averaged and fluctuating terms, the mass and momentum conservation equations become in vectorial form as

$$\nabla \cdot (\rho \bar{\boldsymbol{v}}) = 0 \tag{5. 5}$$

$$\frac{\partial}{\partial t}(\rho \bar{\mathbf{v}}) + \nabla \cdot (\rho \bar{\mathbf{v}} \bar{\mathbf{v}}) = -\nabla \bar{u}_w + [\nabla \cdot (\bar{\boldsymbol{\tau}} - \rho \overline{\mathbf{v}' \mathbf{v}'})] + \vec{\boldsymbol{f}}_{\boldsymbol{g}} \tag{5. 6}$$

Where

$\bar{\mathbf{v}} =$ mean velocity vector

$\mathbf{v}' =$ fluctuating velocity vector

$\vec{\boldsymbol{f}}_{\boldsymbol{g}}$ is the gravitational vector.

$\bar{\boldsymbol{\tau}}$ is the viscous stress tensor

$$\bar{\boldsymbol{\tau}} = \mu[\nabla \bar{\mathbf{v}} + (\nabla \bar{\mathbf{v}})^{\mathbf{T}}] \tag{5. 7}$$

$(-\rho \overline{\mathbf{v}' \mathbf{v}'})$ is the Reynolds stress tensor ($\boldsymbol{\tau}^{\mathbf{R}}$) that results from the fluctuating values and is generally the dominant part of the total shear stress

The expression $(\bar{\boldsymbol{\tau}} - \rho \overline{\mathbf{v}' \mathbf{v}'})$ in (5. 6) corresponds to the total shear stress tensor $\boldsymbol{\tau}^{\mathbf{t}}$:

$$\boldsymbol{\tau}^{\mathbf{t}} = (\bar{\boldsymbol{\tau}} - \rho \overline{\mathbf{v}' \mathbf{v}'}) \tag{5. 8}$$

The expanded form of the viscous stress tensor and the Reynolds stress tensor can be written as (5. 9) and (5. 10) respectively

$$\bar{\boldsymbol{\tau}} = \begin{bmatrix} 2\mu\dfrac{\partial\bar{u}}{\partial x} & \mu\left(\dfrac{\partial\bar{v}}{\partial x}+\dfrac{\partial\bar{u}}{\partial y}\right) & \mu\left(\dfrac{\partial\bar{u}}{\partial z}+\dfrac{\partial\bar{w}}{\partial x}\right) \\ \mu\left(\dfrac{\partial\bar{v}}{\partial x}+\dfrac{\partial\bar{u}}{\partial y}\right) & 2\mu\dfrac{\partial\bar{v}}{\partial y} & \mu\left(\dfrac{\partial\bar{w}}{\partial y}+\dfrac{\partial\bar{v}}{\partial z}\right) \\ \mu\left(\dfrac{\partial\bar{u}}{\partial z}+\dfrac{\partial\bar{w}}{\partial x}\right) & \mu\left(\dfrac{\partial\bar{w}}{\partial y}+\dfrac{\partial\bar{v}}{\partial z}\right) & 2\mu\dfrac{\partial\bar{w}}{\partial z} \end{bmatrix} \tag{5. 9}$$

$$\boldsymbol{\tau}^{\mathbf{R}} = -\rho\begin{pmatrix} \overline{u'u'} & \overline{u'v'} & \overline{u'w'} \\ \overline{u'v'} & \overline{v'v'} & \overline{v'w'} \\ \overline{u'w'} & \overline{v'w'} & \overline{w'w'} \end{pmatrix} \tag{5. 10}$$

Therefore, at this stage, we have four equations (5. 5)and (5. 6) and ten unknowns, namely: $\bar{u}_w$, $\bar{u}$, $\bar{v}$, $\bar{w}$, $\overline{u'u'}$, $\overline{v'v'}$, $\overline{w'w'}$, $\overline{u'v'}$, $\overline{u'w'}$and $\overline{v'w'}$.

Consequently, to solve the RANS equations, six additional equations must be introduced to solve the unknown components of $\boldsymbol{\tau}^{\mathbf{R}}$. The process of calculating these Reynolds stresses is denoted in the literature by turbulence modelling. The purpose of turbulence models is to close the system of equations by representing the fluctuating terms as a function of the mean components.

Boussinesq proposed an approximation based on a simple relationship between Reynolds stresses and velocity mean gradients through the eddy or turbulent viscosity term (μ_t) (5. 11) to (5. 16).

$$\rho\overline{u'u'} = -\mu_t\left(2\frac{\partial\bar{u}}{\partial x}\right) \tag{5. 11}$$

$$\rho\overline{v'v'} = -\mu_t\left(2\frac{\partial\bar{v}}{\partial y}\right) \tag{5. 12}$$

$$\rho\overline{w'w'} = -\mu_t\left(2\frac{\partial\bar{w}}{\partial z}\right) \tag{5. 13}$$

$$\rho\overline{u'v'} = \rho\overline{v'u'} = -\mu_t\left(\frac{\partial\bar{u}}{\partial y}+\frac{\partial\bar{v}}{\partial x}\right) \tag{5. 14}$$

$$\rho\overline{u'w'} = \rho\overline{w'u'} = -\mu_t\left(\frac{\partial\bar{u}}{\partial z}+\frac{\partial\bar{w}}{\partial x}\right) \tag{5. 15}$$

$$\rho\overline{v'w'} = \rho\overline{w'v'} = -\mu_t\left(\frac{\partial\bar{v}}{\partial z}+\frac{\partial\bar{w}}{\partial y}\right) \tag{5. 16}$$

The introduction of the Boussinesq hypotheses leads to 10 equations and 11 unknows due to the introduction of μ_t.

Therefore, a new problem arises since μ_t is a new unknown that needs to be solved (solution of μ_t is known as the closure problem). New equations are to be introduced to resolve μ_t and several methods have been proposed giving rise to different RANS models (e.g. Spalart-Allmaras, Standard k–ε, RNG k–ε, Realizable k–ε, Standard k–ω, SST k–ω)

These models solve μ_t as a function of a modified turbulent viscosity or the turbulent kinetic energy (k_e) and the dissipation rate (ε).

5.1.3 The realizable k- ε model

The realizable k-ε model is the most accurate of all the available turbulence models for a large range of turbulent flows based on investigations carried out by Wasserman, (2016), Yan, (2011) and Qian et al., (2009).

In the realizable k- ε Model, μ_t is computed as a function of the turbulence kinetic energy (k_e) and the dissipation rate of turbulent kinetic energy (ε). Two additional transport equations are introduced for k_e and ε to solve the closure problem.

The transport equation for k_e is as follows (Soe and Khaing, 2017):

$$\frac{\partial}{\partial t}(\rho k_e) + \nabla\cdot(\rho\bar{\mathbf{v}}k_e) = \nabla\cdot\left(\left(\mu + \frac{\mu_t}{\sigma_k}\right)\nabla k_e\right) + G_k - \rho\varepsilon \qquad (5.\ 17)$$

Where

G_k represents the generation of turbulence kinetic energy due to the mean velocity gradient:

$$G_k = \mu_t {S_t}^2 \qquad (5.\ 18)$$

S_t is the modulus of the mean rate-of-strain tensor (5. 19), defined as (5. 20)

$$\mathbf{S_t} = \frac{1}{2}(\nabla\bar{\mathbf{v}} + \nabla\bar{\mathbf{v}}^T) \qquad (5.\ 19)$$

$$S_t = \sqrt{\mathbf{S_t}\cdot\mathbf{S_t}} \qquad (5.\ 20)$$

σ_k is an adjustable constant

The transport equation for ε is as follows (Soe and Khaing, 2017):

$$\frac{\partial(\rho\varepsilon)}{\partial t} + \nabla \cdot (\rho\bar{\mathbf{v}}\varepsilon) = \nabla \cdot \left[\left(\mu + \frac{\mu_t}{\sigma_\varepsilon}\right)\nabla\varepsilon\right] + \rho C_1 S\varepsilon - \rho C_2 \frac{\varepsilon^2}{k + \sqrt{\nu\varepsilon}} \quad (5.\ 21)$$

Where

$$\eta = S\frac{k_e}{\varepsilon} \quad (5.\ 22)$$

$$C_1 = max\left[0.43, \frac{\eta}{\eta + 5}\right] \quad (5.\ 23)$$

C_2 and σ_ε are adjustable constants

Once $k_e(x, y, z, t)$ and $\varepsilon(z, y, z, t)$ have been derived from the transport equations for k_e and ε respectively, the value of μ_t can then be derived from (5. 24) (Soe and Khaing, 2017).

$$\mu_t = \rho C_\mu \frac{{k_e}^2}{\varepsilon} \quad (5.\ 24)$$

The values of the constants that ensure a good performance for a wide range of turbulent flows (5. 25) are employed in commercial software when the specific information for each case cannot be obtained (ANSYS Fluent, 2011; Versteeg and Malalasekera, 2007).

$$\sigma_k = 1; \sigma_\varepsilon = 1.2 \text{ and } C_2 = 1.9 \quad (5.\ 25)$$

Then, the Reynolds turbulent stress term ($-\rho\overline{\mathbf{v}'\mathbf{v}'}$) is obtained as a function of the velocity mean values (5. 26) and introduced in the RANS mass and momentum conservation equations (5. 5) and (5. 6) to solve the flow field for a specific time step.

$$-\rho\overline{\mathbf{v}'\mathbf{v}'} = \mu_t\left(\frac{\partial\bar{u}_i}{\partial x_j} + \frac{\partial\bar{u}_j}{\partial x_i}\right) \quad (5.\ 26)$$

<u>The bottom shear stress</u>

For rough walls that consider the asperities of the ground surface, the RANS turbulence models calculate the bottom shear stress applying the log-law.

The log-law layer is an approximation of the velocity field near walls in turbulent flows and the movement of water is governed by a functional relationship $u^+ = f(y^+)$ (Cebeci and Bradshaw, 1977):

$$u^+ = \frac{1}{\kappa}\ln\left(\frac{y^+}{z_0}\right) \tag{5. 27}$$

Where,

y^+ =dimensionless measure of distance y from the wall;

κ =von Karman's constant (=0.42);

z_0 =roughness length;

The mean velocity at a certain point is proportional to the logarithm of the distance from that point to the wall.

$$\tau_w = \rho\bar{u}^2\left[\frac{\kappa}{\ln\left(\frac{k_s}{30H_d}\right)}\right]^2 \tag{5. 28}$$

Where,

$\bar{u}$ =mean velocity of the closest cells to the wall in the direction parallel to the wall;

κ =von Karman's constant (=0.42) ;

k_s =Nikuradse roughness;

H_d = local water depth;

The roughness length for different types of soils are generally tabulated or calculated using the mean mass median diameter of the surface particles (D_p) (Bagnold, 1938):

$$z_0 = \frac{D_p}{30} \tag{5. 29}$$

Or the equivalent expression

$$k_s = D_p \tag{5. 30}$$

5.1.4 2D Model: The shallow water model

Rainfall runoff flowing from relatively horizontal catchments into steep cuttings are challenging to model using current numerical methods. The use of the 3D NS equations for this type of flows provides accurate simulations of the overtopping events. However, numerical solvers for these equations at a catchment scale requires considerable computational resources, and an alternative to 3D NS equations is required (Shiach et al., 2004).

The shallow water model is ideal for flows where the water depth is much smaller than the characteristic horizontal size of the field of study. The shallow water model is derived by applying simplifications and assumptions to the NS equations that drastically reduces the computational power while conserving good estimations of the flow field (Lee, 2010). As such, the shallow water model is a suitable method for modelling flows in catchments. The use of shallow water equations (SWE) in catchments are extensively utilised by researchers and has become the choice method for flood risk assessment (e.g. Liang et al., 2015; Özgen et al., 2015; Fernández-Pato et al., 2016; Kvočka et al., 2017)

The SWE are obtained by vertically averaging the NS equations. The main simplifications derived from the equations is that the pressure is considered hydrostatic as a consequence of neglecting the vertical accelerations, and the vertical velocity has no equation (Townsend, 2018).

The derivation of the SWE is carried out considering a shallow overland flow (Figure 5-1) where the x-y plane is a reference plane on which the height of the free surface and ground surface are measured. For more details on the derivation of the shallow water equations, the reader is referred to Toro, (2013).

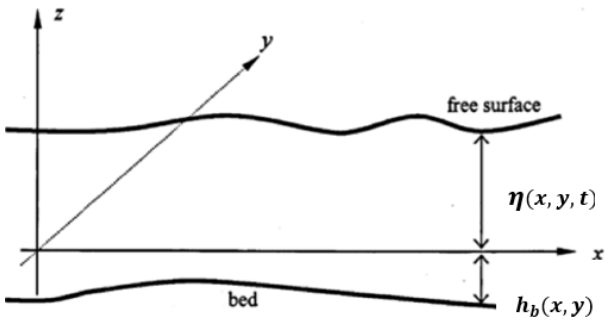

Figure 5-1 Shallow water equation model (Lee, 2010)

The Navier-Stokes mass and momentum conservation equations for an incompressible inviscid fluid in a free stream are as follows:

$$\frac{\partial u}{\partial x}+\frac{\partial v}{\partial y}+\frac{\partial w}{\partial z}=0 \tag{5. 31}$$

$$\frac{\partial u}{\partial t}+u\frac{\partial u}{\partial x}+v\frac{\partial u}{\partial y}+w\frac{\partial u}{\partial z}=-\frac{1}{\rho}\frac{\partial u_w}{\partial x} \tag{5. 32}$$

$$\frac{\partial v}{\partial t}+u\frac{\partial v}{\partial x}+v\frac{\partial v}{\partial y}+w\frac{\partial v}{\partial z}=-\frac{1}{\rho}\frac{\partial u_w}{\partial y} \tag{5. 33}$$

$$\frac{\partial w}{\partial t}+u\frac{\partial w}{\partial x}+v\frac{\partial w}{\partial y}+w\frac{\partial w}{\partial z}=-\frac{1}{\rho}\frac{\partial u_w}{\partial z}-g_z \tag{5. 34}$$

Where,

x and y =space coordinates;

t =time;

u, v and w = flow velocities;

g =gravitational constant;

u_w =water pressure;

After a series of assumptions and simplifications (Toro, 2013; Townsend, 2018; Lee, 2010), by vertically averaging the NS equations the shallow water equations are presented as:

$$\frac{\partial H_d}{\partial t}+\frac{\partial(H_d\bar{u}_d)}{\partial x}+\frac{\partial(H_d\bar{v}_d)}{\partial y}=S \tag{5. 35}$$

$$\frac{\partial(H_d\bar{u}_d)}{\partial t}+\frac{\partial\left(H_d\bar{u}_d^2+\frac{1}{2}g{H_d}^2\right)}{\partial x}+\frac{\partial(H_d\bar{u}_d\bar{v}_d)}{\partial y}=gH_d(S_{ox}-S_{fx}) \tag{5. 36}$$

$$\frac{\partial(H_d\bar{v}_d)}{\partial t}+\frac{\partial\left(H_d\bar{v}_d^2+\frac{1}{2}g{H_d}^2\right)}{\partial y}+\frac{\partial(H_d\bar{u}_d\bar{v}_d)}{\partial x}=gH_d(S_{oy}-S_{fy}) \quad (5.\ 37)$$

Where (5. 35) is the equation of mass conservation, and (5. 36) and (5. 37) are the momentum conservation equations in x and y, and

H_d =local vertical depth of water

$\bar{u}_d$ and $\bar{v}_d$ =depth-average velocities

g =gravitational constant.

S =source term such as rainfall

S_{ox} and S_{oy}[L/L]= the slope terms

S_{fx} and S_{fy} [L/L] =friction terms

The bottom shear stress in the shallow water

For steady, uniform flow, the stress acting on the bed is presented as (Wilcock et al., 2009)

$$\tau_w=\rho g H_d S_b \quad (5.\ 38)$$

Where

H_d = flow depth

S_b = bed slope

The friction slopes S_{fx} and S_{fy} are then defined as the components of the slope in the x and y directions and τ_{wx} and τ_{wy} are obtained as

$$\tau_{wx}=S_{fx}\rho g H_d \quad (5.\ 39)$$

$$\tau_{wy}=S_{fy}\rho g H_d \quad (5.\ 40)$$

Where τ_{wx} and τ_{wy} are the components of the wall shear stress vector ($\boldsymbol{\tau_w}$)in the directions x and y.

Natural overland flows are non-uniform and unsteady flows. For these cases, τ_w is given by the one-dimensional St. Venant equation (Wilcock et al., 2009):

$$\tau_w = \rho g H_d \left(S_b - \frac{\partial H_d}{\partial x} - \frac{U}{g}\frac{\partial U}{\partial x} - \frac{1}{g}\frac{\partial U}{\partial t} \right) \quad (5.\ 41)$$

Where

$U =$ depth-average velocity in the streamwise direction

$x =$ streamwise direction

The unsteady term ($\partial U/\partial t$) in (5. 41) is typically important only with very rapidly changing flow, dropping this term equation (5. 41) becomes:

$$\tau_w = \rho g H_d \left(S_b - \frac{\partial H_d}{\partial x} - \frac{U}{g}\frac{\partial U}{\partial x} \right) = \rho g H_d S_f \quad (5.\ 42)$$

Where

S_f is the slope of the energy grade line given by

$$S_f = \frac{d}{dx}\left(h_b + H_d + \frac{U^2}{2g} \right) \quad (5.\ 43)$$

And, h_b is bed elevation and $\frac{u^2}{2g}$ is the velocity head.

The use of SWE for steep slopes

Since the SWE are depth-averaged, where vertical velocities are considered negligible. Therefore, these equations in theory, are not suitable for models where vertical velocities need to be analysed (Shiach et al., 2004). When SWE are numerically simulated on steep slopes, convergence problems may arise. However, the use of very fine grids and more advanced numerical solvers, have been proved to yield good results. (e.g. Zhang et al., 2014a; Sabbagh-Yazdi et al., 2007; Sabbagh-yazdi and Mastorakis, 2007)

Variations of the SWE have also been developed to better simulate the flow field on steep slopes by removing the assumption of hydrostatic pressure (e.g. Hergarten and Robl, 2015; Zhou and Stansby, 1998; Dutykh and Clamond, 2016; Xia and Liang, 2018)

In this thesis,

5.2 The discrete element method

Continuous numerical methods of analysis consider the soil as a continuum and can be successfully applied to the stability analysis of the majority of slopes. However, washout is a process where the soil does not move as a whole. Instead, each soil ped moves independently as a result of the hydrodynamic forces and therefore continuum numerical methods cannot be applied for the slope stability analysis of this particular case.

Analysis of slope failures where the soil is discretised into particles can be achieved through DEM. DEM is a discrete numerical method for computing the dynamics of an assembly of discrete particles. DEM was first presented by Cundall, (1971) and applied to rock mechanics analyses and was later extended to investigate granular materials by Cundall and Strack, (1979). Since then, DEM has developed rapidly with the dramatic increase in computing power.

5.2.1 The DEM principles

DEM is a discontinuous approach that solves the motion of each individual particles requiring vast computational power (Chen, 2011).

The discrete approach is characterised by solving the movement of particles one by one without the requirement of using a mesh. The relationship between the movement of particles is given by their interactions as they collide (Chen, 2011).

The movement of each particle is obtained by solving Newton's second law of motion, while the contact forces between particles are calculated using force-displacement contact models (Zhao, 2017).

The numerical implementation of the DEM requires time-steps sufficiently small so that, during a single time-step, disturbances from a particle can only affect the immediate neighbouring particles. In other words, the forces acting on any particle are determined solely by the interactions with the particles they are in contact with (Li, 2013). For every time step, the velocities are assumed constants, and so the smaller the time step, the more accuracy in the dynamic behaviour is obtained (Li, 2013).

Figure 5-2 shows the process followed by the algorithm during a time step. First, the contact points between particles are detected, and the overlapping distance during the time step is obtained. Based on the relationship force-displacement specific of each model and material, the repulsive contact forces are calculated and applied to the centre

of each particle. The resulting accelerations are obtained, and the velocity at the middle of the time step is calculated and assumed constant for the whole time step. The particle velocity and displacement are updated at the end of each time step.The same procedure is applied for the following time-steps until completing the total time for the simulation (Zhao, 2017).

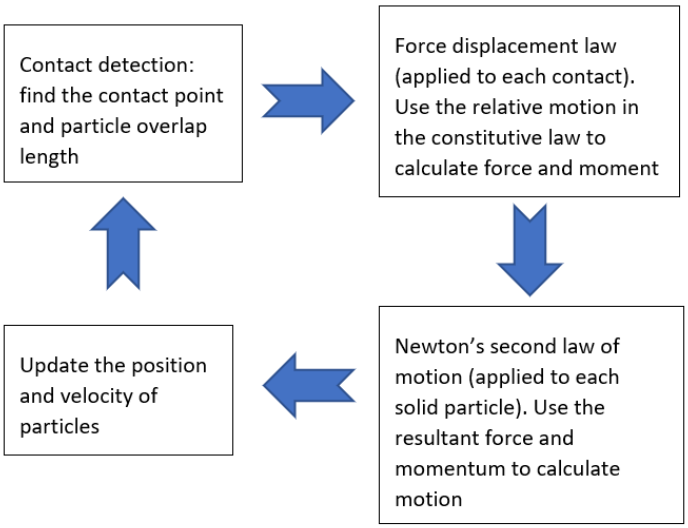

Figure 5-2 Calculation cycle in the DEM (Zhao, 2017)

5.2.2 Equations for the particle motions

The movement of each particle is calculated solving Newton's second law of motion. The translational movement of a particle is given as

$$m^i \frac{d^2}{dt^2}\overrightarrow{\boldsymbol{x_i}} = m_i\vec{\boldsymbol{f}}_{\boldsymbol{g}} + \sum_{N_c}(\vec{\boldsymbol{f}}_{\boldsymbol{n}} + \vec{\boldsymbol{f}}_{\boldsymbol{t}}) + \vec{\boldsymbol{f}}_{\boldsymbol{fluid}} \qquad (5.\ 44)$$

Where m_i is the mass of a particle i; $\overrightarrow{\boldsymbol{x_i}}$ is the centroid position; $\vec{\boldsymbol{f}}_{\boldsymbol{g}}$ is the gravitational acceleration; $\vec{\boldsymbol{f}}_{\boldsymbol{n}}$ and $\vec{\boldsymbol{f}}_{\boldsymbol{t}}$ are the normal and tangential components of the particle-particle contact forces exerted by the neighbouring particles; the summation refers to the number of neighbouring particles in contact (N_c); $\vec{\boldsymbol{f}}_{\boldsymbol{fluid}}$ is the resulting force exerted by the fluid over the particle (Zhao, 2017).

The rotational motion of a single particle is given as

$$I_i \frac{d}{dt}\overrightarrow{\boldsymbol{\omega_i}} = \sum_{N_c}\overrightarrow{\boldsymbol{r_c}} \times \vec{\boldsymbol{f}}_{\boldsymbol{t}} - \overrightarrow{\boldsymbol{M_r}} \qquad (5.\ 45)$$

Where I_i is the moment of inertia about the centroid; $\overrightarrow{\boldsymbol{\omega_i}}$ is the angular velocity; $\overrightarrow{\boldsymbol{r_c}}$ is the vector from the particle centroid to the contact point; and $\overrightarrow{\boldsymbol{M_r}}$ is the rolling resistant moment, which inhibits particle rotation over other particles (Zhao, 2017).

5.2.3 Particle-particle contact models

Contact models are used to calculate forces on the particles based on the particle's colliding velocities and material properties.

One of the differences between continuum and discrete soil models is that in the continuum method, the constitutive equation of the soil is based on stress-strain relationships whereas in the discrete model it is based on force-displacement laws.

The force-displacement laws represent the relationship contact force-relative displacement. The force-displacement laws can be broken down into the normal and tangential components representing the relationship normal contact force- normal displacement and shear contact force-shear displacement (Chen, 2011).

Constitutive behaviour of a material may be simulated using different contact models. Popular contact models that are employed in the literature are a combination of springs, sliders and dash-pots (Gupta, 2015). This configuration is used to estimate the normal and tangential contact forces.

The forces at the point of contact are modelled as a pair of spring-dashpot oscillators. A parallel spring-dashpot model represents the normal force, and a parallel spring-dashpot in series with a slider represents the tangential direction of force with respect to the contact plane normal vector. In both, the spring accounts for the elastic part of the response (stiffness) and the dashpot accounts for energy dissipation during a collision (damping or coefficient of restitution) (D'Apuzzo et al., 2017).

Figure 5-3 shows the assembly for the Hertz-Mindlin contact model through a schematic representation of the contact stiffness and damping between two particles. In the contact normal direction, the spring stiffness K_n represents a simple linear or a nonlinear contact stiffness and the dashpot C_n represents a contact damping. In the tangential direction, the spring stiffness K_t along with the angle of static friction (μ_p or $\emptyset'_\mu$) represent friction between the particles and the dashpot C_t represents contact damping.

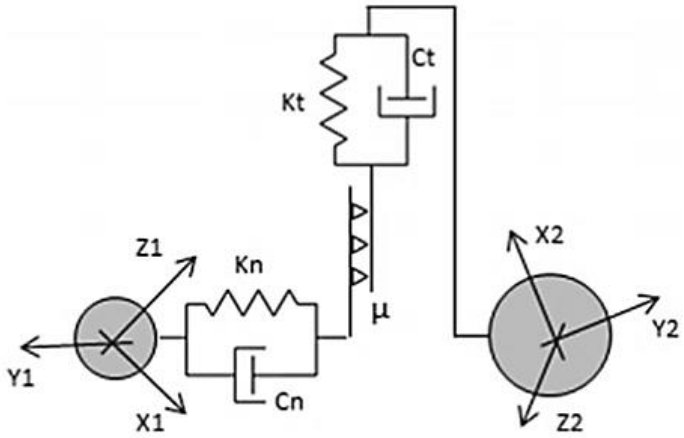

Figure 5-3 Hertz-Mindlin model (D'Apuzzo et al., 2017)

There are different types of contact models to simulate the rheological behaviour of materials: linear elastic (Khan and Pittam, 2018), linear viscoelastic (Kruggel-Emden et al., 2007), nonlinear viscoelastic (Brinson and Brinson, 2015).and elasto-plastic contact force models (Brinson and Brinson, 2015).

The Hertz-Mindlin (HM) is a non-linear spring viscoelastic model and has become the most commonly used contact model in DEM for non-cemented granular soils (Zheng, 2012). This model was used in the development of the novel method.

5.2.4 The Hertz-Mindlin model

Hertz–Mindlin is a well-known model in contact mechanics. An overview may be found in many textbooks (e.g. Johnson, 1987 and Santamarina et al., 2001).

Although this model would normally produce the most precise results (Jaeger, 2005 ; Ng, 2006) and is commonly applied in the investigation of granular material (e.g. Makse et al., 2000; Gu and Yang, 2013; Yan and Ji, 2010), it can be expensive to implement as powerful computer would be required due to the smaller time step, in comparison to the Linear Spring Dashpot model (Khan and Pittam, 2018).

The Hertz-Mindlin model is currently the most commonly used within DEM simulations (e.g. Baran et al., 2013; Chen et al., 2015; Liu et al., 2015; Schmeeckle, 2014) and is applied in geotechnics for the simulation of granular flows (e.g. Zhao, 2014; Shan and Zhao, 2014).

The forces between two spheres, A and B, are described in the Hertz-Mindlin model as:

$$\overrightarrow{\boldsymbol{f_c}} = \overrightarrow{\boldsymbol{f_n}} + \overrightarrow{\boldsymbol{f_t}} \tag{5. 46}$$

Where $\overrightarrow{\boldsymbol{f_n}}$ is the normal and $\overrightarrow{\boldsymbol{f_t}}$ is the tangential force component.

The normal particle-particle contact force

The normal contact interaction entails a spring and a dashpot linked in parallel, such that the normal contact force $\overrightarrow{\boldsymbol{f_n}}$ is a sum of the elastic force in the spring F_n^e and the viscous component F_n^d in the dashpot (Nosewicz et al., 2017).

$$\overrightarrow{\boldsymbol{f_n}} = \left(F_n^e + F_n^d\right)\hat{\boldsymbol{n}} = F_n\hat{\boldsymbol{n}} \tag{5. 47}$$

where, $\hat{\boldsymbol{n}}$ is the unit normal vector pointing from the contact point to the particle centre.

Considering that the relationship between the elastic normal force F_n^e and the overlapping d_n of outer particles surfaces is linear, F_n^e can be represented as

$$F_n^e = -K_n d_n \tag{5. 48}$$

Where

d_n =overlap in the normal direction at the contact point

K_n =normal spring stiffness

$$K_n = \frac{4}{3}E_{eq}\sqrt{d_n R_{eq}} \tag{5. 49}$$

E_{eq} =equivalent Young's modulus expressed as:

$$E_{eq} = \frac{1}{\frac{1-v_A^2}{E_A} + \frac{1-v_B^2}{E_B}} \tag{5. 50}$$

E_A, v_A *and* E_B, v_B are the Young's modulus and Poisson's ratios of the spheres A and B respectively.

The equivalent radius R_{eq} is defined as:

$$R_{eq} = \frac{1}{\frac{1}{R_A} + \frac{1}{R_B}} \tag{5. 51}$$

Where R_A and R_B are the radii of the spheres.

F_n^d is assumed to be a linear function of the normal relative velocity v_n.

$$F_n^d = -N_n v_n \tag{5. 52}$$

Where

N_n =normal damping:

$$N_n = \sqrt{(5K_n M_{eq})} N_{ndamp} \tag{5. 53}$$

M_{eq} =equivalent particle mass:

$$M_{eq} = \frac{1}{\frac{1}{M_A} + \frac{1}{M_B}} \tag{5. 54}$$

M_A and M_B are the masses of sphere A and sphere B.

N_{ndamp} is the normal damping coefficient

$$N_{n\,damp} = \frac{-\ln(C_{n\,rest})}{\sqrt{\pi^2 + \ln(C_{n\,rest})^2}} \tag{5. 55}$$

$C_{n\,rest}$ is the normal coefficient of restitution

The tangential particle-particle contact force

The tangential contact force, $\overrightarrow{\boldsymbol{f_t}}$, is given by adding the tangential spring force, F_t^e , and the tangential damping force, F_t^d (Norouzi et al., 2016).

$$\overrightarrow{\boldsymbol{f_t}} = \left(F_t^e + F_t^d\right)\hat{\boldsymbol{t}} \tag{5. 56}$$

where, $\hat{\boldsymbol{t}}$ is the unit normal vector orthogonal to $\hat{\boldsymbol{n}}$

When tangential forces between particles surpass a threshold, particles slide relative to each other. Therefore, the tangential force between particles depends on the condition(5. 57):

$$|K_t d_t| < |K_n d_n| \mu_p \tag{5. 57}$$

If (5. 57) is satisfied, the particles do not slide over each other and the elastic and viscous components of $\overrightarrow{\boldsymbol{f_t}}$ are given by:

$$F_t^e = -K_t d_t \tag{5. 58}$$

$$F_t^d = -N_t v_t \tag{5. 59}$$

Where,

d_t =overlap in the tangential direction at the contact point;

K_t =tangential spring stiffness;

$$K_t = 8G_{eq}\sqrt{d_n R_{eq}} \tag{5. 60}$$

G_{eq} =equivalent shear modulus;

$$G_{eq} = \frac{1}{\frac{2(2-v_A)(1+v_A)}{E_A} + \frac{2(2-v_B)(1+v_B)}{E_B}} \tag{5. 61}$$

v_t =tangential relative velocity;

N_t =tangential damping;

$$N_t = \sqrt{(5K_t M_{eq})} N_{tdamp} \tag{5. 62}$$

N_{tdamp} is the tangential damping coefficient;

$$N_{t\ damp} = \frac{-\ln(C_{t\ rest})}{\sqrt{\pi^2 + \ln(C_{t\ rest})^2}} \tag{5. 63}$$

$C_{t\ rest}$ is the tangential coefficients of restitution;

If (5. 57) is not satisfied, the particles slide over each other, and the tangential force is given by the Coulomb's friction law

$$\overrightarrow{\boldsymbol{f_t}} = \frac{|K_n d_n| \mu_p d_t}{|d_t|} \hat{\boldsymbol{t}} \tag{5. 64}$$

The particle-particle resistance torque

Particle shape is an important property in the simulation of natural soils. To consider its influence in the DEM, it is convenient to use sphere particles with further consideration of rolling resistance between contacted particles (Shan and Zhao, 2014).

Rolling resistance is a resource used in DEM to model the behaviour of non-spherical particles. An artificial moment is applied to every contact that simulates the resistance of two non-spherical particles to rolling relative to each other (Dubina and Eliáš, 2016).

The implementation of rolling resistance in DEM is accomplished by applying a torque ($\overrightarrow{\boldsymbol{M_r}}$) to the contacting particles. Zhou et al., (1999) introduced a directional contact constant torque to calculate the interparticle rolling torque

$$\overrightarrow{\boldsymbol{M_r}} = -\mu_r F_n R_i \hat{\boldsymbol{\omega}}_{\boldsymbol{i}} \tag{5. 65}$$

with μ_r the coefficient of rolling friction or the coefficient of rolling resistance, R_i the distance of the contact point from the centre of mass and $\hat{\boldsymbol{\omega}}_{\boldsymbol{i}}$, the unit angular velocity vector of the particle at the contact point (Shan and Zhao, 2014;.EDEM, 2014)

This torque is then included in the equation for the rotational motion of a single particle in (5. 45).

5.3 CFD-DEM coupling

The CFD-DEM method is based on the coupling of two independent methods: CFD for the movement of fluids and DEM for the movement of solid particles. Each method determines the governing equations for the representing phase; CFD for the flow field and DEM for the particles system. The two solvers talk to each other due to the coupling arrangement and exchange information for the calculation of the interaction like particle sizes, positions, velocities and resulting interaction forces (Plenker and Grabe, 2016).

In the CFD-DEM, the fluid phase is assumed as a continuum. Flow field parameters such as pressure and velocity are calculated using continuum numerical methods such as the

finite difference, finite element and finite volume methods. Then, pressure and velocity fields are used to solve the interaction of the fluid with particles.

At each time step, the DEM calculates the position and velocity data for individual particles, and the CFD provides the fluid flow parameters for the next time step. The resulting flow velocities and pressures allow the calculation of the fluid-particle interaction (Norouzi et al., 2016).

Previous research using CFD-DEM was concentrated in the investigation of seepage (Kawano et al., 2017;Suzuki et al., 2007; Chen, (2009), consolidation (Chen et al., 2011), fluidisation in granular beds (Liu et al., 2015), internal erosion in granular soils (Kawano et al., 2018; Kawano et al., 2017) and the analyses of granular mass movements in water (Zhao, 2014;Shan and Zhao, 2014; Li Zhao, 2016).

5.3.1 CFD-DEM coupling approaches

There are two methods for coupling between CFD and DEM: the unresolved and the resolved surface approach (Figure 5-4).

In the unresolved method, the size of the fluid cells is larger than the size of the particles and the interaction between the phases are done using semi-empirical formulations.

The resolved surface method, also termed the DNS-DEM method, involves the calculation of the flow field using DNS. DNS-DEM require fluid cells that are much smaller than the diameter of the particles. The interaction between the fluid and particles are resolved by the integration of the fluid stress on the particle surface.

Although the DNS-DEM is the most accurate method to model fluid-particle interactions, the computational cost is so high that it is only feasible for systems containing no more than a few hundred particles (Norouzi et al., 2016)

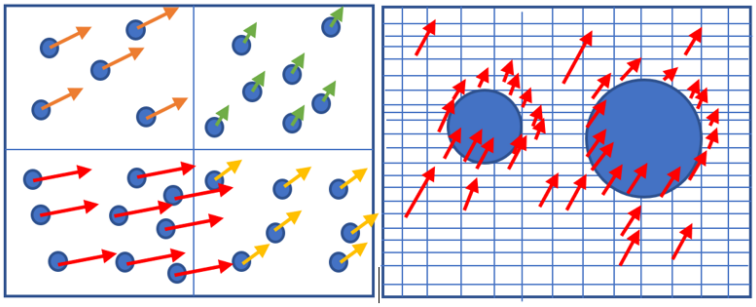

Figure 5-4 CFD-DEM (left) vs DNS-DEM (right)

In the unresolved methods, several particles are located within each cell. The mean pressure and velocity are calculated for each cell and based on these parameters, the forces acting on each particle are calculated using semiempirical equations. The unresolved methods can be classified into three subgroups according to the degree of particle-fluid coupling: one-way coupling, two-way coupling and partial coupling.

In the one-way coupling approach, the forces that the fluid apply on the particles is taken into account, but the fluid is unaffected by the presence of particles.

In the two-way coupling approach, both the forces applied by the fluid to the particles and the particles to the fluid are considered.

The partial coupling approach is similar to the one-way coupling, but the force of the fluid over one particle is affected by the presence of neighbouring particles.

The partial coupling simulation steps are presented in Figure 5-5.

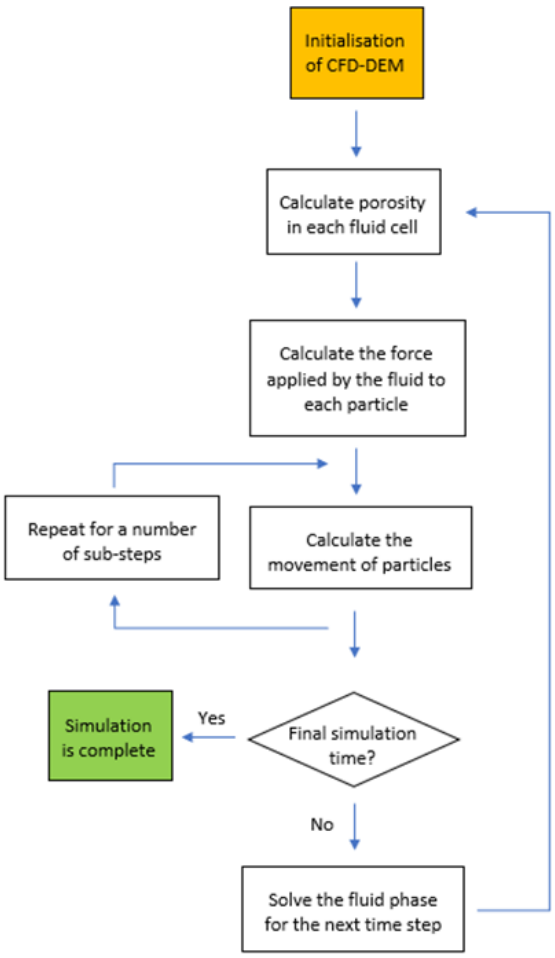

Figure 5-5 CFD-DEM one-way coupling process

Many past studies in the field of sediment transport have avoided fully coupled simulations because of the inconsistency which solvers posed by the volume-averaging

assumption (e.g. Chang and Scotti, 2006; Escauriaza and Sotiropoulos, 2011; Schmeeckle, 2014; Schmeeckle, 2015). Attempts to use the two-way coupling in this thesis have proved to yield numerous convergence issues and the requirement of very coarse meshes.

Moreover, the computational cost associated with the two-way coupling approach is much higher than the cost using the one-way coupling approach. It is therefore not feasible to use the two-way coupling approach when numerous CFD-DEM calculations are required.

The partial coupling method offers higher accuracy than the one-way coupling approach with a low computational cost what makes the method feasible for numerous calculations. This approach was used in the development of the novel method.

5.3.2 Equations of fluid-particle interaction forces

A number of semiempirical equations are used in the DEM solver to estimate the forces applied by the fluid over the particles: the drag force, the particle shear lift force, the drag torque, the buoyant force and the spin lift force (Figure 5-6).

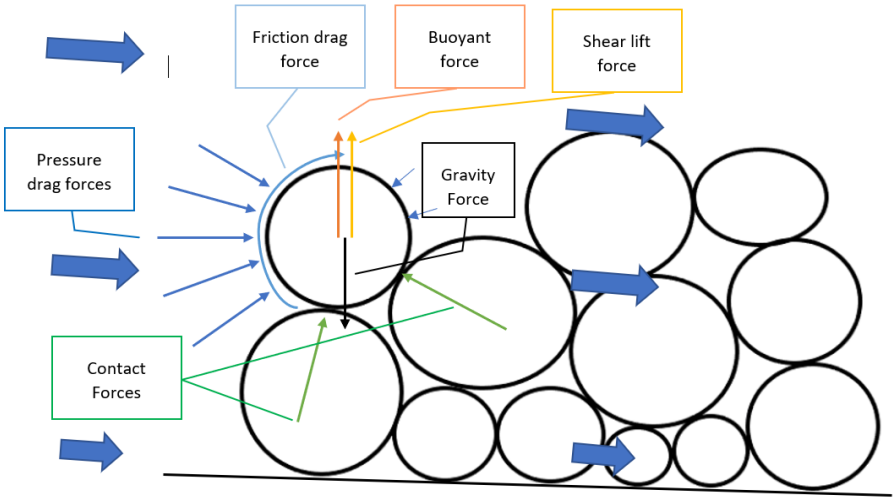

Figure 5-6 forces acting on particles under a fluid flow

Some of the forces presented in Figure 5-6 can be considered negligible when rotations of the particles are of low frequency. The spin lift force is generated by the rotation of particles and the drag torque is proportional to the angular velocity of particles. Therefore, both forces have a negligible effect on these particular cases. This consideration has been followed by Kawano et al., (2017) in the investigation of seepage, by Climent et al., (2014) in the investigation of sand production in oil wells, by Liu et al., (2015) in fluidisation in granular beds, and by Zhao, (2014) and Shan and Zhao, (2014) in the analyses of granular mass movements in water.

The drag force

When a particle moves relative to a fluid experiences a force opposite to the movement called the drag force. The drag force is subject to several factors: The relative velocity of the particle and fluid (higher relative velocity causes greater drag); the size of the particle (larger particles cause greater drag); the density of the fluid (denser fluids cause more drag) and the dynamic viscosity of the fluid (the more viscous is a fluid, the greater is the drag).

The drag force is the sum of the resistance forces in the direction of motion. Drag forces have two components: a) The pressure drag due to pressure forces on the surface), and

b) the friction drag due to viscous shear stresses over the surface of the particle (Figure 5-7).

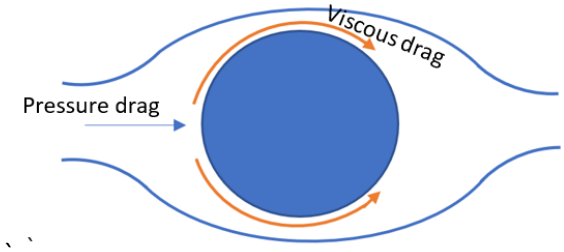

Figure 5-7 Components of the drag force (SLH, 2011)

The complicated effect of the flow conditions around a particle and their effect in the drag force is taken into account by a parameter called the drag coefficient.

There are different drag models in the literature (e.g. Di Felice, 1994; Ergun, 1952; Wen and Yu, 1966). For a list of more drag models, readers are referred to the fluidization handbook by Yang, (2003).

The universal semiempirical drag force equation for a single particle is defined as

$$F_{di} = \frac{1}{2} C_D \rho_p A_p |\boldsymbol{U} - \boldsymbol{V}|(\boldsymbol{U} - \boldsymbol{V}) \tag{5. 66}$$

Where

C_D =drag coefficient of the particle;

ρ_p =density of the soil granules;

$\boldsymbol{U}$ =average velocity of a fluid cell and $\boldsymbol{V}$ is the velocity of a particle;

A_p =projected area of the particle;

For a single particle the expression is well established, while for a particulate system, the problem is more complicated. Having other particles reduces the space for the fluid to flow and hence increases the shear stress at the particle surface. It leads to an enhancement of the drag force, which depends on the particle concentration in each cell (Traoré et al., 2015).

The Di Felice Drag Coefficient Method introduces an extra term in the fluid drag force expression to account for the effect of the presence of adjacent particles.

The Di Felice drag coefficient is given as (Hicks et al., 2014):

$$C_D = \left(0.63 + \frac{4.8}{\sqrt{Re_p}}\right)^2 \varepsilon_i^{-\xi} \quad (5.67)$$

in which the particle Reynolds number is determined by:

$$Re_p = \frac{\rho d_p |\boldsymbol{U} - \boldsymbol{V}|}{\mu} \quad (5.68)$$

Where,

ρ =density of the fluid;

μ =dynamic viscosity of the fluid;

d_p =diameter of the considered particle;

$$\xi = 3.7 - 0.65exp\left[-0.5\left(1.5 - log_{10}Re_p\right)^2\right] \quad (5.69)$$

ε_i =void fraction around a particle;

The term $\varepsilon_i^{-\xi}$ takes into account the effect of enhanced drag on a particle, due to the presence of other particles around it. (Zhao and Shan, 2013)

The Particle Shear Lift Force (Saffman force)

Particles in a shear field are subject to a lift force perpendicular to the direction of flow. The shear lift is caused by the inertia action in the viscous flow around the particle (Figure 5-8).

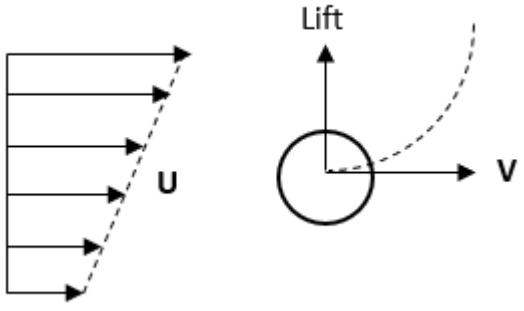

Figure 5-8 Schematic of the Saffman force (Ahmadi, 2005)

This force relates to a particle moving in respect to a fluid where there is a velocity gradient in the fluid orthogonal to the corresponding motion.

The lift force is caused by differences in pressure over the particle due to velocity gradients. The higher velocity on one side of the particle leads to lower pressures, whereas in the lower velocity side, the pressures are higher pushing the particle (Schwarzkopf et al., 2011). In the flow field presented in Figure 5-8, the difference in pressures results in a lift force.

Saffman, (1965) gives the shear lift force as

$$\boldsymbol{F}_{LS} = C_{LS}\frac{\rho\pi}{8}{d_p}^3[(\boldsymbol{U}-\boldsymbol{V})\times\vec{\boldsymbol{\omega}}] \quad (5.\ 70)$$

Where

$\boldsymbol{U}-\boldsymbol{V}$ =fluid velocity relative to the moving particle;

$\vec{\boldsymbol{\omega}}$ =fluid rotation velocity;

ρ =fluid density;

C_{LS} =shear lift coefficient;

$$C_{LS} = \frac{4.1126}{Re_S^{0.5}} \quad (5.\ 71)$$

The buoyant force

The interaction force between fluid and particles depends on hydrostatic and hydrodynamic forces (Shafipour and Soroush, 2008). The hydrostatic force takes into account the fluid pressure gradient around a specific particle (i.e. buoyancy) considering the fluid as hydrostatic (Zeghal and El Shamy, 2004; Kafui et al., 2011). The buoyant force is expressed as (Zhao, 2014):

$$\boldsymbol{F}_p = -V_p\nabla p \quad (5.\ 72)$$

Where V_p is the volume of the particle and ∇p is the pressure gradient in the continuous phase.

5.4 Conclusion

In this chapter, the equations describing the movement of runoff flowing over the face of the cutting have been introduced.

In particular, the theory behind RANS and the Realizable k- ε Model were used in this thesis for the calculation of the shear stress that runoff apply over the ground surface and for the calculation of the critical shear stress that initiates runoff generated debris flows.

A second approach based on simplifications of the NS equations (upon which RANS is constructed) has also been presented. The SWE was an important part in the development of the novel method for the calculation of surface shear stresses where large catchments areas are to be analysed. SWE allows the calculation of runoff generated shear stresses over the cuttings that develop under a specific rainfall intensity.

Finally, the DEM and the coupling of CFD-DEM have also been described. These equations allow the calculation of interactions between runoff and soil particles and is the approach used in the novel method where the assessment of failure will be carried out based on the dislodgment of chunks of soil (i.e. soil peds) under hydrodynamic forces applied by runoff.

In the next sections, the geotechnical parameters that were used in the DEM modelling of UK slopes in chalk and matrix dominated clay-like soils are presented.

Chapter6: Geotechnical parameters and case studies

In this chapter, it is investigated the range of geotechnical values in the UK for the two types of soils analysed using the novel method: Grade D_c chalk and matrix dominated clay-like soils. The novel method introduced later in chapter 8, was developed coupling computational fluid dynamics (CFD) with the discrete element method (DEM). The numerical experiments carried out for the development of the method consited of simulating the condition of a flume test (i.e. interaction between superficial water and soil blocks) with the soil simulated as discrete spheres. For modelling of the soil in DEM, geotechnical parameters corresponding to the types of soil analysed are needed: (i.e. Young's modulus, Poisson's ratio, static fiction coefficient and bulk unit weight).

The novel method was designed to be used for Grade D_c chalk and matrix dominated clay-like soils (i.e. Head deposits, cohesive glacial tills, clay with flints and cohesive alluvium). Grade D_c chalk is a type of structureless chalk consiting of fragments of intact chalk embeded in a matrix of putty (remoulded) chalk. Matrix dominated clay-like soils is defined as fragments of clay embeding coarser particles.

For the development of the novel method in Grade D_c chalk, the soil is discretised into chalk fragments corresponding with clasts of intact chalk with the external boundary corresponding to the properties of putty chalk.

The angle of static friction representing the inter-clast friction in DEM was considered as the residual angle of shearing resistance of remoulded chalk (i.e. putty chalk) embedding the clasts.

For the clay-like soils, coarser particles may be embedded in a fine matrix consisting of clay, silt and sand. In this case, the angles of static friction also known as the interparticle friction angles have been obtained from the residual angles of internal friction encountered in the literature.

The range of geotechnical values for these soils were used in the development of the novel method, so that the charts created for the application of the method cover all variants of Grade D_c chalk and clay-like soils encountered in the UK.

The description of the case studies analysed in chapter 9 using the novel method has also been presented in this chapter. Each case study was broken down into four subsections: a) history of the site, b) accident descriptions (when applicable), c) geology, d) the NR management of the cutting before the failure and e) geotechnical parameters.

For Watford case study, additional information regarding soil evapotranspiration was presented as this case was also analysed in Chapter 7, using traditional method for stability analysis.

The case studies selected present special interest owing to the severity of the accidents or the disruptions in the railway lines. Watford and Hooley were selected for chalk type of soil, the first due to the severity of the accidents and the second due to the recurrent number of failures at this location. For clay-like soiks, Loch Treig was chosen due to the severity of the accidents and St Bees to take advantage of the analysis of two slope failures at the same event. One additional case was investigated corresponding to a runoff generated debris flow failure, this time in a road at Beaminster in clay, due to the high repercussion in the media with two car passengers buried and killed under the failure deposits (BBC News, 2014;The Guardian, 2012).

The soil parameters used were obtained from boreholes, information obtained from experts advice (i.e. Beaminster), geotechnical investigation reports and literature.

Watford cutting was visited on 16 October 2017 and 12 June 2020 and Beaminster was visited on 12 June 2020. No tests were carried out by the author of this thesis.

6.1 Range of geotechnical parameters for chalk and matrix dominated clay-like soils

Variations in source materials, combined with the complex depositional and post depositional processes that occur in the glacial and post glacial environments, results in glacial tills having a wide range of geotechnical properties and the most varied range of particle size distribution of any soil (Marsland and Powell, 1991; Clarke, 2018).

The wide range of soil properties within glacial tills include those present in other types of clay-like soils. Therefore, in this section, special attention was given to properties of glacial tills. The novel method was designed to be applied to cohesive glacial tills, cohesive alluvium, head deposits and clay with flints indistinctly as they all have similar composition (coarse particles embedded in a fine matrix).

Grade D_c chalk presents different geotechnical properties depending on calcium carbonate contents and plasticity, as reported by Clayton, (1978).

In the next sections, the properties of Grade D_c chalk and clay-like soils commonly found in the UK are presented.

6.1.1 Grade D_c chalk properties

Weathering mechanisms in chalk such as stress relief, frost action and solutioning may combine to create additional fractures that are superimposed on the initial joint system present on chalk. When as a consequence of weathering the structure of the rock mass is lost completely, the material reduces into a soil comprising disordered chalk fragments of different sizes set in a matrix of remoulded chalk lacking all type of structure including fissures and fractures what is known as a D_c structureless chalk (Figure 6-13) (Tan, 2003; Bell et al., 1999).

1. Location

The location of outcrops of chalk in England and chalk underlying tertiary deposits is shown in Figure 6-1.

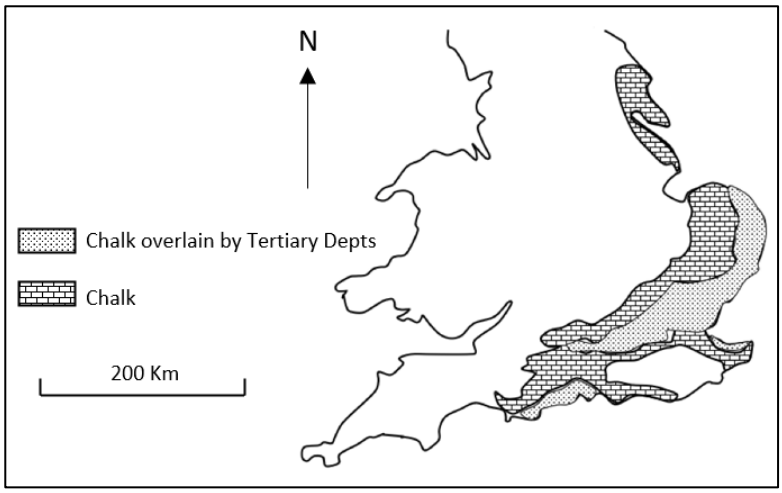

Figure 6-1 Sketch map of the extent of the Chalk in England (Bell et al., 1999)

Since the formation on the seabed, chalk has undergone differing degrees of compaction, cementation and weathering resulting in differences in hardness, density, porosity and strength (Lord et al., 2002)

At the deepest levels, sometimes 30–50 m below ground level, structured chalk is present (ie nearly undisturbed bedding layers and more than 95 percent intact chalk blocks). Structured chalk passes progressively upwards into structureless, often highly disturbed chalk or remoulded chalk (Lord et al., 2002).

2. The bulk unit weight of chalk

To obtain a representation of the unit weight range for D_c chalk in the UK, a representative sample from weak to moderately strong chalk is shown in Table 6-1 with

values obtained both from the literature and ground investigations reports. The locations where the values of unit weight were obtained are presented in Figure 6-2.

Figure 6-2 Location of chalk samples (Google Earth)

Table 6-1 Unit weight for Grade D_c chalk

Chalk Type	Location	Reference	γ_{bulk} (KN/m^3)
Weak Chalk	Cambridge	(Parasnis, 1952)	19.3-19.7
Weak chalk	West Berkshire	(AECOM, 2019)	16.1-20.9
Weak to very weak chalk	Hackney, London	(Fugro, 2016)	19.8-20
Weak Weathered chalk	Rainham (London)	(BRD, 2018)	17.6-19.4
Moderately Weak chalk	Ipswich	(Hamza and Bellis, 2008)	18.5-20
Weak chalk	Winchester	(Ground and Water, 2015)	19.3-20.3
Moderately strong chalk	Yorkshire	(Bell et al., 1999)	22.9
Weak to Moderately weak chalk	Norfolk	(Bell et al., 1999)	20
Very Weak chalk	Kent	(Bell et al., 1999)	19.1
Weak Chalk	Watford	(Lake,1975)	19.4

Values of bulk unit weight in the representative example range from 16.1 kN/m^3 in West Berkshire to 22.9 kN/m^3 in Yorkshire. These values will be used as upper and lower boundary values for the development of the novel method in D_c chalk.

3. Angle of shearing resistance

Cawsey and Farrar, (1976) found that the angle of static friction ($\emptyset'_{\mu}$) on smooth blocks of chalk vary from 33° to 38°. These results are comparable to the range of residual angles of internal friction of structureless chalk found in the literature. The similarity may be due to fact that the superficial roughness of blocks of intact chalk are controlled by the fine fraction.

The residual angles of internal friction for remoulded chalk reported by Clayton, (1978) varies between 29° and 34°, with most values falling in the range 31–33°.

Jenner and Burfitt, (1974) conveyed similar consistent values with a typical design value of 35° and an absolute minimum of 30° (Lord et al., 2002). However, other authors have obtained different values for remoulded chalk as Fletcher and Mizon, (1983), Lake, (1975) and Twine and Wright, (1991) who reported values of 39°.

The strain dependency could be the reason for the discrepancy presented or due to samples preparation, which could have been different, or because the tests were carried out at different stress ranges (Bundy, 2013).

The residual angle of shearing resistance considered for the calculation of the critical shear stress in the design of the novel method for chalk was in the range from the minimum and maximum values found in the literature: 29°(Clayton, 1978) and 39° (Fletcher and Mizon, 1983; Lake, 1975; Twine and Wright, 1991).

4. Superficial chalk Poisson's Ratio

Poisson's ratio (v) for application to Grade D_c chalk in DEM will correspond to clasts fragments of intact chalk.

Poisson's ratio are not simple constants but are related to the level of stress applied (Bell et al., 1999). Few measurements of Poisson's ratio for intact chalk are reported in the literature (Lord et al., 2002) including 0.25 (Halcrow, 1979; Lake, 1975; Ward et al., 1968), 0.32 (Bell, 1977; Bell et al., 1999) and 0.24 (Burland and Lord, 1970).

The Poisson's ratio considered for the calculation of the critical shear stress will be in the range maximum and minimum values described before: 0.24-0.32.

5. Young's Modulus

Young's modulus (E) and v are not simple constants but are related to the level of stress or strain applied (Bell, F.G. 1977; Poulos, 1989). In weak chalk, E decreases slightly with increasing stress whereas the opposite occurs in stronger chalk (Bell, 1977).

Some of the values found in the literature include: 2.5 GPa (Lake,1975), 5 GPa (Ward et al., 1968), 5.7 GPa (Bell, 1977), 6 GPa (Matthews and Clayton, 1993; Jardine et al., 1984), 7.6 GPa (Matthews and Clayton, 2004) and 10.9 GPa (Bell et al., 1999).

The Young's Modulus considered for the calculation of the critical shear stress in the design of the novel method for chalk will be in the range of maximum and minimum values obtained: 2.5-10.9 GPa.

In the next section, the properties of matrix dominated clay-like soils in the UK are presented.

6.1.2 Matrix dominated clay-like soil properties

1. Location

Glacial deposits overlie much of the British Isles and the surrounding sea areas and are of considerable engineering importance.(Marsland and Powell, 1991).

Tills account for the majority of the superficial deposits in the UK. Glacial soils amount to 60% of the soils in the UK with most national infrastructure in the UK founded on them (Trenter, 1999). Clay with flints are located in specific regions below the glacial tills limits and alluvium are dispersed all over the UK in river valleys or deltas (see (Figure 6-3).

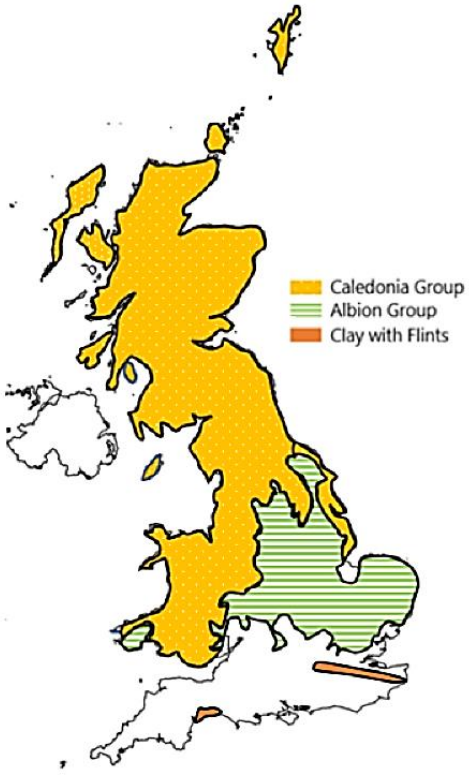

Figure 6-3 Extents of the Albion Glacigenic Group and the Caledonia Glacigenic Group(Culshaw et al., 2017b)

A till may be a matrix-dominated soil which acts as a fine-grained soil but also has coarse-grained particles (at least 35% fine-grained content) or, a clast-dominated soil which performs as a coarse-grained soil but contains fine-grained particles (less than 15% fine-grained content)(Clarke, 2018). The extension of glacial tills by the type of matrix is shown in Figure 6-4

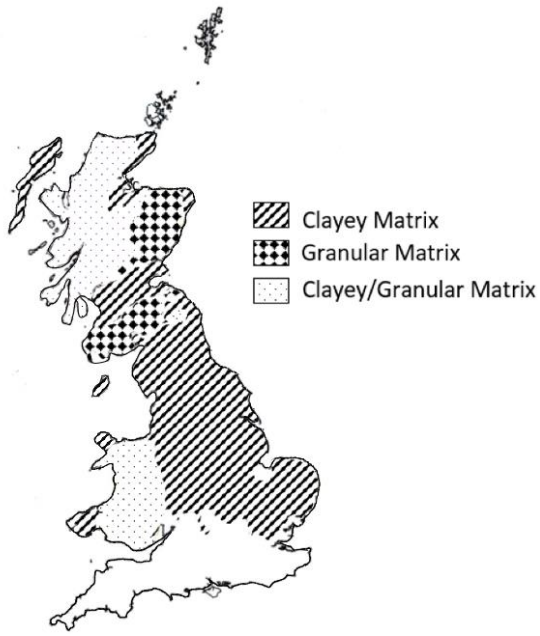

Figure 6-4 Extensions of glacial tills based on the type of matrix(Culshaw et al., 2017b)

2. The bulk unit weight

In order to obtain a representation of the unit weight range for different types of clayey soils in the UK, a representative sample is shown in Table 6-2. The locations where the values of unit weight were obtained are presented in Figure 6-5.

Figure 6-5 Location of glacial tills samples (red) and alluvium and head deposits (yellow)

Table 6-2 Unit weight for different types of glacial tills

γ_{bulk} (KN/m3)	Location	Type of Till	Reference
19.9-21.8	Northern East England	Upper weathered red till	Hashemi et al., (2006)
20.5	Central Lowlands of Scotland	Cohesive till	Mckinlay et al. (1974)
21	Vale of St Albans	chalky clay tills	(Marsland and Powell, 1991)
22.3	Selset, Yorkshire	Boulder Clay	(Skempton and Brown, 1961)
19-22	Northumberland	weathered granular matrix tills	Eyles and Sladen (1981)
19.2-22.1	Anglessey	Red Till	(Boon et al., 2014)
20	Stafford	Red Till	(Atkins, 2012)
20-21	Northumberland	Upper Red Till	(Clarke et al., 2008)
19-23	Milton Keynes	Chalky Boulder Clay	(Culshaw et al., 2017a)
17	London	High Plasticity Alluvium	(C.C.S., 2014)
18	London	Alluvium (silty clay and sandy gravelly silty clay)	(Concept, 2016)
15-20	Hailsham (East Sussex)	Alluvium (clay, silt and sand)	(Southern Water, 2017)
18	Stratford	Alluvium (very soft to soft slightly sandy clay)	(Rankine, 2016)
17	Northampton-Daventry	Alluvium (Firm brown slightly sandy slightly gravelly clay)	(WSP, 2014a)
16.5-21.5	Milton Keynes	Alluvium (soft clay, sandy clay and silt)	(EWR,2020)
18	Wivelrod (Hampshire)	Head deposits (sandy gravelly clay)	(Science, 2010)
19-21	Milton Keynes	Head Deposits (slightly gravelly slightly sandy CLAY)	(EWR,2020)

The values of γ_{bulk} obtained from cohesive glacial tills, alluvium, head deposits and clay with flints range from 15° to 23° and this will be the range of γ_{bulk} that will be considered for the calculation of the critical shear stress in clayey soils.

3. Angle of shearing resistance

The residual angles of shearing resistance for fine matrix dominated soils is directly comparable with the angles of static friction ($\emptyset'_{\mu}$) due to the orientation of fine particles parallel to the slip plane (Horn and Deere, 1962; Skempton, 1964).

Plasticity index in most UK glacial tills range between 10 and 30% (Clarke, 2017).

Tills weather by oxidation, hydration, leaching (e.g. of carbonates) and by mechanical disintegration (Eyles and Sladen, 1981 ; Sladen and Wrigley, 1983). The upper parts of

glacial tills are often weathered specially in the top metres as a result of atmosphere exposure (Culshaw et al., 2017b).

Plasticity index in weathered tills in the North East of England showed an increase in the plasticity index in the range 20% to 40% moving along the T-Line (Clarke, 2017), corresponding to a liquid limit above 40%.

For tills of the Central Lowlands of Scotland, Mckinlay et al. (1974) found that the plasticity index of weathered tills was greater than that of the unweathered till, similar to findings observed for tills of NE England (Bell and Forster, 1991; Clarke et al., 2008). (Clarke, 2017)

The results of work for different UK glacial tills by Skempton and Brown (1961), Jacobson (1970), Tarbet (1973), Vaughan and Walbancke (1973), Eyles and Sladen (1981) and Sladen and Wrigley (1983) show the majority of $\emptyset'_r$ values between 15° and 33° (Figure 6-6) for glacial tills with plasticity indexes between 20% and 40% (Clarke, 2017). These results are in agreement with the values recommended by (Trenter, 1999) and (Eyles and Sladen, 1981). Values of $\emptyset'_r$ for alluvium, head deposits and clays with flints obtained from the literature, ground investigation reports and expert advised are shown in (Table 6-3).

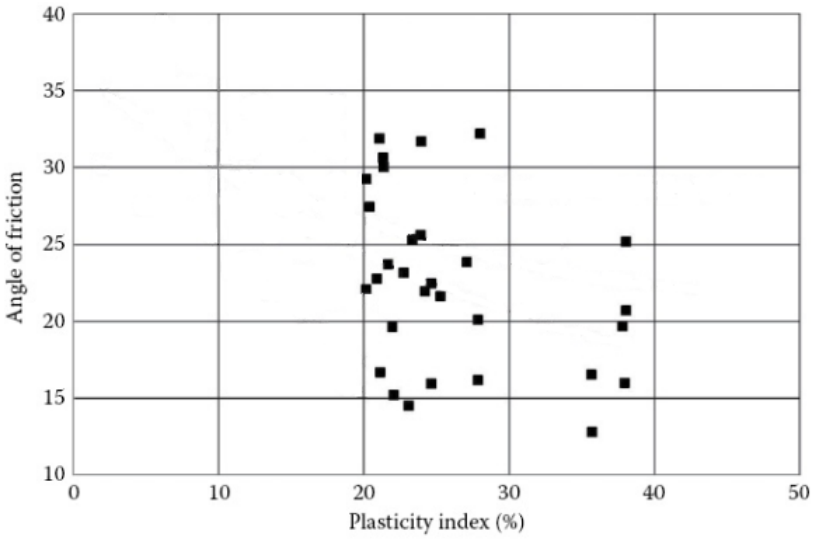

Figure 6-6 Residual angles of internal friction for British glacial tills with plasticity indexes between 20% and 40% (Clarke, 2017)

Table 6-3 Residual angles of internal friction for Alluvium and Head deposits in various locations of the UK

$\emptyset'$	Location	Description	Reference
25	Stratford	Alluvium (very soft to soft slightly sandy clay)	(Rankine, 2016)

31°	Norwich	Alluvium (sands, silts and clays)	(Wilkes, 1974)
19-25	Northampton-Daventry	Alluvium (Firm brown slightly sandy slightly gravelly clay)	(WSP, 2014a)
25	Manchester Ship Canal	Alluvium (Gravel, sand, silt, and clay)	(Galliford-Costain-Atkins, 2014)
28.8	Mucking	Soft Alluvium	(Lupini, 1980)
20-38	Milton Keynes	Alluvium (soft clay, sandy clay and silt)	(EWR,2020)
15-27	Milton Keynes	Head Deposits (slightly gravelly slightly sandy CLAY)	(EWR,2020)
30	Wivelrod (Hampshire)	Head deposits (sandy gravelly clay)	(Science, 2010)
23	Beaminster	Clay with Flints	Ursula Lawrence (personal communication)

The values of $\emptyset'_r$ obtained from clay-like soils range from 15° to 38° and this was considered for the applycation of the novel method in clayey soils.

4. Poisson's Ratio

Poisson's ratio for a matrix dominated till of 0.2 was recommended by Powrie and Li, (1991), Steinbrenner, (1934) and Farrell and Lawler, (2001).

Poisson's ratio for cohesive alluvium between 0.2 and 0.3 have been reported in Galliford-Costain-Atkins, (2014) and Rankine, (2016).

Poisson's ratios coefficients in the range 0.2-0.3 were used for application of the novel method in clayey soils.

5. Young's Modulus matrix dominated clay-like soils

Values of Young's Modulus from the literature and ground investigation reports are shown in Table 6-4.

Table 6-4 Values of Young's Modulus for clay-like soils

	E' (MN/m2)	Location	Reference
Cohesive Glacial Till	7-33	Northamptonshire	(WSP, 2014b)
Cohesive Glacial Till	11	Northern Ireland	(Mouchel, 2011)
Cohesive Glacial Till	10-16		(Cai et al., 1994)
Cohesive Alluvium	5	Stratford	(Rankine, 2016)

Cohesive Alluvium	2	Northampton-Daventry	(WSP, 2014a)
Cohesive Alluvium	9	Manchester Ship Canal	(Galliford-Costain-Atkins, 2014)
Cohesive Alluvium	8-19.6	Milton Keynes	(EWR,2020)
Head Deposits	8.4-9.5	Milton Keynes	(EWR,2020)

The values of E' ranged from 2 MN/m^2 to 33 MN/m^2 and were considered in the development of the novel method.

6.1.3 Particle parameters for chalk and matrix dominated clay-like soils

The restitution coefficients, coefficient of rolling resistance and particles diameters have been obtained from recommended values for soils in the literature.

1. The restitution coefficient

The restitution coefficient is related to energy loss during collisions. A typical value of 0.01 representing high inelastic collisions has been proved to represent well the case of natural soil (e.g. Ferdowsi et al., 2018; Schmeeckle et al., 2001; Schmeeckle, 2014).

2. The coefficient of rolling resistance

The coefficient of rolling resistance, $\mu_r = 0.1$, was described by Huang et al., (2013) as a reasonable estimate for many natural materials. An analysis carried out by Estrada et al., (2011) for two dimensional particles correlates μ_r with an n sided polygon (6. 1) where μ_r =1 corresponds to an octagon in 2D representation.

$$\mu_r = \frac{1}{2} tan\left(\frac{\pi}{2n}\right) \quad (6.\ 1)$$

A coefficient of rolling resistance of 0.1 was obtained by Liu et al., (2020) after a calibration process in a DEM model simulating a full scale test of a debris flow investigated by Ferrero et al., (2015)(Figure 6-7).

The same coefficient was used by Shan and Zhao, (2014); Zhao et al., (2017); Utili et al., (2015), An et al., (2020) and by Liu et al., (2020b) for investigating the movement of debris flows.

$\mu_r = 0.1$ has been established as the value to be used for the simulation of non-spherical soil particles in the literature (Jing et al., 2018; Usuki et al., 2019). This value was selected in the analysis of case studies using the novel method.

Figure 6-7 Full scale test of debris flow carried out by Ferrero et al., (2015)

3. Size of Particles

The calculation of the size of particles in debris flows can be obtained by photoanalytical techniques when the size of the particles are too large for sieving (Casagli et al., 2003, Crosta et al., 2007).

Particles diameter of different ranges have been used by different researchers for the analysis of debris flows: e.g. 20 cm of particle diameter was used by (Zhao et al., 2017); 7cm by Shan and Zhao, (2014), 4cm by Li and Zhao, (2016), between 4cm and 7 cm by Jing et al., (2018), 10cm by Usuki et al., (2019) and between 0.2m and 0.3m by Liu et al., (2020). Diameter particles as large as 1 and 2m was used by Liu et al., (2020b) for debris flows

In the simulation by previous researchers of the movement of debris flows using the DEM, the diameter of the particles has been obtained with some degree of arbitrariness in order to replicate results from laboratory experiments or real cases in the field.

In this thesis, a diameter of the particles of 10cm has been selected that agree well with the real cases analysed.

6.2 The Watford case study

The cutting failure at Watford occurred during an extreme rainfall event where high-intensity runoff flew down the face of the cutting, resulting in superficial deposits of gravelly clay and fragments of underlying chalk falling off the cutting and depositing over the railway track. The cutting failure at Watford is classified as runoff generated debris flow following the proposed classification system.

6.2.1 History of the site at Watford

The Watford tunnels are located between Watford and Kings Langley as part of the London-Birmingham Railway (Figure 6-8). The Watford fast lines tunnel opened on the 20th of July 1837 as part of the Euston to Boxmoor section.

The Watford slow lines tunnel separated by an estimate of 60 metres was inaugurated in 1874 and was constructed to broaden the route to four tracks to improve capacity. The cuttings on both lines were excavated in chalk, but the deposition of sediments over time has covered the cutting faces (Arnold, 2014).

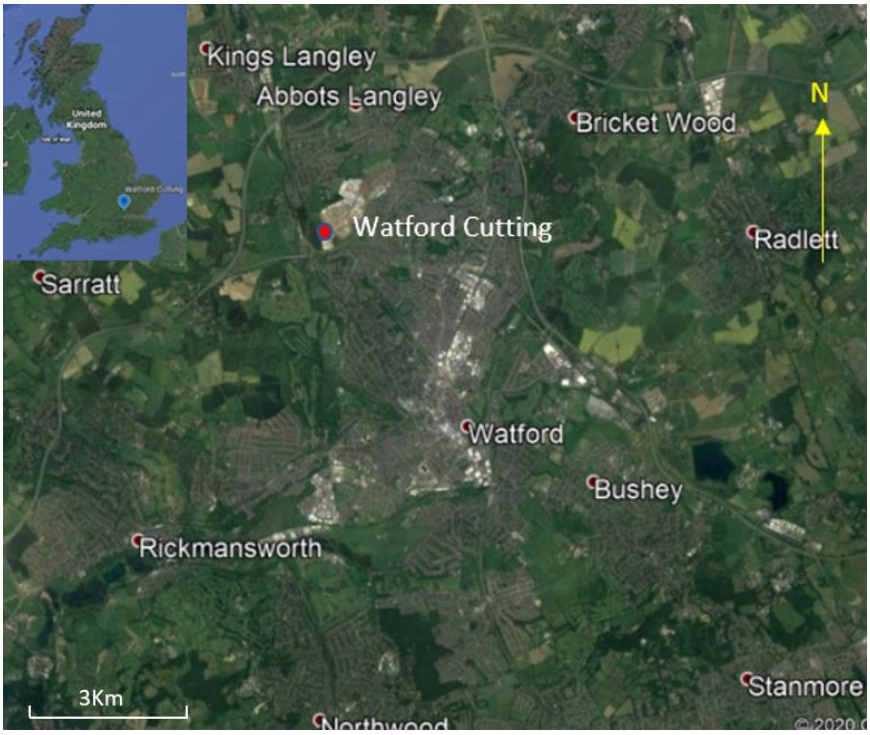

Figure 6-8 Watford Cutting Location (Google Earth)

Surrounding the crest of the slow lines, there is a relatively flat area highlighted by the red dashed line in Figure 6-9. This area was military-civilian airfield but is now part of the Warner Brothers studio compound and is used for the setting up of exterior film sets.

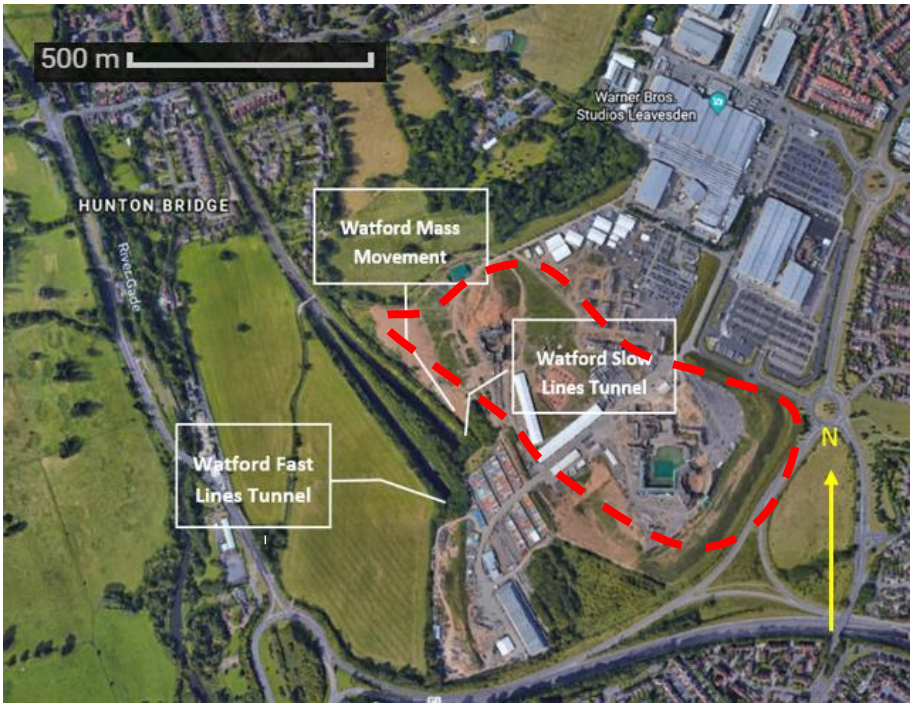

Figure 6-9 Watford Tunnel location (Google Earth)

A failure in the cutting portal of the slow line tunnel occurred on 4 February 1940 as a result of intense rainfall (RAIB, 2017). The London Midland and Scottish (LMS) Railway Company, in charge of the railway network at the time, first repaired the cutting by installing a large masonry 'face wall' to strengthen the slope, but also as a drainage feature to secure a safe path for surface water to drain from the cutting crest to rail track level. In addition, rubble filling of cavities present on the face of the bank was carried out behind the masonry. A channel was constructed along the crest of the cutting to divert surface run off onto the wall face although it was buried with sediments over time. The RAIB identified this as proof to demonstrate that the masonry wall was projected to have a drainage function, stopping surface water flows unrestricted down the cutting slope (RAIB, 2017).

The flat area was acquired by Warner Bros Entertainment Inc (WBE) in 2000. In 2006, WBE started a series of earthworks of considerable magnitude for the construction of film sets, which continue to be carried out depending on the requirements of the films. In 2013, an embankment was built at the NW edge of the flat area for the installation of film sets and in 2016 an access was built to the top of the embankment. In 2018 the embankment and the access were removed from the area. The historical evolution of the flat area is illustrated in Figure 6-10.

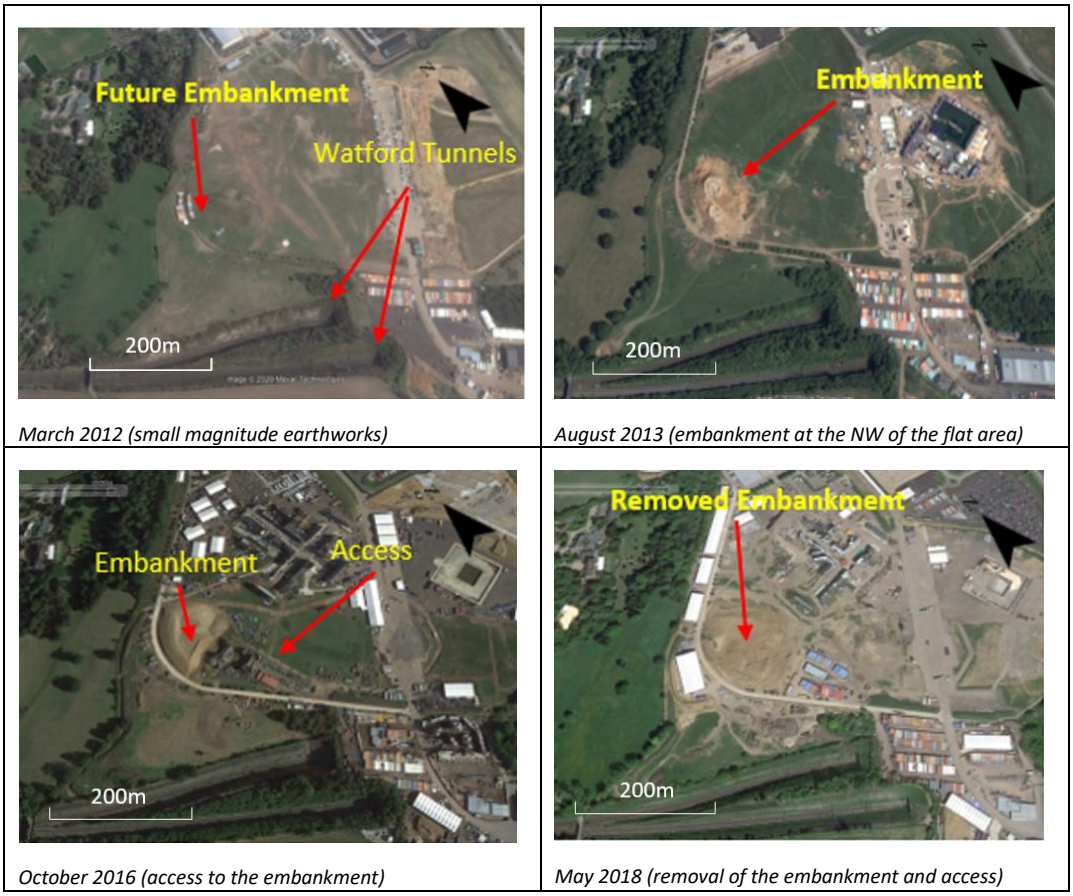

Figure 6-10 Historical Evolution of Catchment at Watford (Google Earth Pro)

A cutting failure took place at Watford Tunnel on 16 September 2016 during a short and intense rainfall event (RAIB, 2017).

6.2.2 Accident description at Watford

The runoff generated debris flow occurred at about 06:56 hrs on 16 September (RAIB, 2017). As a consequence of the mass movement, material deposits accumulated on the up slow line of the north portal blocking the railway line and causing the crashing of two trains.

The cutting failure consisted primarily of chalk blocks falling and rolling from the face of the cutting. A large number of chalk fragments were deposited over the railway track (Figure 6-11).

Figure 6-11 Cutting failure at Watford(RAIB, 2017)

As a consequence of the failure, material deposits accumulated on the up slow line of the north portal blocking the railway line.

The accident occurred after a few days of hot and dry weather. According to RAIB, (2017), the amount of rainfall that triggered the cutting failure was comparable to the average rainfall between 2009-2016 for the entire month of September in the Watford area. The rain commenced at 17:00 on the 15 of September and intensified at 03:00 am on 16 September 2016, with the failure taking place nearly four hours later.

Chenies, in Hertfordshire, at approximates less than 8km from the Watford cutting, has a meteorological office weather radar which recorded for the four-hour period between 02:45 hrs and 06:45 hrs, a rainfall of 50.7 mm. This is equal to a 4h storm with a 1 in 42 year return period (RAIB, 2017).

Similar rainfall intensity was obtained from amateur weather stations close to the cutting failure that registered 12.5mm/h between 02:45 hrs and 06:45 hrs RAIB, (2017).

Both the RAIB and representatives of the Warner Bros studio conducted an inspection of the site on 16 September 2016 where proof was found that a substantial volume of water had run in the direction of the crest of the failed cutting. The RAIB, (2017) concluded that intense rainfall led to a runoff generated debris flow failure.

A considerable amount of water emanated from a point about half-way up the slope adjacent to the masonry wall (The emanating water is adjacent to an area where the slope was filled with rubble behind the masonry) (Figure 6-12).

RAIB, (2017) concluded that the emanating water could have contributed to both the February 1940 and the September 2016 failures although the main contributing factor was attributed to rainfall runoff.

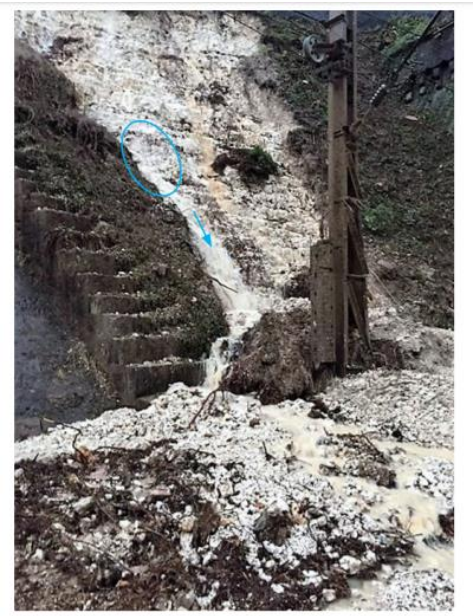

Figure 6-12 Image showing water emanating from part-way down the cutting slope (courtesy of Network Rail) (RAIB, 2017)

6.2.3 Network Rail management of the cutting at Watford

NR evaluates the risk related to cutting failure through a combination of EHC and EACB.

In August 2014, a 5 chain length including the failed cutting, were examined and classified in accordance with the Earthworks Hazard Category (EHC) as a 'B', in a scale ranging from 'A' (the least likely to fail case) to 'E' (the most likely to fail case), and a EACB of 5 (1 being less critical and 5 the most). However, due to the presence of other steeper lengths, graded as 'E', the entire cutting was considered, and therefore managed, as a high risk (likelihood) of failure (RAIB, 2017)..

As a consequence of the high EHC and EACB assigned to the cutting, a number of maintenance works were programmed in order to eliminate the high risk of disruption of the railway line in the likely event of failure due to trees falling into the tracks. Works consisted mainly of the removal of trees and large vegetation, as well as the installation of rock-fall netting.

By removing trees, the root growth was reduced and therefore, the risk related to root jacking moving blocks of rock was minimised further. The surface of the slope, and roots binding the soil and rock layers, were left undisturbed.

The netting was installed to restrain the movement of blocks of rock as well as containing other material falling from the cutting face, and stopping them at the toe of the cutting slope before they would enter the railway lines.

NR staff were unaware at the time of the examination of the cutting failure that had happened at roughly the same location on 4 February 1940.

NR did not appreciate that the masonry wall constructed after the 1940 cutting failure had a drainage role. Therefore, previous issues with runoff were not evident on the cutting at the moment of the examination. An evaluation of the surface water drainage management by the design consultant in their Geotechnical Assessment Report concluded that drainage infrastructure to cater for surface water runoff was not required (RAIB, 2017).

6.2.4 Geology at Watford

a) Bedrock Geology and Superficial Deposits

A window sample borehole carried out by Amey in May 2015 at the crest of the failed cutting, classified the bedrock as Grade D_c structureless chalk according to the Chalk CIRIA Grading Scheme (Lord et al., 1994).

The same window sample revealed superficial deposits consisting of a 55cm sandy gravelly silt layer overlaying 65 cm of clayey gravel. According to the 1:50000 BGS digital geological map, superficial geology at the cutting location belongs to the Gerrards Cross Gravel formation containing sand and gravel, locally with lenses of silt, clay or peat and organic material. This is consistent with the description of glacial clayey gravel given by Harries et al., (1982) and in RAIB, (2017) for superficial deposits at Watford.

Figure 6-13 CIRIA grade Dc chalk (Mortimore, 2014)

The thickness of the top layer and superficial deposit overlying the chalk is considerably thinner along the face of the cutting (about 50cm) according to Amey Technical Director Townend, Helen via personal communication on 23 January 2019, and Figure 6-14. Inspection of the cutting by the RAIB described that the lower part of the cutting comprised only chalk rock (RAIB, 2017).

Figure 6-14 Failure at Watford (PA Media, 2016)

b) Engineering geological model

Based on the information from the geology at Watford, an engineering geological model at Watford cutting is presented in Figure 6-15. A layer of superficial deposits consisting of sand, clay and gravels overlies the D_c chalk beyond the crest of the cutting and gets thinner at the cutting face.

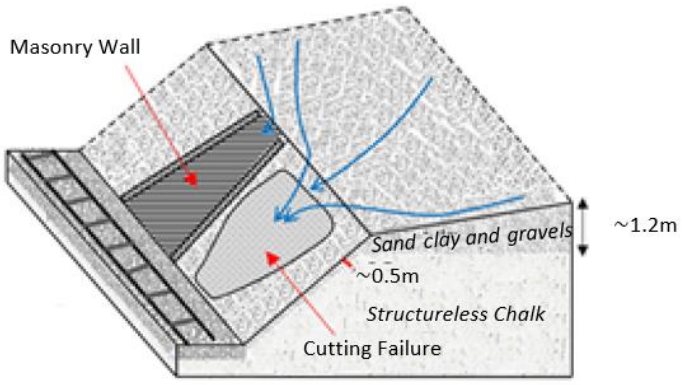

Figure 6-15 Engineering geological model of Watford Cutting

6.2.5 Geotechnical properties and climatic conditions at Watford

The stability of the Watford slope against translational slides was assessed in Chapter 7, accounting for the effect of long term climatic conditions and weather (short term) conditions including the extreme rainfall event that triggered the failure at Watford.

For the case studies presented in this chapter (i.e. Watford, St Bees, Beaminster, Hooley and Loch Treig), only Watford was further analysed using continuum methods and additional climatic and geotechnical parameters have been described (i.e. unsaturated shear strength, saturated hydraulic conductivity, soil water characteristic curve, hydraulic conductivity function) to account for the effects of infiltration and evapotranspiration.

1. Geotechnical Parameters

   Geotechnical parameters for chalk and superficial deposits are described in the next subsections.

   <u>Geotechnical parameters of Grade Dc Chalk</u>

   a) Shear Strength

The shear strength of chalks at Watford was obtained from the work of Lake, (1975) who investigated the shear strength parameters of chalks along the North Orbital Road. The section from the west of Rickmansworth through Chorley Wood to the north west of Watford was examined.

Lake, (1975) performed a series of drained direct shear box tests in a 6 cm square shear box apparatus modified to allow the box to be reversed so that the shearing could be carried out to the residual value ($\emptyset'_r$). Lake, (1975) obtained an average value of $\emptyset'_r$=39°.

For unsaturated chalk, ϕ^b is the parameter to account for the contribution of matric suctions to the shear strength according to the Fredlund and Morgenstern's approach. $\phi^b = 19^\circ$ was considered in the analysis according to the recommendation of Fredlund and Rahardjo, (1993) who suggested a constant value for ϕ^b of about half the residual angle of internal friction.

b) Unit Weight

A mean bulk density of 1940Kg/m^3 was obtained by Lake, (1975) at North Orbital Road from a series of open drive samples.

c) Saturated Hydraulic Conductivity

Lake, (1975) obtained a mean dry density of 1440Kg/m^3 for chalk, corresponding to the type of soft chalk according to Lord et al., (2002). Soft Dc chalk are conformed of clasts of intact chalk covered by putty chalk with lack of cracks and fissures. Soft D_c chalks have proportions of fines greater than 15% where the hydraulic conductivity of the material as a whole is controlled by the fine fraction. (Razoaki, 2000;Puig, 1973;Rat and Schaeffner, 1990). As no fissure or cracks are present, the permeability corresponds to that of putty chalk similar to the one of intact chalk (Bundy, 2013) that is controlled by the fine fraction, with values of K_s ranging between 10^{-7} to 10^{-9} m/s (Lord et al., 1994).

Five triaxial dissipation tests were carried out by Lake, (1975) in Grade D_c chalks at Watford. Values for K_s ranged from 0.8x10^{-8} m/s to 1.3x10^{-8} cm/s with a mean value of 10^{-8} m/s. This value is consistent with the value for structureless chalk quoted by Higgibottom, (1965) and was used for the analysis at Watford.

d) Soil Water Retention Curve and Hydraulic Conductivity Function

Croney and Coleman, (1954) obtained the wetting SWCC for soft chalks using gravimetric water contents. To adapt the SWCC obtained by Croney and Coleman, (1954) to the properties of the soft chalk at Watford, a saturated volumetric water content of 43% corresponding to D_c chalk at Watford (Lake, 1975) was used in the conversion together with (6. 2) to obtain volumetric water contents from gravimetric water contents (Figure 6-16).

$$\theta = w \cdot \frac{\gamma_{bulk}}{\gamma_{water}} \qquad (6.\ 2)$$

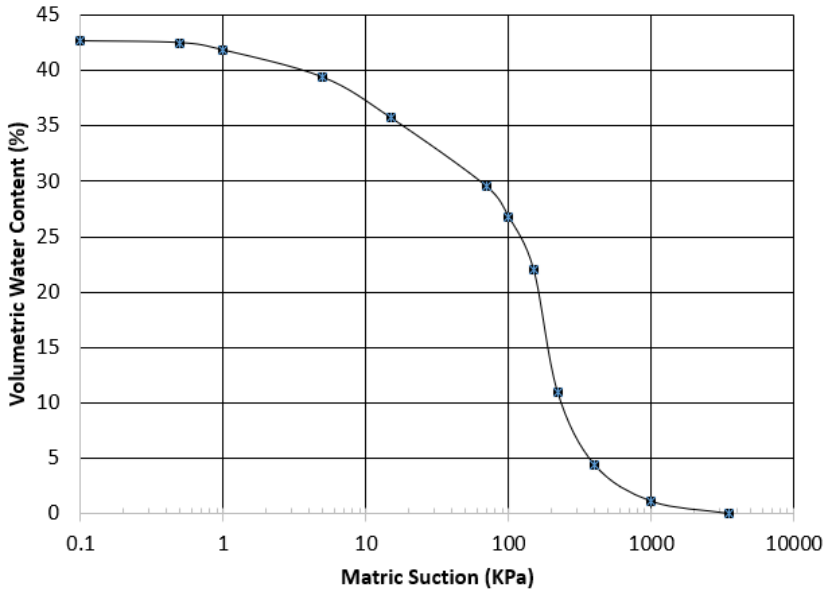

Figure 6-16 SWCC for soft chalks (after Croney and Coleman, 1954)

The hydraulic conductivity function for the chalks at Watford Tunnel has been obtained by applying the Mualem's, (1976) model to the SWCC with the introduction of the saturated hydraulic conductivity K_s=10^{-8} m/s.

The hydraulic conductivity function obtained from Mualem's, (1976) model using the SWCC has been derived in SEEP/W, (2016)(see section 4.1.3). The software obtains the best fitting parameters for the van Genuchten's model, and the resulting function is presented in Figure 6-17.

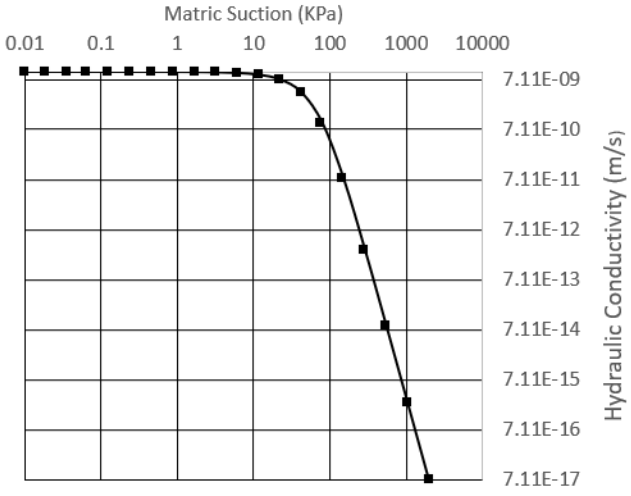

Figure 6-17 Hydraulic conductivity function of chalk at Watford

<u>Geotechnical parameters of superficial deposits (glacial clayey gravel)</u>

a) Shear Strength

Little, (1984) classified superficial deposits at St Albans as low to medium plasticity glacial till. Little, (1984) obtained a shear strength parameter of $\emptyset'_r$=25° from drained shear box tests on reconstituted till. This result matches the recommended values for low to medium plasticity glacial till in Trenter, (1999). $\phi^b = 12.5^\circ$ was considered in the analysis according to the recommendation of Fredlund and Rahardjo, (1993).

b) Unit Weight

Mean values of bulk unit weight of 21kN/m3 were reported by Marsland and Powell, (1991) and Little, (1984) at the Vale of St Albans and Watford respectively.

c) Saturated Hydraulic Conductivity

According to the investigation carried out by Harries et al., (1982) at Watford area, superficial deposits comprise Glacial Sand and Gravel with a mean grading of fines 17%, sand 41% and gravel 42% giving an overall mineral classification of 'clayey gravel'.

Characteristics of binary granular mixtures have been investigated by a number of researchers. Shakoor and Cook, (1990) and Shelley and Daniel, (1993) found that the hydraulic conductivity was significantly increased with percentages of coarse soil higher than 60%.

Since the percentage of sand and gravel at Watford clayey gravel is 83% (Harries et al., 1982), the soil was considered highly permeable. The high permeability of the superficial deposits was also manifested by Amey Technical Director Townend, Helen via personal communication on 23 January 2019.

A K_s value of 10^{-4}m/s was considered in the analysis according to the value obtained by Rahardjo et al., (2007) for highly permeable soils with 10% of fines

d) Soil Water Characteristic Curve and Hydraulic Conductivity Function

A representative soil water characteristic curve (Figure 6-18) and the hydraulic conductivity function (Figure 6-19) obtained by Rahardjo et al., (2007) for a highly permeable (HP) soil with a saturated hydraulic conductivity of 10^{-4}m/s and a 10% of fines were considered for the analysis of superficial deposits.

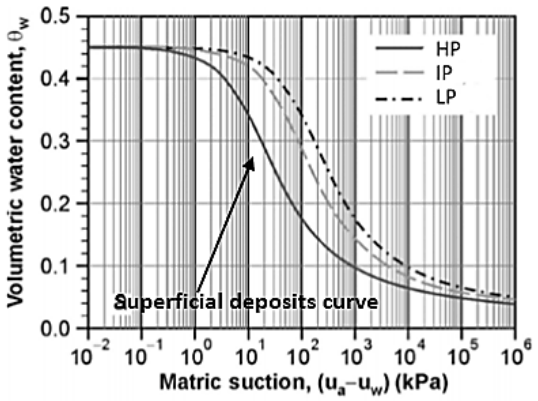

Figure 6-18 Representative soil water characteristic curves for high (HP), intermedium (IP) and low permeability soils (LP) Rahardjo et al., (2007)

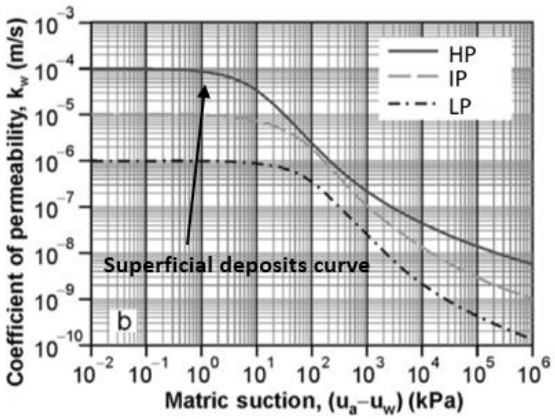

Figure 6-19 Representative hydraulic conductivity functions for high (HP), intermedium (IP) and low permeability soils (LP) Rahardjo et al., (2007)

A summary of the geotechnical parameters used for Grade Dc Chalk and Superficial deposits in the analysis of the Watford Tunnel is shown in Table 6-5.

Table 6-5 Geotechnical Parameters for Grade D_c chalk and superficial deposits at Watford

Geotechnical Parameter	Grade D_c chalk	Superficial Deposits
$\emptyset'_r$	39°	25°
γ_{bulk} (kN/m^3)	19	21
ϕ^b	19.5°	12.5°
K_s (m/s)	10^{-8}	10^{-4}

2. Climate Parameters

The analysis of evapotranspiration requires information relative to climate conditions (evaporation), and vegetation (transpiration) (see Chapter 4). In this section, the parameters used for Watford using continuum methods are presented.

Climatic data required by the Wilson-Penman equation consist of: Air temperature, precipitation, relative humidity and wind speed. These parameters were obtained from the closest weather station with hourly records installed at Northolt-Rothamsted, located at approximately 13 Km south of Watford Cutting.

Two independent analyses were carried out for Watford. A daily analysis from 16/01/2010 to 16/09/2016 (i.e. the date of failure) and an hourly analysis from 16/01/2016 to 16/09/2016. Climatic parameters in a daily and hourly bases were used for the calculations.

Rainfall data was adjusted at the day of failure by considering the 12.5mm/h intensity rainfall between 02:45 hrs and 06:45 hrs recorded from the amateur weather stations Wind Speed was converted from 10m height obtained at the weather station to 2m to be used in the Wilson-Penman equation. Climatic parameters used in the calculations include:

a) Rainfall

   A rainfall intensity of 50 mm/day for the daily analysis and 12.5mm/h between 02:45 hrs and 06:45 hrs in the hourly analysis was considered, corresponding to the data described in RAIB, (2017) and obtained from amateur weather stations close to the cutting failure.

b) Wind Speed

The wind speed at 2m height was calculated using the log wind profile (Holmes, 2018).

According to the Amey Principal Engineer Manager of Railway Earthworks David Frost via personal communication on 14 February 2019, the Watford cutting was covered by mature deciduous trees, principally Quercus (oaks), Beeches and ashes (>3m height), and a dense grass layer before they were removed in July 2016.

Historic imagery seems to indicate that the cutting has been fully covered by trees (the canopy covered the entire surface of the cutting), at least since 1999 (Figure 6-20).

September 1999

October 2013

Figure 6-20 Evolution of trees at Watford (Google Earth Pro)

In July 2016 Amey carried out the removal of trees and large vegetation from the slope at Watford tunnel but roots were left undisturbed.

Under these circumstances, before the removal of trees, the zero-plane displacement given by (4.29) is above 2m and therefore the wind speed is considered as zero, from May to September, when the tress are plenty of leaves. This was not the case after the vegetation clearance took place.

From October to April (2010-2016), the trees have shed their leaves, but the grass remains green. Watford cutting was visited on 12 June 2020 and grass was about 20cm high. A zero plane displacement of $d \approx 13\ cm$ and roughness length for grass of z_0=0.025 m (4.28) (Holmes, 2018) were considered from October to April.

c) Albedo

Barry and Chambers, (1966) presented Albedo data from different types of cover in Southern England. They obtained a mean value of 17.9% for deciduous woods and 25.1% for grass.

Watford cutting was assumed to be covered by grass located under the trees all over the year. The value of albedo for grass was considered from October to April in a yearly basis and for deciduous trees from May to September until 01/07/2016 when the vegetation was removed and albedo for bare soils of 17% (Román et al., 2010) was considered.

Daily climatic parameters obtained from the Northolt-Rothamsted meteorological station used for the calculations are shown in Figure 6-21. Climatic data from 2010 to 2016 is characterised by:

* Cyclic variations in air temperatures with maximums values from June to September
* Cyclic variations in wind speeds with zero values from May to September and non-zero values from October to April due to shedding of trees
* Cyclic variations in relative humidity with minimum values from July to September
* Cyclic variations in rainfall with maximum days of rainfall from November to January and maximum daily rainfall intensity in August and September as a consequence of convective storms.

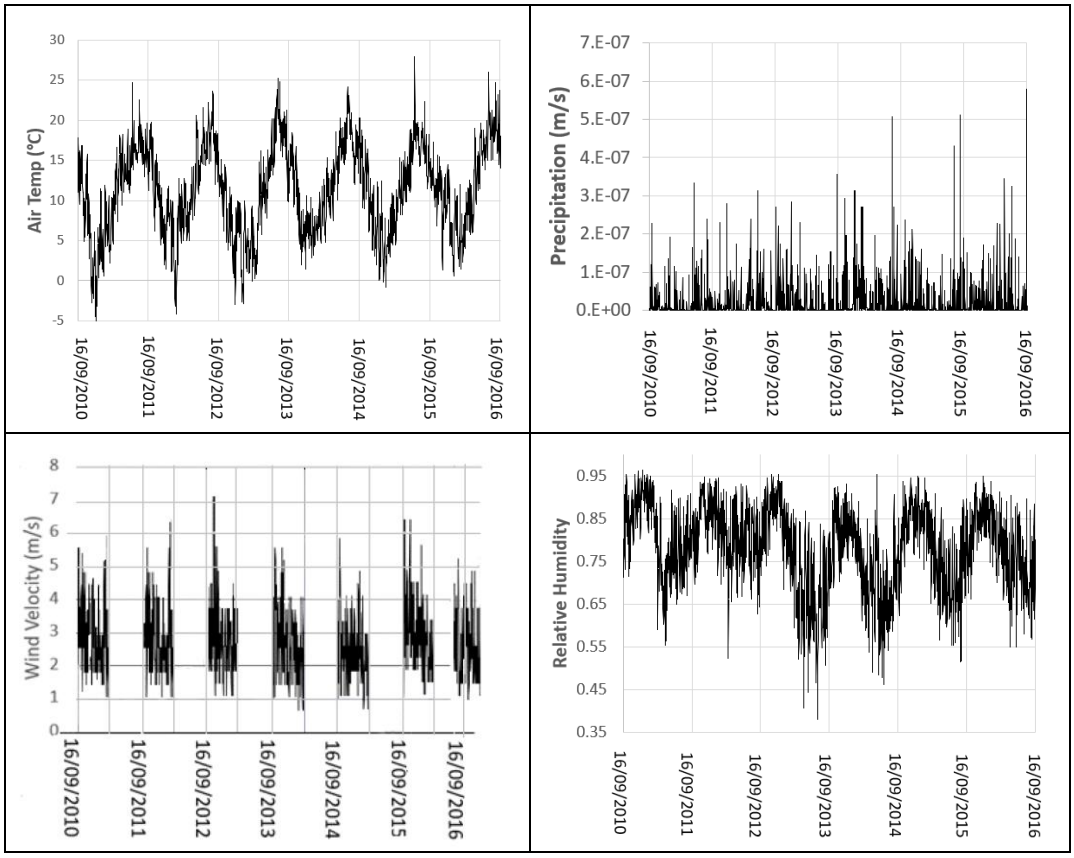

Figure 6-21 Daily climatic parameters 16/09/2010 to 16/09/2016

Hourly climatic parameters used for the calculations are shown in Figure 6-22.

* Values of air temperature steadily increasing from March to September.
* Peaks in hourly rainfall observed in June due to convective storms
* Wind speed >0 from 1 July when removal of vegetation took place
* Higher values of relative humidity during the night and vice-versa.

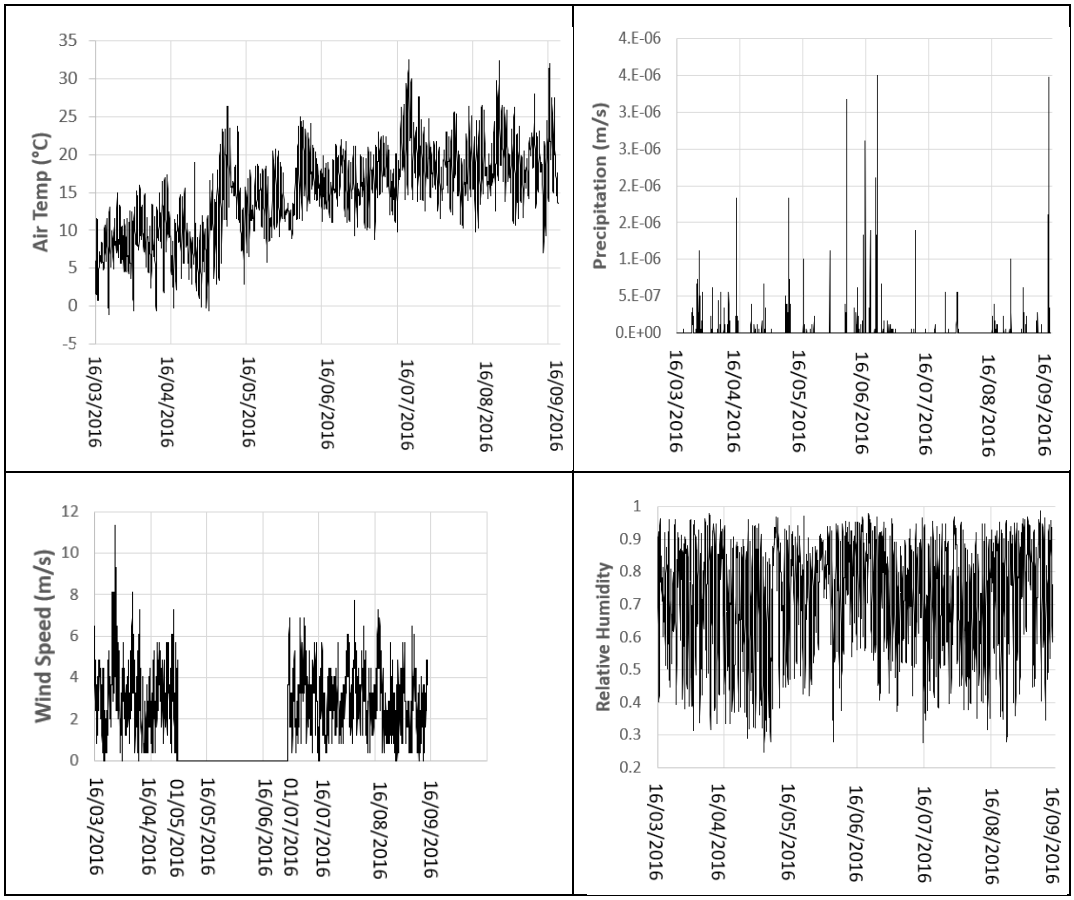

Figure 6-22 Hourly climatic parameters 16/03/2016 to 16/09/2016

3. Contribution of Vegetation

In addition to the climatic conditions, the analysis of evapotranspiration also requires information relative to vegetation for the calculation of the effect of root suctions in the distribution of soil moisture content within the soil.

The following parameters are needed for the calculation of transpiration (the reader is referred to Chapter 4 for background): LAI vs Time, Plant Moisture Limiting Factor (PLF), Root Depth vs Time, Normalised Water Uptake Distribution (NWD) and SCF versus LAI.

a) Leaf Area Index vs Time

For deciduous trees at Watford, the LAI is variable depending on the season. However, the slope is also covered by high dense bushes and grass that remain green all over the year.

The calculations at Watford Cutting was carried out considering that the slope surface remained permanently covered by grass before July 2016. This condition allocates most of the solar energy to plant transpiration rather than bare ground evaporation and corresponds to a constant value LAI=2.7 over time as suggested by Tratch, (1995).

b) SCF versus LAI

The relationship between LAI and SCF is given by equation (6. 3) with the value of ς variable depending on the type of vegetation.

$$SCF = 1 - e^{-\varsigma(LAI)} \quad (6.\ 3)$$

Larcher, (1975) suggested the following values of ς: 0.35 for grass and 0.65 for trees. Values of ς=0.35 from October to April 2010-2016 and ς=0.65 from May to September 2010-2015 and May to June 2016 were used in the assessment until the removal of vegetation when ς=0.

c) Normalized root density versus normalized root depth (vertical direction)

Trees at Watford tunnel included oaks and beeches, species where roots successfully thrive into the chalk (Wood and Nimmo, 1962).

At Watford Cutting, the slope was covered by trees, bushes and grass. Intermingling of bushes, grass and tree roots were simulated making the total root density constant over the entire depth. This approach corresponds to the Feddes' et al., (1978) model and has been recommended by (Novák, 2012) for steep slopes.

d) Maximum root depth versus Time

From historic imagery (Figure 6-19), the depth of bush, tree and grass roots was considered constant from January 2000 to September 2016 since no records of seeding or vegetation removal have been found before July 2016.

The grass cover has been considered with a rooting depth of 1 m in the direction perpendicular to the ground surface, in agreement with existing grass root models (Smethurst et al., 2006; Greenwood et al., 2001; Allen et al., 1998)

For Watford, there is evidence that tree roots penetrated the chalk as episodes of root jacking displacing blocks of chalk were recurrent in the failed cutting.(RAIB, 2017). Tree roots have the capacity to penetrate intact and structureless chalk. Roots depths >0.5m in oaks and >1m in beeches through chalk are in the probable range (e.g. Figure 6-23) (Crow, 2005).

Figure 6-23 Example of a beech root plate when grown over chalk (depth 1.1 m) (Crow, 2005).

Considering 0.5m thick superficial deposits a root depth of 1m perpendicular to the slope surface is a reasonable estimate and has been considered in SEEP/W for the root system at Watford Cutting. SEEP/W considers root depth in the vertical direction, therefore, as the angle of the cutting is 45°, a root depth of 1.4m was used in the model.

e) The plant limiting factor function (PLF)

The Tratch et al., (1995) relationship was used to model the decrease in root water absorption due to soil drying, as the plant stresses and reduces transpiration as a result. This was corroborated as a good approximation by Barbour et al., (2006). This model assumes unrestricted transpiration at soil suctions less than 100 kPa and a wilting point of 1500 kPa where transpiration is considered negligible. Between these two points, the reduction of transpiration is considered linear (Figure 6-24).

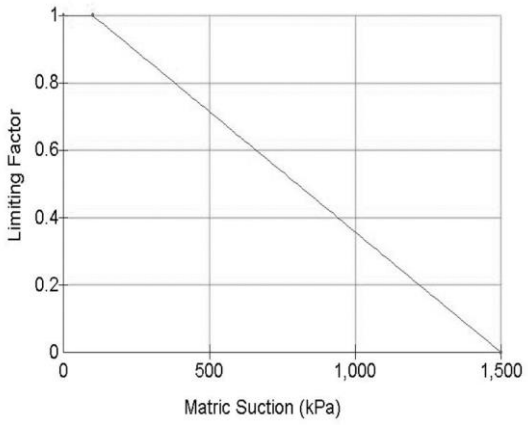

Figure 6-24 Limiting factor vs Matric suction (Barbour et al., 2006)

In the next sections, the remaining case studies are addressed. As only the assessment of their stability against debris flow was carried out using the novel method, only the information requires for this method has been discussed.

6.3 The Hooley cutting case study

Cutting failures in the Hooley cutting have been frequent since it was constructed (RAIB, 2008a). The vulnerability of the cutting to failure has been associated to the geology and over steepness (Parker, 2012).

As the number of failures at different locations became more frequent since 2001 (RAIB, 2008a), the general characteristics of the cutting (i.e. angle of the cutting and geology) instead of a single section was used in the assessment using the novel method. The cutting failures at Hooley are classified as hillslope debris flows following the proposed classification system.

6.3.1 History of the site at Hooley

Hooley cutting is situated on the London to Brighton Main Line (Figure 6-25), through the tunnels across the North Downs Chalk cliff (Birch and O'Donovan, 2015). The tunnel cuttings at the portals, consists of two parallel steep-sided excavations of 1,300m in length and up to 30m in depth.

Figure 6-25 Hooley cutting location (Google Earth)

The first of the two railways uses the Merstham tunnel along the 'dry valley'and was constructed in 1840 to reduce the length of more expensive tunnelling required along the North Downs and also to take advantage of the reduced gradient (Birch and O'Donovan, 2015). Although the tunnel was built by the London and Brighton Railway (L&BR), as it was located between Croydon and Redhill, area managed by South Eastern Railway (SER), the line had to be shared when they started to operate on their route to Dover in 1842. The rail line sharing situation resulted in a contentious relationship between the SER and the London Brighton and South Coast Railway (LB&SCR), who

replaced the L&BR, during the 19th century. As a consequence, a second tunnel to the east and 7.6 metres above the level of the original was constructed.

Both lines became part of the Brighton Main Line, the older line was called the 'Redhill Line' passing through the Merstham tunnel, and the new line became known as the 'Quarry Line' passing through the Quarry Tunnel, which opened on 8 November 1899 (Turner, 1979). The lines are separated by a central spine of land which extends to the full height of the actual topography of the area (Figure 6-26).

Figure 6-26 Hooley Cutting towards London (Birch and O'Donovan, 2015)

The cuttings comprise a layer of gravels overlying weathered Upper Chalk (Birch and O'Donovan, 2015).Cutting failures in the chalk and gravel have been frequent since its original construction of the Up and Down Redhill cuttings (RAIB, 2008a).

Hooley cuttings where originally excavated to around 53 degrees (RAIB, 2008a) which are extremely steep by modern standards (Parker, 2012). Following this, due to weathering of the chalk faces, together with the action from rock and debris falls, the profile has changed significantly and the overall angle is now between 60° and 70° (Birch and O'Donovan, 2015). The over steepness of the cutting has led historically to a large number of failures(Parker, 2012; RAIB, 2008a).

Some of the failures consist of small lumps of soils falling from the face of the cutting whereas other failures have been bigger such as those of 1841 and 1947.

A cutting failure occurred on 27 October 1841 on the eastern side of the Redhill Line (spine) close to the mouth of Merstham the tunnel. The failure took place in the chalky

slope and covered 30m in length of rails. Smith, (1841) reported that with the exception of the slip in question, the cutting showed scarcely any symptom of having been affected by previous heavy continued rains, nor by the severe frost of the previous winter.

Two cutting failures in 1947, where deposits of chalk and gravel covered the railway tracks in the chalky Down Redhill and Up Redhill cuttings are mentioned in (RAIB, 2008a).

More recently, cutting failures have resulted in derailments on 1 January 2003 and 13 January 2007, none of them attributed to superficial runoff (Birch and O'Donovan, 2015; RAIB, 2008a).

From 2007 to 2011, failures consisting of dislodgements of trees, and rolling of gravel and chalk fragments have been frequent in the Red Hill Cutting spine according to the geotechnical manager at BAM Ritchies O'Donovan, Andrew via personal communication on 23 January 2019.

Historical cutting failures at the Down Redhill cutting are shown in Figure 6-27.

Figure 6-27 Location of historical cutting failures at the Down Redhill Cutting (Google Earth)

6.3.2 Network Rail management of the cuttings at Hooley

In the early 60', British Rail decided to install a wall either side of the cutting in an attempt to minimise disruption on the railway line due to rock fall on the tracks. It was later replaced in 2003 by a king post wall, currently still in use (RAIB, 2008a).

During the 2000/2001 winter, a great number of tree and chalk falls took place, resulting in parts of the cutting being ranked by NR as a high risk, and in need of urgent remedial action (RAIB, 2008a). A grid of concrete columns and beams was constructed in the Up Redhill cutting (slow line) completed by the end of 2002.

Following a derailment in January 2003, a steel post and netting fence was constructed at the foot of the concrete grid at the UP and Down Redhill (slow lines) (RAIB, 2008a).

Following a derailment in January 2007, NR decided to take serious action and in March 2012 works began to reduce the quantity of gravel from the top of the cuttings and regrading of the upper part of the cutting at the Down Redhill cutting (Figure 6-28) (Parker, 2012).

Further works in the Up Redhill cutting were carried out consisting of a buttressing grid of concrete beams and columns to support the unstable gravels and chalk on the western (up side) and a fully nailed mesh in the gravels and weathered Upper Chalk profile (Birch and O'Donovan, 2015). The works were completed in early 2013 (Birch and O'Donovan, 2015).

Figure 6-28 Removal of weak material at central spine of Down Redhill Cutting (O'Donovan, 2014)

6.3.3 Geology at Hooley

a) Bedrock Geology and Superficial Deposits

As part of the Hooley cutting stabilisation works, logging of the geological strata exposed in the Redhill cutting faces was carried out using rope access from the top of the cutting crest to the bottom (Bam Ritchies, 2010).

The geological strata encountered during the logging of the cutting face showed an average thickness of 9.5m of 'dry valley gravels' overlying, in average, 10.5m of Grade D_c chalk.

b) Engineering Geological Model

A lithological section based on average thicknesses obtained in Bam Ritchies, (2010) is presented in Figure 6-29.

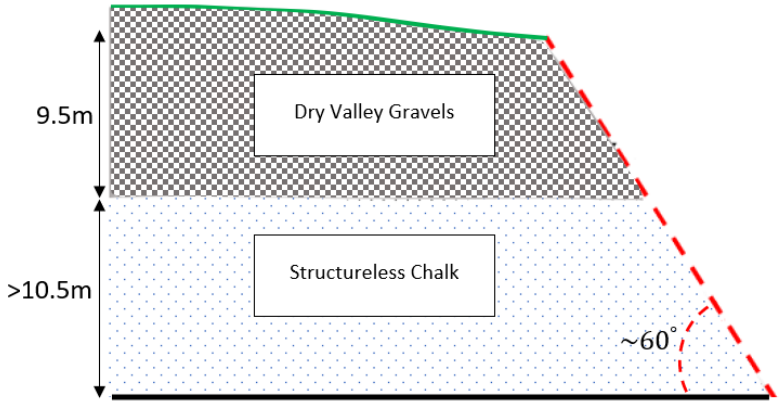

Figure 6-29 Lithological cross section at Hooley Cutting

6.3.4 Geotechnical properties at Hooley

A total number of 21 exploratory boreholes were undertaken at Hooley cutting using both the cable percussion and rotary drilling methods (Bam Ritchies, 2010). An average value of the residual angle of internal friction of 39° under low confining pressure and γ_{bulk} =23 kN/m^3 was obtained for the chalk.

6.4 St Bees cuttings case Study

At about 06:43 hours on Thursday 30 August 2012 the front carriage of a passenger service trainline crashed against deposits of a cutting failure laying on the tracks between St Bees and Nethertown on the Cumbrian coast at 68 miles 59 chains. A second failure occurred at 68 miles 64 chains at approximately the same time. The cutting failures at St Bees are classified as runoff generated debris flows following the proposed classification system.

6.4.1 History of the site at St Bees

The railway line running from Carlisle to Barrow-in-Furness via Workington and Whitehaven, is known as the Cumbrian coast line in north West england, which forms part of Network Rail route NW 4033. It joins the West Coast Main Line at Carnforth (Joy et al., 2017).

The cumbrian coast line has been esspecially vulnerable to earthwork failures since its construction at stages between 1844 and 1866. The section between St Bees and Nethertown is specially prone to damage by the sea and heavy rainfalls. A series of heavy rainfalls closed the line in 1852 after the destruction of a portion of the sea wall and the railway behind it at Whitehaven. In the February 1869 gale, the rails at St Bees were torn (Duck, 2015). Breaches by the sea leading to continual repairs and the periodic

installation of additional protection measures have been a constant feature of this line throughout the twentieth century right up to the present day (Duck, 2015)

On Thursday 30 August 2012, five earthwork failures took place between St Bees and Nethertown after a heavy rainfall event. Three of the failures occurred in embankments and two of them in cuttings at 68 miles 64 chains and 68 miles 59 chains (Figure 6-30). The cutting failure at 68 miles 59 chains led to derailment (RAIB, 2014).

Figure 6-30 Soil cutting failures at St Bees (Google maps)

6.4.2 Accident description at St Bees

The accident occurred in an area where the railway run as a single line on a ledge cut into the sea cliffs, about 19 metres above the railway (Figure 6-31).

Two cutting failures took place on Thursday 30 August 2012 at 68 miles 64 chains and at 68 miles 59 chains that led to derailment.

At around 6 km from the accident site, in St Bees Head, there is a rainfall gauge which reports hourly data. Information gathered from that day suggests that a total rainfall of 51.6mm fell between 22:00 hrs on 29 August and 03:00 hrs on 30 August, a 1 in 57 year event. The rain instigated serious inundation and considerable disruption to adjacent properties (RAIB, 2014).

Cutting Failure at 68 miles 59 chains

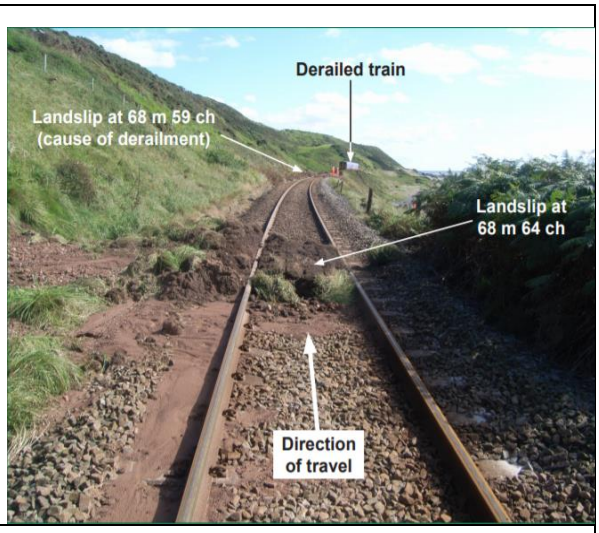

Cutting Failure at 68 miles 64 chains

Figure 6-31 Cutting Failures at St Bees (RAIB, 2014)

6.4.3 Network Rail management of the cutting at St Bees

The earthwork slopes at the locations where the derailments took place had last been inspected on 4 April 2005, when they were classified as serviceable. As the adjacent land were of relatively low gradient towards the slopes, this was seen as a low risk of failure (RAIB, 2014).

In accordance with Network Rail standard NR/L3/065, 'Examination of Earthworks', no further remedial action was required at the time and it would be re-examined during the next routine inspection in 2015 (RAIB, 2014)..

6.4.4 Geology at St Bees

a) Bedrock Geology and Superficial Deposits

Geological information of the area has been obtained from the ground investigation carried out ~1 km north-west from the location of the failures for the construction of a proposed turning circle for public transport vehicles at the south end of St Bees on March 1975 (Boreholes NX91SE 294,295,296,297,298 and 299) (see Figure 6-32).

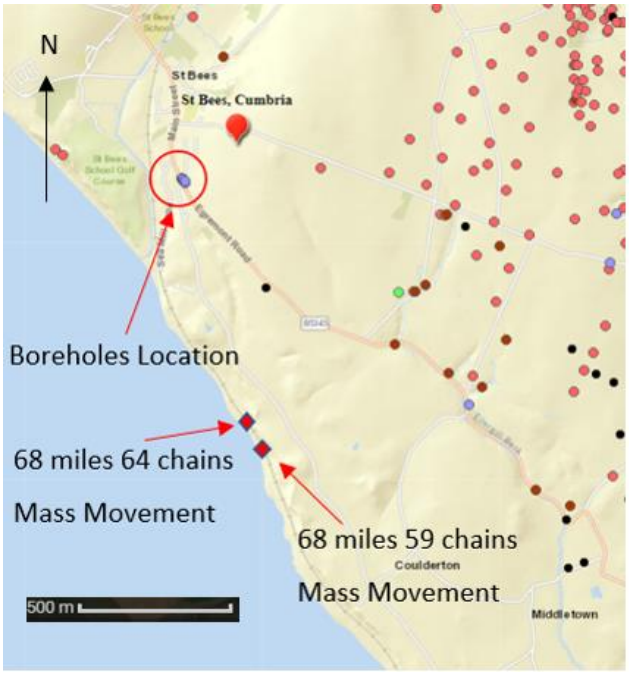

Figure 6-32 Boreholes Location (BGS)

From the historical boreholes, soft silty clay was found from ground surface to a depth of 1m , followed by soft to firm sandy clay and fine gravel and silty sand to 4.8m depth. The superficial deposits belong to the Caledonia Glacigenic group and in particular to the Gosforth Glacigenic Formation made up of a fine matrix of clay with coarse particles according to the national glacial till formations map in Great Britain (Culshaw et al., 2017).

Bedrock comprises weathered sandstone from 4.8 to 5.3m and solid sandstone at 5.3m.

b) Engineering Geological Model

A 3D engineering geological model with catchment areas obtained from ArcGIS has been built from the 1m digital terrain model and boreholes information (Boreholes NX91SE 294,295,296,297,298 and 299) 1km NW (see Figure 6-33).

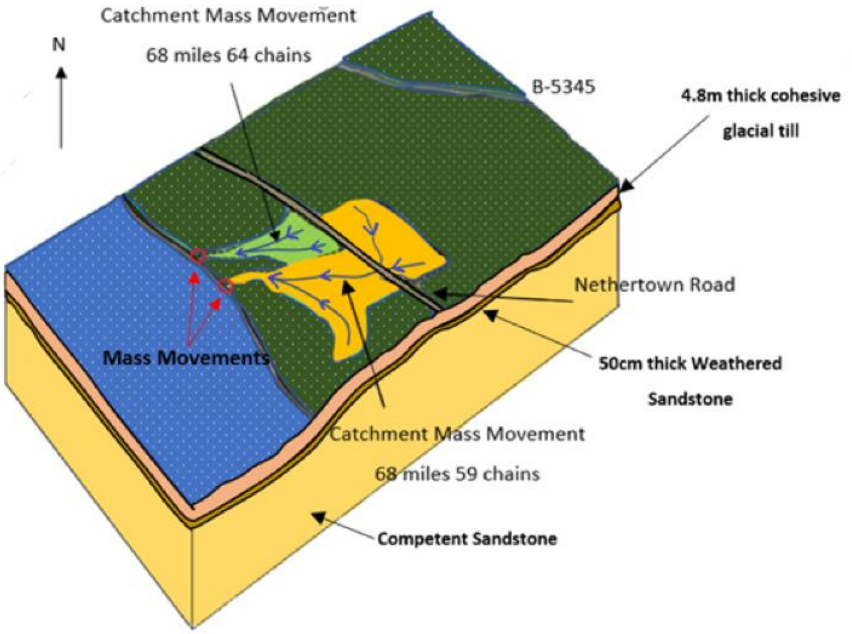

Figure 6-33 St Bees Engineering geological model

6.4.5 Geotechnical properties at St Bees

Geotechnical parameters for superficial deposits pertaining to the Gosforth Glacigenic formation were obtained from a ground investigation carried out at the site of a major failure in the till of the coastal cliffs above the village of Parton (Ferley, 2013).

The location of the boreholes were located approximately 9km north west of the study case. Mean values of bulk unit weight γ_b=21 kN/m^3 and residual shear strength 31° were obtained.

6.5 The Beaminster case study

At around 22:10 on 7 July 2012 a partial collapse of the north side of the Beaminster tunnel on the A3066 road occurred (Ashcroft, 2014) during a day of heavy showers. Two people were killed when their car was buried by muddy deposits , resulting in the closure of the tunnel for over a year. The cutting failures at Beaminster are classified as runoff generated debris flow following the proposed classification system.

6.5.1 History of the site at Beaminster

The Beaminster tunnel, also known as the Horn Hill Tunnel, is a road tunnel of 105 m in length, located in Dorset, on the A3066 between Beaminster and Mosterton (Figure 6-34).

Figure 6-34 Beaminster Tunnel Location (Google Earth)

The road tunnel, one of the first in Britain, was built between 1830 and 1832 and is still in use. It was one of the first road tunnels built in Britain and is the only pre-railway road tunnel in the country still in use. The purpose of the tunnel was to facilitate travelling from the coast to the hinterland of Dorset, due to the presence of very steep hills to the north of Beaminster (Stanley et al., 1933).

Tree-felling was carried out in May 2004, after an ash tree fell on to the carriageway. The assessment carried out exposed that there were a considerable amount of trees in poor condition posing a significant risk to the road users in case of falling on the road. As a result, a total of 42 trees were removed from both tunnel portals (The Guardian, 2014).

A small runoff generated debris flow occurred in 2009 in a 42.5° slope located at the south side of the tunnel (Figure 6-35) (BBC News, 2014).

Figure 6-35 Beminster failure 2009 at the south portal (Google Earth)

A partial collapse of a 42°-43° slope cutting located at the north side of the Beaminster tunnel took place on 7 July 2012 as a consequence of an extreme rainfall event (Ashcroft, 2014).

6.5.2 Accident description at Beaminster

The slope failure of July 2012 was described by witnesses as a 'wall of mud and water'. The tunnel was overtopped by the slope failure at the frontal and east flank of the tunnel portal (Figure 6-36).

Yeovilton meteorological station located at approximately 13km north-east from the tunnel, recorded 30mm of rainfall at the day of failure with maximum hourly intensities of 7mm/h. Coombe Farm meteorological station located at approximately 3Km south-west of the tunnel, recorded 51.6mm at the day of failure. Mike Winter, head of Dorset highways management estimated that at the location of the failure, daily rainfall could have been significantly higher (The Guardian, 2014). PC Rodger Clark of Dorset police reported that the failure materialised after England, and specifically the south-west, experienced the wettest summer in 100 years (The Guardian, 2014).

For the analysis using the novel method, the 51.6 mm recorded in Coombe Farm have been assumed to fall in the four hours previous to the failure that is a reasonable estimate for the purpose of the analysis.

After the failure, the tunnel was fully reopened to traffic at the end of July 2013 when remedial works were completed (Figure 6-28).

Figure 6-36 Beaminster north portal tunnel after collapse((BBC News, 2014)

6.5.3 Management of the cutting at Beaminster

Works starting in April 2013 were carried by the main contractor Raymond Brown, the ground engineering contractor Can Geotechnical and the consultant Parsons Brinckerhoff.

The consultant's assessment predicted a deep-seated failure type, but no evidence was found to support this hypothesis while the remedial works took place. Instead, the failure was a consequence of shallow instability, according to Dorset County Council principal engineer Matt Jones via personal communication on 13 February 2020. Soil nails were used to stabilise any possible future deep-seated failures and active netting was used to control any shallow failures.

Long inclined drains were installed to reduce the ground water, and the slope angle above both portals was reduced (Smith, 2013).

6.5.4 Geology at Beaminster

a) Bedrock Geology and Superficial Deposits

According to 1:50000 BGS geological maps, the geology consists of clay-with-flints formation superficial deposits (clay, silt, sand and gravel) over upper greensand formation (Figure 6-37).

The clay-with-flints formation is an in situ residual soil formed from the insoluble remnants of the Chalk Group and the reworked Lambeth Group.

At this location the Clay-with-flints Formation directly overlies Upper Greensand Formation.

1:50 000 scale superficial deposits: Clay-with -flints Formation

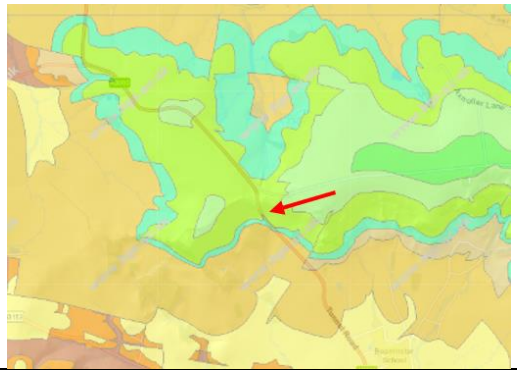

1:50 000 scale bedrock geology description: Upper Greensand Formation

Figure 6-37 Superficial deposits and bedrock geology at Beaminster tunnel (BGS 1:50000 scale geological maps)

According to Dorset County Council principal engineer Matt Jones via personal communication on 13 February 2020, superficial deposits at Beaminster tunnel consist of a shallow layer approximately 2m thick over the greensand bedrock.

b) Engineering Geological Model

A 3D engineering geological model based on BGS maps information and Matt Jones private conversations regarding the thickness of the superficial layer is presented in Figure 6-38. The drainage lines have been obtained from Arc GIS 1m digital terrain model.

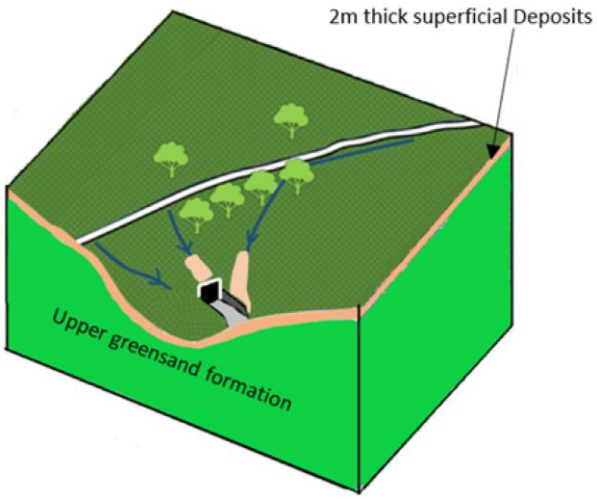

Figure 6-38 Beaminster tunnel collapse

6.5.5 Geotechnical properties at Beaminster

According to the Associate Director of Engineering Geology at the University of Surrey Ursula Lawrence via personal communication on 11 September 2020, the clay with flints formation at the location presents an estimated bulk density of 19kN/m^3 and a value of residual angle of shearing resistance $\emptyset'_r$=23°.

6.6 The Loch Treig case study

On Thursday 28 June 2012, at approximately 19:05 hours, a train of five wagons derailed when another train travelling on the West Highland line hit a failed slope alongside Loch Treig (Figure 6-39 left). No injuries or fatalities were reported, but three of the wrecked wagons overturned and the locomotive ran part way down the natural slope towards the loch (Figure 6-39 right) (RAIB, 2014). The cutting failure at Loch Treig is classified as hillslope debris flow where an initial slide transitioned to flow and material ranges from clay to boulders.

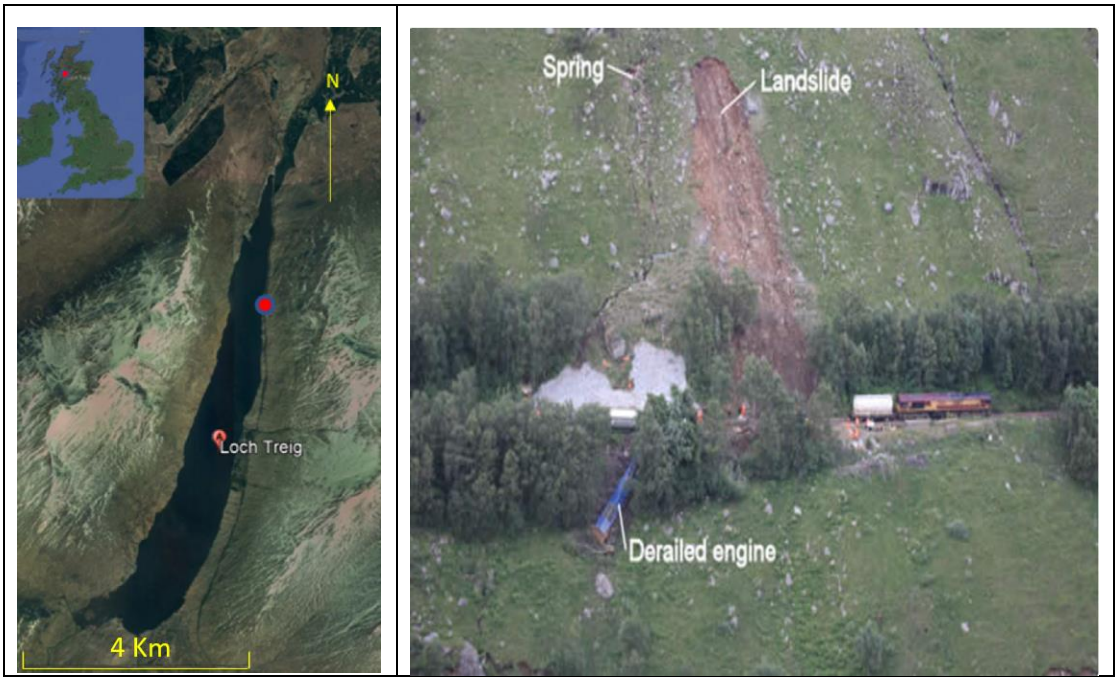

Figure 6-39 Loch Treig failure location left (Google Earth Pro)and derailment right (RAIB, 2014)

6.6.1 History of the site at Loch Treig

In 2010, just north of where the landslide occurred, remediation works to stabilise an existing retaining wall were carried out, consisting of installation of rock armour. The repairs were identified as part of routine inspections of the lines and not related to any slope failure. Since the railway started operating in 1894, there is no record of disruption and historic maps of the area do not show any evidence of slope failure (BGS, 2017).

6.6.2 Accident description at Loch Treig

Where the accident occurred, the railway consist of a single line which runs along the side of a mountain, with approximately 1 in 1.5 slopes and around 700m in height above the railway line. The landslip materialised at around 35m above the railway boundary.

The Meteorological Office gauged weather radar data to report that approximately 23 mm of rain fell during 24 hours starting at 10:00 am on 28 June, of which about 18 mm fell between 16:00 hrs and 19:00 hrs. this type of storm events are likely to occur more than once a year (RAIB, 2014). Furthermore, it was also estimated that 6 mm of rain fell between 18:05 hrs and 18:35 hrs, which is characteristic of events likely to occur only once a year (RAIB, 2014).

The mass movement that developed into a debris flow of mud-rich sediment and boulders, was initiated by a shallow planar movement. Signs of saturation were observed

at the area surrounding the landslide scar. The landslide event is recorded as National Landslide Database ID NLD 18683/1. (BGS, 2017).

6.6.3 Network Rail management of the cutting at Loch Treig

As part of the routinely earthworks inspections carried out by NR, slopes around the area where the incident occurred were examined, with the last one taking place before the accident on the 5 of March of 2011. The earthwork examiner concluded there was evidence of water streams flowing towards the railway boundary and discharging into culverts underneath the tracks. No defects in the drainage system were reported and the slope was classified as 'marginal', from a categorisation of poor, marginal or serviceable,

6.6.4 Geology at Loch Treig

a) Bedrock Geology and Superficial Deposits

Geological map of the area obtained from the British Geological Survey, show superficial deposits consisting of till (boulder clay) and morainic deposits (Figure 6-40 right). Glacial till at This location belongs to the Ardverikie Till formation described as gravelly, sandy CLAY with angular to subrounded cobbles and boulders. (Culshaw et al., 2017a).

Bedrock consist of Loch Treig Schist and quartzite bedrock, metamorphic rocks of Neoproterozoic age (Culshaw et al., 2017a)(Figure 6-40 left).

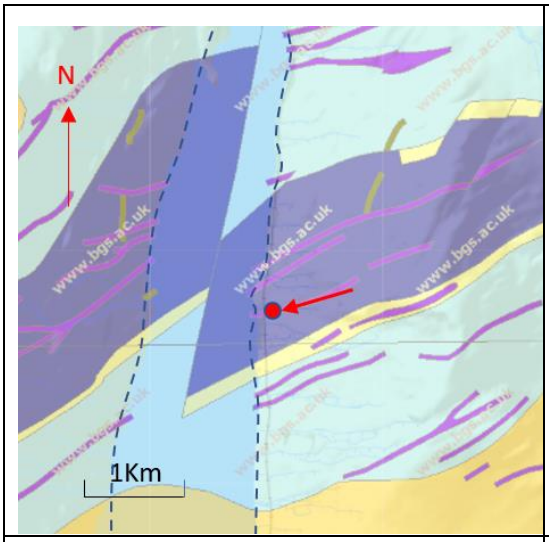

Leven Schist Formation	Till and Morainic deposits
1:50 000 scale bedrock geology map	1:50 000 superficial deposits map

Figure 6-40 Bedrock geology (left) and superficial deposits (right) at Loch Treig (BGS)

b) Lithological cross section

According to BGS, (2017), bedrock is not visible within the back scarp but is expected to be within 1 m of the slip surface.

From Figure 6-41, a shallow no more than 2m thick slip surface has been assumed in the analysis.

Figure 6-41 Debris pathway downslope BGS, (2017)

A lithological cross section is illustrated in Figure 6-42 based on a profile section included in RAIB, (2014).

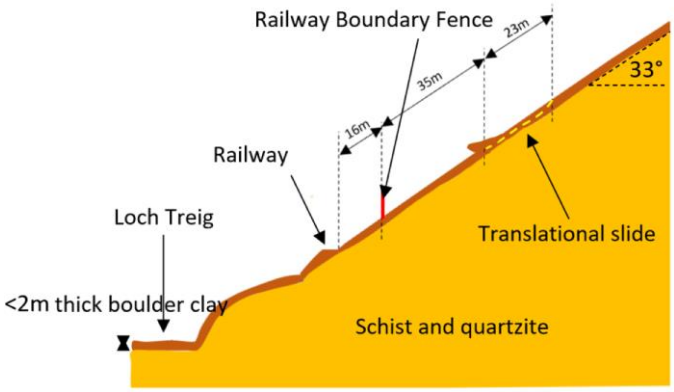

Figure 6-42 Lithological cross section of Loch Treig mass movement (RAIB, 2014)

6.6.5 Geotechnical properties at Loch Treig

1:50000 BGS geological maps for Cowal (West Scotland), show the same till superficial deposits as the accident location.

Shear strength parameters for superficial deposits in Cowal were obtained by McGown, (1975) through a series of laboratory tests (Figure 6-43).

Ardverikie tills are of generally low plasticity (PI 10–20%), which reflects their sandy character (Aitken et al., 2003).

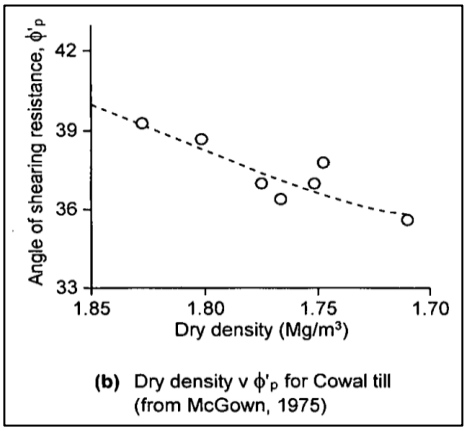

Figure 6-43 Values of $\emptyset'_p$ for Cowal till. (McGown, 1975)

A medium value of $\emptyset'_p = 38^{\circ}$ and $\gamma_{dry} \approx 18 KN/m^3$ were obtained by McGown, (1975) for Ardverikie tills. On the basis of laboratory data analysed by Lupini et al., (1981), at low plasticity, $\emptyset'_r$ is relatively high and not significantly different from the peak value $\emptyset'_p$.

For the calculation of the saturated density, a water content of 30% in saturated conditions was suggested by Trenter, (1999) as a typical value for saturated tills corresponding to γ_{sat}=23 KN/m^3.

Crabb and Atkinson, (1991) suggested that for tills it is likely that at very low confining pressures the Mohr's envelope is curved so that c' becomes zero.

A summary of the cases analysed using the novel method are presented in Table 6-6

Table 6-6 Summary of properties and cases analysed using the novel method

Location	Watford	Hooley	St Bees	Beaminster	Loch Treig
Principal type of slipped material	Grade D_c chalk	Grade D_c chalk	Glacial till	Clay	Glacial till
Rainfall intensity	12.7mm/h during 4 hours	No Rainfall	10.32mm/h during 5 hours	12.9mm/h during 4 hours	6mm/h during 3 hours
$\emptyset'_r$	39°	39°	31°	23°	38°
γ_{bulk} (kN/m³)	19.4	23	21	19	23

In the next chapter, the Watford cutting failure was analysed using continuum methods. The investigation was carried out to dismiss rise in pore water pressures as the trigger of failure.

Chapter7: Analysis of Watford cutting using continuum methods

In this chapter, the stability of the cutting failure at Watford that took place on 16 September 2016 will be analysed using continuum methods of analysis.

The cutting failure at Watford occurred during an extreme rainfall event where high-intensity runoff developed over the cutting.

There is no certainty about the main trigger factor that led to the cutting failure without performing stability analyses. The failure at Watford cutting could have been classified as a hillslope debris flow if the main agent initiating the mass movement was gravity, or as a runoff generated debris flow if the main agent was overland flow.

To investigate the triggering mechanism that led to the failure, first the stability of the cutting using continuum methods has been carried out to analyse whether raising of pore water pressures was the mechanism of failure.

To do that, the stability analysis at Watford cutting has been carried out coupling the pore water pressures field calculated in SEEP/W, (2018) with the limit equilibrium method in SLOPE/W, (2018).

7.1 Model set up

The analyses will be carried out coupling two commercial geotechnical software: SEEP/W and SLOPE/W.

SEEP/W is a finite element based software that analyses the distribution of soil pore water pressures over a specified time. SEEP/W is capable of analysing the effect of atmospheric conditions by including infiltration for rainfall and the Wilson-Penman boundary equation at the ground surface for evapotranspiration. SEEP/W has become a popular software of research for distribution of soil moisture content accounting for seasonal climate, slope vegetation and soil permeability (e.g. Loveridge et al., 2010; Briggs, 2010; Briggs et al., 2013).

In SEEP/W, a modified 1D Richards equation is used in the boundary soil-atmosphere with a source term to account for infiltration by precipitation and a sink term to account for evapotranspiration at the ground surface. The bottom of the 1D Richards equation model constitutes the upper boundary condition of the 2D Richards equations used for the movement of water below the ground surface (Yoo et al., 2016).

SLOPE/W is a limit equilibrium analysis software that allows the assessment of slope stability using the most recognised limit equilibrium methods of analysis: The analysis of

Watford cutting has been carried out using the Spencer's method and the Fredlund and Morgenstern's approach for the calculation of the shear strength.

Both SEEP/W and SLOPE/W software are coupled. First, SEEP/W calculates the pore water pressures field at the entire soil domain for each time-step and the information is transferred to SLOPE/W. At the end of the last time-step, the evolution of the FoS vs time is shown as part of the analysis.

Slope/W evaluates the element that is found closest to the centre of each slice base and uses the pore water pressure calculated for the element (Tsaparas et al., 2002).

For the analysis of the cutting stability at Watford coupling SEEP/W and SLOPE/W, two types of parameters were needed: 1. geotechnical parameters and 2. climatic parameters, both introduced in Chapter 6.

7.1.1 Time analysed

Major differences can be expected in the analysis of the slope stability using daily and hourly rainfall data. Two independent analyses were carried out for Watford. A daily analysis comprising 6 years from 16 January 2010 to 16 September 2016 (i.e. the date of failure) and an hourly analysis comprising 6 months from 16 January 2016 to 16 September 2016.

The analyses were conducted with the soil and climatic parameters obtained in section 6.2. Both analyses were carried out no considering root reinforcement.

a) daily analysis

Daily rainfall data involves a larger temporal averaging of rainfall data used in numerical analyses than hourly rainfall data. The available rainfall intensity in the daily analysis is smoother than the hourly analysis and the distribution of pore water pressures as a consequence of rainfall infiltration is less accurate (Batalha et al., 2018).

However, seasonal variations of pore water pressures can be fairly represented using daily climate data (e.g. Briggs et al., 2014; Briggs et al., 2013). Daily simulations are not projections of the actual magnitude and spatial distribution of pore water pressures within a cutting, but offer valuable insights into overall patterns of behaviour (O'Brien, 2013).

The daily analysis was conducted to assess the yearly months where the cutting presented higher vulnerability to failure (lower FOS) and whether the vulnerability of the cutting at the time of failure was a result of changing climate conditions over the years.

The analysis simulated the full climate year with 2-hour time step increments as suggested by Barbour et al., (2006) for long term analyses. The analysis was saved every 12 steps corresponding to 1 day. This analysis was carried out in 26280 steps. No transpiration was assumed since 1 July 2016 when the vegetation was removed. Values of 0 wind velocity at 2m height were considered from May to September each year and a reduction of albedo to 0.17 (corresponding to bare soil) was assumed after the vegetation clearance.

b) hourly analysis

Hourly time steps during simulations better capture the effect of short rainfall events than daily simulations and therefore can be utilised to better assess the effect of short and high intensity rainfall events on the stability of slopes (Schilirò et al., 2015; Rouainia et al., 2009).

The hourly analysis was carried out to assess the effect of the rainfall in the vulnerability of the cutting during the event that led to derailment on 16 September 2016.

This analysis was carried out in 200 days. The analysis was conducted in 4800 steps, each of them representing 1 hour. No transpiration was assumed since 1 July 2016 when the vegetation was removed. Values of wind velocity at 2m height were assumed 0 from May to June and a reduction of albedo to 0.17 (corresponding bare soil) was assumed after the vegetation clearance.

7.1.2 Ground water table

To avoid the effect of the initial ground water table at the start of the daily analysis (16 January 2010), evapotranspiration analysis was carried out from 16 January 2000 to 16 January 2010. The distribution of pore water pressures at the later date was considered for the initial configuration of the model in the daily analysis. The distribution of pore water pressures on 16 January 2016 groundwater table in the daily analysis was considered for the initial configuration of the model in the hourly analysis

Minimum values of groundwater levels at Watford Cutting are normally in the range between 72m AOD and 68m AOD (UK Environmental Agency, 2019). Considering that the

toe of Watford Cutting is located at 74m AOD, an initial water table at -2m from the toe of the cutting was considered on 16 January 2000 in the analysis from 2000 to 2010.

The initial condition of pore water pressures distribution on 16 January 2010 was therefore established by imposing 10 years of climate data as suggested by Briggs et al., (2013).

There is no evidence of hollows in chalk at Watford cutting. However, while the presence of hollows could have a localised effect in ground water levels, it is unlikely that it would influence pore water pressures at shallow depths where the failure took place.

7.1.3 Description of the finite element mesh design for the seepage analysis

A fine mesh was used in the surface area, where high-pressure gradients were likely to occur. The finite element mesh near the ground surface consists of very fine 8-noded quadrilateral elements (0.1×0.1 m) to a depth of 0.5 m perpendicular to the ground surface.

Below the surface mesh, a fine 8-noded and 6-noded quadrilateral and triangular elements of approximate global element size of 0.5m was used in the analysis.

This mesh configuration was found to produce satisfactory and stable results and could be used to solve the problem in a reasonable time.

A total of 17097 elements were used in the model. Models with the same mesh density in SEEP/W were validated against field data in previous evapotranspiration research (e.g. Briggs et al., 2014; Briggs et al., 2016).

7.1.4 Geometry

The profile of the Watford Cutting was obtained from a 1m resolution Digital Terrain Model (DTM) of the area (Figure 9-5). At the crest, the elevation of the cutting is 90m (Above Ordinance Datum, AOD) and 74m (AOD) at the bottom. The height of the cutting is 16m, and the average angle is 45°.

Lateral boundaries were located far enough away (80m beyond the crest and the toe) to minimise their influence over water pressures in the immediate vicinity of the cutting face which is the key area of interest (reader is referred to section 7.3).

The same was done for the bottom boundary that was located to a depth of 30m below the cutting toe. The geometry of the model and the mesh used in SEEP/W are presented in Figure 7-1.

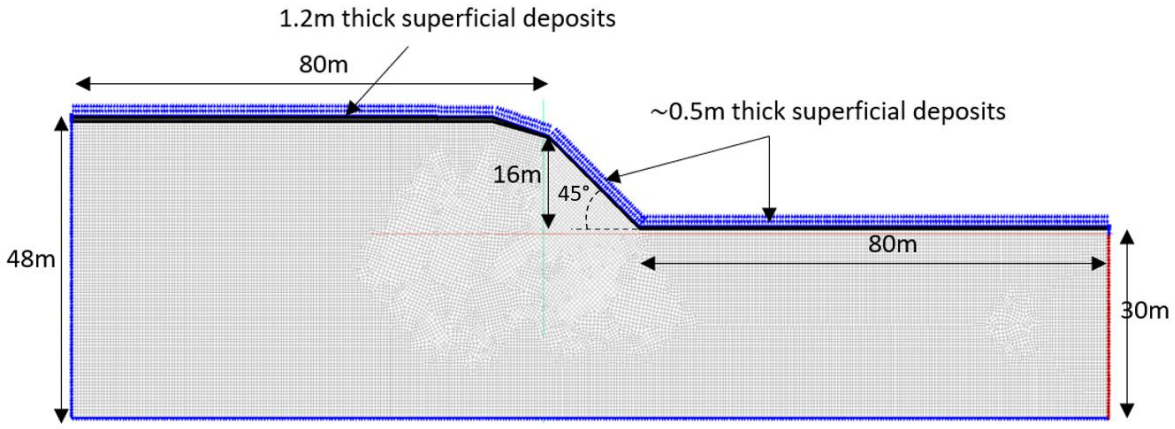

Figure 7-1 Geometry and mesh of Watford Cutting in SEEP/W

7.1.5 Boundary conditions

A climatic boundary condition (i.e. Land Climate Interaction), representing the Wilson-Penman equation for evapotranspiration is assigned at the ground surface. A zero flux conservative assumption was given to the lower boundary (i.e. no water is leaving the model at the base) following the recommendations of Rahardjo et al., (2007).

The left lateral boundary was assigned a zero flux assumption and the right lateral boundaries are: a) a zero flux from -2m to the ground surface (Figure 7-2 dashed blue line) and b) a constant head boundary conditions of -2m (Figure 7-2 dashed red line). The right constant head boundary condition was used to allow the movement of water across the boundary in horizontal direction and avoid the bathtub effect due to water accumulation as reported by Gupta, (2016).

Several attempts were made with other boundary configurations that resulted in water table with curved shapes in the vicinity of the boundaries to comply with the boundary restrictions. The configuration near the boundaries proved to be the one presenting the best performance for the case analysed. The initial position of the water table on 16 January 2000 was assumed at 72m (AOD) (section 7.1.2) that is a good estimation at Watford.

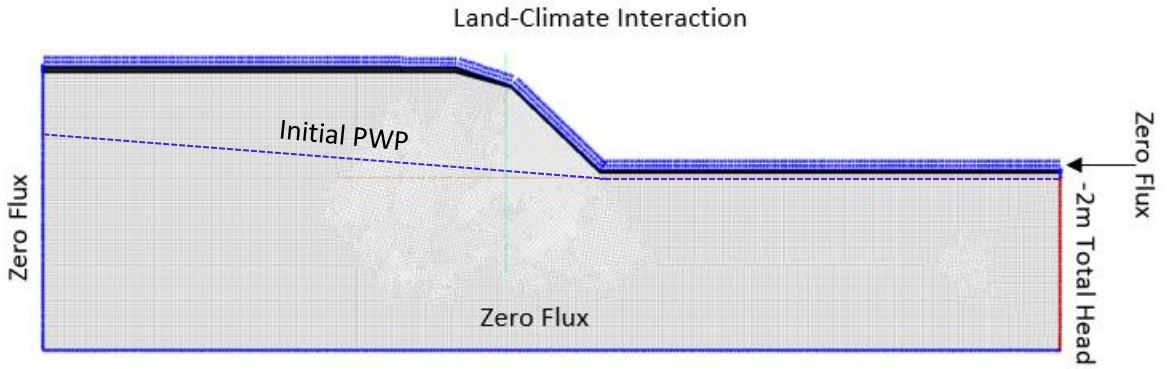

Figure 7-2 Boundary conditions for numerical modelling at Watford cutting

7.1.6 SLOPE/W configuration

For the slope stability analyses, the Spencer's method was considered, satisfying moment and forces equilibrium. The slip surface was modelled at a maximum depth of 1m perpendicular to the ground surface at the cutting face so that the mass movement was analysed considering the slip surface within the chalk.

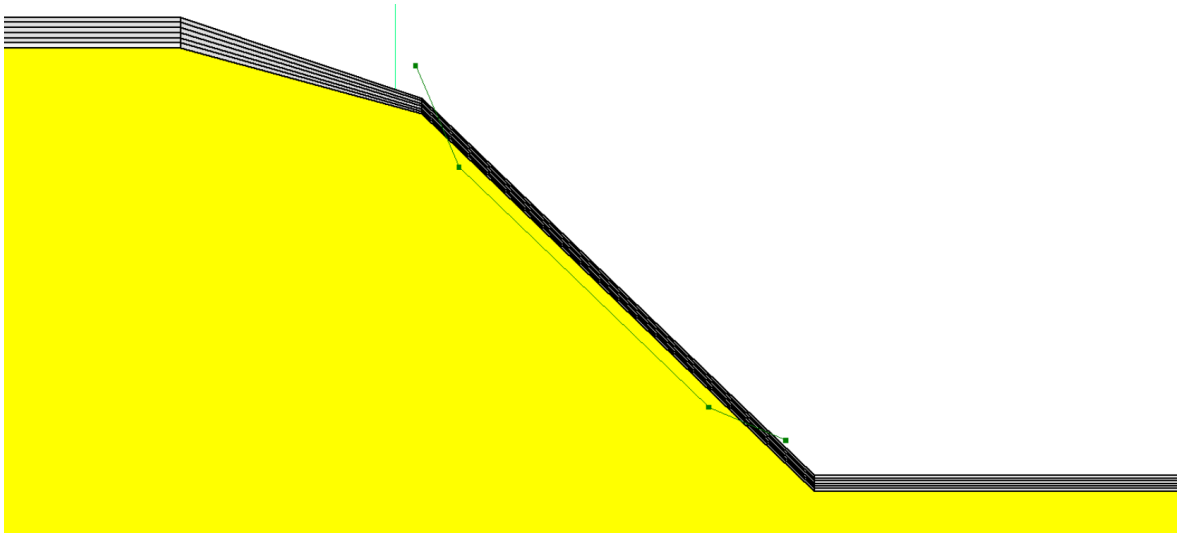

Figure 7-3 Slip surface at Watford in SLOPE/W

7.2 Input parameters

Soil parameters used in the analyses were introduced in chapter 6. A summary of these parameters is presented in Table 7-1.

Table 7-1 Parameters used in the analysis of Watford cutting

	$\emptyset'_r$	ϕ^b	γ_{bulk} (KN/m^3)	K_s(m/s)
D_c Chalk	39°	19°	19.4	10^{-8}
Superficial Deposits	25°	12.5°	21	10^{-4}

7.3 Results

The initial configuration of the model

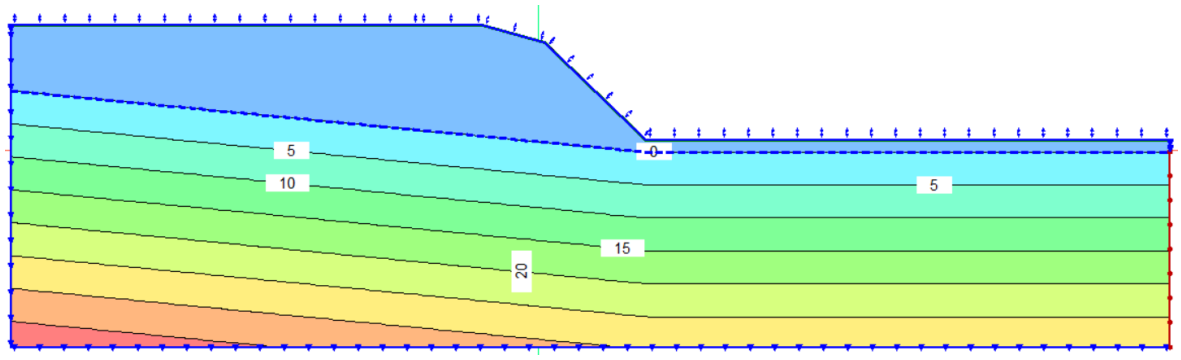

Figure 7-4 Initial configuration on 16 January 2000

Daily analysis 16/09/ 2010-16/09/2016

The evolution of the FoS vs Time is presented in Figure 7-5 where no extra root cohesion is considered for the soil. FoS<1 is recurrent during the winter months and therefore, using a back analysis, an extra root cohesion of 3KPa has been considered so that the FoS remains >=1 during the time analysed (Figure 7-6).

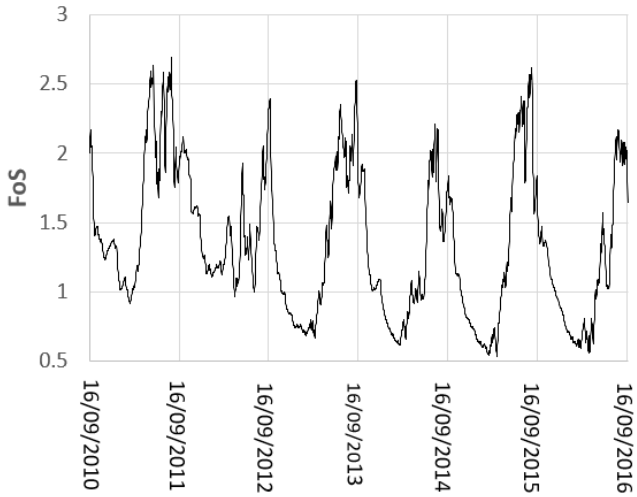

Figure 7-5 Daily evolution of the FoS considering no extra root-cohesion

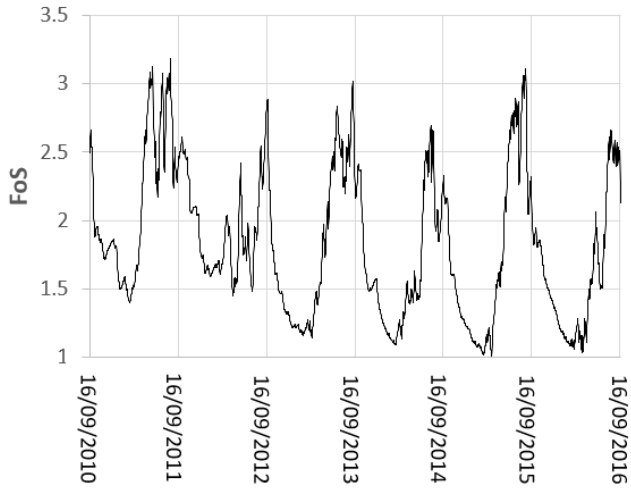

Figure 7-6 Daily evolution of the FoS considering extra root-cohesion of 3KPa

A cyclic variation of the FoS was observed during the daily analysis, with the lowest values from January to April and the highest in August and September in the period 2010-2016.

a) FoS at local minimum

On 11 April 2016, a local minimum of the FoS=1.02 was obtained (Figure 7-6). WT rose 5m along the cutting face but matric suctions between 0 and -5KPa remained in the upper part of the cutting. The WT located below ground level downslope and upslope at approximately -2m.

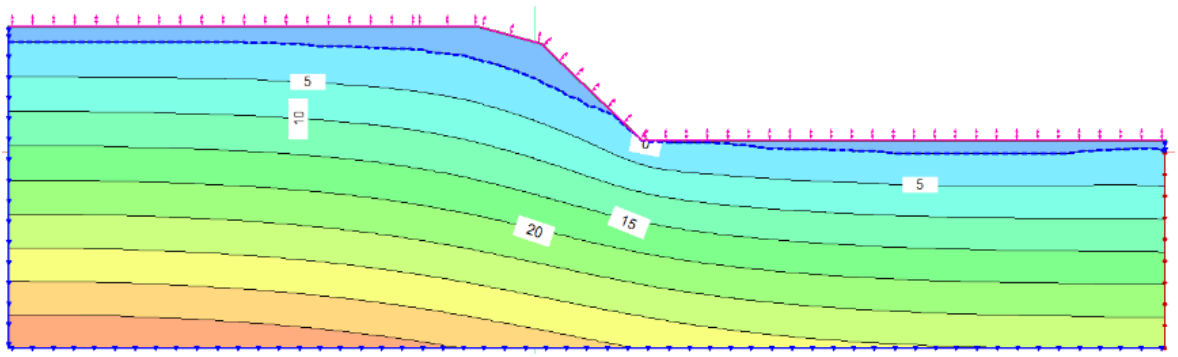

Figure 7-7 Distribution of PWP at 11/04/2016

b) FoS at local maximum

On the 17 August 2015 a local maximum of the FoS=3.1 was obtained (Figure 7-6). Matric suctions slightly higher than -5KPa developed all over the cutting face and WT level reduced to approximately -6m below ground level upslope and -5.5m downslope. (Figure 7-8).

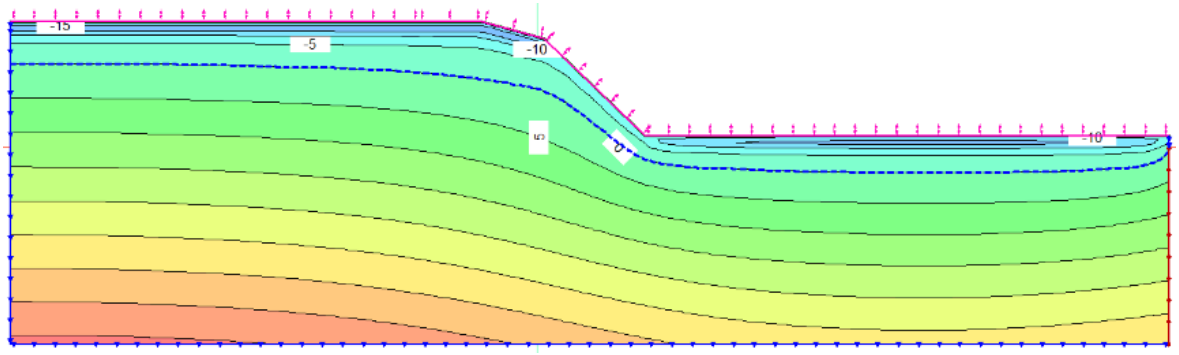

Figure 7-8 Distribution of PWP at 17/08/2015

c) FoS at the day of derailment

In the daily analysis, the lowest FoS of the series did not corresponds to the day of derailment at Watford. A reduction of the FoS from 2.5 to 2.18 took place on 16 September 2016, as a consequence of the intense rainfall that was not enough to cause a translational slide.

The day before the failure took place, matric suctions between -5kPa and -10kPa were obtained at the cutting surface (Figure 7-9). After the rainfall event, matric suctions were completely removed at the cutting face and surface water runoff developed at ground surface (Figure 7-10).

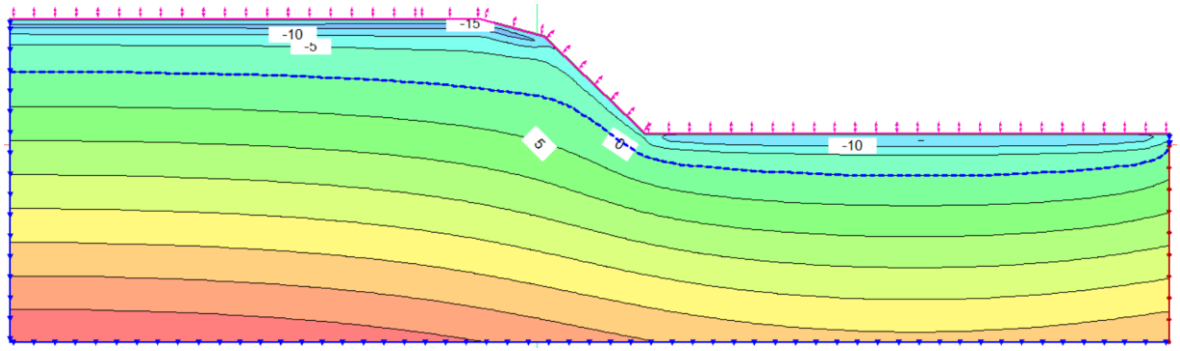

Figure 7-9 Distribution of PWP at the day before the failure

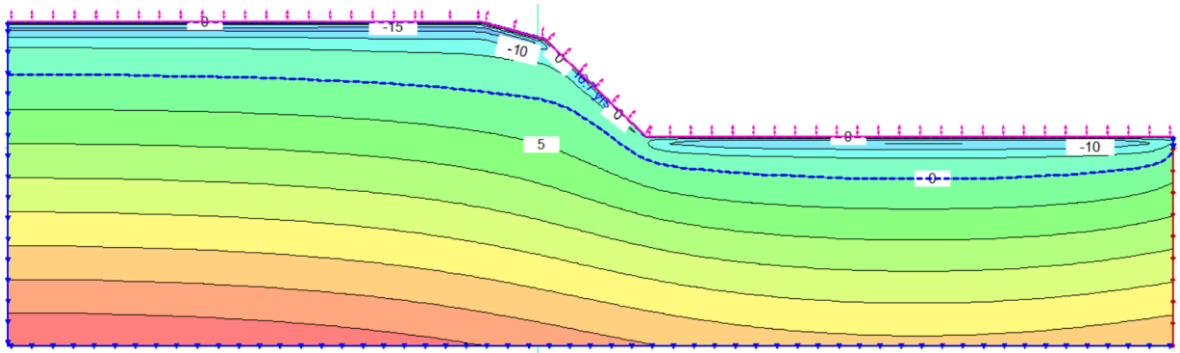

Figure 7-10 Distribution of PWP at the day of failure

WT fluctuated from -2m to -7m below ground surface during the data series analysed. This result relatively agree with fluctuations of groundwater levels recorded at Amersham Road (approximately 10Km South West of Watford Cutting) for the same chalk, where registered seasonal fluctuations of groundwater level are similar (UK Environmental Agency, 2019).

Hourly analysis 01/03/2016-16/09/2016

The evolution of the FoS vs Time is presented in Figure 7-11.

The initial conditions for this analysis was obtained from the output of the daily analysis on 16 March 2016.

From 16 March 2016 until the day of failure, a continue increase of the FoS was obtained. This result is in agreement with the daily analysis where maximum values of the FoS correspond to the months of August and September.

A reduction of the FoS from 3 to 2.6 was obtained at the day of failure that was not enough to cause the cutting failure.

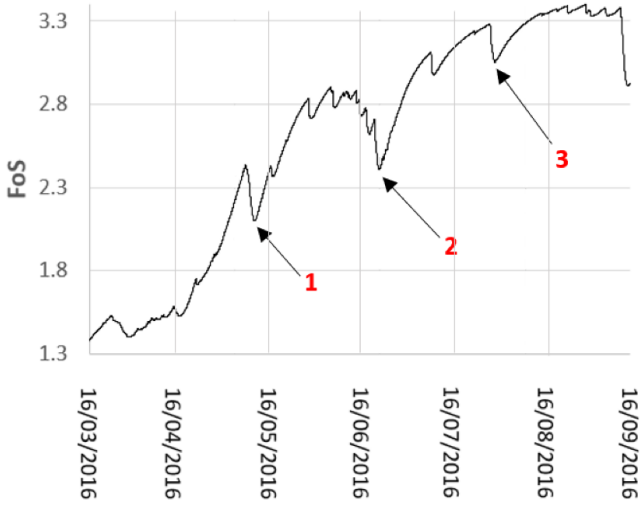

Figure 7-11 Hourly evolution of the FoS considering extra root-cohesion

Three significant reductions in the FoS can be observed in Figure 7-11, marked in red as 1, 2 and 3.

The reduction of the FoS in 1, 2 and 3 were a consequence of non-intense but prolonged rainfall during the days 9,10 and 11 of May for 1, 23 of June for 2 and 1 and 2 of August for 3.

At the start of the daily analysis on 16 March 2016 (Figure 7-12), matric suctions between 0 and -5KPa developed at the cutting face.

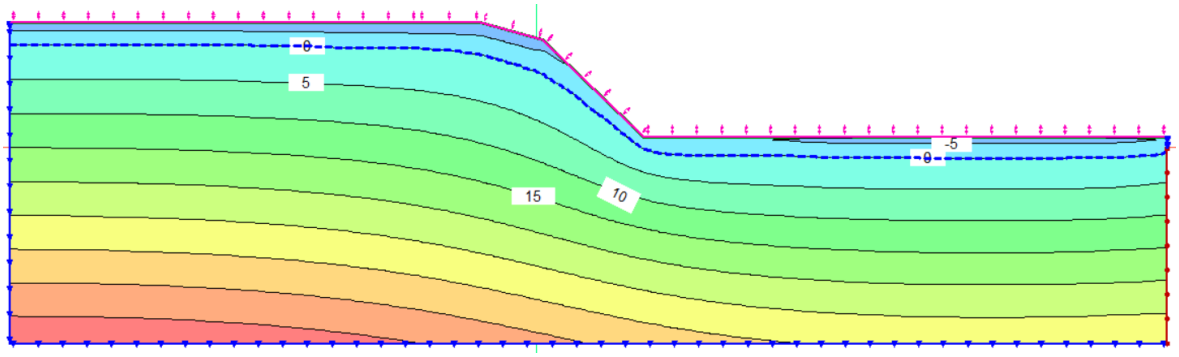

Figure 7-12 Distribution of PWP at the start of the analysis on 16/03/2016

Water suctions continued to increase at the cutting face from 16 March 2016 until the day before the failure as shown on 15 September 2016, corresponding to the day before the rainfall event (Figure 7-13). On 15 September 2016 matric suctions between -5KPa and -10KPa developed on the cutting face and the WT was located at approximately -8m below ground surface, up and downslope.

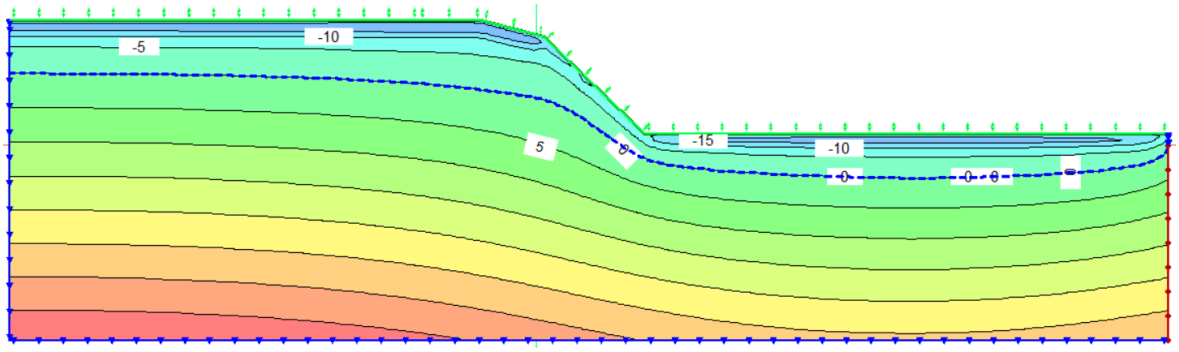

Figure 7-13 Distribution of PWP at the day before failure 15/09/2016

After the extreme rainfall on the 16 September 2016, surface water runoff developed at the ground surface but matric suctions from 0 to -5KPa remained below the ground surface at the cutting face (Figure 7-14). There were no variations in the WT immediately after the rainfall event.

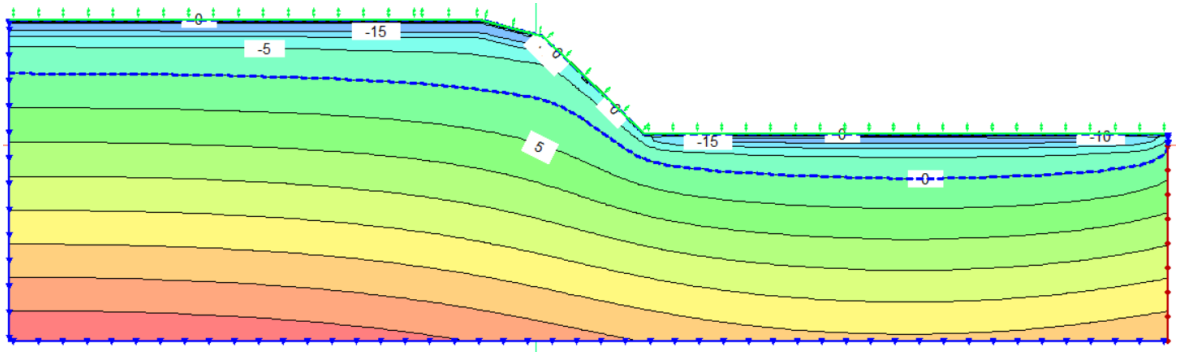

Figure 7-14 Distribution of PWP at 07:00 am 16/09/2016at the time of failure

7.4 Discussion

The daily analysis shows a cyclic variation of the FoS with peaks in August and September and lows from January to April where the ground water table approximates the ground surface at approximately -2m in average.

The hourly analysis shows a steady rise in the FoS from 01/03/2016 until the date of failure.

A reduction of the FoS caused by the extreme rainfall on 16 September 2016 resulted in a noticeable decline of the FoS for the hourly analysis and a less acute decline in the daily analysis. The reduction of the FoS in both cases was not enough to compromise the stability of the slope. The rainfall intensity at the day of failure (i.e. 12.5mm/h) was more than two orders of magnitude higher than the saturated hydraulic conductivity of the chalk, (i.e.10^{-8} m/s or 0.036mm/h). Part of the rainfall infiltrated into the chalk and slightly reduced the matric suctions in about 5KPa whereas other part of the rainfall transformed into surface water runoff. Due to the low permeability of the chalk, rise in pore water pressures and groundwater levels occurred slowly and smoothed over time and the rainfall event had no dramatic effect over the FoS in agreement with the findings of Rahardjo et al., (2007) for low permeability soils.

The results from daily and hourly analyses showed that hourly analyses better capture variations of the FoS under extreme rainfall events in agreement with the conclusions obtained by Schilirò et al., (2015) and Rouainia et al., (2009).

Analysis of slope stability showed that an extra root cohesion of -3KPa was needed for the cutting to remain stable from 2010 to September 2016.

It has been noticed that the weathering grade of chalk is the principal attribute to consider when analysing the stability of cuttings. Low weathered chalk presenting joints and fissures is a high permeable soil and the stability of the slope can be seriously

compromised under extreme weather events. Both dissipations of matric suctions and fast and significant rise in the water table level are expected during extreme rainfall events for this type of chalk.

On the contrary, high weathered structureless chalk, is a highly impermeable material with very different properties to fractured chalk. During extreme rainfall events, some dissipation of matric suctions may be present, but variations of groundwater table are slow. As a result, grade D_c chalk is far more stable than less weathered chalk under high intensity rainfall events.

The assessment of the cutting using continuum methods of analysis showed in this case that the failure at Watford on 16 September 2016 was not triggered by increase in pore water pressures.

In the next chapter, the novel method for the assessment of stability is introduced and the assessment of the stability at Watford using this method will be addressed in Chapter9:.

Chapter8: The novel method for the analysis of runoff generated debris flow

A new method for the assessment of the stability of railway cuttings in Grade D_c chalks and matrix dominated clay-like soils against runoff generated debris flows was derived in this thesis by coupling CFD and DEM. The method consists of the calculation of the shear stress that superficial water runoff applies over the face of the cuttings during a rainstorm, and the threshold shear stress that cuttings in chalk and clayey soils can withstand at different angles.

The novel method has been developed in two variants: The Direct Numerical-based Method (DNM) and the Rapid Routine Method (RRM).

DNM is a method where direct applications of numerical models are required whereas RRM is an analytical method based on the outputs of DNM where no numerical methods need to be applied. RRM is a method that requires less time than DNM and is envisioned as a first estimation to assess the susceptibility of a cutting to failure caused by runoff.

DNM has been conceived to be applied by using a software capable of calculating the shear stress caused by water flows over the face of the cuttings. RRM has been designed to be used without the need of numerical computation and can be applied only with the calculation of the watershed area, degree of funnelling, rainfall intensity and cutting angle.

The assessment of the stability of slopes/cuttings against runoff is based on the comparison of the bottom shear stress applied by overland flow against the critical shear stress that initiates the generalised scouring process.

For calculating the critical shear stress that initiates the mass failure of the cutting, the soil has been discretised in spheres for the analysis using the discrete element method. In the next section, a critical review is carried out of the existing work in this area, and whether it is or is not appropriate for the cuttings subject to analysis in this thesis.

8.1 Background

Short and intense rainfall events cause overland flows running over the face of natural slopes and cuttings whose magnitude depends on the permeability of the soil within the catchment and the intensity and duration of the rainfall event. Water flowing over the face of a slope causes a series of destabilising forces over the superficial material that, if

of sufficient magnitude, causes the movements of soil fragments with the potential to trigger a larger scale failure.

When a stream flows over ground with an erodible surface, the condition at which shear stress applied by the flow initiates movement of a few particles is known as the **threshold of incipient movement** (Shields, 1936).

The **threshold of incipient movement** has been profusely investigated in the field of sedimentology. Shields, (1936) was the first to investigate the problem by applying dimensional analysis to determine the initiation of motion in a granular bed. The results obtained were presented in form of a graph of dimensionless shear stress (τ^*) (8. 1) against Particle Reynolds number (R_*) (8. 2)(Figure 8-1).

$$\tau^* = \frac{\tau_b}{(\rho_s - \rho) g d_p} \tag{8. 1}$$

$$R_* = \left(\frac{\tau_c}{\rho}\right)^{\frac{1}{2}} \frac{d_p \rho}{\mu} \tag{8. 2}$$

Where,

τ_b= bed shear stress

d_p = particles diameter

ρ_s =density of soil granules

ρ =density of water

μ =dynamic viscosity

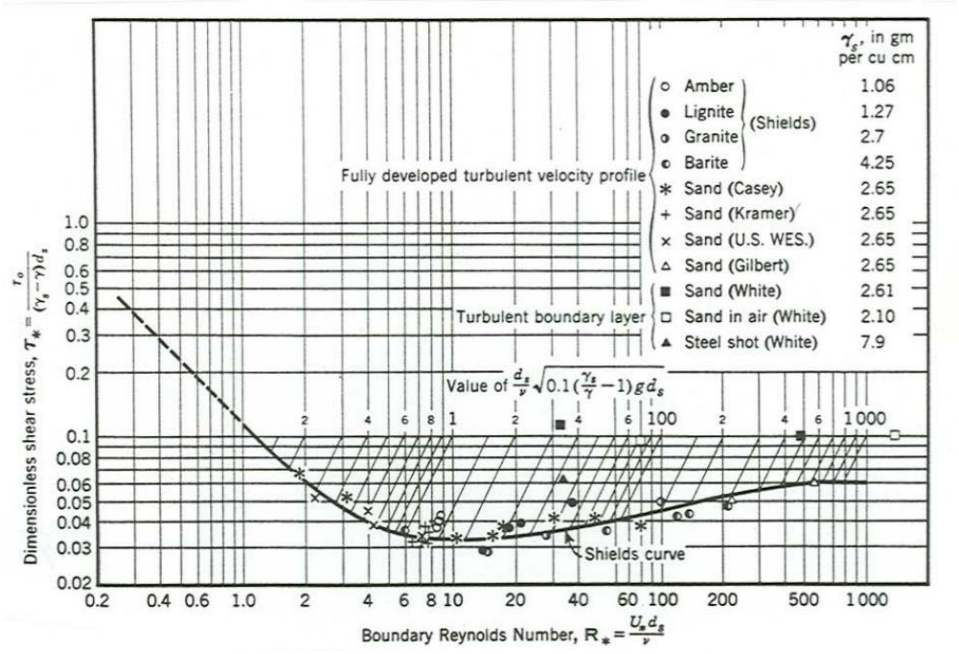

Figure 8-1 The Shields diagram. (Vanoni, 1975)

This graph is used to determine the critical shear stress (τ_c) that a flow need to apply over the surface of a particulate bed to initiate the movement of particles. Subsequent modifications of the Shields diagram have been proposed after applying corrections to the critical Shields' shear stress due to longitudinal slope effects (Chiew and Parker, 1994; Christensen, 1995).

In rivers and channels, the definitions of this threshold is very important as it is used in the stable design of channels and to establish adequate preventative measures against erosion (Dey and Debnath, 2000).

As the shear stress applied by runoff over the ground surface is increased beyond the threshold initiating particle movement, there comes a point where an abrupt scour process takes place and the entire bed layer is scoured in a few seconds Gregoretti, (2000). This second shear stress threshold leads to the mass failure of the slope through debris flows.

The majority of research has been carried out for the shear stress threshold of incipient movement in the field of sedimentology since the work of Shields in 1930 (e.g. Mantz, 1973; Yalin and Karahan, 1979, Brownlie, 1981; Ikeda, 1982; Wiberg and Smith, 1987; Chiew and Parker, 1994; Christensen, 1995; Dey and Debnath, 2000; Zanke, 2001;Guo, 2002; Zanke, 2003). However, it is only in the last two decades that researchers started to investigate the mechanisms leading to the initiation of debris flows (e.g. Gregoretti, 2000; Tognacca et al., 2000; Armanini and Gregoretti, 2005; Buffington and Montgomery, 1998; Mergili, 2008)

The critical shear stress calculated by Shields, (1936) corresponds to the incipient movement of particles and cannot be applied to a generalised mass scouring process. This was pointed out by Gregoretti, (2000) who after conducting flume experiments with gravel particles observed that the mass failure process was associated with shear stresses well above the critical shear stress corresponding to the incipient motion predicted by Shields, (1936).

Despite of the efforts carried out during these years and as pointed out by Cannon et al., (2003) and Berti and Simoni, (2005), the initiation of debris flows by surface water runoff have not still been extensively studied and continue to be poorly understood compared with other triggering factors.

Previous investigations of the mechanisms leading to the initiation of debris flows have been carried out for conditions similar to channelised river beds (i.e. sands and gravels) and no attempt has been made for man-made slopes.

8.1.1 Mass failure due to runoff

In soil mechanics, soil slopes fail essentially due to shear and as such, the Mohr-Coulomb failure criterion can be applied to analyse the stability (Aysen, 2002). However, the process that takes place in the dislodgement of soil material at ground level is not uniquely governed by shearing stresses. The discretisation of superficial soils into soil peds or chalk clasts of variable shapes has a key role in the initiation mechanism of this type of failures where resistance to torque and hydrodynamic forces play a fundamental role.

The process of runoff triggering mass failure for granular soils has been described by Gregoretti, (2000) as a different mechanism from the incipient motion of particles investigated in sedimentology.

A similar process of mass failure has been observed in clay-like soils beyond the threshold of **incipient movement**. Mehta et al., (1989) observed that at the beginning of the erosion process in a clay-like soil, fine particles start to detach from the superficial soil layer. When a critical shear stress is passed, different erosion patterns take place involving the detachment of soil peds.

'*When rapidly accelerating flows occur, the bed may fail at some plane below the surface and clumps of material are mass eroded*' (Mehta et al., 1989)

The same pattern was observed by Jain and Kothyari, (2009) who conducted experiments in a tilting flume consisting of clay-sand-gravel mixtures with different proportions of clay material. The results showed that for the soils with higher percentages of clay (i.e., 40% or more) mass failure occurred in the form of lumps of the sediment. When the clay proportion was about 50% in the bed material, removal of chunks of sediment from the bed surface occurred leaving it with several potholes that eventually developed into a big pothole along the channel bed.

The process of detachment of clumps of material in clay-like soils is not completely understood. There is however evidence in natural slopes and cuttings that cracking may be responsible for the discretisation of the clayey soil in chunks of soil peds.

Discretisation of the superficial soil layer into soil peds during mass failure can be attributed to the presence of shrinkage cracks that become permanent due to repeated wetting and drying cycles. Cracks develop during the drying season due to evapotranspiration and are partially filled with dust or silty sediments (Cammeraat, 2002). During the wetting season, swelling of clays takes place and cracks are closed. However, the discontinuity in the macrostructure of the cracked layer remain during winter and vertical cracks reopen in the following drying season (Norris et al., 2008).

A different theory was proposed by Hutchinson, (1970) and Vallejo and Morris, (1979). During the winter months, if frost action takes place, the fissures will be filled by ice that may grow using the water contained within the blocks of clay. After the clay structure has been broken into pieces due to the processes mentioned above the structure of the clay at shallow depths during rainfall will then consist of hard lumps of clay surrounded by a mixture of clay and water.

Discretisation of boulder clay into soil peds attributed to shrinkage cracks has been identified by Foster, (2010) as the main contributor to failure in the East Yorkshire (Holderness) mass movements (Figure 8-2).

Mass movement block deposits in Boulder clay

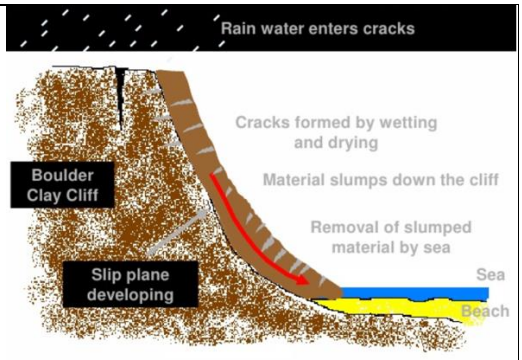

Process leading to the failure in the form of discrete chunks of clays

Figure 8-2 Discretisation of cohesive soil into large blocks (Foster, 2010)

In a visit on 12 June 2020 to the Beaminster cuttings where two cutting failures took place as a consequence of runoff, the presence of desiccation cracks were observed (Figure 8-3 left). Hitting the cracked soil surface resulted in the dislodgment of big chunks of soil as in Figure 8-3 right.

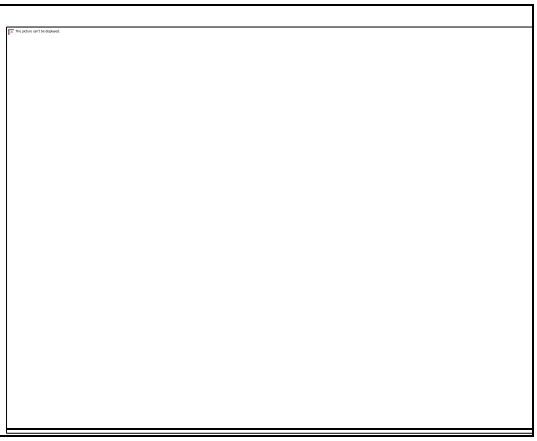

Figure 8-3 Desiccation cracks at Beaminster (left), dislodged chunk of soil (right)

The discretisation of clay-like soils into a network of blocks separated by shrinkage cracks reinforces the validity of using DEM in such soils for the analysis of the initiation of runoff generated debris flows.

DEM considering clayey soils as a network of soil peds has previously been carried out by Hung et al., (2018) in the analysis of the dynamic runout process in a clayey soil slope failure using DEM particles of 8 and 9 cm radii.

Agglomerates of particles can also be observed in Dc chalk deposits where initial intact chalk fragments embedded in putty chalk are dislodged by surface runoff hydrodynamic forces as in the Watford case study (Figure 8-4).

Structureless chalk is defined as cohesionless calcitic silt (Meigh and Early, 1957) and has been reported to lose the cohesion of intact chalk (Clayton, 1977). Although structureless chalk can recover some of the initial true cohesion after a process of recementing (Clayton, 1977), structureless chalk at ground surface undergoes physical and chemical water weakening (Donnez, 2012;Risnes et al., 2005) what makes unlikely that the process of recementing takes place when it is subjected to atmosphere agents. The lack of cohesion facilitates the dislodgement of chalk clasts by superficial water runoff.

Figure 8-4 D_c chalk clasts at Watford (PA Media, 2016)

Grade D_c chalk is composed of clasts of intact chalk embedded in putty chalk. Grade D_c chalk has been simulated in DEM using spheres that represent chalk clasts with the boundary conditions (i.e. interparticle friction angle, Poisson's ratio and Young's modulus) presenting the properties of putty chalk.

In the case of matrix dominated clay-like soils, it has been simulated in DEM as spheres representing soils peds with the properties of the fine fraction as the boundary conditions.

8.1.2 Previous research on mass failure due to runoff

Takahashi (1978) was the first to introduce a physical approach for the investigation of the mass failure of slopes subject to runoff in order to investigate the initiation of debris flows. Takahashi's model is based on the equilibrium of a sediment block, where. the shear stress applied by overland flows over the slope face is used as the destabilising force. By equating the shear stress and the resisting stress at a critical depth where failure occurs, he came up with an equation for the threshold initiation of slope failure. Takahashi's model was based on the assumption that the hypothetical shearing stress, τ,

which acts to drag the sediment block downstream and the resisting stress, τ_r, are distributed in straight lines ad the slip surface occurs when $\tau = \tau_r$ (Figure 8-5).

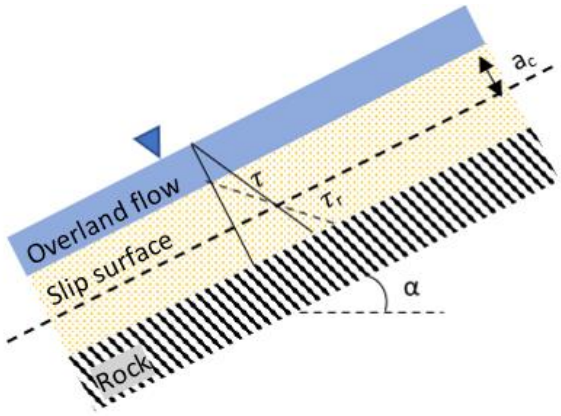

Figure 8-5Takahashi's, (1978) model for the initiation of slope failure due to overland flow

Although Takahashi pioneered the investigation of the initiation of slope failure due to runoff, his approach was based on considering the soil as a continuum, and therefore, the limitations associated with this approach are inherent in this model.

Further investigations of the initiation of debris flows in granular soils have been carried out by Gregoretti, (2000), Tognacca et al., (2000) and Armanini and Gregoretti, (2005) considering equilibrium of discrete particles and moving apart from the continuum approach of Takahashi Gregoretti, (2000).

Gregoretti, (2000) performed experimental tests in a laboratory flume filled with a layer of nearly uniform gravel (three gravel sizes employed) with slope angle between 12° and 20° to study the critical condition for sediment bed stability.

Gregoretti, (2000) showed that the onset of the scour occurs at a shear stress above the critical shear stress corresponding to incipient motion identified by Shields, (1936).

According to Gregoretti, (2000), such discrepancy was plausible, considering that Shields' incipient motion and subsequent work in the field of sediment transport has been empirically and theoretically derived studying the instability of a single grain and not the scour of the entire layer as was recognised by Luque and van Beek, (1976) and Gyr and Schmid, (1997).

Gregoretti, (2000) also observed that the critical shear stress for the scour of the entire layer was significantly below the threshold estimated by Takahashi, (1978) and Takahashi, (1991). Gregoretti, (2000) stated that the Takahashi criterion was not valid since the intense particle by particle collisions raised by the scouring process increased

further the bottom shear stress causing movement of particles before the sliding mechanism hypothesised by Takahashi (1978, 1991) took place (Figure 8-5).

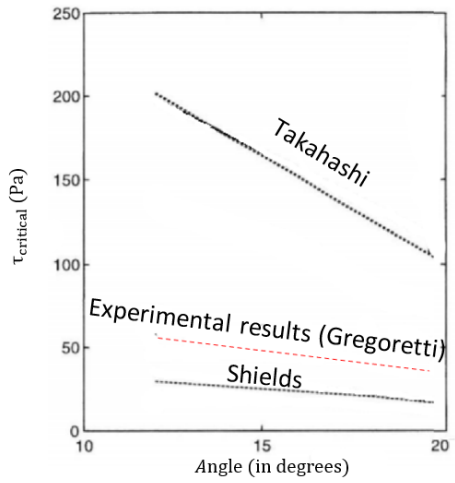

Figure 8-6 Critical shear stress for gravels comparing Shields, Takahashi and experimental results

Tognacca et al., (2000) determined the critical shear stress of mass failure from experiments performed in a laboratory flume filled with a layer of a mixture of sand and gravel with slope angles between 14° and 30°. Based on the experimental results Tognacca developed an empirical formula of threshold criterion for the mass failure of a mixture of sands and gravels.

Tognacca et al., (2000) equation defines the minimum surface discharge per unit width q_u necessary to move the debris material filling a channel and to trigger a debris flow event as a function of the bed slope β and the mean grain size d_M of the debris material.

Armanini and Gregoretti, (2005) also developed an analytical formula for the mass failure of loose gravels at steep slopes. They obtained the flow depth of the stream flow triggering mass failure as a function of the bed slope, the particle repose angle and the exposure of the sediment particles.

For the case of cohesive soils, experimental work and semiempirical formulas for the initiation of the motion of particles have been conducted by a number of researchers (e.g. Otsubo and Muraoka, 1988; Amos et al., 1997; Reddi and Bonala, 1997; Meng et al., 2012; Mehta et al., 1989; Jain and Kothyari, 2009). However, these were generally carried out in the field of coastal engineering under conditions similar to a river delta in horizontal beds.

8.1.3 The use of CFD-DEM as a tool for the analysis of runoff generated debris flows

Previous investigations of the critical shear stress leading to debris flows have been carried out exclusively for gravels and sands with gravels in tilting flume tests at inclinations lower than the ones encountered in failed transportation cuttings: 14°-30° by Tognacca et al., (2000) and 12°-20° by Armanini and Gregoretti, (2005).

As the critical shear stress in the semiempirical equations proposed by Tognacca et al., (2000) and Armanini and Gregoretti, (2005) is obtained as a function of the flow depth, the validity of the equation has only been analysed for relatively shallow slope angles. For steeper slopes, the critical shear stress has not been analysed probably due to the reduction of the flow depth that makes the calculation of the critical shear stress less accurate.

The equation proposed by Armanini and Gregoretti, (2005) differs from the experimental results of Gregoretti, (2000) due to the difficulties in the derivation of the degree of exposure of gravels to runoff that varies depending on the inclination of the slope. The application of the Armanini and Gregoretti, (2005) equation for slopes steeper than 20° would need of additional work for the derivation of the degree of exposure at a number of slope angles. In addition, this equation has only been analysed for gravel particles and the performance of the equation for soils other than gravels is unknown.

The use of CFD- DEM to investigate the critical shear stress that initiates runoff generated debris flows at different angles has been chosen in this thesis.

CFD-DEM allows the configuration of particles for any type of soil where the critical shear stress is to be obtained. CFD-DEM is a powerful tool that offers some advantages over flume tests. Conducting laboratory flume experiments for the different types of clay-like soils and Grade D_c chalk in the UK would become cumbersome since samples of the soils would have to be transported to the location of the flume and soil properties would be altered during the sample collection.

An additional incentive to using CFD-DEM is to showcase the possibilities of CFD-DEM for research into slope failure initiation that has not yet been attempted.

In the next section, the design of the novel method is described.

8.2 Overall approach

The novel method is based on the shear stress that runoff apply over the cutting surface and the critical shear stress that initiate the mass movement of particles.

The process followed for the generation of the two variants of the novel method, the DNM and the RRM, is illustrated in Table 8-1.

The application of DNM requires the use of a shallow water equations-based software to calculate the actual shear stress over the face of the cutting for a particular case study. The RRM calculates the actual shear stress from the flow rate at the crest of the cutting.

Table 8-1 Methodology for the design of DNM and RRM

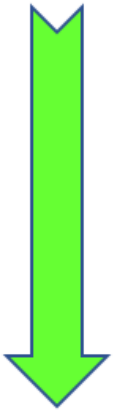

DNM and RRM	
OBJECTIVE	Determine the relationship between the critical shear stress and slope angle for different materials
DATA COLLECTION	DEM particle parameters for clay-like soils and Grade D_c chalk
NUMERICAL METHOD USED	CFD-DEM
MODELLING	Design of a tilting flume in CFD-DEM
RESULT	Chart of critical shear stress vs slope angle
RRM	
OBJECTIVE	Determine the relationship between bottom shear stress and flow rate per unit width for different slope angles
DATA COLLECTION	Surface roughness of soil
NUMERICAL METHOD USED	CFD (RANS)
MODELLING	Design of a tilting flume in CFD
RESULT	Chart of bottom shear stress vs flow rate per unit width

8.3 Methodology for the application of DNM and RRM

The assessment of the stability of cuttings using the DNM and RRM methods is presented in Table 8-2 as a process consisting of seven steps.

Table 8-2 Methodology for the application of DNM and RRM

VARIANT	DNM	RRM
STEP 1	Obtain DTM of cutting and catchment	
STEP 2	Calculation of the drainage lines (e.g. using GIS software)	
STEP 3	Calculation of slope angles	
STEP 4	Obtain rainfall characteristics (rainfall intensity and duration)	
STEP 5	Obtain the bottom shear stress at the slope/cutting face: Use of shallow water equations via numerical simulation: e.g. FLOW-3D	Obtain the bottom shear stress at the slope/cutting face: 5a- Calculate the catchment area (e.g. using GIS software)

		5b- Calculate the flow rate per unit width at the crest of the cutting 5c- Read the bottom shear stress of the design chart according to the flow rate and slope angle
STEP 6	Calculation of the critical shear stress at each slope/cutting by use of the design chart	
STEP 7	Assessment of the stability of the cuttings[1]	

[1] Assessment of the stability of the cuttings by comparing the critical shear stress (τ_c) with the bottom shear stress (τ_b)at the face of the cutting.

If $\tau_b \geq \tau_c$ then the cutting is unstable for the applied rainfall intensity

If $\tau_b < \tau_c$ then the cutting is stable for the applied rainfall intensity

A FoS can be derived as

$$FoS = \frac{\tau_c}{\tau_b}$$

8.3.1 Input parameters

Input parameters required are:

a) 1m DTM obtained for the area including the catchment and the cutting to be analysed.
b) Drainage lines calculated from the 1m DTM using GIS software (e.g. ArcGIS)
c) The average slope angle of the cutting analysed obtained following the drainage line over the face of the cutting and using GIS software (e.g. ArcGIS).
d) Rainfall characteristics (rainfall intensity and duration) obtained from meteorological stations at the location of the cutting analysed.
e) Values of particle parameters (see Chapter 6) to be used in CFD-DEM for the simulation of soils

8.3.2 Calculation of drainage lines and catchments using ArcGIS

Drainage networks are derived from DTMs through an algorithm in ArcGIS. A grid of cells is generated in ArcGIS where each cell is characterised by its elevation. The algorithm identifies the direction of the flow based on the heights of each cell and drainage lines and catchment areas are generated. The process in ArcGIS to generate the drainage lines and catchment areas is as follows:

1) Flow Direction: This function computes the direction of flow in the area analysed. The area is discretised by cells in a grid and each cells is assigned a value corresponding with the flow direction by comparing the elevation of neighbouring cells (Merwade, 2019).
2) Flow Accumulation: Each cell is assigned a value related to the accumulated number of cells upstream.
3) Stream Definition: cells with a high value calculated in flow accumulation are areas of concentrated flow and are used to identify stream channels. This function calculates a threshold defined by the user and a stream grid derived from a flow accumulation grid. For the flow accumulation grid, the cells in the input that have a value greater than the threshold are allocated a value of 1 in the stream grid. All other cells are given no value. The threshold for stream calculation recommended to be used is the value that represents 1% of the maximum flow accumulation and the one used in the analyses (ESRI, 2011) and this the threshold widely used in GIS tools (Ozulu and Gökgöz, 2018). Other cell threshold values may be used, but lower thresholds than the default value may result in catchment areas that become more questionable (Maidment and Morehouse, 2002).
4) Stream segmentation: drainage lines in the area are calculated by grouping the stream channels that have a common outlet.
5) Batch Subwatershed Delineation: For a selected point, the cells that contributes to the stream channels with the common outlet at the specified are grouped and the catchment area is delineated (ESRI, 2011).

8.3.3 Calculation of the bottom shear stress from numerical simulation (DNM)

When using DNM, the bottom shear stress can be obtained by application of shallow water equations over a DTM containing the catchment area and the cutting for each case study.

Commercial software such as HEC-RAS or FLOW-3D, is available for the calculation of the bottom shear stress using digital terrain models. In this thesis, FLOW-3D has been used for the application of the novel method owing to the ability of this software to deal with steep slopes present in transportation cuttings.

For every case study analysed using FLOW 3D, the bottom shear stress at the cutting face must be obtained. In case of a variable bed shear stress along the cutting face, the

highest value shall be considered. The methodology used for the calculation of the bottom shear stress in FLOW-3D is as follows:

1. Meshing of the are analysed

Once the DTM has been integrated in FLOW-3D, a mesh is generated over the area analysed to apply the shallow water equations.

FLOW 3D uses an algorithm to detect and convert the DTMs into a wall boundary. The algorithm implies that the mesh cells need to cover the lowest and highest points of the DEM in the vertical direction. In addition, a second row of cells in the vertical direction is also required. Although the resultant mesh form factor is not applicable in other numerical methods (e.g. FEM, FVM), it is not an issue for the analyses in FLOW 3D since the shallow water equations are in essence two-dimensional. A detail of the mesh used in Watford case study is shown in Figure 8-7.

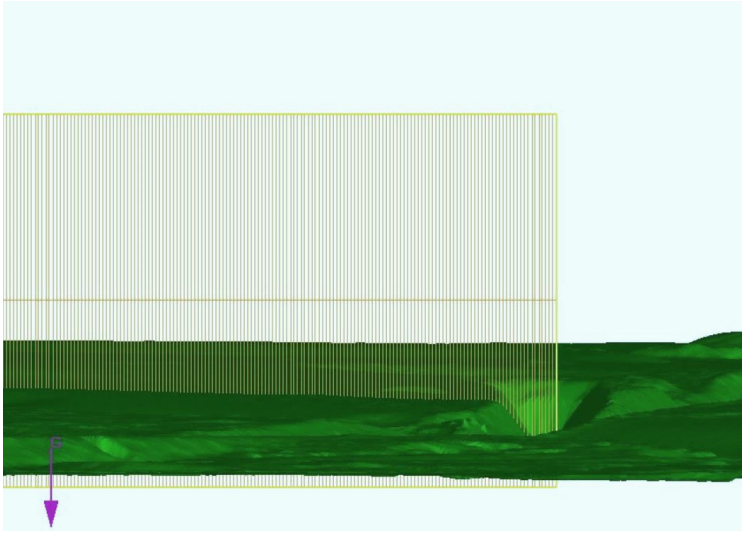

Figure 8-7 Detail of the mesh used for shallow water equations at Watford

2. Boundary Conditions

The boundaries applied to the mesh are chosen considering:

- The sides of the mesh are treated as continuation boundaries consisting of zero normal derivatives for the momentum conservation equations This condition represents an outflow with a smooth continuation of the flow through the boundary. Continuation boundaries avoid false accumulation of water at the contours of the mesh.
- The ceiling is considered as a symmetry boundary and the ground surface as a rough wall boundary. The roughness parameter introduced here corresponds

to the Nikuradse roughness coefficient of 0.0006m of the soil at a mesoscale level, as will be explained in Section 8.4.

- Rainfall is implemented as a uniform source of water distributed all over the area. FLOW 3D allows the introduction of rainfall with variable intensity over time.

The ground surface is treated here as an impermeable material over which the surface water runoff flows towards the cuttings.

Short duration-high intensity rainfalls are prone to form surface crusting and sealing, which reduce infiltration rate and increase runoff (De Roo and Riezebos, 1992;Vandervaere et al., 1997). The fact that the novel method was designed for extreme rainfall events support the assumption that infiltration may be considered negligible (Rango et al., 2006), particularly in clays and chalk where the hydraulic conductivity is of several orders of magnitude lower than the rainfall intensity.

3. Model Configuration in FLOW-3D

The configuration of FLOW 3D used in the analyses is:

Models:

- Gravity and non-inertial reference frame
- Shallow Water:
    - Flow Type: Turbulent
    - Numerical Approximation: Implicit
- Viscosity and Turbulence:
    - Viscous Flow
    - Wall Shear Boundary Conditions: No-Slip

Time Steps: 0.0001s

Surface Roughness: 0.0006m

4. Bottom shear stress at the cutting face

Once the numerical analysis is concluded in FLOW-3D, a representation of the bottom shear stress at each location of the area analysed is presented as a colour map. To obtain the maximum bottom shear stress at the cuttings analysed, FLOW-3D allows the isolation of the cutting of interest.

8.3.4 Calculation of the bottom shear stress from RRM

Assuming that the duration of the rainfall is larger than the time that the flow takes to travel from the farthest point of the catchment to the cutting, the actual rate of runoff at the cutting per unit width (Q_n) is obtained from:

$$Q_n = \frac{A \cdot I}{n} \tag{8. 3}$$

Where,

$A =$ area of the catchment;

$I =$rainfall intensity;

$Q_n =$runoff flow rate per unit width;

$n =$width of water runoff

This assumption has been demonstrated to be correct in the cuttings analysed in this thesis even for non-circular catchments with shallow slopes of which the most representative case is the Watford cutting. Using a virtual probe in FLOW-3D at the cutting crest, the time at which superficial runoff flow rate reached its peak was 2400 seconds (40mins) whereas the rainfall duration was 4 hours (Figure 8-8).

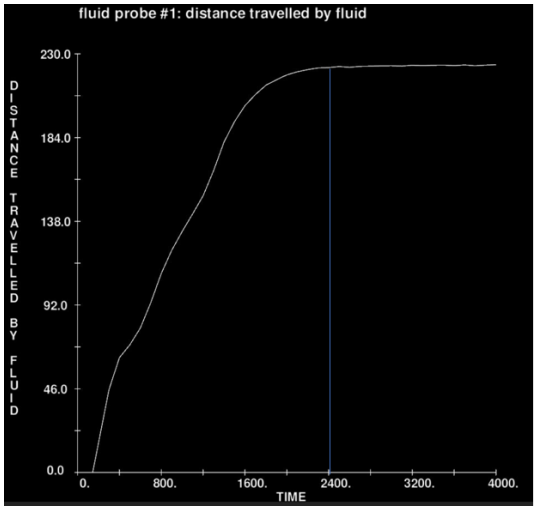

Figure 8-8 Distance travelled by runoff at the crest of Watford cutting

One of the limitations of RRM is the difficulty of calculating the width of runoff when flowing down the cutting. In the cases analysed in chapter 9, the assumption of n=1 worked well for all of them and this will be discussed in section 9.7.

To obtain Q_n, the area of the catchment needs to be calculated. In this thesis, this process was carried out in ArcGIS software.

Once the catchment area (A), and the rainfall intensity (I) have been obtained, Q_n is derived. Then, a correlation between Q_n and the bottom shear stress needs to be established though a designed chart actual shear stress vs flow rate.

Once the actual shear stress is obtained, the stability of the cutting is assessed by comparing the actual shear stress with the critical shear stress.

The methodology for application of the novel method needs the design of two charts: a) actual shear stress vs flow rate and b) critical shear stress vs slope angle. In the next section, the methodology followed for the calculation of the design charts is introduced.

8.4 Correlation between flow rate per unit width and bottom shear stress: Methodology

A correlation between the flow rate per unit width, the slope angle and the bed shear stress can be obtained through a numerical experiment using 3D RANS models (Figure 8-9). Modelling a tilting flume, different inflow rates were imposed in the upper part and the averaged bed shear stress was measured in the second half of the flume where the flow is more uniform. A relationship between flow rate per unit width and averaged bottom shear stress was obtained for different slope angles.

8.4.1 Geometry

The flume consistsed of two parts of 4 and 5m length in the direction of the flow. Bed shear stresses were calculated at the 5m length slab where perturbations from the inflow boundary are lower.

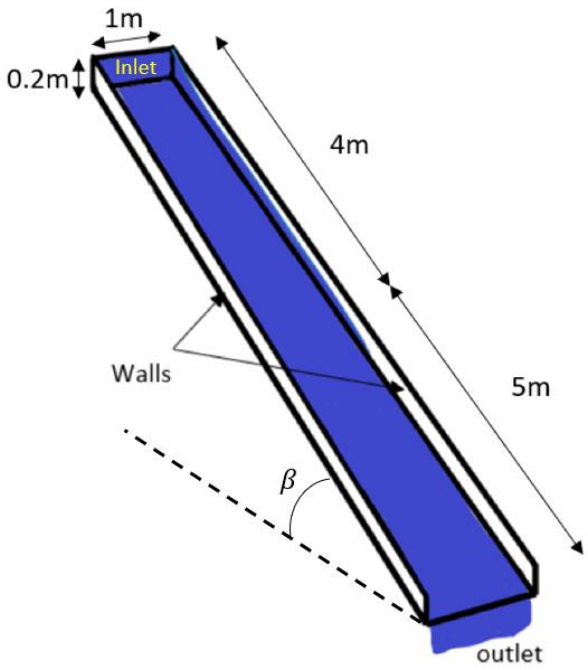

Figure 8-9 Geometry of slab test in STAR-CCM+

8.4.2 Data collection

In sheet flows as in the case of runoff, the height of the flow is shallow (in the order of a few centimetres) and features such as grass, shrubs and trees protruding from the stream surface must therefore be considered as physical obstacles. Consequently, it is not reasonable to introduce roughness lengths associated with terrains representing these features in the turbulent flow equations to obtain the bed shear stress. Rather, the roughness of the terrain at the mesoscale over which the runoff flows such as the asperity of chalk and clayey blocks is what should be introduced in the calculations. A common value for the equivalent surface roughness has to be chosen for general application of the catchments analysed.

For the case of chalk and clays where the diameter of the particles is in the order of micrometres, the value of k_s would be of the same order of magnitude. However, in real catchments, where the soil surface has been subjected to weathering, it is not reasonable to assume a roughness coefficient as the one encountered for example in intact chalk. The clayey soils in the catchments analysed also contain silt and sand particles which makes the selection of an appropriate roughness length more difficult.

The maximum surface roughness where the y^+ wall treatment can be applied corresponds to $y^+ = k_s^+$ (Brezgin et al., 2017). In the slab experiments, a maximum value

of $k_s = 0.0006m$ could be applied to the model. Any other value of k_s >0.0006m yielded the same roughness effect (Figure 8-10) (Brezgin et al., 2017) .

According to (5. 30), a value of $k_s = 0.0006m$ yields a median diameter of the surface particles $\mathrm{D_p} = 0.6\mathrm{mm}$ which is approximately equivalent to the asperities presented by concrete (Bai and Bai, 2005). In this thesis, a value of $k_s = 0.0006m$ was used for the analyses, as the bed shear stresses obtained results in a conservative approach for application of the novel method.

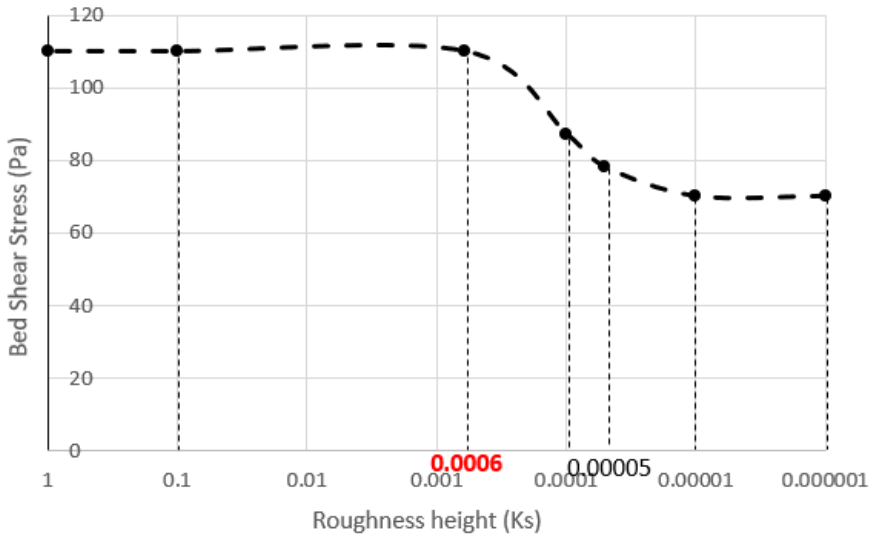

Figure 8-10 Ks vs Bed shear stress for 85l/s and 45 degrees slope angle

8.4.3 Boundary conditions

The slab was modelled with symmetry boundary conditions for the lateral walls, atmospheric pressure at the top of the slab to simulate an open surface, and the bottom as a rough wall with a roughness coefficient of $\mathrm{k_s} = 0.0006\mathrm{m}$

a) Mesh

A fine uniform mesh of hexahedral elements, of 2cm side length was used for the entire slab. A refined mesh of elements having a 0.165cm sides length was used adjacent to the bottom boundary to meet the y^+ log-law criterion.

b) Methodology for the calculation of the bottom shear stress

The procedure for the calculation of the bottom shear stress for a certain slab angle and the flow rate was as follows:

First, the slab was tilted to the desired angle by changing the gravity vector, and then a constant flow rate was applied at the inflow boundary until a steady flow was obtained.

Then, the shear stress at the bottom of the 5m length slab portion was surface averaged in STAR-CCM+ software.

A visual representation of the bed shear stress is presented in Figure 8-11. It can be observed how the bed shear stress at the inflow boundary increases as runoff flows down the slab until reaching a terminal bed shear stress when the component of gravity in the direction of flow and the shear force in the opposite direction balance.

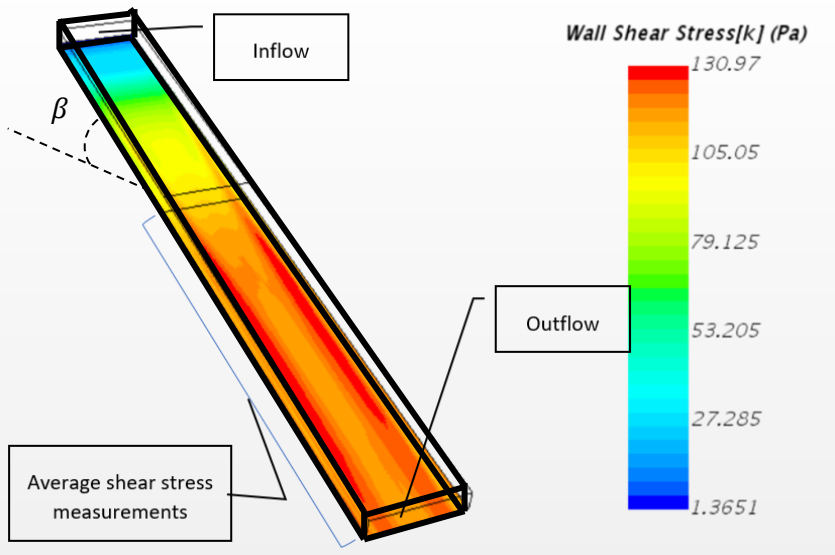

Figure 8-11 Wall shear stress in the slab test using STAR-CCM+ for 45° and 100l/s

The same procedure was repeated for the range of slope angles: 0,5,10,15, 20, 25, 30, 35, 40 and 45 (in degrees) and the range of entry flow rates: 5, 10, 20, 30, 40, 50, 60, 70, 100, 150, 200 and 300 $(\mathrm{l/s})$. From this process, a design chart bottom shear stress vs flow rate for a number of slope angles was obtained.

In the next section, the derivation of the critical shear stress for different materials and slope angles is addressed.

8.5 Correlation between slope angle and critical shear stress: Methodology

The single parameter in the flow field that best represents the threshold of mass failure is the critical shear stress applied by the fluid over the bed surface (τ_c)(Figure 8-12). This parameter has been used in sedimentology for the initiation of motion in a bed packed with particles subject to a parallel flow (e.g. Shields, 1936; Meyer-Peter and Müller, 1948; Engelund and Fredsøe, 1976; Fernandez Luque and Van Beek, 1976; Parker, 1990; Wilcock and Crowe, 2003). The parameter has also been used for the initiation of mass failure in runoff generated debris flows (e.g. Tognacca et al., 2000; Gregoretti, 2000; Armanini and Gregoretti, 2005)

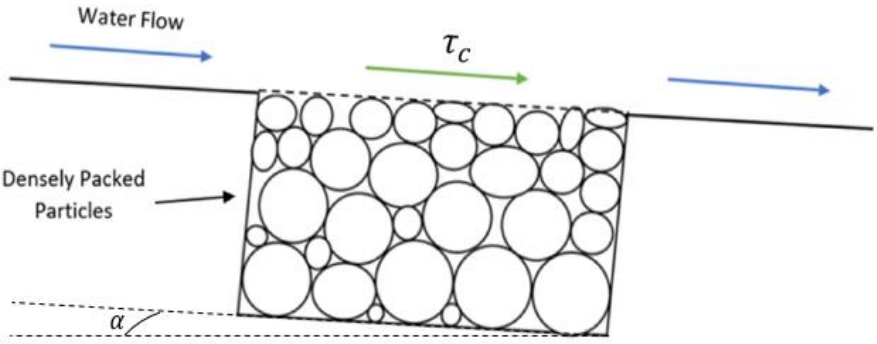

Figure 8-12 Experiment conducted for the calculation of the critical shear stress

The critical shear stress initiating cutting failure depends on the type of material (i.e. chalk or clay-like soils) and the angle of static friction. Therefore, a chart critical shear stress vs angle of the slope is needed for different soil parameters (i.e. unit weight and angle of static friction) in the proposed method.

To obtain the critical shear stress at different slopes angles, a flume test was designed using CFD-DEM in Star CCM+.

The critical shear stress for different soils at different slope angles was obtained by simulating a tilting flume in CFD-DEM in STAR CCM+.

8.5.1 Flume concept

Different apparatuses in the field of sedimentology have been used to measure the critical shear stress but all are based on the same principle: a continuous stream of water is released at one side of a tilting flume over an already saturated sediment bed. In laboratory flumes, the depth of the water flow and the flow rate are obtained to calculate indirectly the shear stresses that initiates the failure. Detailed descriptions of the apparatuses used in research can be found in (Shvidchenko and Pender, 2000; Kuriqi et al., 2019; Le Hir et al., 2008; Houwing and van Rijn, 1997; Roberts et al., 1998; Lick et al., 2004; Armanini and Gregoretti, 2005)

The model used in this thesis is based on the IFREMER erosion flume (Le Hir et al., 2008) in which a core sample is exposed to a flow current in a tilting flume as illustrated in Figure 8-13.

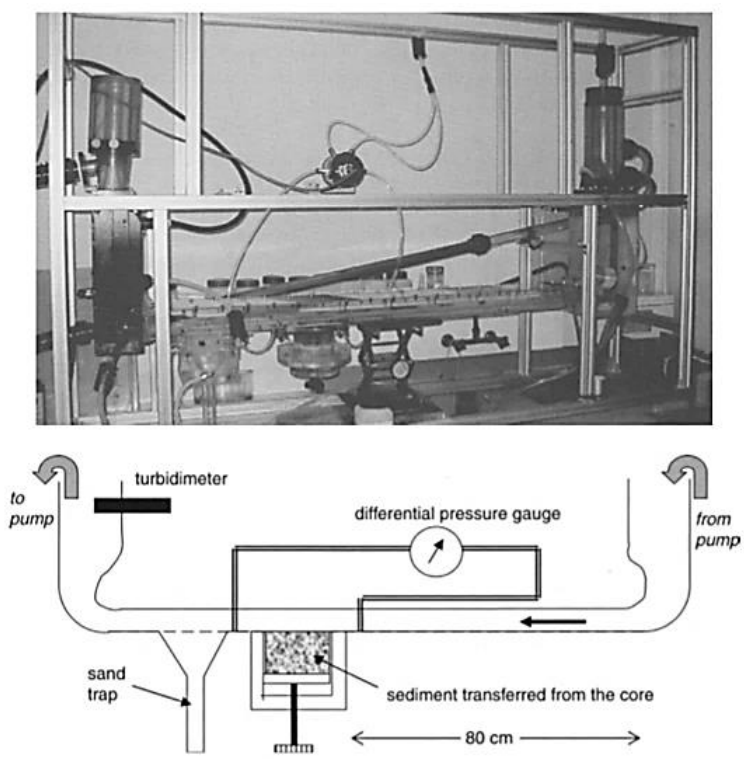

Figure 8-13 The IFREMER erosion flume (Le Hir et al., 2008)

A flume was numerically modelled in STAR-CCM+, (2017) replicating the conditions in Figure 8-13. A close conduit with a back pressure regulator creates atmospheric pressure at the outlet of the flume and the pressure is increased at the other end of the valve to maintain a specific constant velocity. The geometry of the flume designed in STAR-CCM+, (2017) corresponds to the section indicated in Figure 8-14. The backpressure regulator is modelled by applying boundary conditions at the inlet and outlet sections.

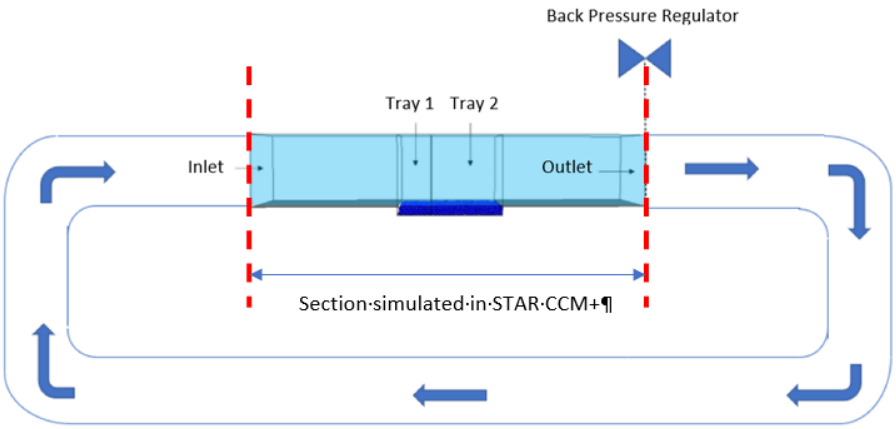

Figure 8-14 Geometry of the flume test

The soil is simulated in STAR CCM+ using the discrete element method where trays 1 and 2 are filled with particles (i.e. soil peds) replicating the properties of the soil investigated.

8.5.2 Geometry of the flume

The flume used in the analyses was a conduit of square cross section (2.5mx2.5m) with two trays fixed to the bottom of the central part. The dimensions of the apparatus are shown in Figure 8-15.

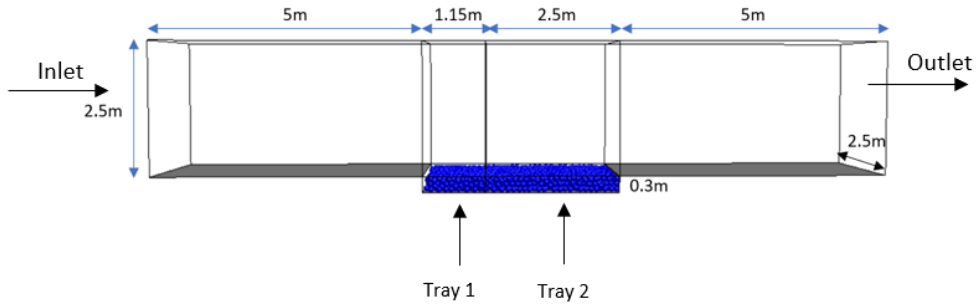

Figure 8-15 Flume geometry in Star CCM+

The trays were designed so that approximately 3 to 4 layers of spheres were arranged in the vertical direction. Tray 1 was located 5m distance from the inflow to distance it from disturbances at the entry boundary condition such that the flow field reaching the trays were as uniform as possible.

Tray 1 was designed to be long enough to contain the eddy (backflow) generated at the start of the tray (Figure 8-16). This tray was modelled only with the purpose to contain the backflow eddy that takes place at the entry step.

The shear stresses that initiated the mass failure were obtained at the surface of tray 2 (Figure 8-16 in red), where the flow is uniform. The dimensions of tray 2 correspond to the maximum number of particles that can be analysed in a reasonable amount of time. Approximately 2500 particles were placed in tray 2.

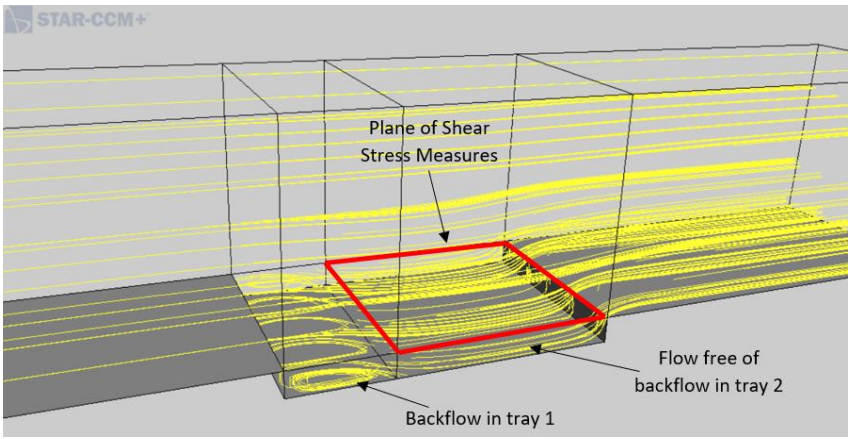

Figure 8-16 Streamlines at tray 1 and 2 in the flume test

8.5.3 Data collection

The numerical experiments in the flume test were carried out with the tray full of particles simulating chalk clasts for Grade D_c chalk and soil peds for clay-like soils. The parameters introduced in the numerical model to simulate both types of soils were bulk unit weight of soil peds or chalk clasts, angle of static friction, coefficient of restitution, Poisson's ratio, Young's Modulus and coefficient of rolling resistance.

It should be noted that in the analysis of slope failures using DEM, there are a number of particle parameters involved that require elaborated techniques to obtain the highest level of accuracy. Representative parameters are normally used for the analysis of slope failures rather than trying to replicate the different characteristics of every particle involved (Zhao, 2014).

The Young's Modulus, bulk density, angles of static friction and Poisson's ratios were obtained independently for Grade D_c chalk and clay-like soils from the literature and existing ground investigations carried out across the UK (see Chapter6:).

A summary of the range of parameters used in the analyses for Grade D_c chalk and clayey soils is shown in Table 8-3 (see Chapter6: for more information).

Table 8-3 Particle parameters used for the calculation of the critical shear stress

Grade D_c chalk			
γ_{bulk} (kN/m3)	$\emptyset'_{\mu}$	v	$E\ (GPa)$
16.1-22.9	29°-39°	0.24-0.32	2.5-10.9
Clay-like soils			
γ_{bulk} (kN/m3)	$\emptyset'_{\mu}$	v	$E\ (MPa)$
15-23	15-38	0.2-0.3	2-33

8.5.4 Boundary conditions

The boundary conditions were designed to replicate the close conduit illustrated in Figure 8-17. The boundary where the flow enters the flume is modelled as 'velocity inlet'. The outflow is modelled as 'atmospheric pressure outlet'.

The bottom boundaries were smooth because the application of roughness here does not influence the calculation of the critical shear stress, and a smooth bottom results in less disturbance of the flow when it reaches the tray. Side walls, the entry step wall and the ceiling, are modelled as symmetry planes avoiding local disturbances of the flow.

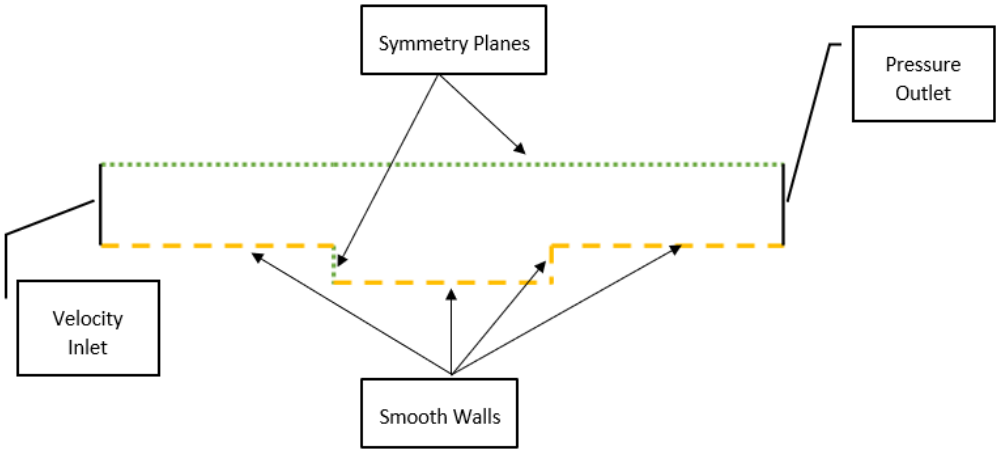

Figure 8-17 Schematics of the boundary conditions at the flume test

8.5.5 Meshing

The mesh comprised hexahedral elements with an average side length of 15cm (Figure 8-18). Meshes with side lengths less than or equal to the particles diameter were found to present convergence problems.

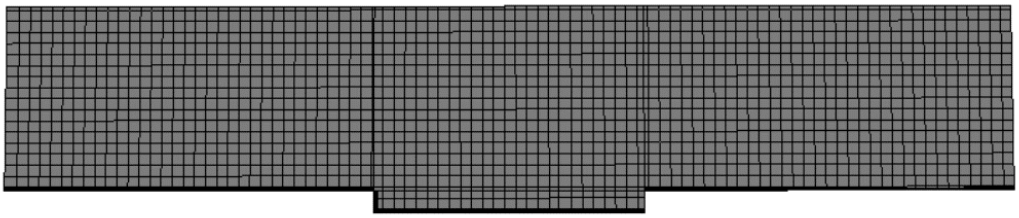

Figure 8-18 Hexahedral mesh used in the analyses

A fine mesh was implemented at the bottom of the flume so that the centroid of the first row of cells were within the log-law region ($30 < y_p^+ < 300$). The velocity of the flow at the initiation of particle movement depended on the slope angle. Since the thickness of the log-law region depends on the velocity of the flow, the resolution of the mesh in the near wall region was adjusted for each analysis so that y_p^+ is within the range $30 < y_p^+ < 300$. Example values of y_p^+ that meets the criterion are illustrated in Figure 8-19.

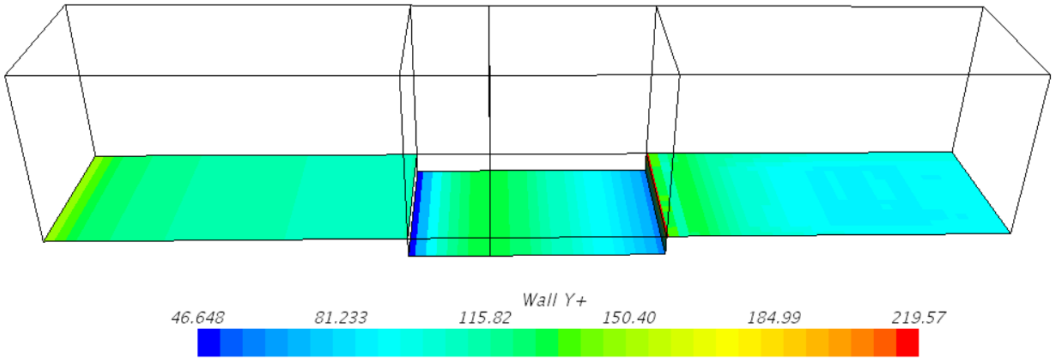

Figure 8-19 Near the wall y^+ distances meeting the y+ criterion

8.5.6 Model configuration in STAR CCM+

All the analysis involving CFD-DEM was carried out in STAR-CCM+, (2017) using the Realizable k–ε turbulence model. This model was chosen in this thesis since it has become the most proven, well-quantified and widely-documented of all turbulence models (Wasserman, 2016).

To solve the governing equations of the flow fields, the segregated flow model for the simulation of runoff was used in preference to the coupled flow model.

The segregated flow model utilises a smaller system of equations than the coupled flow model. As a consequence, the computational cost is vastly reduced with little compromise of the accuracy (Honorio and Maliska, 2014).

The Realizable $k-\varepsilon$ turbulence model with a high y^+ wall treatment was used to model the turbulent flow owing to its better performance compared with other RANS turbulence models.

The simple implicit algorithm was used for the flow phase, which is more stable than the explicit and the PISO algorithms (STAR-CCM+, 2017; FLOW 3D, 2016).

The time step for perceiving collision between a particle and its adjacent should be less than the time it takes for the Rayleigh wave to transverse the minimum size particle in the assembly (Ning and Ghadiri, 2006; Afkhami et al., 2015). The Rayleigh time step equation for the calculation of the minimum time step to prevent numerical instabilities and nonphysical results is given by (8. 4) proposed by Thornton and Randall, (1988) with time steps Δt usually selected equal to 10– 20% of the critical time step Δt_c.(Yan et al., 2015; O'Sullivan and Bray, 2004).

$$\Delta t_c = \pi r_p \frac{\sqrt{\rho_p / G_p}}{0.1631\nu + 0.8766} \quad (8.\ 4)$$

Where

r_p =radius of the particle;

ρ_p =particle density;

G_p =particle shear modulus $[E = 2G(1+\nu)]$;

ν =Poisson's ratio.

For the fluid solver, the maximum time-step is given by the Courant Number (Niyogi et al., 2006):

$$C = \frac{u\Delta t}{\Delta x} \leq 1 \quad (8.\ 5)$$

The critical time-steps were calculated according to equations (8. 4) and (8. 5).

For the flow solver considering a maximum fluid velocity of 5 m/s and the minimum cell side of 5cm:

$$\Delta t \leq \frac{\Delta x}{\mathrm{u}} \quad (8.\ 6)$$

$$\Delta t \leq \frac{0.05}{5} = 0.01s$$

For the DEM solver, different time steps are required for Grade D_c chalk and clayey soils.

For matrix dominated clay-like soils, the maximum allowable time step (Δt) was calculated considering γ_{bulk} = $15kN/m^3$, E=33MPa and ν=0.3 and by applying (8. 7):

$$G = \frac{E}{2(1+\nu)} \quad (8.\ 7)$$

Substituting E and ν for their respective values

$$G = \frac{33000000}{2(1+0.3)} = 12692307Pa$$

And from (8. 4):

$$\Delta t_c = 3.14 \cdot 0.05 \cdot \frac{\sqrt{\frac{1500}{12692307}}}{0.1631 \cdot 0.3 + 0.8766} = 0.0018s$$

Considering the selected time-step as 10% of the Δt_c the maximum time step for clayey soils was obtained:

$$\Delta t = 0.1 \cdot 0.0018s \approx 0.00018s$$

For Grade D_c chalk, the maximum allowable time step (Δt) was calculated considering $\gamma_{bulk} = 23\mathrm{kN/m^3}$, $\mathrm{E} = 10.9\mathrm{GN/m^2}$, ν=0.32

$$G = \frac{10900000000}{2(1 + 0.32)} = 4128787879Pa$$

$$\Delta t = 3.14 * 0.05 \cdot \frac{\sqrt{\frac{1500}{4128787879}}}{0.1631 \cdot 0.32 + 0.8766} = 0.000102s$$

Considering the selected time-step as 10% of the Δt_c, the maximum time step for Grade D_c chalk was obtained

$$\Delta t = 0.1 \cdot 0.000102s \approx 0.0000102s$$

All the calculations were carried out using a time step for the flow solver of 0.000001s that is one order of magnitude lower than the limit.

8.5.7 Methodology for the calculation of the critical shear stress

The methodology for the calculation of the critical shear stress in CFD-DEM follows a six steps algorithm:

1. The flume was 'tilted' by modifying direction of the gravity force vector.
2. A porous membrane was temporarily placed at the interfaces trays-flume to prevent particles moving out of the tray. The CFD solver was frozen and the trays filled with the maximum number of particles as shown in Figure 8-20. To achieve the maximum density of particles, the angle of static friction and the coefficient of rolling resistance were set to zero during filling.

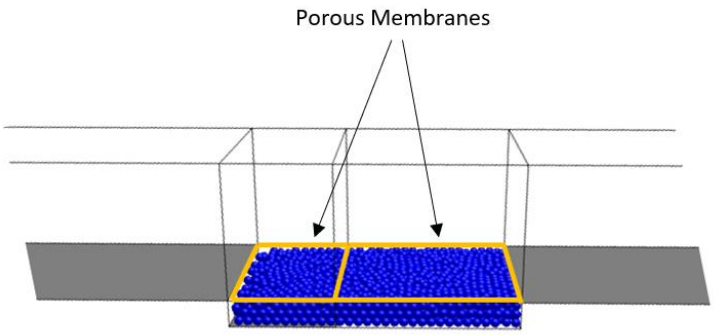

Figure 8-20 Trays filled with particles before the flow is started

3. Once the trays were filled with particles, enough time was allowed for the particles to stop moving. Then, the angle of static friction and the coefficients of rolling resistance were assigned to the particles, and the porous membranes at the interfaces trays-flume were removed. Following that, the DEM solver was frozen, and the CFD unfrozen. A low velocity flow was imposed at the beginning of the analysis until a steady condition was reached (Figure 8-21).

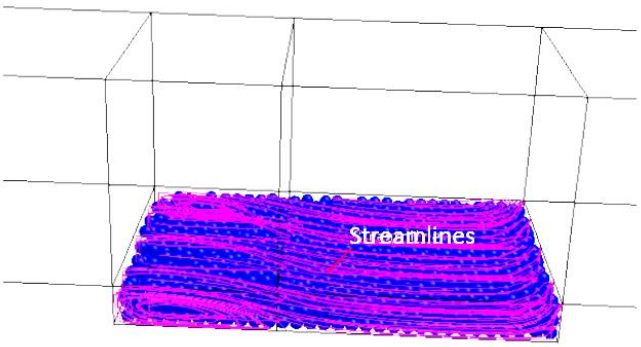

Figure 8-21 Streamlines of steady turbulent flow

The DEM solver was then unfrozen and the particles started interacting with the fluid.

4. If groups of particles started moving out of tray 2 (Figure 8-22), the surface averaged shear stress at the interface tray 2-flume was recorded as the critical shear stress for the specific slope angle. The algorithm was then terminated.

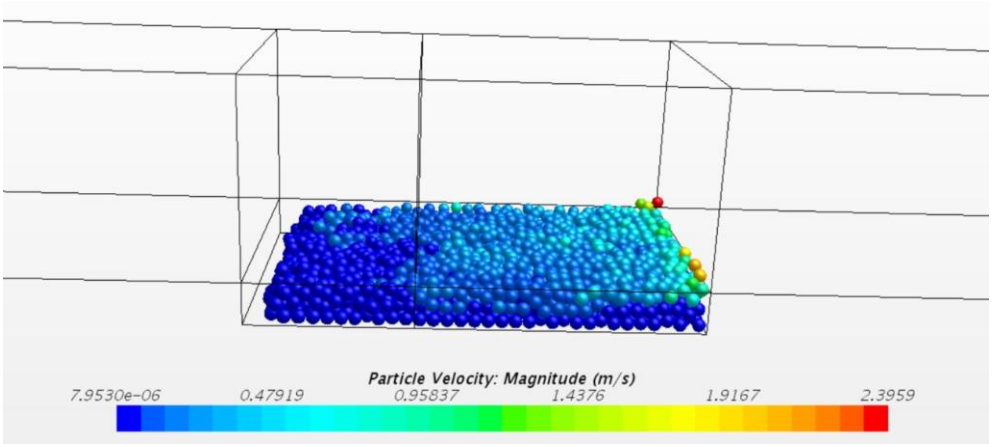

Figure 8-22 Generalised mass movement of particles at the critical shear stress

5. If particles did not move out of the tray, the DEM solver was frozen, the inlet flow velocity was increased and the CFD run until reaching a steady state. After that, the algorithm was returned to step number 4.

The shear stress at the interface tray-flume was calculated according to the Bousinessq hypothesis at the interface between tray 2 and the flume:

$$\tau_{xz} = (\mu + \mu_t)\frac{\partial u_x}{\partial z} \quad (8.\ 8)$$

Where

x is the direction of the flow;

z is the direction perpendicular to the flow;

τ_{xz} is the shear stress acting parallel to the interface tray-flume.

An example of the representation of the shear stress in STAR-CCM+ is illustrated in Figure 8-23.

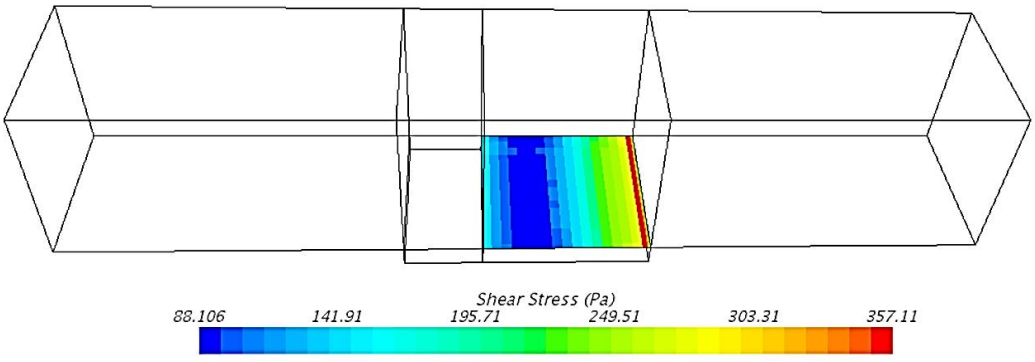

Figure 8-23 Threshold Shear Stress at the interface tray 2-flume for a 45 degrees chalk bed

8.6 Validation

Validation of the numerical model (i.e.CFD-DEM) for the calculation of the critical shear stress that initiates the mass failure was carried out following the experiment conducted by Gregoretti, (2000). The experiment consisted in the calculation of the critical shear stress that initiates the mass failure in a laboratory flume test inclined at 20° with a tray full of 34mm in diameter gravels. More details about the experiment can be obtained in Gregoretti, (2000).

The experiment was replicated in STAR CCM+ using CFD-DEM as follows:

a) Geometry of the flume and meshing

The same flume described in section 8.3.3. was used for the simulation.

b) Particles parameters

Particle parameters for gravels affecting the critical shear stress were obtained from Gregoretti, (2000).

* Particle diameter (d_p)=34mm, angle of static friction $\emptyset'_\mu$=47.7°, density of gravel particles ρ_p=2600Kg/m^3.

Other particles parameters were obtained from typical values for gravels found un the literature.

* E=3GPa (Kumar et al., 2019), v=0.2 (Kumar et al., 2019).

A coefficient of rolling resistance of 0.1 was used in the analysis.

c) Methodology

The methodology described in Section 8.5.7 was used for the validation of the model. The trays full of particles 34mm in diameter are presented in Figure 8-24.

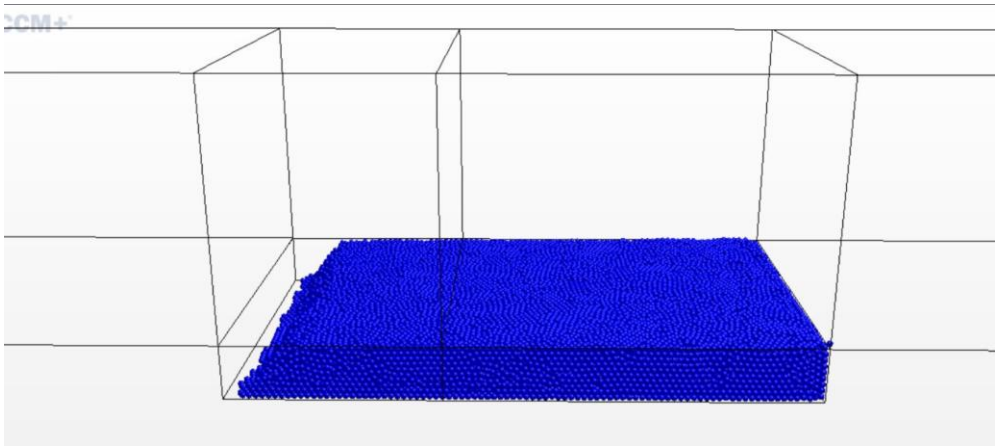

Figure 8-24 Tray full of particles at the start of the validation model

The velocity of the flow was increased from 0.2m/s in steps of 0.2m/s until the mass failure took place at 2.8m/s corresponding to a shear stress of 52.5Pa (see Figure 8-25).

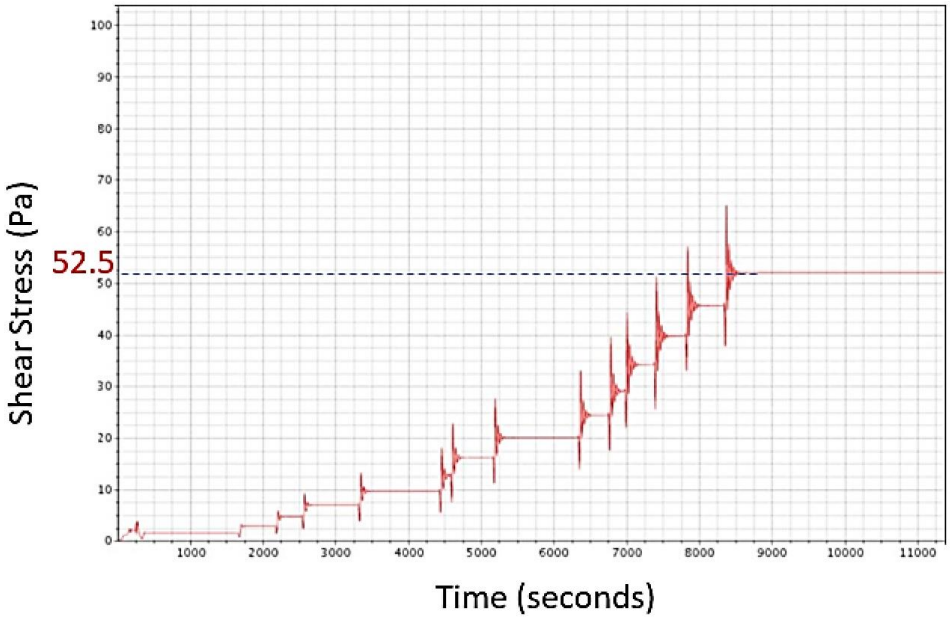

Figure 8-25 Shear stress analysed at different flow rates

d) Results

The mass failure took place at a critical shear stress of 52.5 Pa. A circular shape defining the failure was observed as illustrated in Figure 8-26.

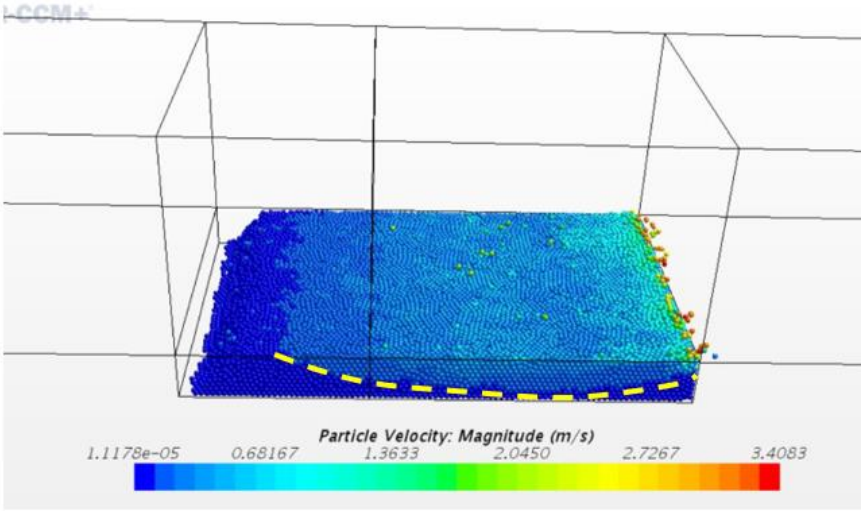

Figure 8-26 Mass movement of particles at the critical shear stress

The critical shear stress obtained is in agreement with the experiment conducted by Gregoretti, (2000) who obtained a critical shear stress of $\sim 52\text{Pa}$.

8.7 Sensitivity analysis

For the calculation of the relationship between the slope angle and the critical shear stress, a number of particle parameters are introduced in the DEM model: Young's Modulus, Poisson's ratio, angle of static friction, particle density, particle diameter, coefficient of rolling resistance and restitution coefficient.

The influence of these parameters on the relationship between the slope angle and the critical shear stress is analysed in this section.

Effect of Young's Modulus, Poisson's ratio, and restitution coefficient

Young's Modulus, Poisson's ratio, and restitution coefficient did not show any influence in the critical shear stress.

Effect of the bulk unit weight and the angle of static friction

The curves critical shear stress vs slope angle were calculated for all possible combinations of a series of selected γ_{bulk} and $\emptyset'_{\mu}$ values.

For the bulk unit weight, γ_{bulk}=15kN/m^3 (the lower boundary value encountered in clay-like soils), 19 kN/m^3 and 23kN/m^3 (the upper boundary value encountered in Grade D_c chalk and clay-like soils) were used in the analysis.

For the angle of static friction, $\emptyset'_{\mu}$=15° (the lower boundary value encountered in clay-like soils), 23° (Beaminster), 31° (St Bees) and 39° (the upper boundary value encountered in Grade D_c chalk were used in the analysis.

The sensitivity analysis was carried out using particle diameter=10cm and μ_r=0.1.

The resulting chart critical shear stress vs angle of the cutting is presented in Figure 8-27.

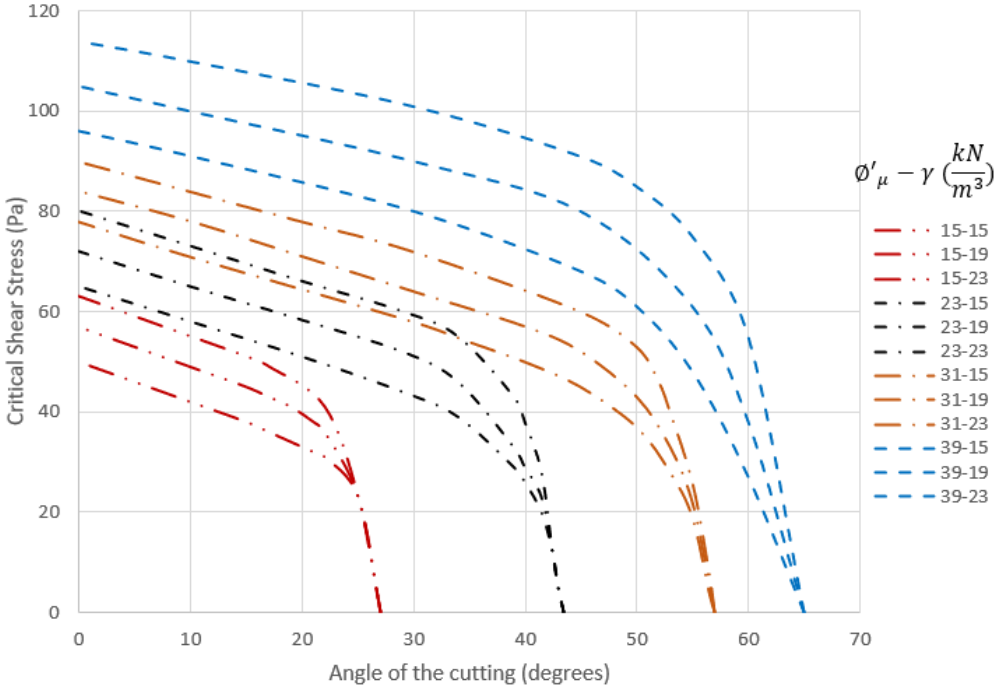

Figure 8-27 Critical shear stress vs cutting/slope angle for different angles of static friction

Regarding $\emptyset'_\mu$, for a constant value of γ_{bulk}, higher values of the angles of static friction resulted in higher values of the critical shear stress for a given slope angle, while maintaining the shape of the curve (Figure 8-27).

Regarding γ_{bulk}, for $\emptyset'_\mu$=15° the critical shear stress remains the same (overlap) for γ_{bulk}=15kN/m^3, 19 kN/m^3 and 23kN/m^3 in the range of cutting angles (24°-27°) near the ultimate angle of the cutting (27°). For lower values of the cutting angle, the critical shear stress is higher the higher is γ_{bulk} but the curves are approximately parallel.

For values of $\emptyset'_\mu$=23° the trend remains similar but the range of cutting angles where the curves overlap is narrower (42.5°-43.5°).

Finally, for values of $\emptyset'_\mu$=31° and $\emptyset'_\mu$=39°, the only point where the curves overlap for γ_{bulk}=15kN/m^3 ,19 kN/m^3 and 23kN/m^3 is at the ultimate angle of the slopes (57° for $\emptyset'_\mu$=31° and 65° for $\emptyset'_\mu$=39°.

Effect of particle diameter

The chart critical shear stress vs angle of the cutting/slope was obtained for particles with values γ_{bulk}=23kN/m^3, $\emptyset'_\mu$=39° and particles diameter of 10cm and 6cm (Figure 8-28).

The results show that for smaller particles, the critical shear stress is lower as a result of lower lifting forces needed to initiate the dislodgement of particles. The reduction in particle diameter from 10cm to 6cm had the same effect as a reduction in $\emptyset'_{\mu}$ from 39° to 31°.

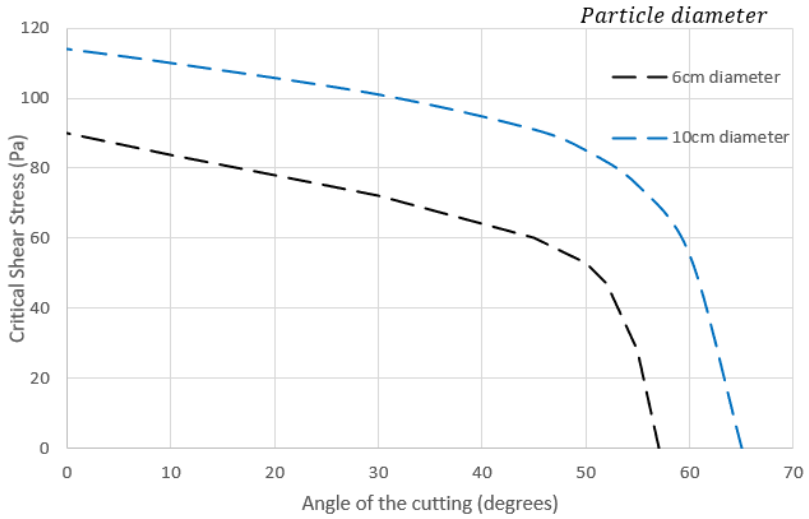

Figure 8-28 Critical shear stress vs cutting/slope angle for different particle diameters

Effect of the coefficient of rolling resistance μ_r

The sensitivity analyses carried out before, where done for a coefficient of rolling resistance μ_r=0.1. For γ_{bulk}=2300Kg/m^3, $\emptyset'$=39° and particles diameter of 10cm, a reduction of μ_r from μ_r=0.1 to μ_r=0.055 resulted in the same chart as Figure 8-28. The reduction of μ_r had a similar effect as the reduction in $\emptyset'_{\mu}$ or the particle diameter.

8.7.1 Discussion

A design chart critical shear stress vs slope angle has been calculated for different combinations of γ_{bulk} and $\emptyset'_{\mu}$ considering d_p=10cm and μ_r=0.1.

The particles diameter (d_p) presents a high degree of uncertainty. However, it has been proved from the sensitivity analysis that variations in d_p do not modify the shape of the curves. Calculating the correct values of d_p for the assessment of slope stability against runoff generated debris flows would be ideally carried out through calibration of the model. However, calibration against natural slopes and transportation cuttings is not feasible since the critical shear stress at the moment of failure is unknown unless measurement equipment is installed previous to the day of failure.

In this thesis, values of d_p=10cm and μ_r=0.1 have resulted in a good performance of the novel method when assessing the vulnerability of real case studies.

8.8 Design charts

From the numerical experiments carried out following the methods in section 8.4 and section 8.5, the design chart for the application of the novel method have been obtained.

a) Chart bed shear stress vs flow rate

This chart has been obtained from the application of section 8.4, and is used for the derivation of the actual shear stress from the flow rate. This chart is to be used for the RRM and is presented in Figure 8-29.

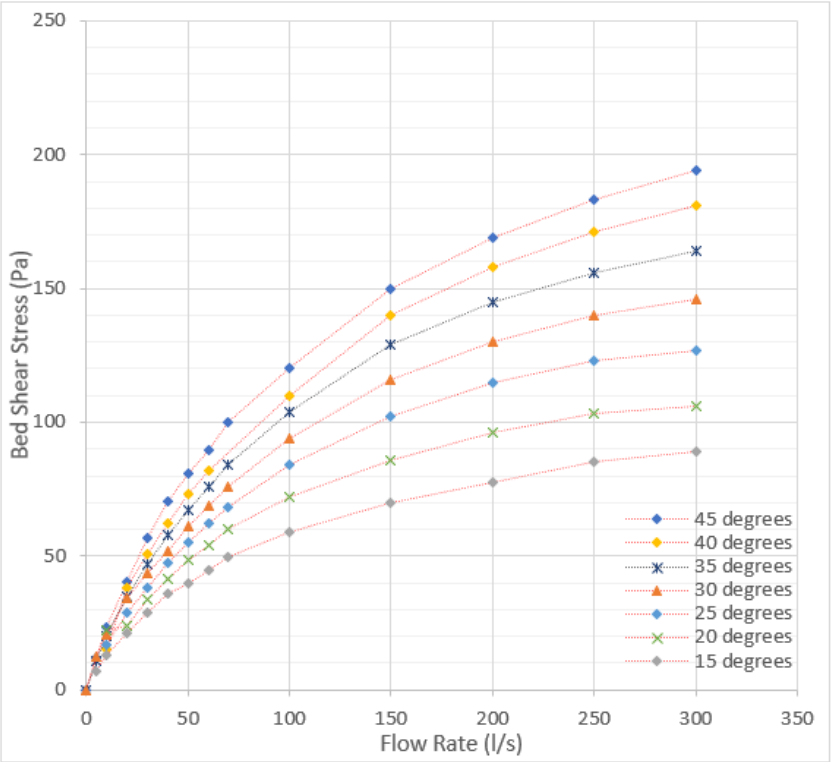

Figure 8-29 Relationships flow rate-bed shear stress

As expected, the higher the flow rate at the crest of the cutting, the higher is the shear stress that surface runoff apply over the cutting face. For the same flow rate, the shear stress at the cutting face is also higher at higher slope angles due to the increase in flow velocity.

b) Critical shear stress vs slope angle

This chart has already been presented in the sensibility analysis (Figure 8-27) and is to be applied for both the DNM and the RRM methods.

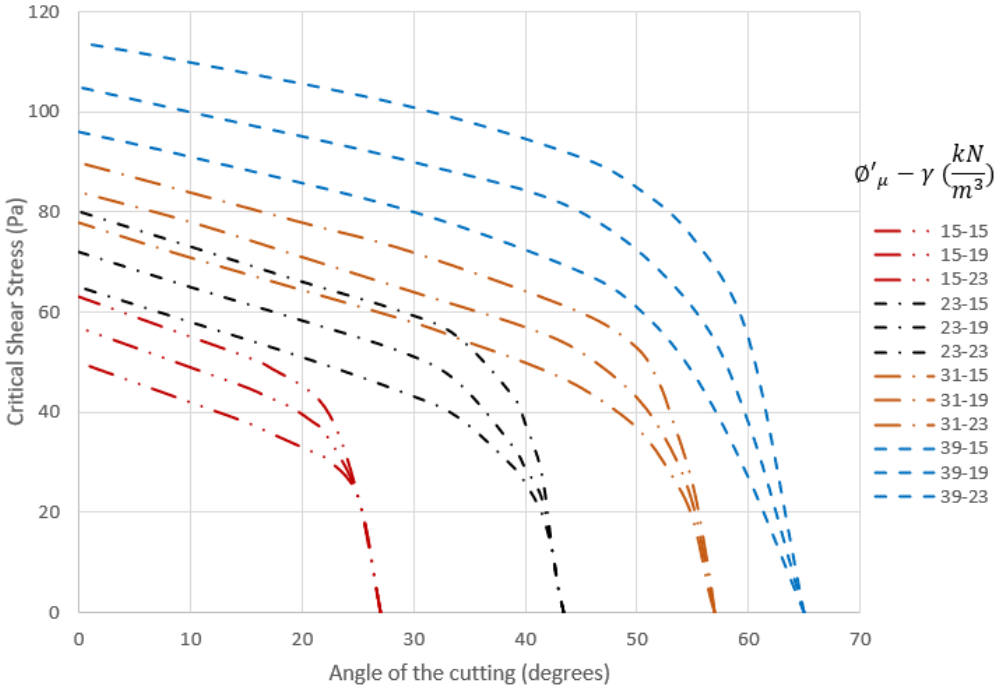

Figure 8-27 bis. Critical shear stress vs slope angle for different angles of static friction

8.8.1 Discussion

The chart flow rate vs bed shear stress shows an exponential reduction in the increase rate of shear stress with the flow rate, becoming significantly flatter at flow rates of 300 l/s. This may be attributed to the water reaching a terminal velocity where increases in flow rate would result in increasing flow depths but the same velocity.

From the chart critical shear stress vs slope angle, it can be concluded that for values of $\emptyset'_\mu$= 15° and 23° and for angles of the cutting near the ultimate angle (i.e. where particles collapse without the presence of runoff), the mechanism of failure is mostly by sliding and the unit weight has not a considerable effect. At lower angles of the cutting, lifting forces and destabilising torques (rolling) become more important and hence the value of the unit weight have a higher effect on the critical shear stress that initiates the mass failure.

For higher values of $\emptyset'_\mu$ (i.e. $\emptyset'_\mu$=31° and $\emptyset'_\mu$=39°), resisting sliding forces are higher and lifting and rolling are more relevant in the mechanism of failure. The results obtained in Figure 8-27, agree relatively well with the results obtained by Gregoretti, (2000) for gravels and angles between 12.5° and 20° where not a substantial difference of critical shear stress was expected.

8.9 Discussion

A novel method for the assessment of the stability of slopes against runoff generated debris flow has been introduced in this chapter. The method is based on the use of the critical shear stress as the parameter that triggers the mass failure of the sloping bed.

The novel method proposed has been designed from the combination of distinct areas of research (i.e. Navier Stokes equations for turbulent flows, shallow water equations, discrete element methods and CFD-DEM).

Shallow water equations have been implemented in the model to calculate the actual bottom shear stress during a rainfall event. This approach has been used before using a number of debris flow software (e.g. DAN, DAN3D, EDDA 2.0, FLATModel)

The most important factor in the initiation of debris flow is the critical shear stress. Most of the existing computer debris flow related software, do not simulate the initiation of runoff generated debris flows. Instead, they estimate an erosion rate in the flowing water until a predetermined concentration of soil is achieved (e.g. DAN, DAN3D, EDDA 2.0).

This latter approach has been applied to debris flows that develop by entrainment and accumulation of eroded soil during the water flow along long distances (Liu and He, 2020).

The novel method, uses a new approach based on the observations by Gregoretti, (2000) that distinguished the onset of particle movement from the mass failure (runoff generated debris flow) that occurs at higher shear stresses.

Two variants of the method were introduced: DNM that uses the shallow water equations to obtain the actual shear stress at the cutting face during a rainfall event, and the RRM method that uses the catchment area to obtain the actual shear stress.

The DNM should result in more accurate values to obtain the bed shear stresses since shallow water equations are applied over 1M DTM simulating the ground surface. The RRM assumes that water flowing down the cutting face is 1m wide and inaccuracies are expected when water flows down the cutting extending more or less than 1m wide. Numerical CFD-DEM flume experiments were designed to obtain the critical shear stresses initiating the mass failure in transportation cuttings for different slope angles and soil properties.

From the sensitivity analysis, the only factors in CFD-DEM that affect the critical shear stress are the unit weight, the diameter of particles, the angle of static friction and the coefficient of rolling resistance. Differences in soil plasticity have not been observed to have an effect in the critical shear stress.

The critical shear stress vs slope angle chart was designed for soils with different values of γ_{bulk} and $\emptyset'_{\mu}$. μ_r=0.1 was used in the analysis as recommended in the literature and a value of d_p=10cm.

Several attempts were made for different values of d_p until coming to the value of d_p=10cm that successfully assessed the stability of the real case studies in Chapter 9.

Vegetation and soil cohesion were not considered in the novel method. Vegetation cover results in the reduction of runoff shear stress, diminishing the soil erosion potential (Vásquez-Méndez et al., 2010). However, experiments conducted by Chen et al., (2018) showed that the effect of vegetation cover in the reduction of dislodgement of particles is significantly diminished for the case of steep slopes under high intensity short duration rainfall. It is expected that non considering vegetation in steep transportation cuttings will not significantly affect the performance of the method. Cohesion has not been accounted for in the analysis since the soil is assumed to be discretised by shrinkage cracks (Mochtar and Mochtar, 2018) in clay-like soils and cohesion is not expected in superficial Grade D_c chalk. In addition, the not inclusion of these parameters result in a conservative approach for the novel method.

So far, we have put the basis for the new method to analyse runoff generated debris flows. In the next section, real cases were analysed to test the applicability of the novel method.

For each of the cases analysed both the DNM and the RRM were applied to cuttings located at Watford, St Bees, Beaminster and Loch Treig. For the case of Hooley, where cutting failures are recurrent due to excessive steepness, only the critical shear stress vs angle of the cutting design chart was applied.

The assessment of stability was carried out following the 7 steps process described in Table 8-2.

Chapter9: Application to case studies

The proposed novel method to assess the stability of cuttings under surface water runoff was applied to real case studies in transportation cuttings. The purpose of the analyses is to validate the accuracy of the novel method and whether it can be implemented as a tool to determine the vulnerability of cuttings against surface water runoff.

17 cuttings were analysed: 4 stable and 1 failed at Watford Tunnel for Grade D_c chalk, 1 cutting at Watford in conditions prior to earthworks within the catchment, 3 stable and 2 failed cuttings at St Bees in clay-like soil, 2 failed and 2 stable cuttings at Beaminster in clay-like soil, 1 slope failure at Loch Treigh in clay-like soil but not attributed to runoff, and the overall instability of cuttings at Hooley in Grade D_c chalk.

Each case was analysed using the DNM and RRM methods following the steps described in Table 8-2 and the same strict methodology has been followed for each of them.

Calculation of the flow rate in RRM was carried out considering a width value of n=1

9.1 Watford

In this section, the stability of four stable cuttings adjacent to the failed one, as well as the failed cutting itself, are analysed using the DNM and the RRM. Two cases have been analysed at the failed cutting at Watford. 1) the stability of the cutting after the earthworks and 2) the stability of the cutting prior to earthworks.

9.1.1 Stability of the cuttings after the construction of the embankment access

In this section, first the assessment of the area against runoff generated debris flow was analysed using the DNM approach. The same analysis was conducted later using the RRM approach.

Assessment of Cuttings using the DNM Approach

Step 1: Obtain DTM of cutting and catchment

The extension of the catchment analysed and the corresponding 1m DTM are shown in Figure 9-1 left and right respectively. The 1m DTM from 2017 was used in the analysis, it should be noted that at the time the DTM was generated the access to the embankment had been removed. As such, the access was included in the DTM as an obstacle in ArcGIS.

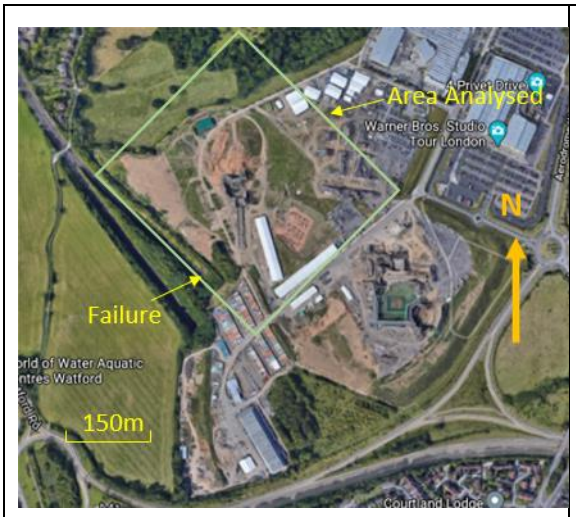

Area Analysed at Watford

(Google Maps, 2016)

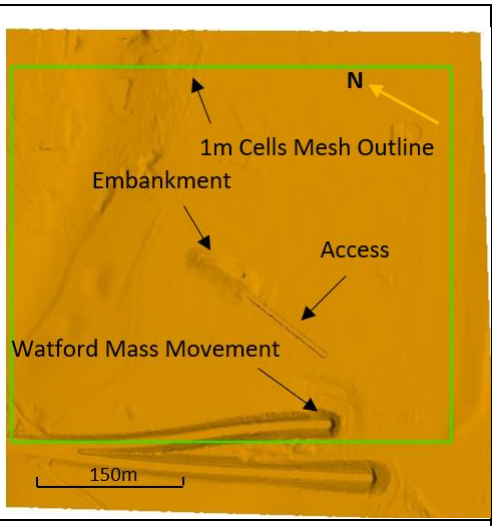

1m DTM of the area analysed at Watford, 2017

Figure 9-1 Area and DTM analysed in the Watford case study

Step 2. Obtain rainfall characteristics (rainfall intensity and duration)

A rainfall of 4-hour duration equivalent to 12.7mm/h, characteristic of short duration-high intensity rainfall events, was recorded at the location where the failure took place. This is the rainfall used in the assessment.

Step3: Calculation of the drainage lines

The drainage lines have been calculated in ArcGIS as described in section 8.7.1. Five locations were analysed: SC1, SC2, SC3, SC4 and FC (SC stands for Cutting Failure and FC for Failed Cutting), corresponding to the outlet of the main drainage lines. The drainage lines are presented in Figure 9-2.

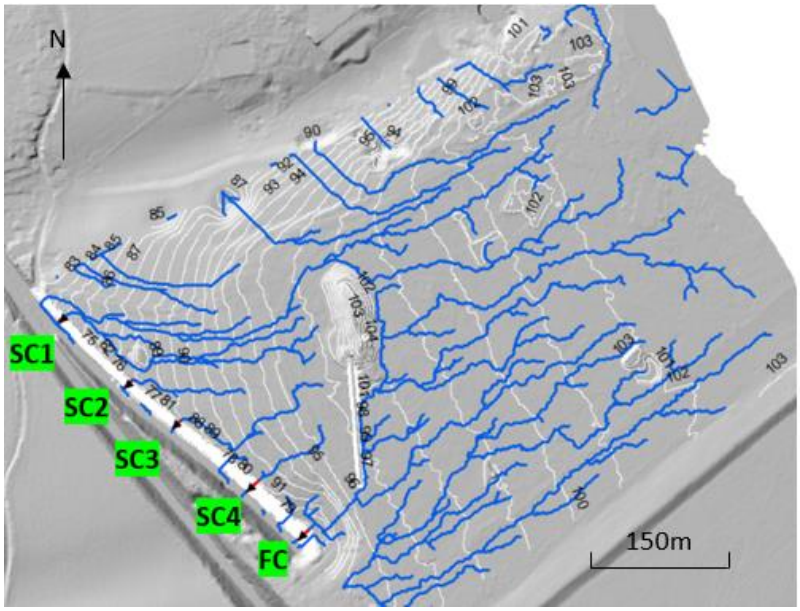

Figure 9-2 Drainage Lines at Watford (ArcGIS)

Step 4 in DNM: Obtain the bottom shear stress at the slope/cutting

The surface shear stress at Watford were obtained in FLOW-3D, and expressed as a colour map (Figure 9-3), which in this particular case shows five locations of the cutting where the shear stresses were higher (red colour represents the areas of higher shear stresses and the blue areas the lower shear stresses).

It can be observed that the cuttings presenting the highest levels of shear stress coincide with the outlets identified in the analysis of the drainage paths (Figure 9-2.

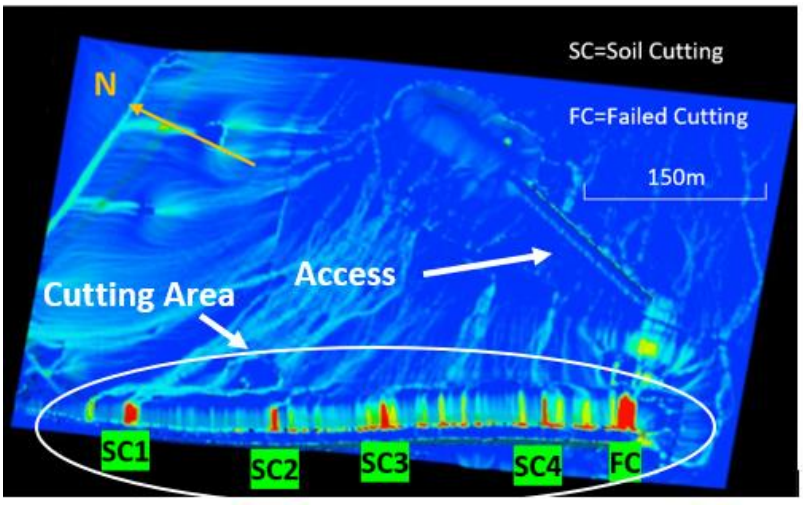

Figure 9-3 Surface shear stress map at Watford

To identify the maximum surface shear stresses at each of the locations obtained, SC1, SC2, SC3, SC4 and FC, each area was isolated so that the results can be seen as shown in

each area was isolated so that the results can be seen as shown in (Figure 9-4). The maximum shear stress at FC has not been isolated since it corresponds to the maximum shear stress overall.

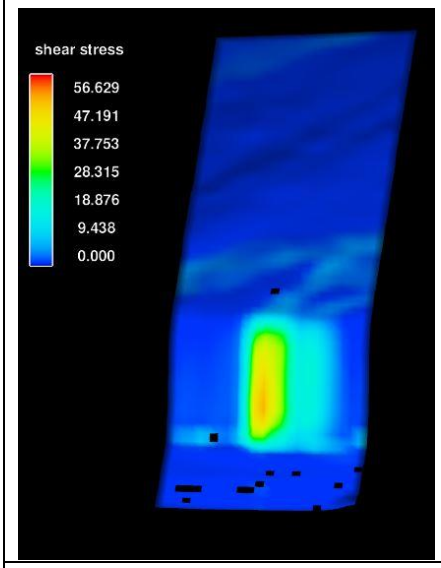

SC1-56.63Pa

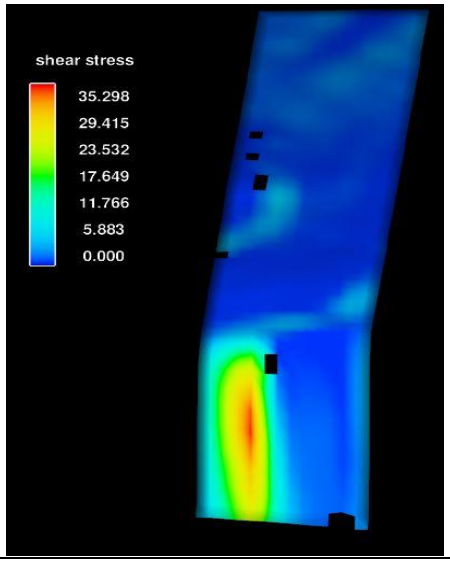

SC2-35.30Pa

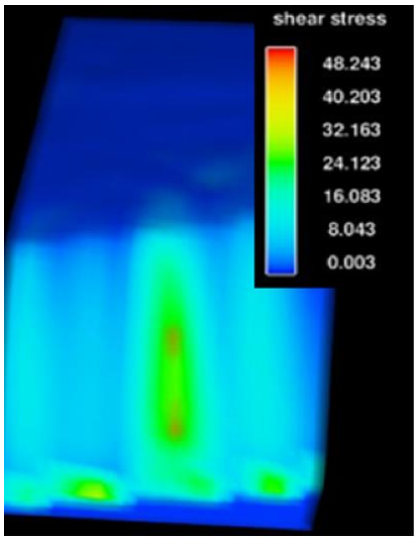

SC3-40.24Pa

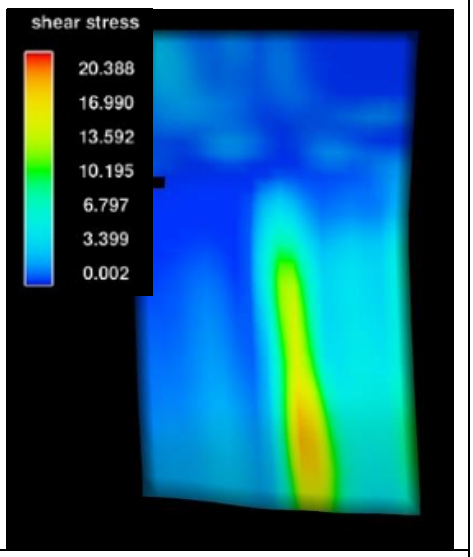

SC4-20.39Pa

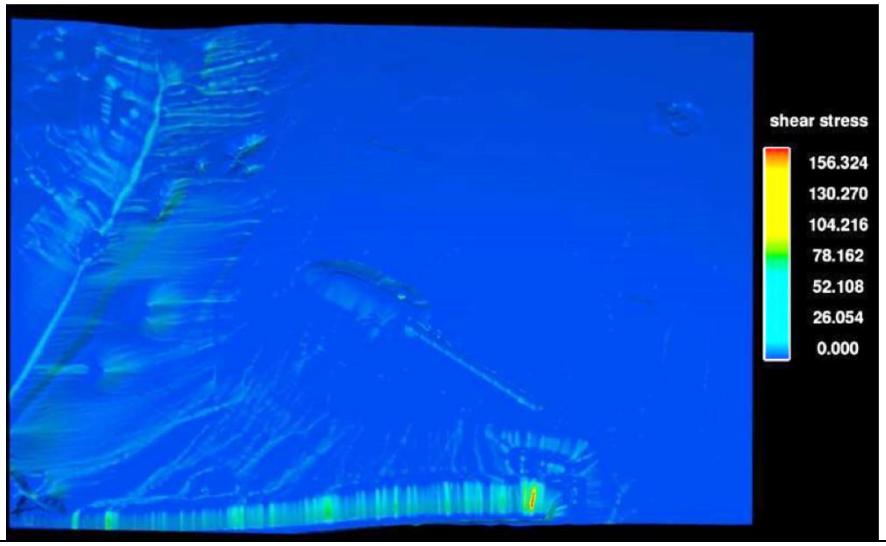

FC=156.32Pa

Figure 9-4 Maximum shear stress of each cutting at Watford after construction of embankment access

Step 5: Calculation of the cutting angles at the selected cuttings

The transversal profiles of the critical areas identified within the cuttings were obtained from ArcGIS following the drainage lines along the faces of the cuttings (shown as red arrows). The location and the profiles themselves are shown in Figure 9-5.

SC1

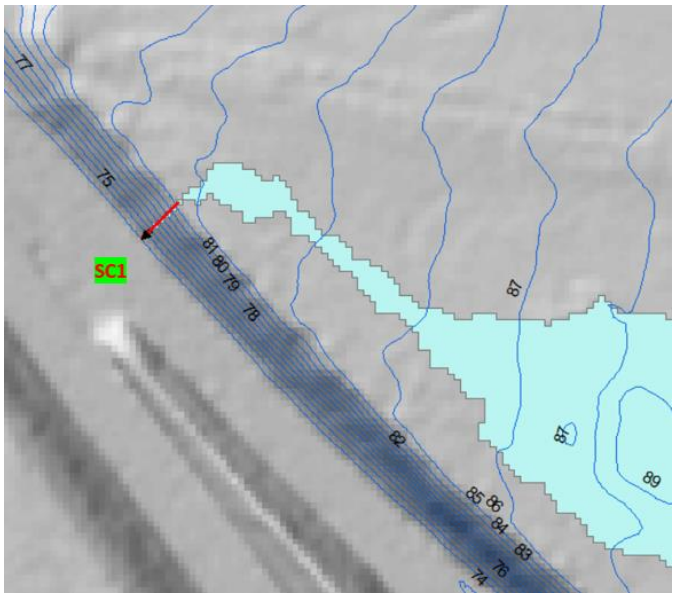

Drainage Line in SC1

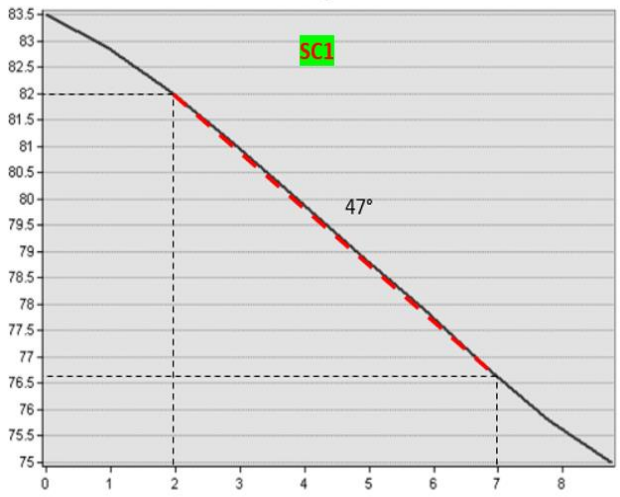

Cutting Profile in SC1

SC2

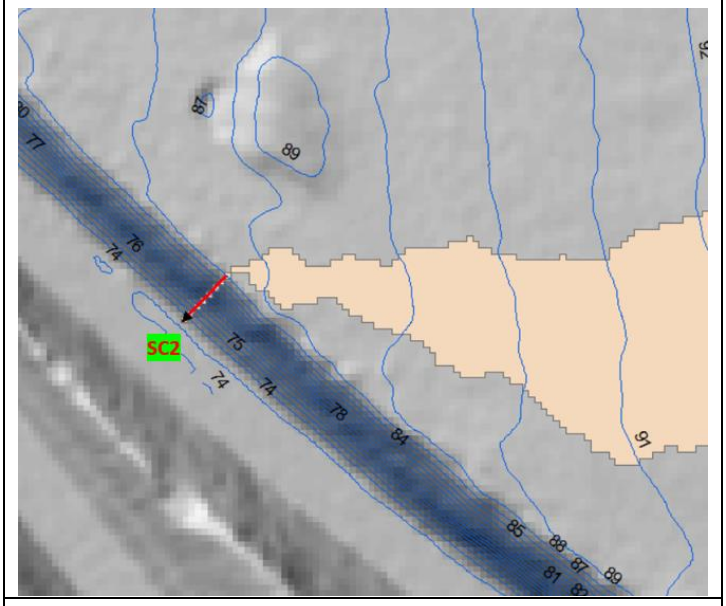

Drainage Line in SC2

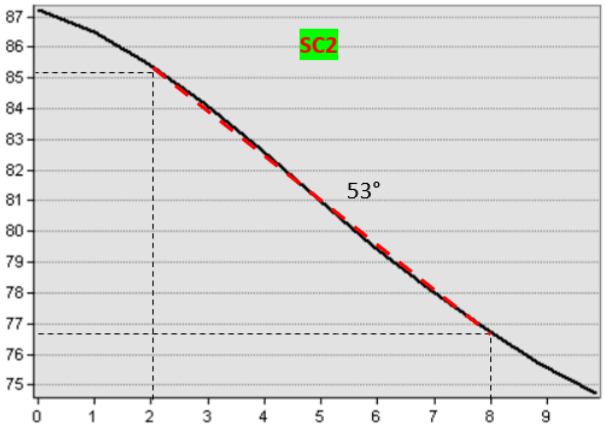

Cutting Profile in SC2

SC3

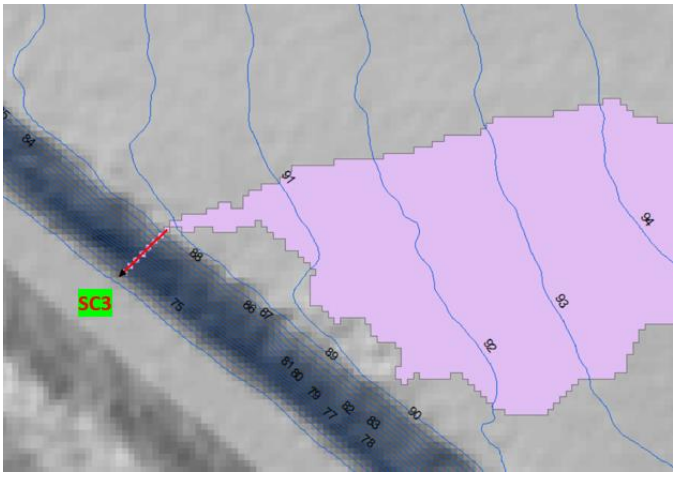

Drainage Line in SC3

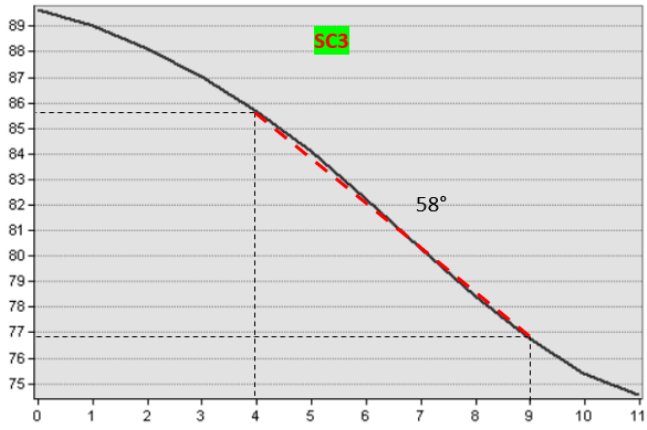

Cutting Profile in SC3

SC4

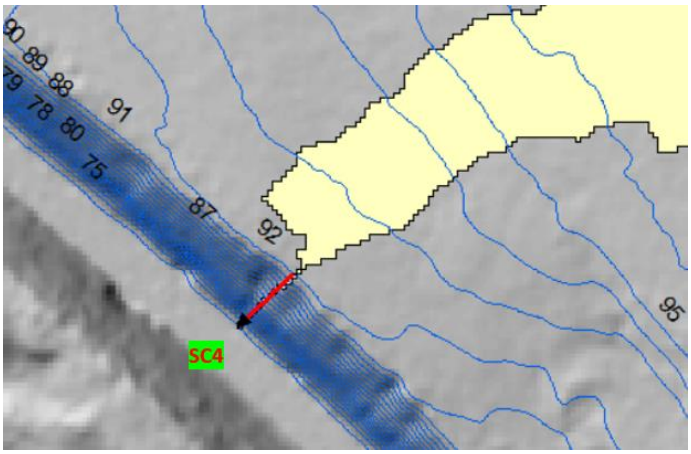

Drainage Line in SC4

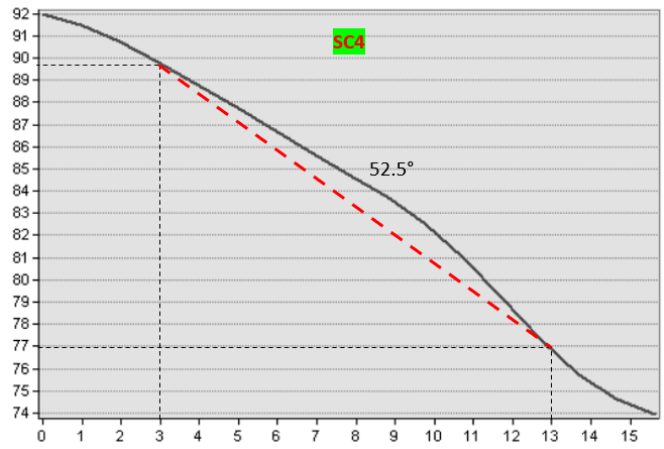

Cutting Profile in SC4

FC

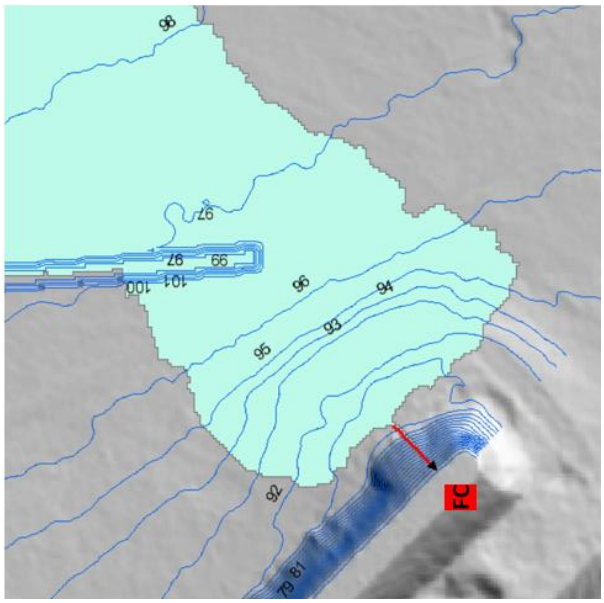

Drainage Line in FC

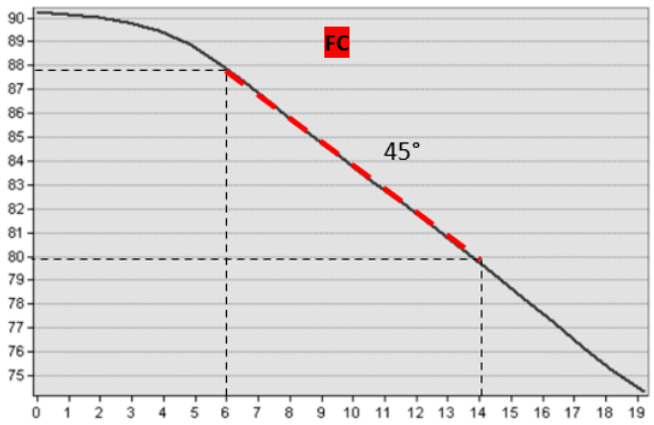

Cutting Profile in FC

Figure 9-5 Average angles of the cuttings at Watford

Step 6: Calculation of the critical shear stress at each slope/cutting

The critical shear stress at SC1, SC2, SC3 and SC4 and FC are presented in Figure 9-6 and Table 9-1 for values of $\emptyset'_r$=39° and γ_{bulk}~19 kN/m³.

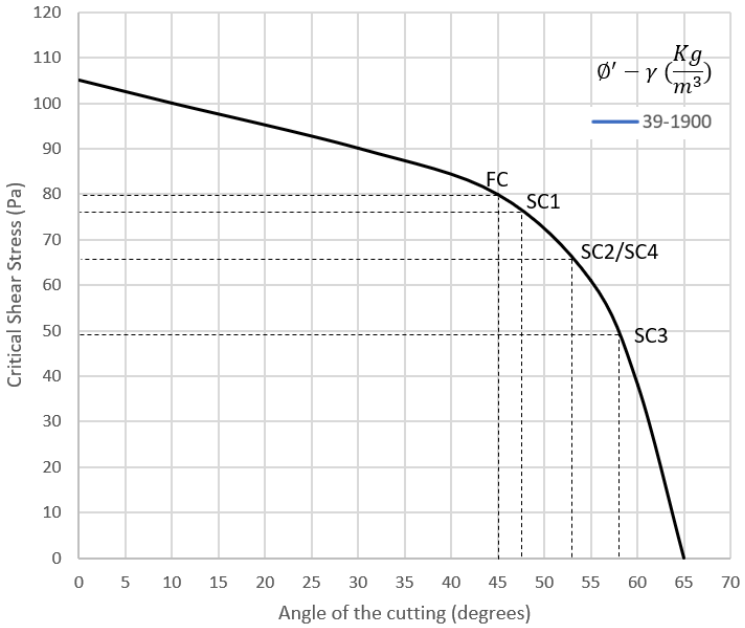

Figure 9-6 Critical Shear Stress at Watford Cuttings

Table 9-1 Critical Shear Stress at Watford Cuttings

Cutting	SC1	SC2	SC3	SC4	FC
Critical Shear Stress (Pa)	76	66	49	66	80

Step 7: Assessment of the stability of the cuttings

Once the critical shear stress and the surface shear stress were obtained for each cutting, the FoS for each critical area was calculated as: FoS=Critical Shear Stress/Actual Shear Stress, and the vulnerability of the cuttings assessed based on whether FoS greater than 1 (cutting stable) or less than 1 (cutting at risk of failure, highlighted in red). The results are presented in Table 9-2.

Table 9-2 Assessment of the stability at Watford using DNM

	SC1	**SC2**	**SC3**	**SC4**	**FC**
Critical Shear Stress	76	66	49	66	80
Actual Shear Stress	56.63	35.30	48.24	20.39	156.32
FoS	**1.34**	**1.86**	**1.02**	**3.25**	**0.51**

Cuttings SC1, SC2, SC3 and SC4 were assessed as stable and FC as vulnerable in agreement with the real outcomes.

Assessment of the stability of cuttings at Watford using the RRM approach

Steps 1,2, 3 and 7 have already been carried out in the DNM approach and therefore not shown in the sections below.

Step 4: Calculation of the catchment area (e.g. using GIS software)

Calculation of Catchment Areas was carried out in ArcGIS as described in section 8.3.2. The results are presented in Figure 9-7. The location where the cutting failure took place presents the largest catchment area. It can be seen that the embankment access modified the natural flow of runoff and contributed to the deviation of superficial runoff to the failed cutting.

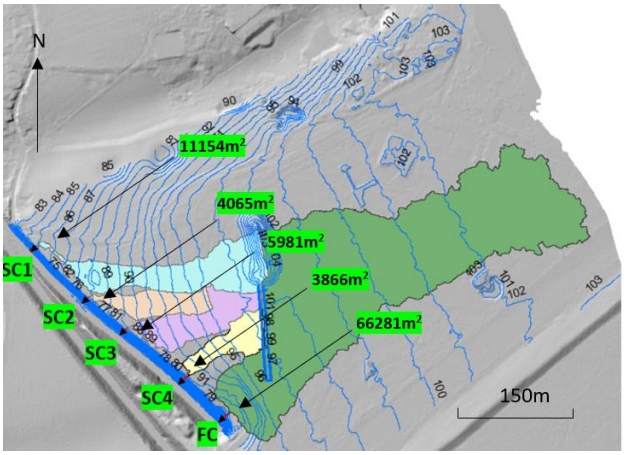

Figure 9-7 Catchment areas at Watford

Step 5: Calculation of the flow rate at the crest of the cutting using Q=IxA/n

Calculation of the flow rate has been obtained considering a width value of n=1

SC1 $$Q_n = \frac{A \cdot I}{n} = 11154m^2 \cdot \frac{0.0125m}{3600s} = 0.038m^3/s = 38l/s \quad (9.\ 1)$$

SC2 $$Q_n = \frac{A \cdot I}{n} = 4065m^2 \cdot \frac{0.0125m}{3600s} = 0.014m^3/s = 14l/s \quad (9.\ 2)$$

SC3 $$Q_n = \frac{A \cdot I}{n} = 5981m^2 \cdot \frac{0.0125m}{3600s} = 0.020m^3/s = 20l/s \quad (9.\ 3)$$

SC4 $$Q_n = \frac{A \cdot I}{n} = 3866m^2 \cdot \frac{0.0125m}{3600s} = 0.013m^3/s = 13l/s \quad (9.\ 4)$$

FC $$Q_n = \frac{A \cdot I}{n} = 66281m^2 \cdot \frac{0.0125m}{3600s} = 0.230m^3/s = 230l/s \quad (9.5)$$

Step 6: Calculation of the bottom shear stress at the slope/cutting from the chart flow rate vs angle of the slope/cutting

From the chart in Figure 8-29 for the slope angles identified in Figure 9-5, the superficial shear stress was obtained for each cutting. The results are presented in Figure 9-8.

<table>
<tr><td>SC1</td><td>SC2</td></tr>
<tr><td> 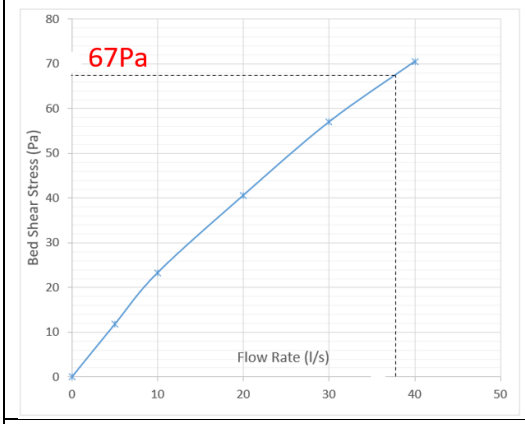
</td><td> 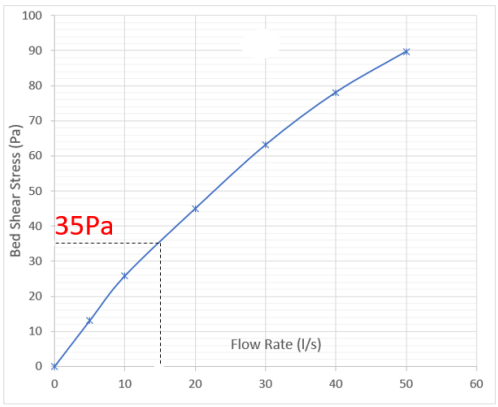
</td></tr>
<tr><td>SC3</td><td>SC4</td></tr>
<tr><td> 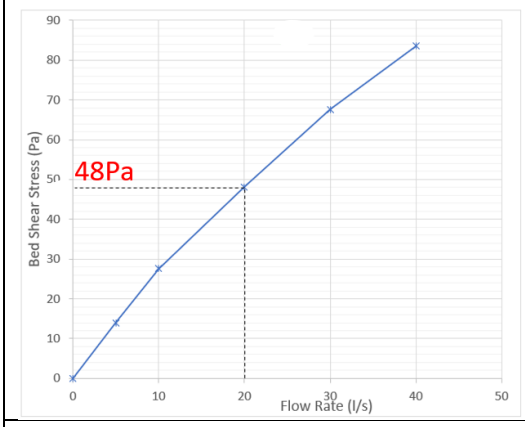
</td><td> 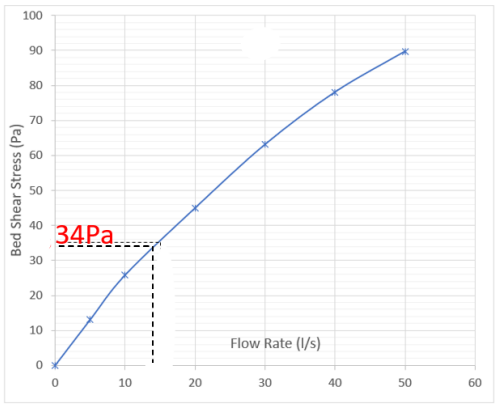
</td></tr>
<tr><td colspan="2">FC</td></tr>
</table>

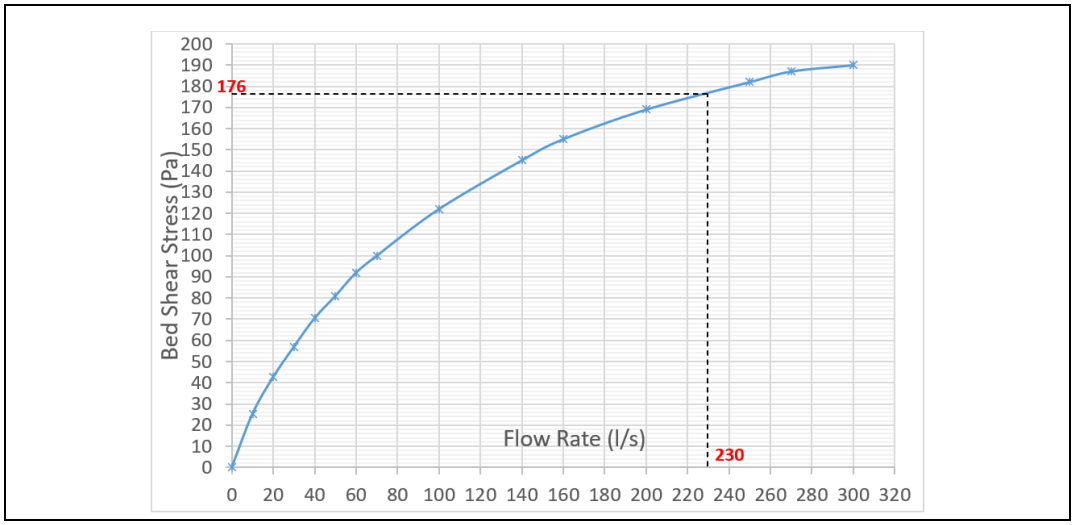

Figure 9-8 Actual Shear Stress at Watford Cutting obtained in RRM

Step 8: Assessment of the stability of the cutting

The vulnerability of the cutting is assessed as described in Step 7 of the DNM method, based on the value of the FoS. The results are presented in Table 9-3.

Table 9-3 Assessment of the stability at Watford using RRM

	SC1	SC2	SC3	SC4	FC
Critical Shear Stress	76	66	49	66	80
Actual Shear Stress	67	35	48	34	176
FoS	**1.13**	**1.88**	**1.02**	**1.94**	**0.45**

Cuttings SC1, SC2, SC3 and SC4 were assessed as stable and FC as vulnerable in agreement with the real outcomes.

The values of the FoS using the RRM approach agreed relatively well with the ones obtained using DNM for SC2 and SC3, but more conservative in SC1, SC4 and FC. The conservatism observed in some of the results is believed to be due to the assumption made for the generation of the chart presented in Figure 8-29 in terms of flow per unit width (width considered as 1m). In this particular case, these results indicate that the actual width may be greater than the 1m considered, which would have an impact on the shear stress values obtained and therefore the FoS.

9.1.2 Assessment of the stability of cuttings at Watford before embankment access

In this section, the stability of the failed cutting was carried out under the same rainfall event but before the construction of the embankment access.

Step 1: Obtain DTM of cutting and catchment

The extension of the catchment analysed and the corresponding 1m DTM are shown in Figure 9-9 left and right respectively. The 1m DTM is the same as in the case before but without the embankment access.

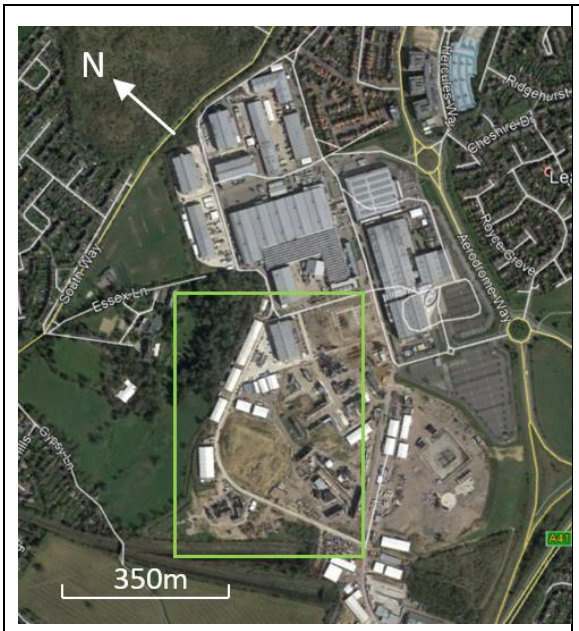

Area Analysed at Watford

(Google Earth, 2020)

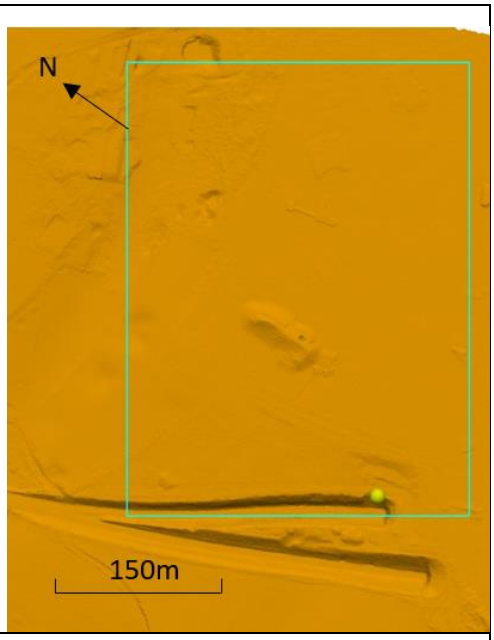

1m DTM of the area analysed at Watford, 2017

Figure 9-9 Catchment area (left) (Google Earth) and 1m digital terrain model (right)

Step 2. Obtain rainfall characteristics (rainfall intensity and duration)

The short duration high intensity rainfall of 12.7mm/h during for hours that took place just before the failure was used in the analysis

Step3: Calculation of the drainage lines

The drainage lines are presented in Figure 9-10. Two drainage lines were identified at the crest of the failed cutting. One line was over the face of the failed cutting (sub-catchment 1) and a second drainage line over the historic masonry wall (sub-catchment 2).

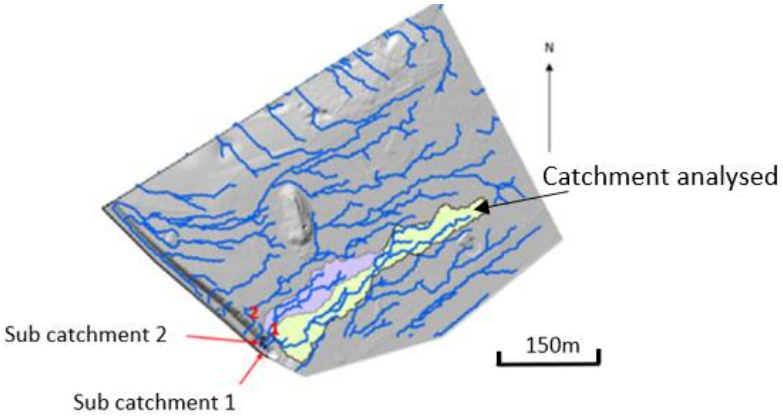

Figure 9-10 Catchment at Watford Cutting before the embankment access

Step 4 in DNM: Obtain the bottom shear stress at the slope/cutting

The surface shear stress at the cutting failure is presented in Figure 9-11. A maximum shear stress at the failed cutting of 77.77Pa was obtained in FLOW-3D. This value is significantly lower than 156.32Pa presented at the same location after the construction of the embankment access.

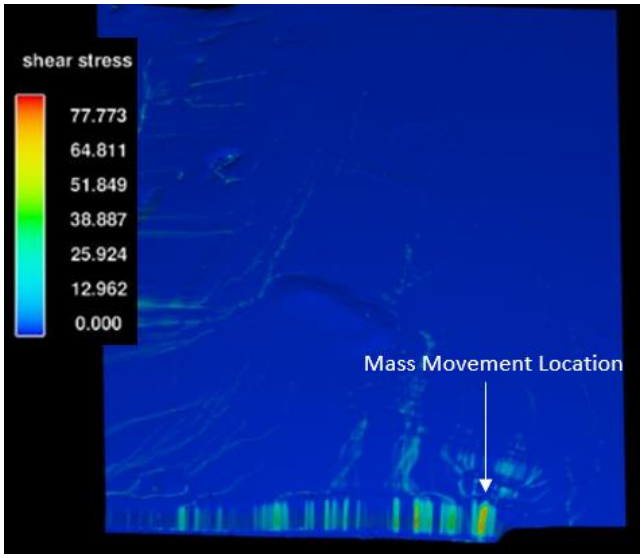

Figure 9-11 Shear stresses before access at Watford

Step 5: Calculation of the cutting angles at the selected cuttings

The profile of the cutting was obtained before in (Figure 9-5)

Step 6: Calculation of the critical shear stress at each slope/cutting

The critical shear stress at the failed cutting remains constant and therefore was obtained from the previous analysis =80Pa (Figure 9-6).

Step 7: Assessment of the stability of the cuttings

Once the critical shear stress and the surface shear stress were obtained, the calculation of the FoS was obtained as:

FoS=80Pa/77.77Pa=**1.03**

The result obtained in DNM indicates that the cutting would have remained stable but in a critical condition should the embankment access had not been constructed.

Assessment of Cuttings using the RRM Approach

Step 4: Calculation of the catchment area (e.g. using GIS software)

The results are presented in Figure 9-12. It can be seen how the catchment area before the construction of the embankment access = 17962m^2 was significantly smaller than the catchment area after the construction of the embankment access = 66281m^2.

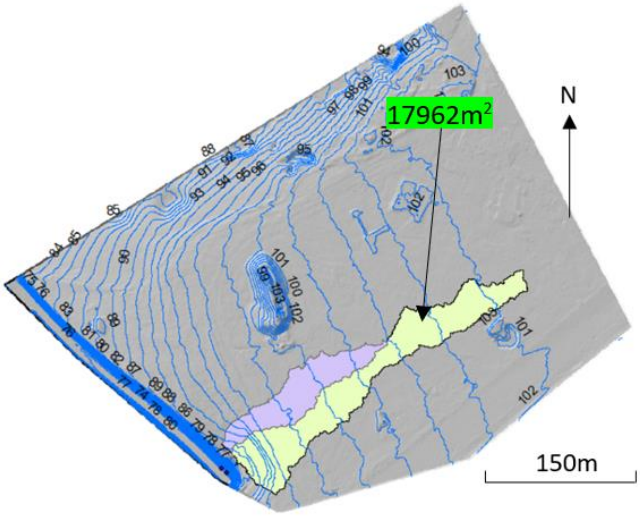

Figure 9-12 Catchment area at Watford Cutting before access

Step 5: Calculation of the flow rate at the crest of the cutting using Q=IxA

SC1 $$Q_n = \frac{A \cdot I}{n} = 17962m^2 \cdot \frac{0.0125m}{3600s} = 0.062m^3/s = 62l/s \quad (9.6)$$

Step 6: Calculation of the bottom shear stress at the slope/cutting from the chart flow rate vs angle of the slope/cutting

From the chart in Figure 8-29 and the soil properties $\emptyset'_r$=39° and γ_{bulk}~19 kN/m^3, the superficial shear stress was obtained for the cutting.

The result is presented in Figure 9-13. The surface shear stress =94Pa is considerably lower than the on obtained after the construction of the embankment access =176Pa.

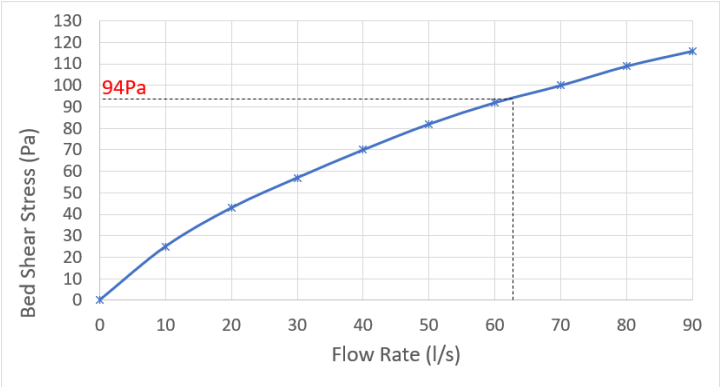

Figure 9-13 Actual Shear Stress at Watford Cutting failure before access in RRM

Step 8: Assessment of the stability of the cutting

Once the critical shear stress and the actual shear tress were obtained, the calculation of the FoS was calculated as:

FoS=80Pa/94Pa=**0.85**

The RRM approach was in this case more conservative than the DNM approach where the FoS=1.03 and considered the cutting as vulnerable to failure.

9.1.3 Conclusion

The construction of the access track along the embankment, built by WB prior to the failure, has been proved to have a significant effect on the contributing catchment area and therefore the surface water flows running towards the crest of the failed cutting. The novel methods agreed well with the real outcomes for the cuttings analysed.

The results for the pre and post access track construction, both considering the same rainfall intensity, show that although the cutting would have been classified as stable in accordance with DNM (FoS>1) pre-track construction, it is clear that the cutting was already very closed to its critical point (FoS =1.03), or vulnerable in accordance with the RRM method (FoS=0.83). In any case, this indicates that any changes which would introduce additional water runoff into the cutting would have had a detrimental effect in the stability of the cutting, as it was proven later on after the construction of the access track and the diversion of additional flows towards an already critical areas which ultimately resulted in the failure of the cutting.

Whether the failure of the cutting would have occurred without the access to the embankment is not possible to predict from the calculations. However, the results show that the cutting was already in a state of potential vulnerability regardless of the construction of the access track, and further investigation was required to be undertaken in order to prevent major incidents.

In the next sections, the same methodology was carried out for the remaining cases.

9.2 St Bees

In this section, the stability of four stables cuttings and two failed cuttings at St Bees are analysed using the DNM and the RRM approaches.

Assessment of Cuttings using the DNM Approach

Step 1: Obtain DTM of cutting and catchment

The extension of the catchment analysed and the corresponding 1m DTM are shown in Figure 9-14 left and right respectively. A local road is located parallel to the cuttings flanked by small earth abutments that serves as water barriers. The cutting failure at 68 miles 59 chains could be explained by a localised discharge of water from the road at a spot where the earth wall disappears (Figure 9-15 and Figure 9-16). This could explain the cutting failure by concentrated runoff in this cutting.

The DTM used in the analysis of water runoff does not present this feature of the road. In order to account for the catchment above the road, a 2m mesh quadrant was used at this area (Figure 9-14 right).

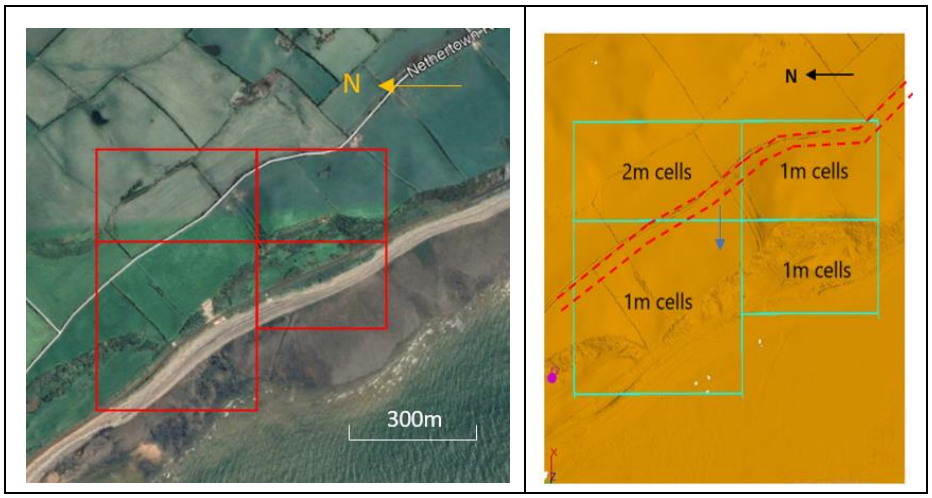

Figure 9-14 Extension of the catchment analysed (left) and 1M DTM (right) at St Bees

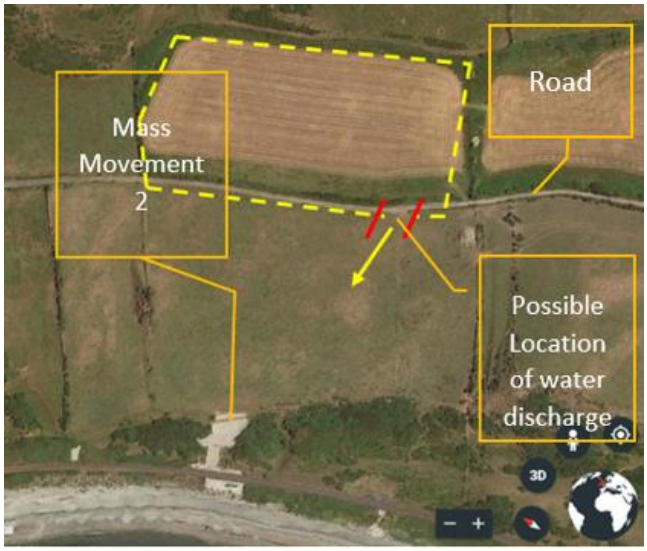

Figure 9-15 Discharge of water from the road at St Bees

Figure 9-16 Possible area of water discharge at St Bees

Step 2. Obtain rainfall characteristics (rainfall intensity and duration)

The rainfall at the day of the event had an intensity of 10.32mm/h and lasted 5 hours.

Step3: Calculation of the drainage lines

Result of the drainage lines calculated in ArcGIS are presented in Figure 9-17. The results show five drainage line outlets at the crest of the cuttings SC1, SC2, FC1, FC2 and SC3. SC standing for Stable Cutting and FC for Failed Cutting.

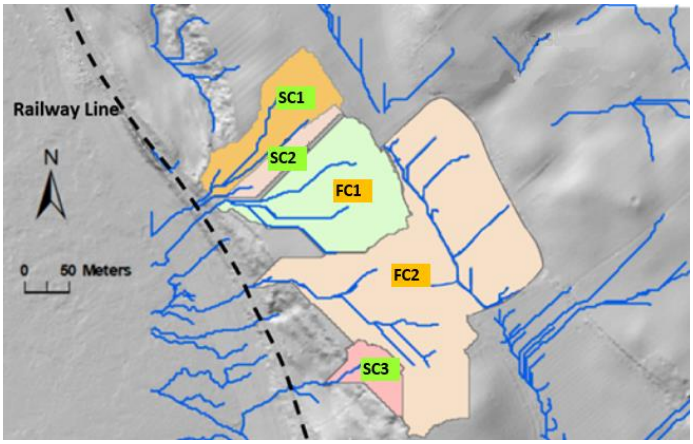

Figure 9-17 Drainage lines at St Bees

Step 4 in DNM: Obtain the bottom shear stress at the slope/cutting

The surface shear stress map obtained in FLOW-3D (Figure 9-18), shows five locations of the cutting where the shear stresses are higher. It can be observed that the cuttings presenting the highest levels of shear stress in FLOW-3D coincide with the cuttings with concentration of runoff water.

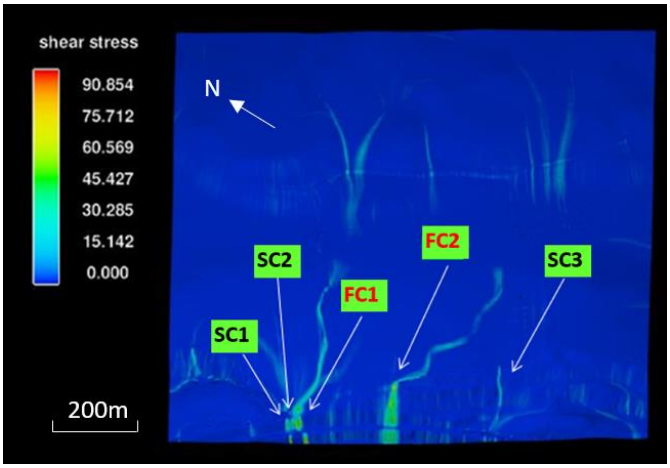

Figure 9-18 Shear stresses at St Bees

The Maximum surface shear Stress at SC1, SC2, FC1, FC2 and SC3 are presented in Figure 9-19.

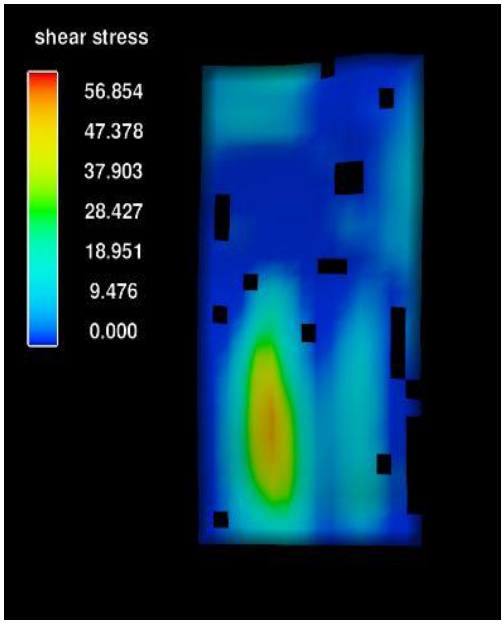

SC1=56.85Pa

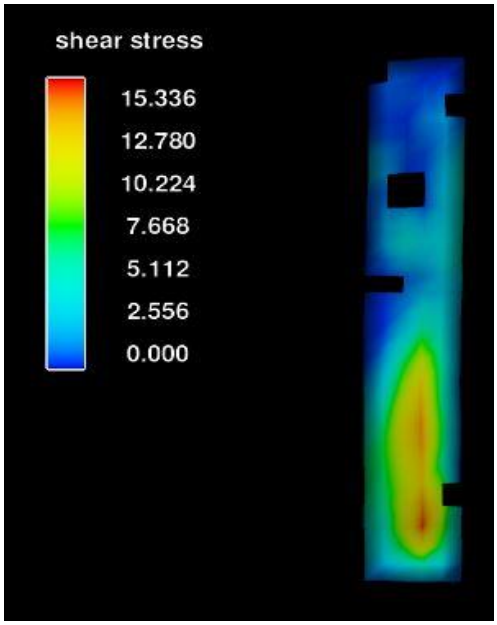

SC2=15.33 Pa

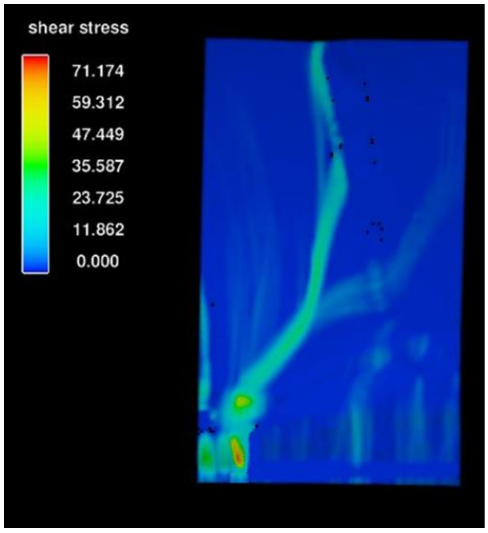

FC1=71.74Pa

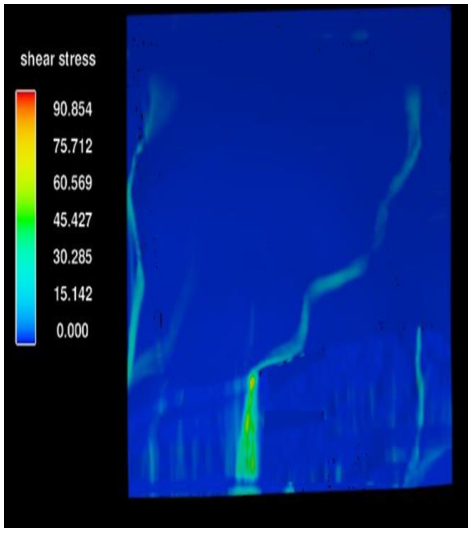

FC2=90.85 Pa

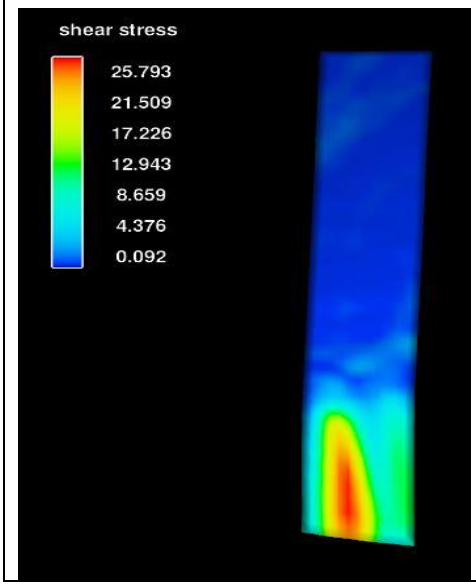

SC3=25.79	

Figure 9-19 Maximum bed shear stress at St Bees area slopes

Step 5: Calculation of the cutting angles at the selected cuttings

The location of the cutting profiles and the profiles themselves are shown in Figure 9-20.

SC1
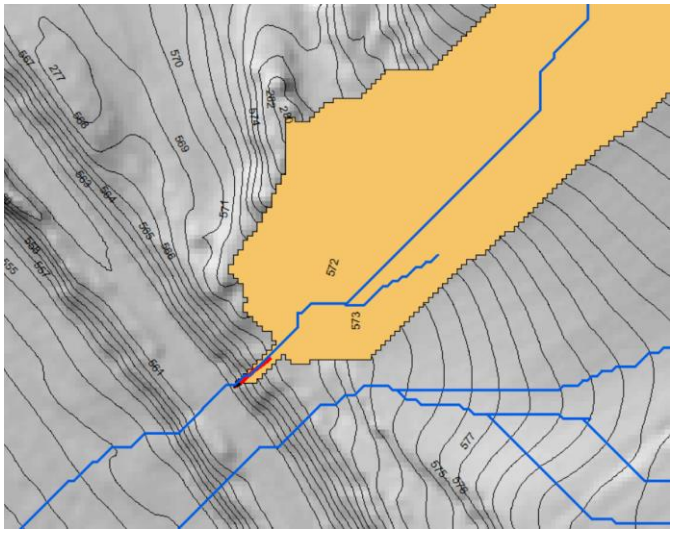 Drainage Line in SC1
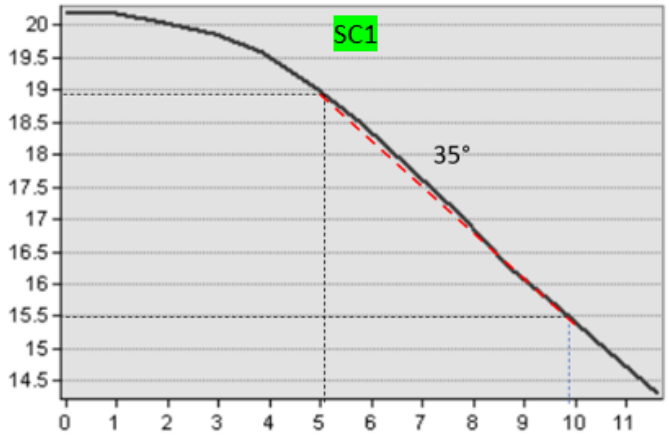 Cutting Profile in SC1
SC2

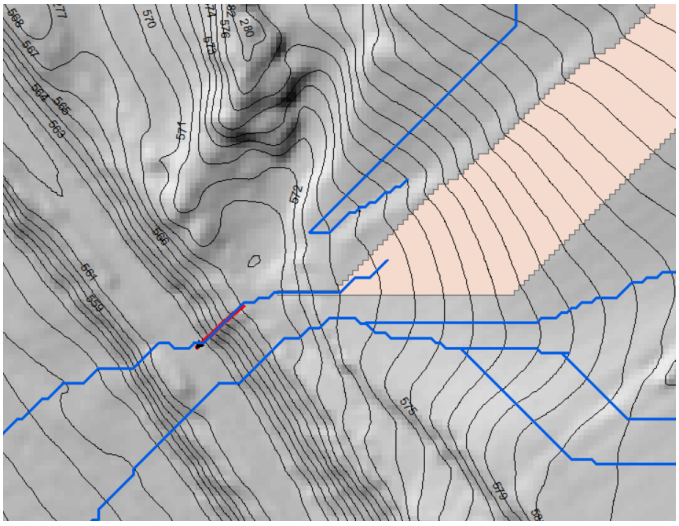

Drainage Line in SC2

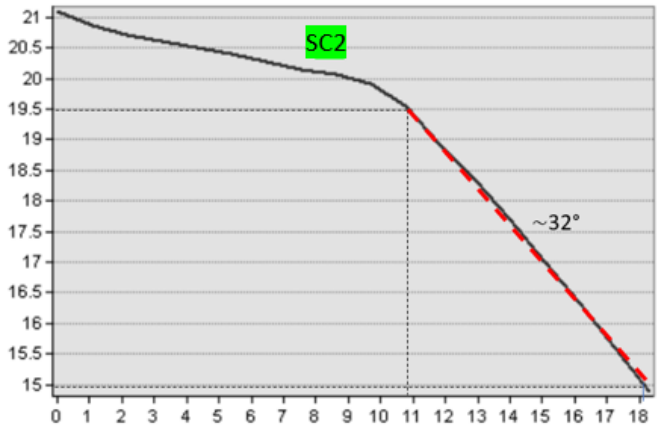

Cutting Profile in SC2

FC1

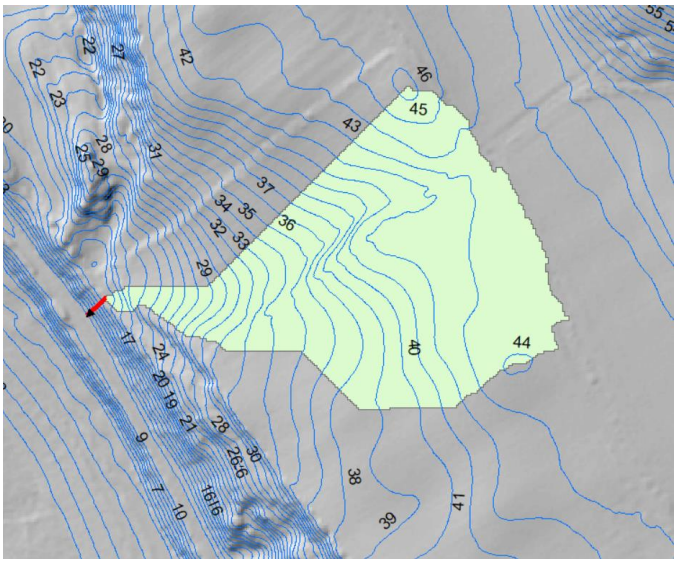

Drainage Line in FC1

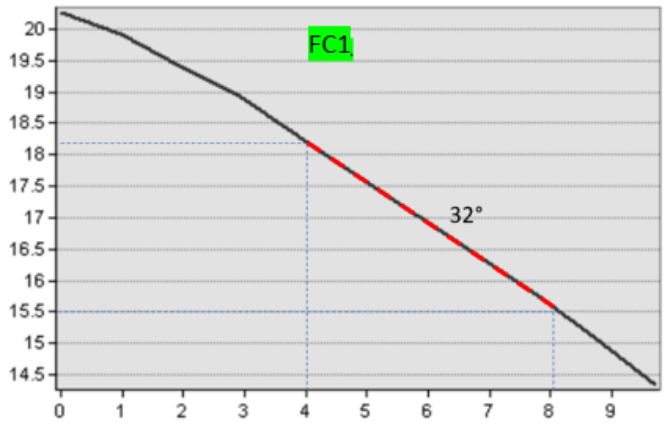

Cutting Profile in FC1

FC2

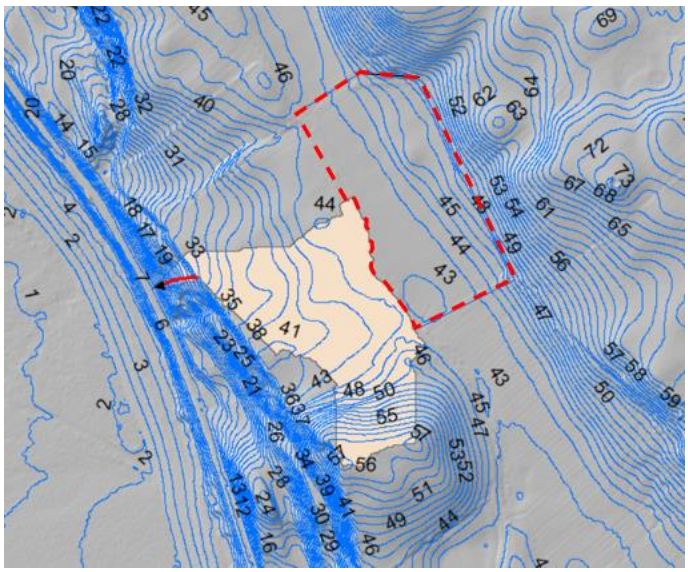

Drainage Line in FC2

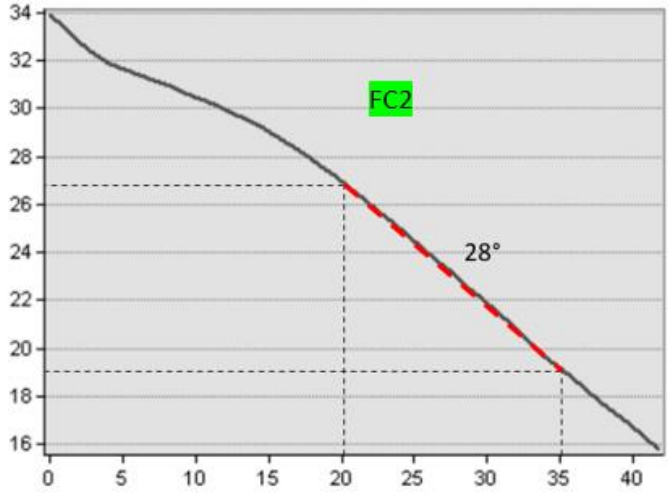

Cutting Profile in FC2

SC3

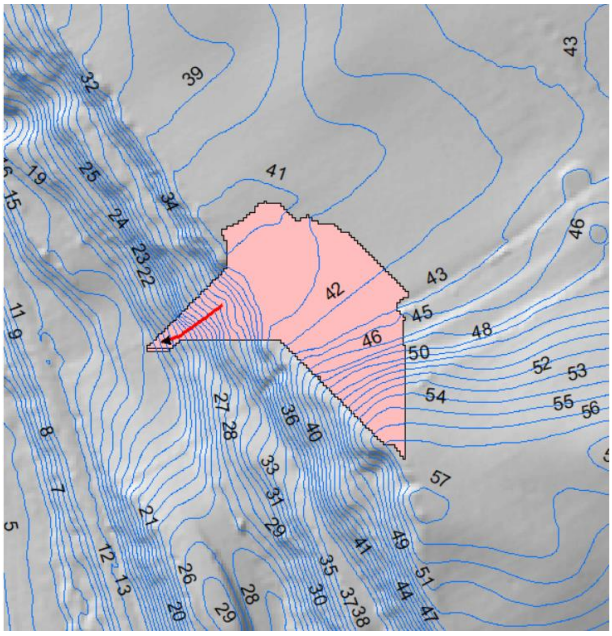

Drainage Line in SC3

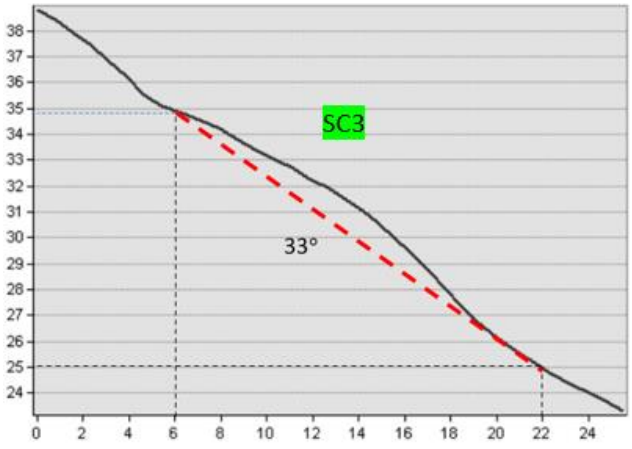

Cutting Profile in SC3

Figure 9-20 Average angles of the cuttings at St Bees

Step 6: Calculation of the critical shear stress at each slope/cutting

The critical shear stress at SC1, SC2, FC1, FC2 and SC3 are presented in Figure 9-21 and Table 9-4 for values of $\emptyset'_r$=31° and γ_{bulk}=21kN/m^3

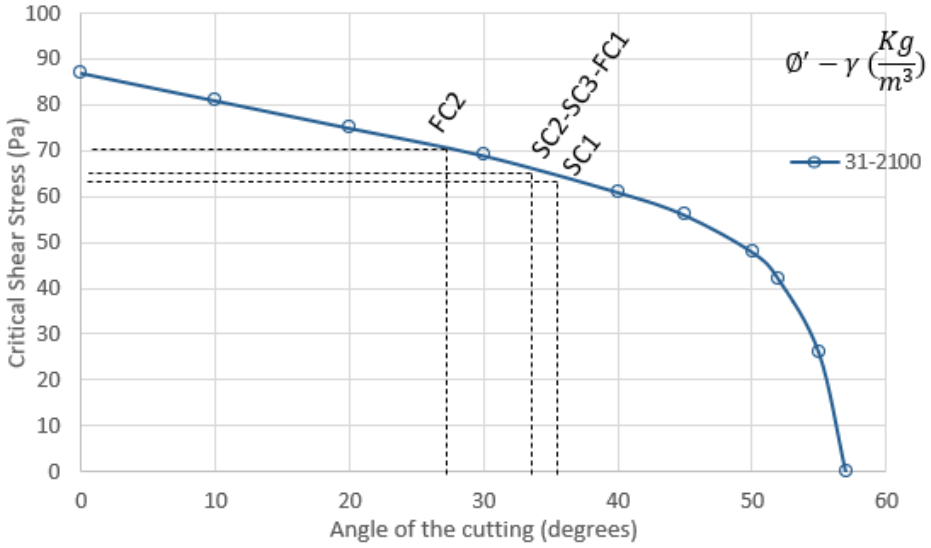

Figure 9-21 Critical Shear Stresses at St Bees Cuttings

Table 9-4 Critical Shear Stress at St Bees Cuttings

Cutting	SC1	SC2	SC3	FC1	FC2
Critical Shear Stress (Pa)	63	66	33	66	70

Step 7: Assessment of the stability of the cuttings

Once the critical shear stress and the surface shear stress were obtained for each cutting the assessment of stability was calculated from the FoS:

Table 9-5 Assessment of the stability at St Bees using DNM

	SC1	**SC2**	**SC3**	**FC1**	**FC2**
Critical Shear Stress	63	66	33	66	70
Actual Shear Stress	56.85	15.33	25.7	71.74	90.85
FoS	**1.11**	**4.30**	**1.28**	**0.92**	**0.77**

Cuttings SC1, SC2 and SC3 were assessed as stable and, FC1 and FC2 as vulnerable in agreement with the real outcomes

Assessment of the stability of cuttings at Watford using the RRM approach

Steps 1,2, 3 and 7 have already been carried out in the DNM approach.

Step 4: Calculation of the catchment area (e.g. using GIS software)

The results of the catchment areas in ArcGIS are presented in Figure 9-22.

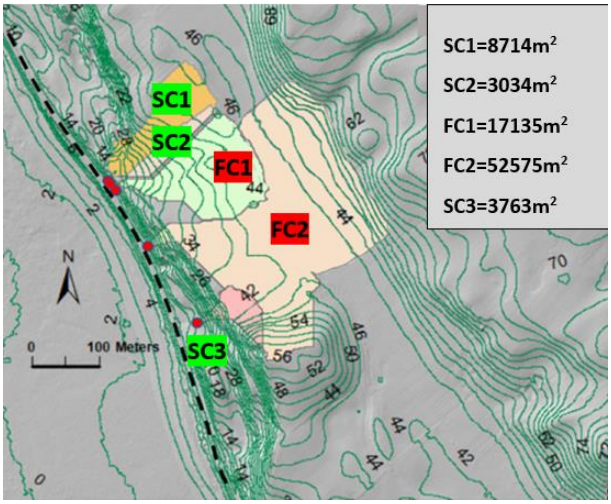

Figure 9-22 Catchment areas at St Bees

Step 5: Calculation of the flow rate at the crest of the cutting using Q=IxA

SC1 $$Q_n = \frac{A \cdot I}{n} = 8714m^2 \cdot \frac{0.0125m}{3600s} = 0.030m^3/s = 30l/s \quad (9.\ 7)$$

SC2 $$Q_n = \frac{A \cdot I}{n} = 3034m^2 \cdot \frac{0.0125m}{3600s} = 0.010m^3/s = 10l/s \quad (9.\ 8)$$

FC1 $$Q_n = \frac{A \cdot I}{n} = 17135m^2 \cdot \frac{0.0125m}{3600s} = 0.059m^3/s = 59l/s \quad (9.\ 9)$$

FC2 $$Q_n = \frac{A \cdot I}{n} = 52575m^2 \cdot \frac{0.0125m}{3600s} = 0.183m^3/s = 183l/s \quad (9.\ 10)$$

SC3 $$Q_n = \frac{A \cdot I}{n} = 3763m^2 \cdot \frac{0.0125m}{3600s} = 0.013m^3/s = 13l/s \quad (9.\ 11)$$

Step 6: Calculation of the bottom shear stress at the slope/cutting from the chart flow rate vs angle of the slope/cutting

From the chart in Figure 8-29, the superficial shear stress was obtained for each cutting. The results are presented in Figure 9-23.

SC1	SC2

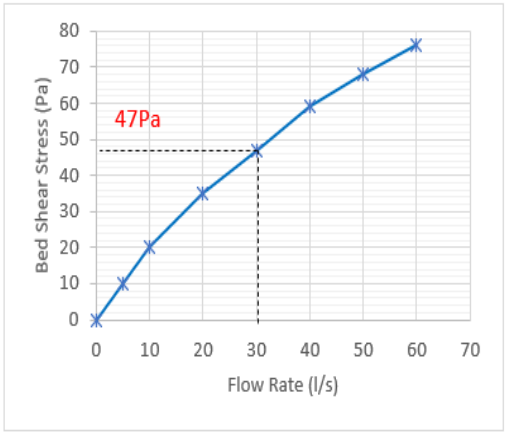

FC1

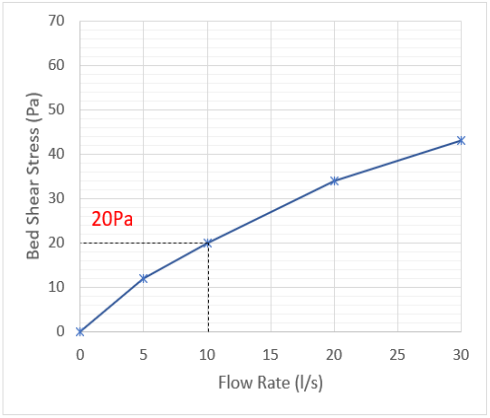

FC2

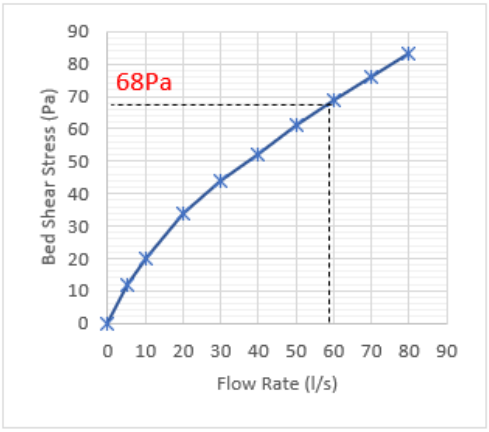

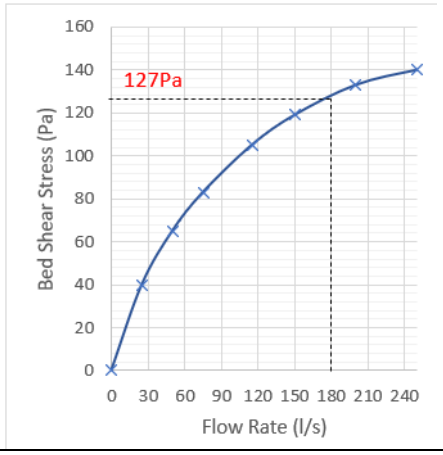

SC3

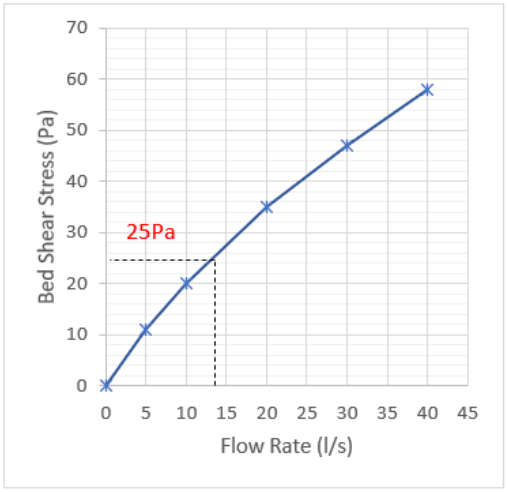

Figure 9-23 Actual Shear Stress at St Bees in RRM

Step 8: Assessment of the stability of the cuttings

Once the critical shear stress and the surface shear stress were obtained for each cutting the assessment of stability was calculated from the FoS o:

Table 9-6 Assessment of the stability at St Bees using RRM

	SC1	SC2	SC3	FC1	FC2
Critical Shear Stress	63	66	33	66	70
Actual Shear Stress	47	20	25	68	127
FoS	**1.34**	**3.3**	**1.32**	**0.97**	**0.55**

Cuttings SC1, SC2 and SC3 were assessed as stable and FC1 and FC2 as vulnerable in agreement with the real outcomes.

In this case, the RRM have shown more conservative results in SC2 and FC2 and less conservative results in SC1, SC2 and FC1 than the DNM.

9.3 Beaminster tunnel

In this section, the assessment of the stability using the DNM and the RRM methods was carried out for a number of cuttings:

*A cutting that remained stable at the north portal

*Two cuttings that failed the day of the rainfall event at the north portal

*One cutting that remained stable at the south portal.

Assessment of Cuttings, using the DNM Approach in the north tunnel portal

Step 1: Obtain DTM of cutting and catchment

The extension of the catchment analysed and the corresponding 1m DTM are shown in Figure 9-24 left and right respectively.

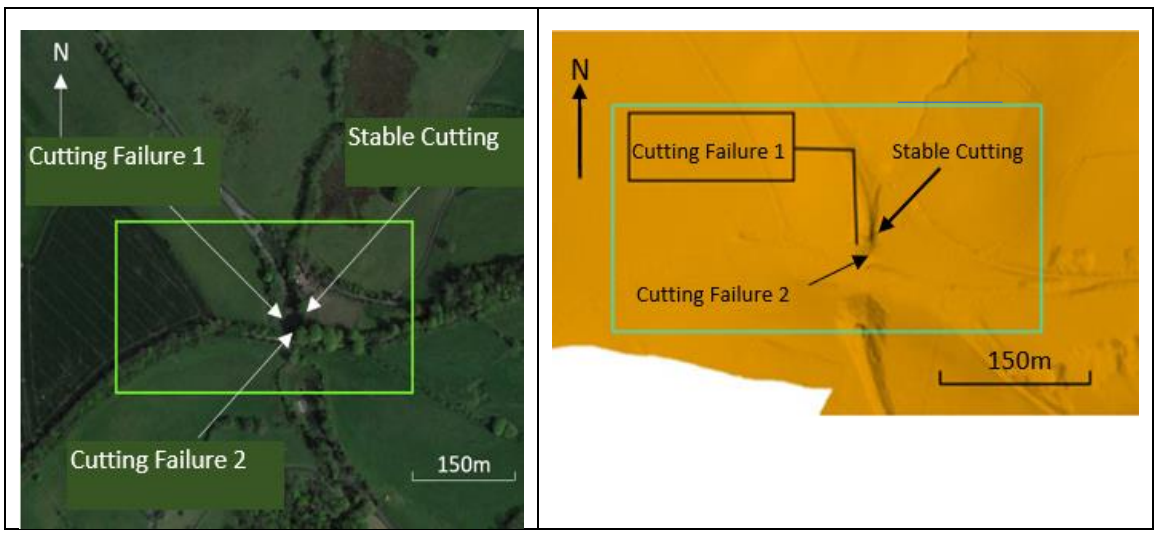

Figure 9-24 Extension of the area analysed (left) and 1M DTM at Beaminster

Step 2. Obtain rainfall characteristics (rainfall intensity and duration)

The short duration high intensity rainfall of 12.9mm/h during four hours that took place just before the failure was used in the analysis

Step3: Calculation of the drainage lines

The drainage lines are presented in Figure 9-25. Three main drainage lines have been obtained in the north tunnel portal. Two of them (FC1 and FC2) in the locations where cutting failures took place and the third one (SC1) in a cutting that remained stable.

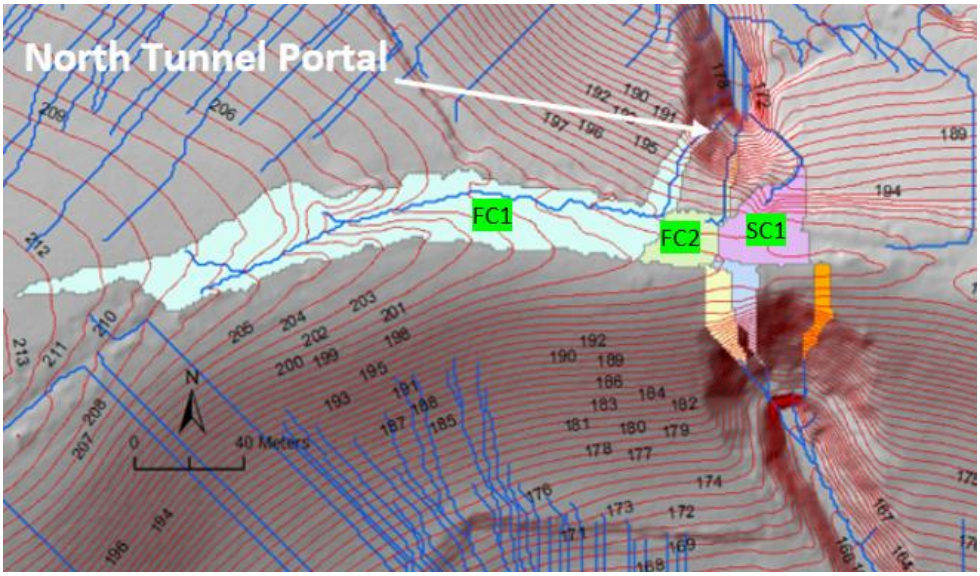

Figure 9-25 Drainage Lines for the north portal tunnel at Beaminster

Step 4 in DNM: Obtain the bottom shear stress at the slope/cutting

The surface shear stress map obtained in FLOW-3D is presented in Figure 9-26. The highest shear stresses (in red) correspond to the location of the retaining walls that were treated in FLOW-3D as vertical slopes and therefore was ignored. Shear stresses at SC1, FC1 and FC2 are indicated in Figure 9-26.

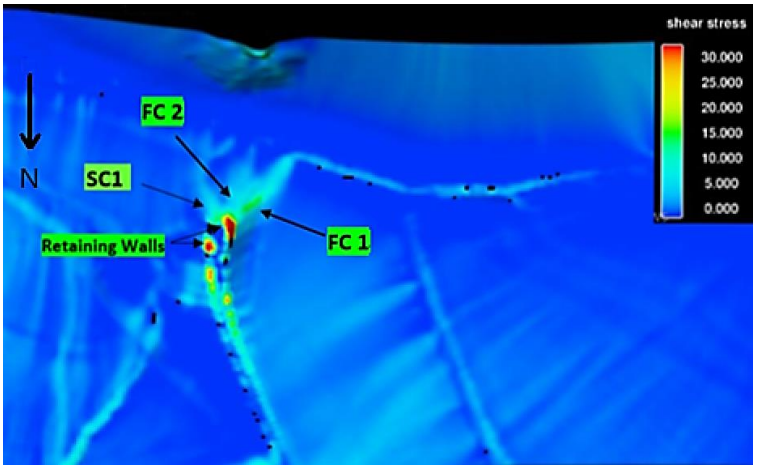

Figure 9-26 Shear stress at Beaminster

The Maximum Bed Shear Stress at SC1, FC1 and FC2 are presented in Figure 9-27.

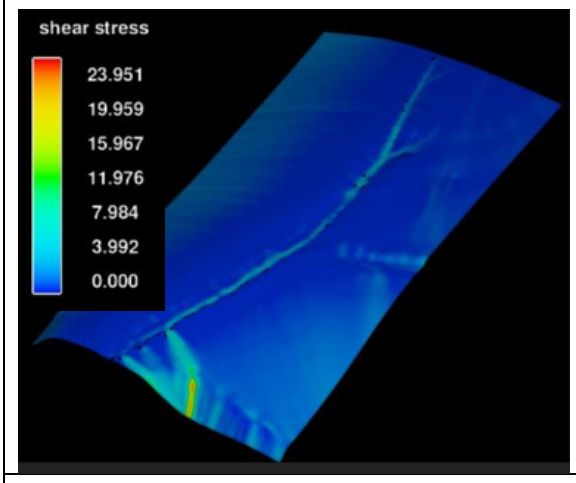

FC1=23.95Pa

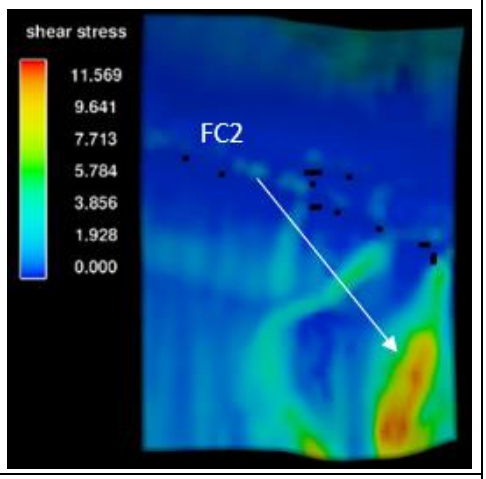

FC2=11.57 Pa

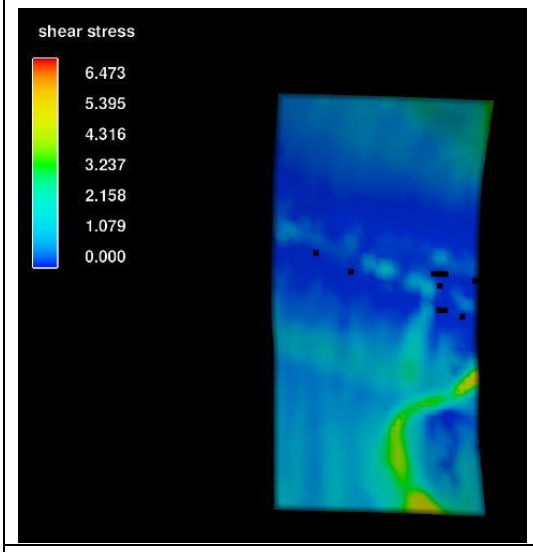

SC1=6.47 Pa

Figure 9-27 Maximum shear stress of each cutting at Beaminster

Step 5: Calculation of the cutting angles at the selected cuttings

The profiles of the cuttings were calculated following the drainage lines along the faces of the cuttings (Figure 9-28).

FC1-FC2-SC1

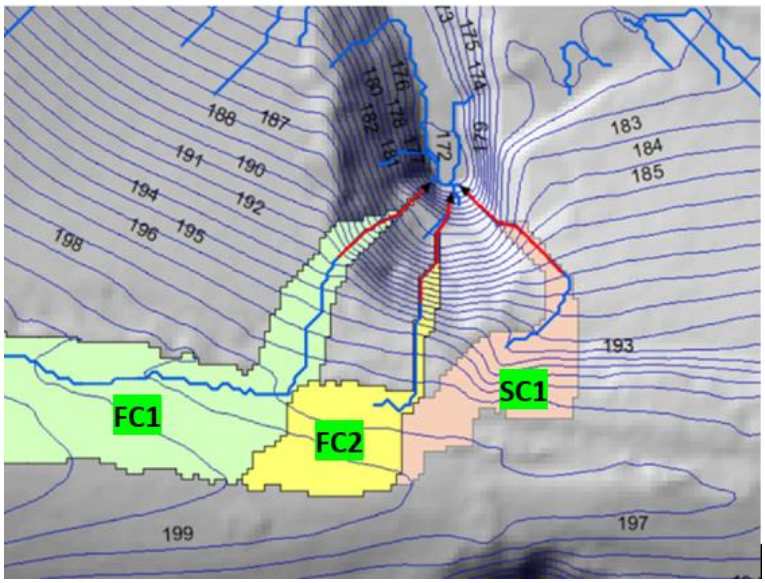

Drainage Lines FC1,FC2, SC1

FC1

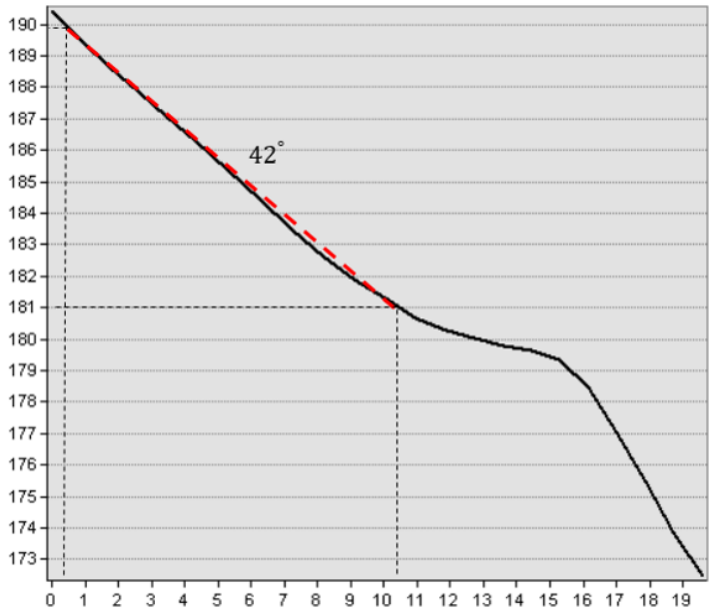

FC2

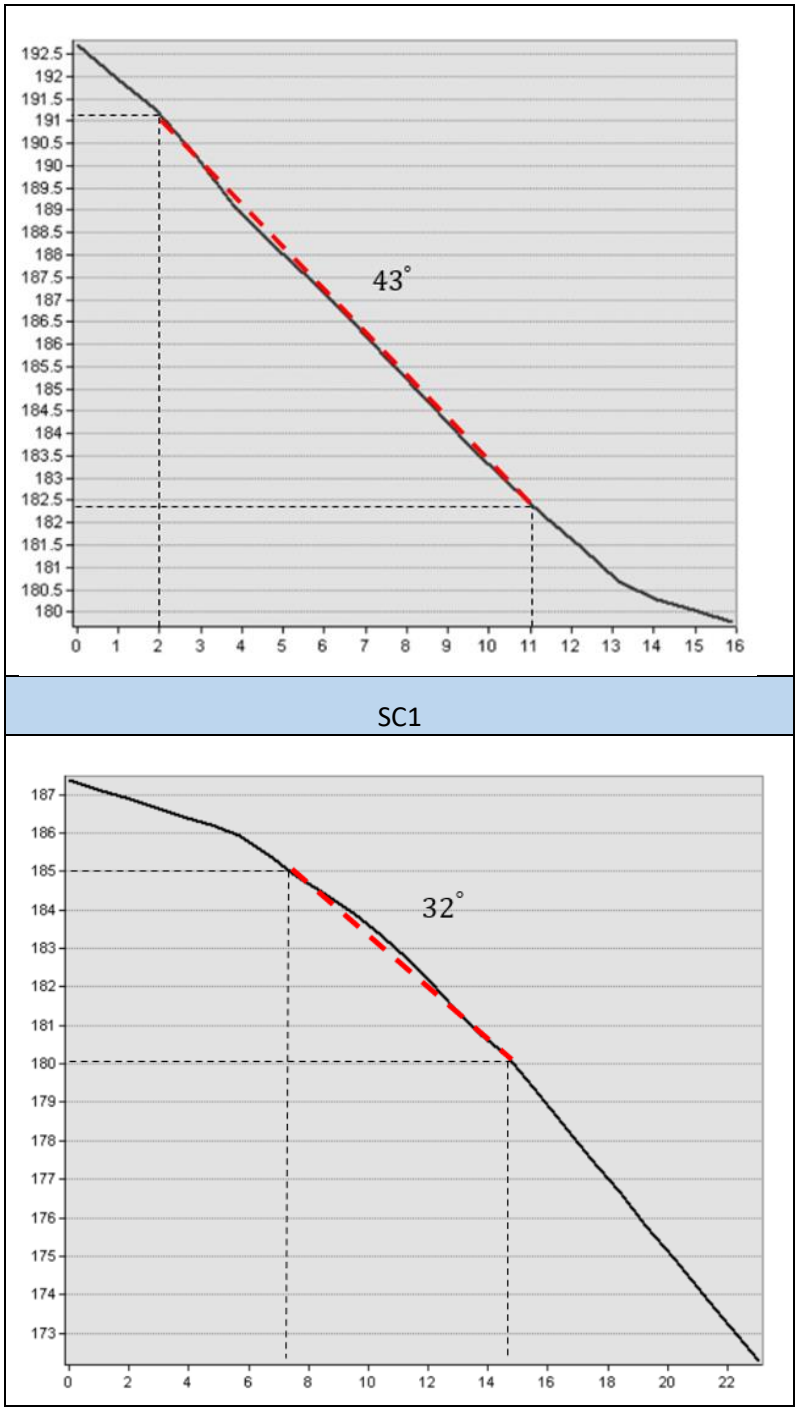

Figure 9-28 Average angles of the cuttings at Beaminster

Step 6: Calculation of the critical shear stress at each slope/cutting

The critical shear stress at FC1, FC2, and SC1 are presented in Figure 9-29 and Table 9-7 for values of $\emptyset'_r$=23° and γ_{bulk}=19kN/m^3

.

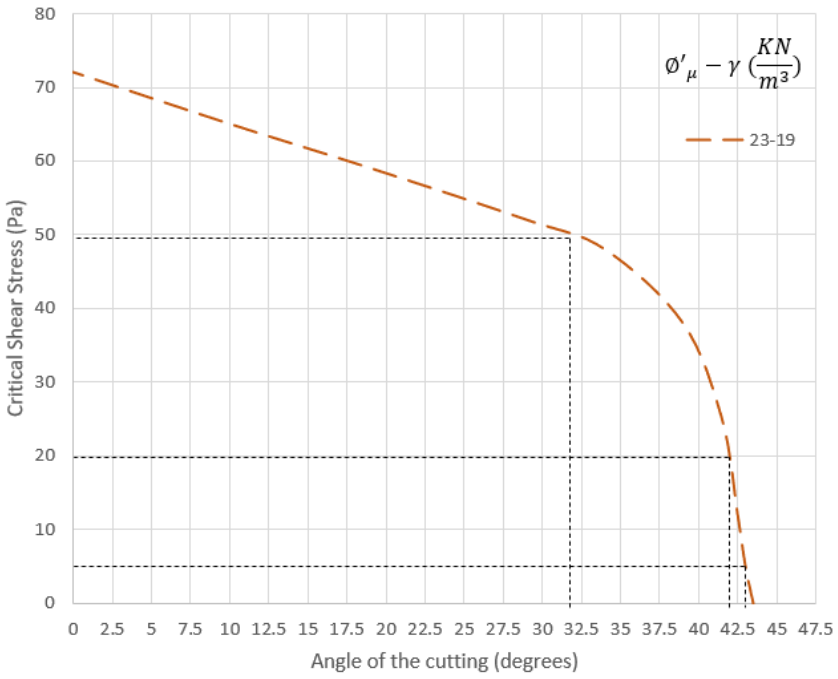

Figure 9-29 Critical Shear Stress at Beaminster north portal

Table 9-7 Critical Shear Stress at Beaminster north portal

Cutting	SC1	FC1	FC2
Critical Shear Stress (Pa)	50	20	5

Step 7: Assessment of the stability of the cuttings

Once the critical shear stress and the surface shear stress were obtained for each cutting the assessment of stability was calculated and the FoS obtained:

Table 9-8 Assessment of the stability at Beaminster north portal using DNM

	SC1	**FC1**	**FC2**
Critical Shear Stress	50	20	5
Actual Shear Stress	6.47	23.95	11.57
FoS	**7.72**	**0.83**	**0.43**

Cutting SC1 was assessed as stable and FC1 and FC2 as vulnerable in agreement with the real outcomes.

Assessment of the stability of cuttings at Watford using the RRM approach

Steps 1,2, 3 and 7 have already been carried out in the DNM approach.

Step 4: Calculation of the catchment area (e.g. using GIS software)

The results of the catchment areas in ArcGIS are presented in Figure 9-30.

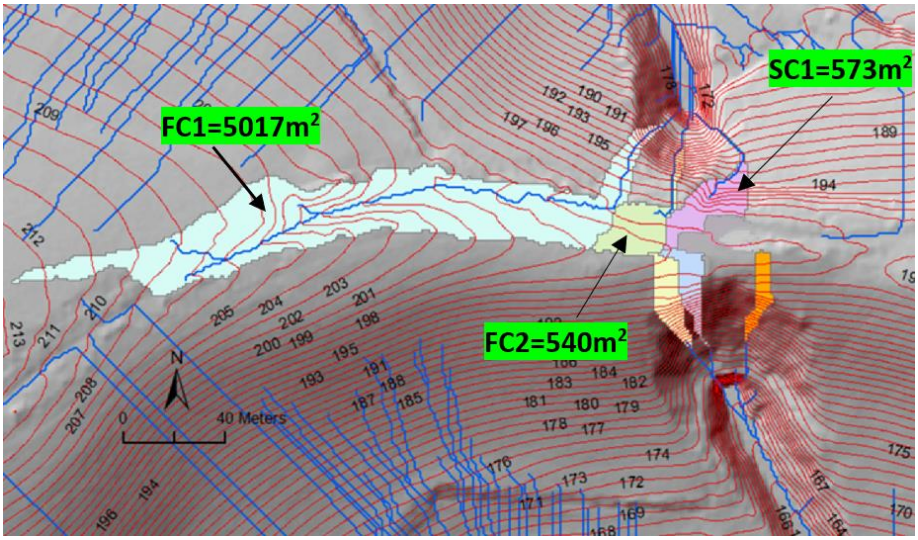

Figure 9-30 Catchment areas at Beaminster

Step 5: Calculation of the flow rate at the crest of the cutting using Q=IxA

FC1 $$Q_n = \frac{A \cdot I}{n} = 5017m^2 \cdot \frac{0.0125m}{3600s} = 0.017m^3/s = 17l/s \quad (9.\ 12)$$

FC2 $$Q_n = \frac{A \cdot I}{n} = 540m^2 \cdot \frac{0.0125m}{3600s} = 0.002m^3/s = 2l/s \quad (9.\ 13)$$

SC1 $$Q_n = \frac{A \cdot I}{n} = 573m^2 \cdot \frac{0.0125m}{3600s} = 0.002m^3/s = 2l/s \quad (9.\ 14)$$

Step 6: Calculation of the bottom shear stress at the slope/cutting from the chart flow rate vs angle of the slope/cutting

From the chart in Figure 8-29, the superficial shear stress was obtained for the each cutting. The results are presented in Figure 9-31.

FC1	FC2
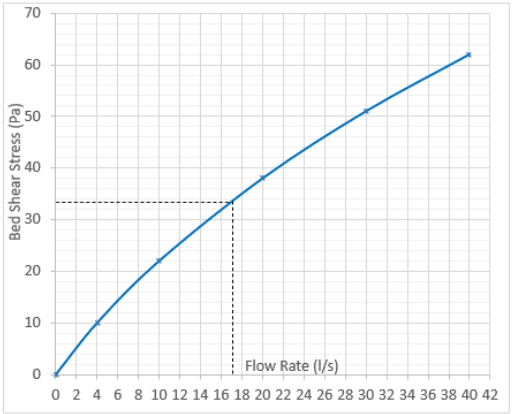	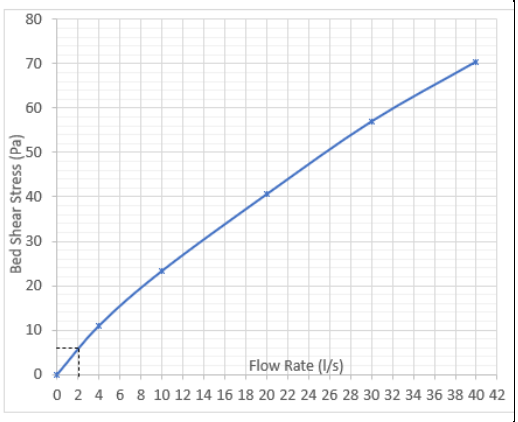
SC1	

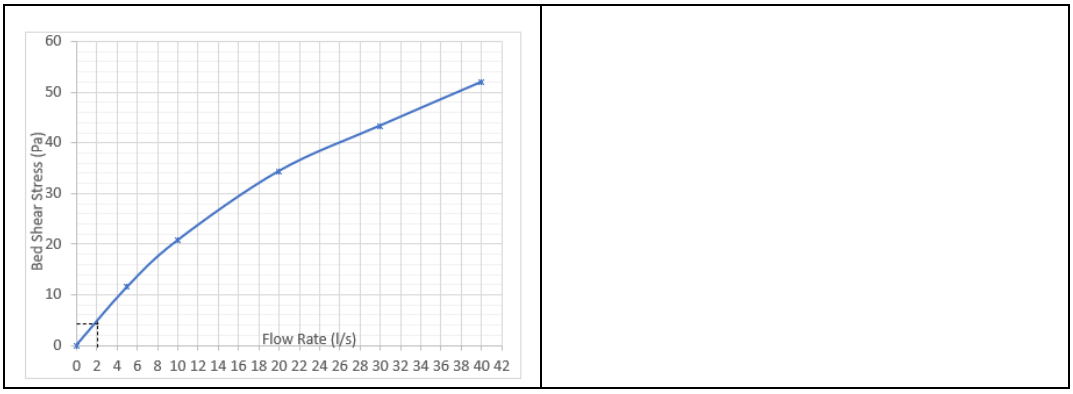

Figure 9-31 Actual Shear Stress at Beaminster in RRM

Step 8: Assessment of the stability of the cuttings

Once the critical shear stress and the surface shear stress were obtained for each cutting the assessment of stability was calculated from the FoS:

Table 9-9 Assessment of the stability at Beaminster north portal using RRM

	SC1	**FC1**	**FC2**
Critical Shear Stress	50	15	5
Actual Shear Stress	4	33	6
FoS	**12.5**	**0.45**	**0.83**

Cutting SC1 was assessed as stable and FC1 and FC2 as vulnerable in agreement with the real outcomes.

In this case, the RRM have shown more conservative results in FC1 and less conservative results in SC1 and FC2 than the DNM.

Assessment of Cuttings, using the DNM Approach in the south portal

Step 1: Obtain DTM of cutting and catchment

The extension of the catchment analysed and the corresponding 1m DTM are the same as in the north portal.

Step 2. Obtain rainfall characteristics (rainfall intensity and duration)

The rainfall characteristics are the same as in the north portal.

Step3: Calculation of the drainage lines

The drainage lines are presented in Figure 9-32. Three main drainage lines were obtained, with SC1 corresponding to the location where a small runoff generated debris flow took place in 2009.

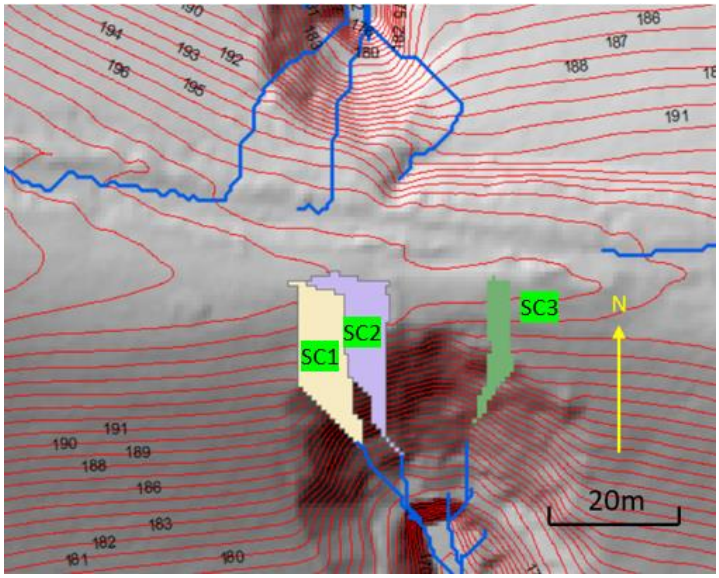

Figure 9-32 Drainage Lines for the south portal tunnel at Beaminster

Step 4 in DNM: Obtain the bottom shear stress at the slope/cutting

The surface shear stress obtained in FLOW-3D is presented in Figure 9-33. Higher shear stresses could be observed at the locations of the drainage lines obtained in ArcGIS.

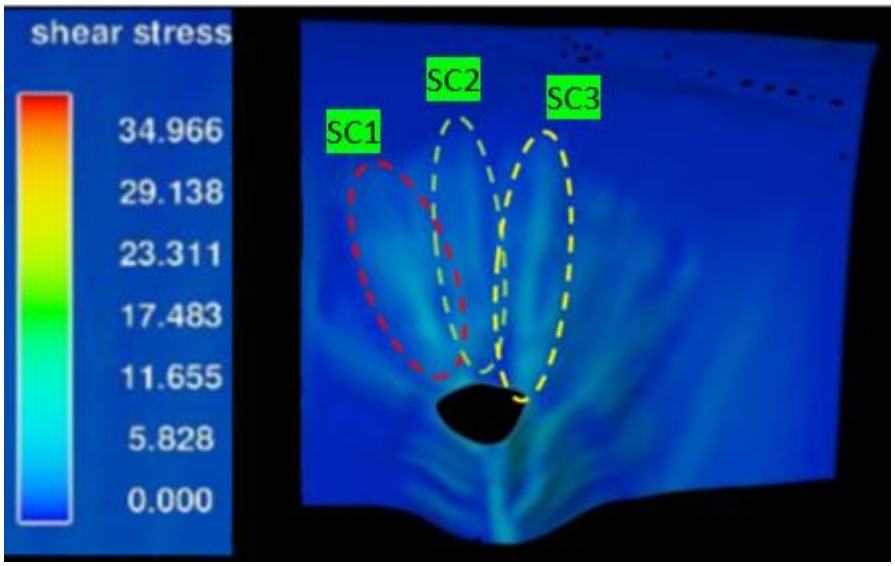

Figure 9-33 Shear stress at Beaminster south portal

The maximum surface shear stress corresponds to the location of SC1 (Figure 9-34). In this case, only the stability of the most critical cutting (SC1) was assessed using the novel method

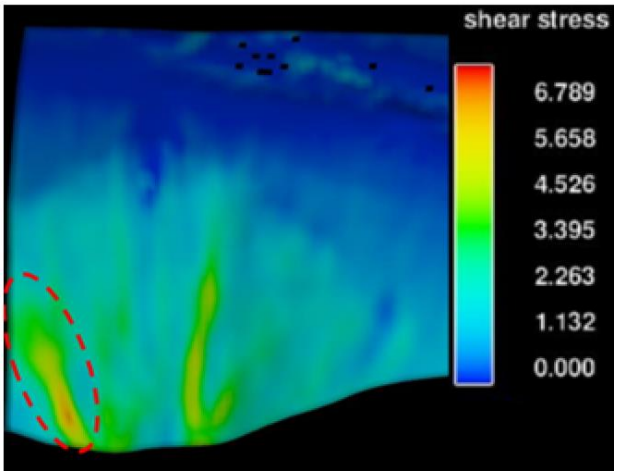

Figure 9-34 Maximum shear stress at Beaminster south portal

Step 5: Calculation of the cutting angles at the selected cutting

The profile of SC1 (Figure 9-28), was calculated following the drainage line in ArcGIS.

SC1

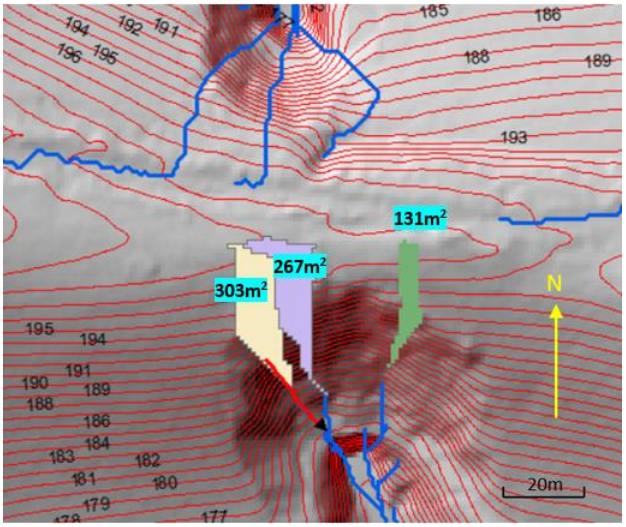

Drainage Lines SC1, SC2 and SC3

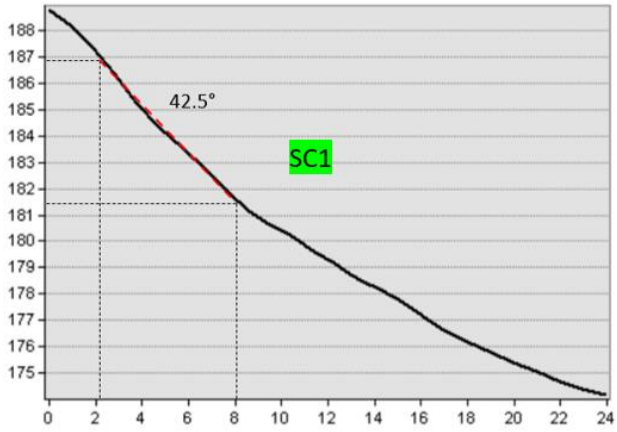

Profile of SC1

Figure 9-35 Angle of the cutting at Beaminster south portal

Step 6: Calculation of the critical shear stress at each slope/cutting

The critical shear stress at SC1 is presented in Figure 9-36 and Table 9-10.

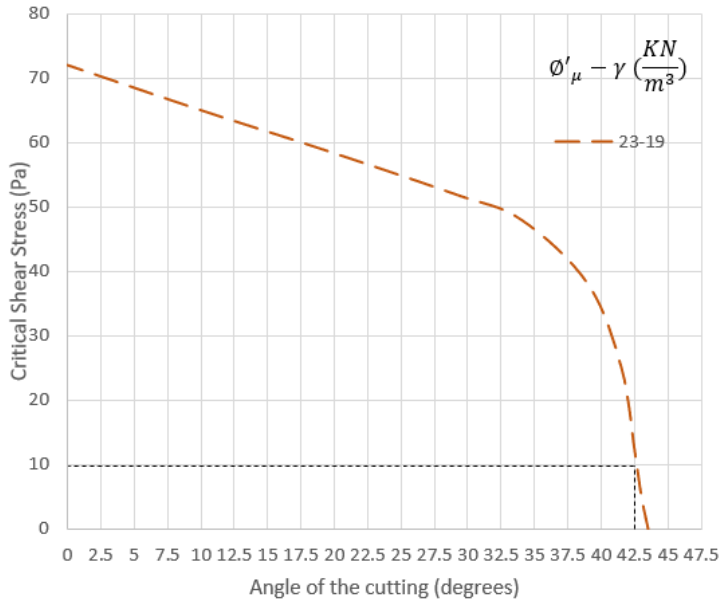

Figure 9-36 Actual Shear Stress at Beaminster south portal in RR

Table 9-10 Actual Shear Stress at Beaminster south portal in RR

Cutting	SC1
Critical Shear Stress (Pa)	10

Step 7: Assessment of the stability of the cuttings

Once the critical shear stress and the surface shear stress was obtained, the assessment of stability was calculated from the FoS:

Table 9-11 Assessment of the stability at Beaminster south portal using DNM

	SC1
Critical Shear Stress	10
Actual Shear Stress	6.78
FoS	**1.47**

Cutting SC1 was assessed as stable in agreement with the real outcomes.

Assessment of the stability of cuttings at Watford using the RRM approach

Steps 1,2, 3 and 7 have already been carried out in the DNM approach.

Step 4: Calculation of the catchment area (e.g. using GIS software)

The results of the catchment areas are presented in Figure 9-37. Catchment SC1 present the largest catchment in agreement with the location of the highest shear stress obtained in DNM.

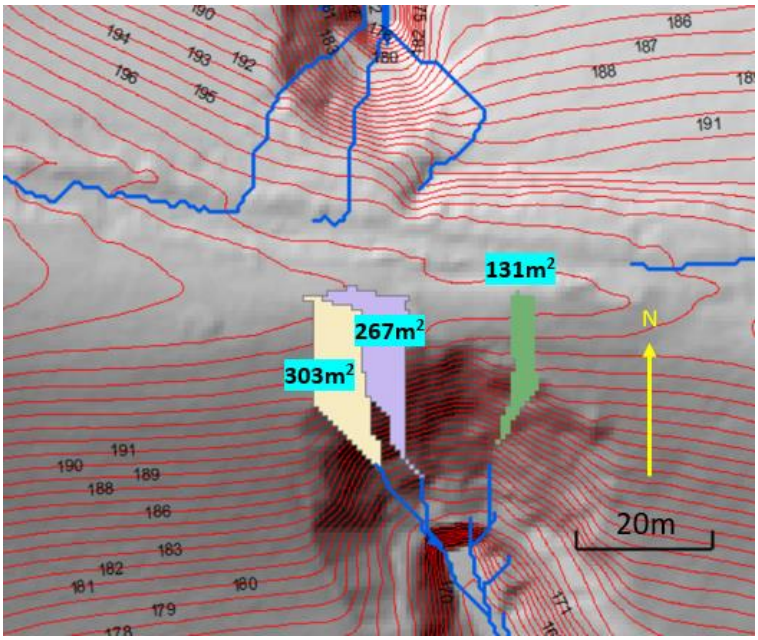

Figure 9-37 Catchment areas at Beaminster south portal

Step 5: Calculation of the flow rate at the crest of the cutting using Q=IxA

Calculation of the flow rate was as:

SC1 $$Q_n = \frac{A \cdot I}{n} = 303m^2 \cdot \frac{0.0125m}{3600s} = 0.00105m^3/s = 1.05l/s \quad (9.\ 15)$$

Step 6: Calculation of the bottom shear stress at the slope/cutting from the chart flow rate vs angle of the slope/cutting

From the charts obtained in Figure 8-29, and the soil properties $\emptyset'_r$=23° and γ_{bulk}=19kN/m³, the surface shear stress was obtained for the cutting. The result is presented in Figure 9-38.

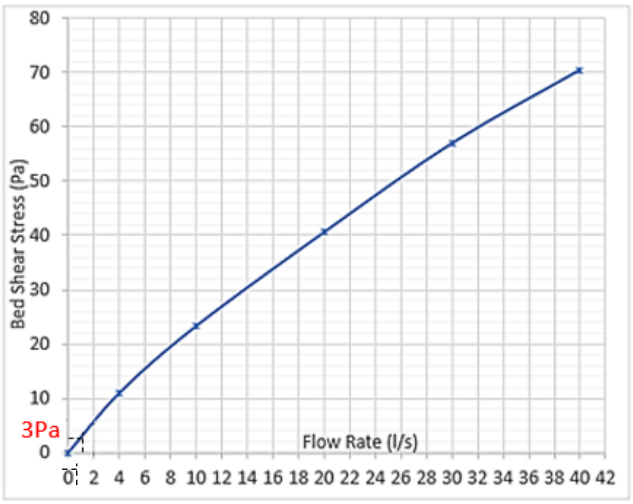

Figure 9-38 Actual Shear Stress at Beaminster south portal in RRM

Step 8: Assessment of the stability of the cuttings

Once the critical shear stress and the surface shear stress were obtained for the cutting the assessment of stability was calculated from the FoS:

Table 9-12 Assessment of the stability at Beaminster south portal using RRM

	SC1
Critical Shear Stress	10
Actual Shear Stress	3
FoS	**3.33**

Cutting SC1 was assessed as stable in agreement with the real outcome. In this case, the RRM have shown less conservative result than DNM.

9.4 Loch Treig

In this section, the stability of the natural slope at the location where the derailment at Loch Treig took place was analysed using DNM and RRM.

Assessment of the slope using the DNM Approach

Step 1: Obtain DTM of cutting and catchment

The extension of the catchment analysed and the corresponding DTM are shown in Figure 9-39 left and right respectively. The DTM was generated from a topography map with 1m contour lines.

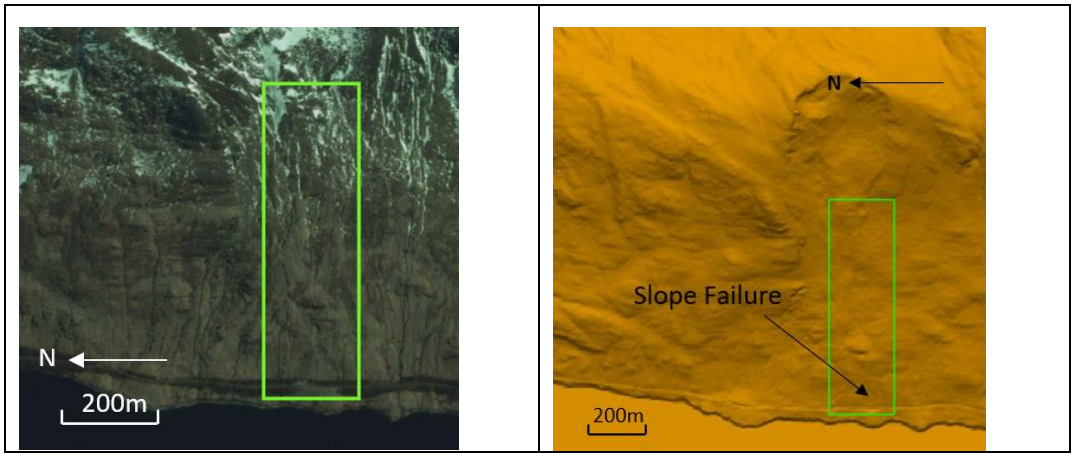

Figure 9-39 Extension of the area analysed (left) and 1M DTM at Loch Treig

Step 2. Obtain rainfall characteristics (rainfall intensity and duration)

The short duration rainfall of 6mm/h during 3 hours that took place just before the failure was used in the analysis

Step3: Calculation of the drainage lines

The drainage lines are presented in Figure 9-40. It can be observed that the location of the slope failure is not located over one of the principal drainage lines.

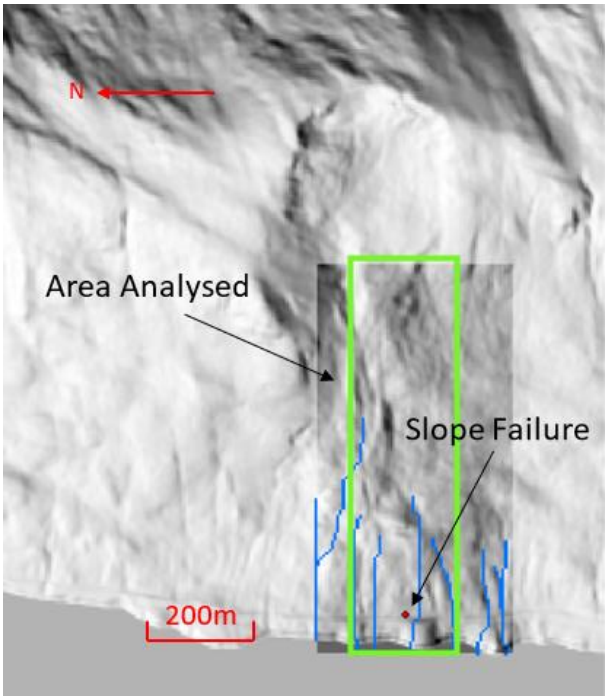

Figure 9-40 Drainage lines at Loch Treig area

Step 4 in DNM: Obtain the bottom shear stress at the slope/cutting

The surface shear stress at the slope failure is presented in Figure 9-41. The highest shear stresses does not correspond with the location of the slope failure.

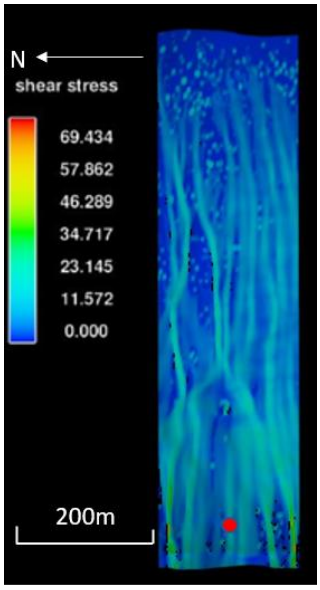

Figure 9-41 Shear Stress at Loch Treig

The Maximum superficial Ssear stress at the location of the failure is presented in Figure 9-42 corresponding to 24.86Pa.

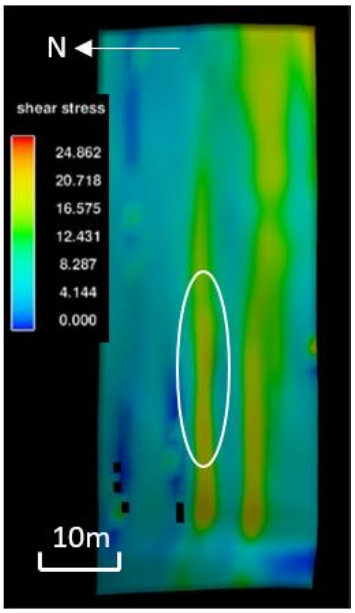

Figure 9-42 Maximum shear stress at Loch Treig slope failure

Step 5: Calculation of the cutting angles at the selected cuttings

Since no drainage line is observed at the location of the failure, the angle of the slope has been obtained from Figure 6-42 in chapter 6 with a value of 33°.

Step 6: Calculation of the critical shear stress

The critical shear stress is presented in Figure 9-43 for values of $\emptyset'_r$=38° (Table 6-6) and γ_{bulk}=23kN/m^3, with a resulting value of 98Pa.

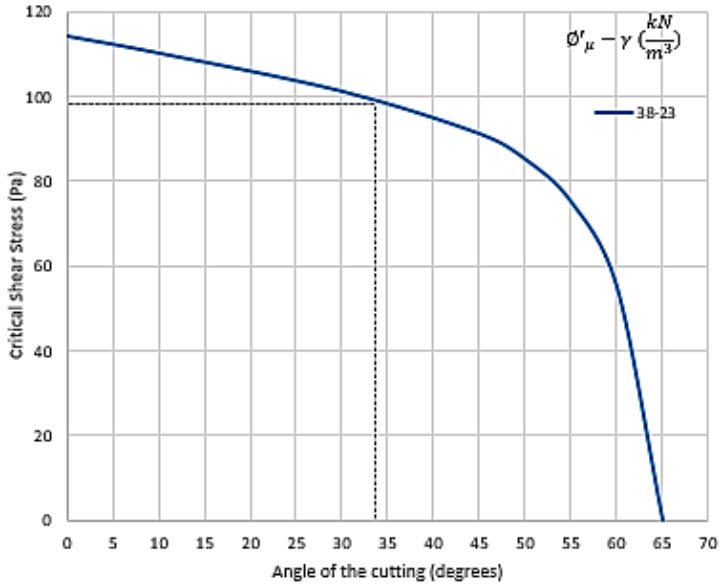

Figure 9-43 Critical Shear Stress at Loch Treig

Step 7: Assessment of the stability of the cuttings

Once the critical shear stress and the surface shear stress were obtained, the assessment of the stability was calculated from the FoS:

Critical Shear Stress	80
Actual Shear Stress	24.66
FoS	**3.24**

The result shows that the slope was not vulnerable to failure triggered by runoff.

Assessment of the stability of cuttings at Watford using the RRM approach

Steps 1,2, 3 and 7 have already been carried out in the DNM approach.

Step 4: Calculation of the catchment area (e.g. using GIS software)

The result of the catchment area is presented in Figure 9-44.

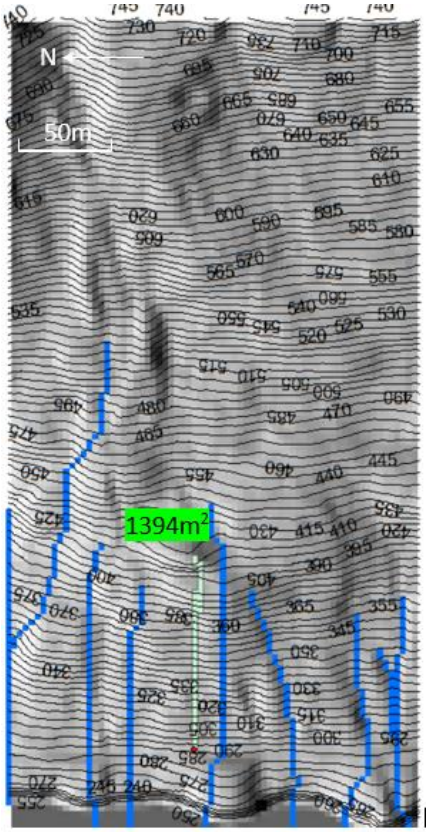

Figure 9-44 Catchment area at Loch Treig

Step 5: Calculation of the flow rate at the crest of the cutting using Q=IxA

Calculation of the flow rate was obtained as:

SC1 $$Q_n = \frac{A \cdot I}{n} = 1394m^2 \cdot \frac{0.012m}{3600s} = 0.0046m^3/s = 4.6l/s \quad (9.16)$$

Step 6: Calculation of the bottom shear stress at the slope/cutting from the chart flow rate vs angle of the slope/cutting

From the chart in Figure 8-29, the surface shear stress was obtained. The result is presented in Figure 9-45 with a resulting value of 12Pa.

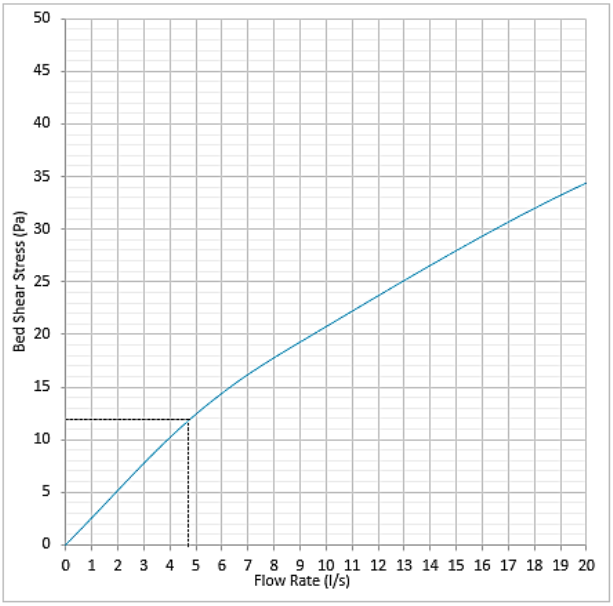

Figure 9-45 Actual Shear Stress at Loch Treig in RRM

Step 7: Assessment of the stability of the cuttings

Once the critical shear stress and the surface shear stress were obtained, the assessment of stability was calculated from the FoS:

	SC1
Critical Shear Stress	80
Actual Shear Stress	14
FoS	**5.71**

The result shows that the slope was not vulnerable to failure triggered by runoff.

In this case, the RRM has shown a less conservative result than the DNM

9.5 Hooley

In this section, the stability of cuttings at Hooley, were analysed using the novel method in the case that superficial water runoff is not present. Since the failures at this location are a consequence of over-steepness of the cuttings, the analysis only consisted of the calculation of the maximum stable angle of the cutting with a critical shear stress=0, in the chart critical shear stress vs angle of the slope for the bulk unit weight and angle of static friction obtained at Hooley.

Figure 9-46 shows that the maximum angle of a cutting with this characteristic corresponds to 65°. From the application of the chart, cuttings with these characteristics

would remain stable in the absence of superficial water runoff for angles lower than 65° and would be unstable for higher angles.

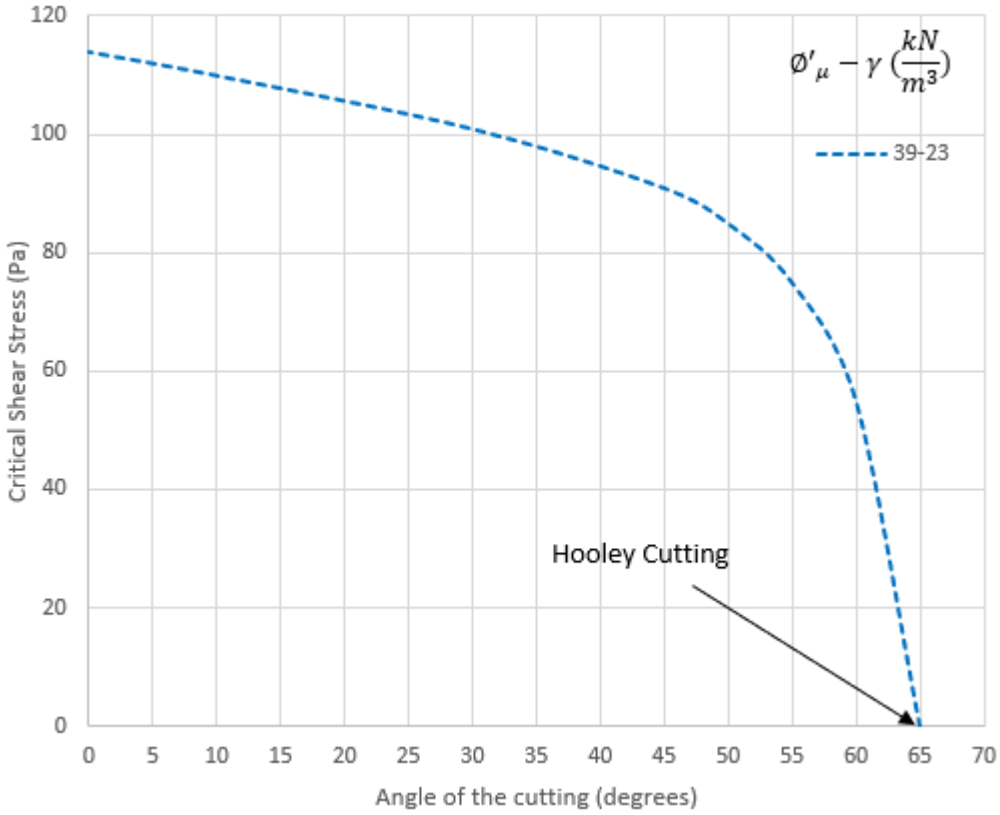

Figure 9-46 Maximum stable angle at Hooley Cuttings

Cuttings at Hooley presents angles between 60° and 70° that according to the chart in Figure 9-45 are at the limit of stability.

The result shows that the steepest stable angle considered in the chart agree well with the steepest stable angle observed in Grade Dc chalk at Hooley.

9.6 Summary of results

A summary of the results obtained for the case studies analysed is presented in Table 9-13.

SC corresponds to the case studies that remained stable after the rainfall events or the failed was not attributed to runoff, and FC the case studies that failed due to runoff. FC(1) corresponds to Watford case after the construction of the embankment access and FC(2) before the construction.

Table 9-13 Summary of the stability assessments using the novel method

Watford (FoS)						
Case Study	**SC1**	**SC2**	**SC3**	**SC4**	**FC1**	**FC2***
Real Outcome	**Stable**	**Stable**	**Stable**	**Stable**	**Unstable**	**Semi-stable**
DNM	**1.34**	**1.86**	**1.02**	**3.25**	**0.51**	**1.03**
RRM	**1.13**	**1.88**	**1.02**	**1.94**	**0.45**	**0.85**
St Bees (FoS)						
Case Study	**SC1**	**SC2**	**SC3**	**FC1**	**FC2**	
Real Outcome	**Stable**	**Stable**	**Stable**	**Unstable**	**Unstable**	
DNM	**1.11**	**4.30**	**1.28**	**0.92**	**0.77**	
RRM	**1.34**	**3.3**	**1.32**	**0.97**	**0.55**	
Beaminster North Portal (FoS)						
Case Study	**SC1**	**FC1**	**FC2**			
Real Outcome	**Stable**	**Unstable**	**Unstable**			
DNM	**7.72**	**0.83**	**0.43**			
RRM	**12.5**	**0.45**	**0.83**			
Beaminster South Portal (FoS)						
Case Study	**SC1**					
Real Outcome	**Stable**					
DNM	**1.47**					
RRM	**3.33**					
Loch Treig (FoS)						
Case Study	**SC1**					
Real Outcome	**Stable to runoff**					
DNM	**3.24**					
RRM	**5.71**					

***Calculation of FC before the construction of the embankment access.**

From Table 9-13, the two variants of the novel method were successful assessing the vulnerability of failure against runoff generated debris flow in the 16 cases analysed. In addition, the maximum steepness of stable cuttings in Grade D_c calculated by the novel method (65°) agreed well with the cuttings at Hooley (60°-70°).

9.7 Discussion

The novel method has been tested against 17 real case studies of transportation slopes: (5 at Watford before WB earthworks, 1 at Watford after WB earthworks, 5 at St Bees, 4 at Beaminster, 1 t Loch Treig and 1 at Hooley). The validity of the novel method was tested against cuttings that failed and cuttings that remained stable but located at water concentration places.

The assessment of the vulnerability against runoff generated debris flow was carried out following the well-defined 7 steps methodology introduced in Table 8-2.

All the cases were analysed using 1m resolution DTM. Further attempts were made using 2m DTM leading to a significant reduction in processing time, but the maximum shear stresses obtained were significantly lower and in overall the method became less conservative. An increase in resolution using 0.5m DTM resulted in similar results to 1m DTM at Watford.

The implementation of 1m DTM in FLOW-3D resulted in colour maps of superficial shear stresses that agreed well with the location of the drainage lines calculated in ArcGIS. This result showed confidence that the shallow water equations used in FLOW-3D and the algorithm behind ArcGIS to calculate the drainage lines, resulted in similar distribution of water flowing over the areas analysed.

Runoff generated debris flows analysed using the shallow water equations in FLOW-3D were all located in areas of high superficial shear stresses (except for Hooley where it is N/A). The use of shallow water equations showed on its own an important contribution demonstrating that the locations more vulnerable to runoff generated debris flows can be assessed using numerical simulations.

In particular, by analysing the shear stresses at Watford cutting before and after the earthworks carried out within the catchment, a significant increase in shear stresses at the cutting after the earthworks was obtained in FLOW-3D using the DNM. The same conclusion was obtained in RRM where a dramatic increase of the contributing catchment was obtained in ArcGIS.

The angle of the cuttings plays an important role in the calculation of shear stresses using the RRM. The use of drainage lines to calculate the cutting profiles, supposed an important contribution as they can be obtained unambiguously following the steepest path of water flowing down the slope faces. For the cases analysed, an average angle of

the cutting profiles was the most sensible approach to obtain appropriate shear stresses in RRM. In some of the cases analysed, localised steeper angles were present in the cutting face, however, for local over steepness of just a few meters, water may not have sufficient length to reach the terminal velocity associated to the steeper angle, and using the maximum inclination of the cuttings in RRM can result in overconservative values of shear stresses.

Some of the cuttings analysed showed catchments that gradually reduced in width as they approached the crest of the cutting (e.g. SC1, SC2 and FC1 at St Bees, SC1, SC2, SC3, SC4 and FC at Watford and FC1, FC2, SC1 at Beaminster north portal). However, other cuttings showed lateral accumulation of water at the cutting face that resulted in a gradual increase of flow rate along the cuttings (e.g. FC2 and SC3 at St Bees). In these cases, the contributing catchment area can vary significantly depending on the point selected at the cutting face and the flow rate near the toe of the cutting was used in the calculations for a conservative approach.

One of the limitations of RRM is the assumption of water runoff width of 1m. As the topography of cutting faces can be very variable with some of them presenting features leading to funnelling of water, the use of 1m width worked relatively well in the cases analysed and validated the purpose RRM was designed for: filtering those cases with potential to failure. However, non-realistic values of superficial shear stress cannot be ruled out in future analyses, although it would likely result in overconservative calculations.

Both the DNM and the RRM approaches agreed well in the assessment of the vulnerability of cuttings except in the vulnerability of Watford cutting before WB earthworks. However, the disagreement was not substantial.

Regarding the FoS of the other cases analysed, whereas in some of the cases DNM and RRM agreed well, other cases resulted in RRM having a more or less conservative approach than DNM. The difference could be attributed to cuttings having more or less than 1m width water runoff.

It was important to recognise elements in the topography that are not present in DTM due to more recent construction and influenced the movement of superficial water.

The most significant case was at Watford, where the construction of an artificial barrier was not present in the DTM. A barrier had to be included in the 1m DTM to analyse this case that otherwise would have led to an inconclusive cause of failure.

The novel method was applied to the Watford cutting failure before and after the construction of the embankment access. From the application of FLOW-3D using shallow water equations, the results showed a significant increase in the superficial shear stress at the face of the cutting in relation to the same rainfall event without the presence of the embankment access.

The same result was showed by in RRM after obtaining the catchment areas. The embankment access showed a significant increase in the catchment draining to the failed cutting after the construction of the embankment access.

The application of DNM and RRM showed that the cutting was extremely vulnerable to runoff generated debris flow for the rainfall event with FoS of 0.51 from DNM and 0.45 from RRM.

The analysis before the construction of the embankment access resulted in a FoS from DNM of 1.03 and from RRM of 0.85 indicating that the cutting was already in a situation of potential vulnerability to high-intensity and short-duration rainfall events.

The method predicted the vulnerability of Watford cutting in both the DNM and RRM variants and should the novel method was applied to Watford for a rainfall similar to the one at the day of failure, the high vulnerability of the cutting to runoff could have triggered asset management action to reduce the risk of failure.

A second casee was found at St Bees where a small earth abutment to the side of the road served to channelise water runoff. At one location of the road, the abutment was not present to give access to farm vehicles, and water drained to a contributing catchment at the FC2 cutting that eventually failed. This case was analysed using a 2m mesh in FLOW-3D in the area affected by this feature to remove the abutment barrier.

Both DNM and RRM did not predict in an initial assessment the vulnerability of this slope. However, after considering the removal of the abutment, it resulted in a significant increase of the catchment area from an adjacent parcel and both DNM and RRM obtained a high vulnerability for the slope.

This case demonstrated the importance of assessing field features before addressing the analysis.

The vulnerability of cuttings at Beaminster was predicted well by DNM and RRM. The difficulty associated to this case was caused by a vertical wall at the toe of the cuttings. DNM considered the wall as a steep slope from the 1m DTM and unreal values of the

shear stresses were calculated at the location of the wall. The problem was solved by disregarding shear stress values at the wall. It is therefore important to check for the existence of artificial structures and to interpret the shear stresses resulting from DNM.

For the case of Loch Treig, the location of the slope failure did not correspond with a drainage line and both RRM and DNM resulted in a small catchment and maximum shear stress considerable lower than the critical shear stress. It was in agreement with BGS, (2017) that attributed the slope failure to a 'shallow translational failure'.

In the case of Hooley, the recurrent failures at the central spine cutting where no catchments are possible, was enough evidence to dismiss runoff as the cause of failure. In this case, the application of DNM and RRM were reduced to the calculation of the critical angle of the cutting for a null shear stress. The critical shear stress vs angle of the slope chart, showed that for Grade D_c chalk, cutting angles above 65° are vulnerable to failure in agreement with Hooley cuttings where failures are common in the area.

Chapter10: Conclusions and recommendations

10.1 Overall conclusions

Since the year 1997, the asset management of railway earthworks have been carried out in a proactive manner, involving periodic inspections. Prioritisation of interventions is given by a safety risk matrix involving the risk of failure and the consequence of failure. The risk of failure is assessed by an algorithm based on the logging during cyclic inspections of a range of predefined features that may contribute to failure. In 2014, a fully statistical algorithm was introduced in the NR management system so that the risk of failure could be assessed as objectively as possible. However, failure records of cuttings indicate that the new algorithm did not result in a reduction of the number of failures.

The algorithm used from 2003 to 2014, accounted for the type of potential failures and it was considered a sounded approach. However, the current algorithm does not account for it and considers that features such as vegetation cover, tilting of tress, sign of slope erosion or presence of crest drainage among others, do contribute equally to any type of failure.

From 2012 to 2018, 56% of the earthwork failures corresponded to soil cutting failures. Shallow slope failures account for 89% of the soil cutting failures and they were involved in the 72% of derailments from 1994 to 2016.

In this thesis, a new algorithm for the type of shallow failures has been proposed based on the knowledge gained from the previous algorithms: fully statistical removing subjectivity associated to engineering judgement, and accounting for the potential types of failures.

Analysis of the current NR classification system showed a number of limitations that made the process of classification difficult. Lack of conservatism in the use of terms, overlapping of categories, classification based on triggering mechanisms difficult to detect by visual inspections and the lack of a detailed description affected the robustness of the classification system.

To implement the propose algorithm, a robust classification system of failures was required. A proposed classification system for shallow type of failures was introduced in this thesis that was specifically designed to be used in transportation cuttings. The classification system is based on visual features so that the process of classification can be carried out by a trained operative in a routine basis. The categories of the system

have been described in detail, the terms used correspond with definitions given in the most popular classification systems, and a system of scores has been introduced so that the process of classification can be performed as objectively as possible.

Runoff generated debris flows is one of the most frequent and dangerous type of failures in transportation cuttings and were involved in 5 out of the 9 derailments recorded since 2007.

In geotechnical engineering, continuum method of analysis has been the standard to assess the stability of cuttings. However, an analytical method to assess the vulnerability of cuttings against surface water runoff was still missing. Runoff generated debris flows involve the hydrodynamic forces applied by water runoff over the face of the cuttings, and it is in essence an event that cannot be analysed considering the soil as a continuum. Continuum methods of analysis are not designed to account for the dynamic forces of water runoff and therefore cannot be used for the assessment of vulnerability of cuttings against runoff.

The analysis of the Watford cutting failure is a representative example of a case where application of continuum methods of slope stability analysis would have assessed the Watford cutting as stable under the same rainfall event that led to failure.

The analysis of discrete soil particles and the interaction between particles and water can be carried out by using discrete numerical methods. However, it has not been until recently that advances in computational power have made these methods available for research.

In this thesis, the coupling of the discrete element method with computational fluid dynamics (CFD-DEM) has been applied to the analysis of runoff generated debris flows initiation for the first time.

The objective was to develop a method to assess the vulnerability of cuttings and natural slopes that can be implemented in the management system of transportation cuttings.

One of the difficulties using DEM was associated to the numerical simulations of natural soils. At the existing state of the art, DEM is still far from been able to simulate soils particle by particle due to the limitations of computational resources. However, there is enough evidence in runoff generated debris flows in clayey soils, that failures consist of a generalised dislodgement process of aggregates of particles (soil peds) rather than individual particles. The same evidence was found in Grade D_c type of chalk where chalk clasts has the potential to be dislodged by hydrodynamic forces.

Under this premises, the use of CFD-DEM was chosen to obtain the critical shear stress that superficial water must apply for the initiation of runoff generated debris flows.

DEM input parameters to simulate soil peds and chalk clasts were carefully examined. They were simulated as discrete spheres with a coefficient of rolling resistance of 0.1 to account for the non-sphericity.

Parameters corresponding with the stiffness of the particles (i.e. Young's Modulus, Poisson's ratio and the coefficient of restitution) did not show any effect in the calculation of the critical shear stress in the range of soils analysed. This result indicated that differences in plasticity of soils were not relevant in runoff generated debris flows. This result was relevant as the novel method developed can be potentially used for any variant of clayey soil and Grade D_c soil with the only consideration of unit weight and the angle of static friction as input parameters.

A careful investigation regarding the different values of bulk unit weight and angle of static friction was carried out for clayey soils and Grade D_c chalk commonly encountered in the UK. From this, a range of possible values was obtained to be applied in UK transportation cuttings and the novel method was designed to be applied for the whole range of parameters.

The vulnerability of cuttings against surface water runoff was investigated by numerically simulating flume tests where a flow of water was increased over a try flume of particles, simulating the conditions of different types of soils, until the triggering of a mass failure.

A number of numerical flume experiments were performed in CFD-DEM using the boundary soil parameters and representative values obtained from the case studies analysed to generate a chart correlating the critical shear stress for a range of slope angles.

The next step in the process for the development of the novel method was to investigate the actual shear stress that surface water runoff applies over the face of the cutting considering the characteristics of the rainfall event.

For this process, the shallow water equations resulted adequate to calculate the superficial shear stress in the catchment areas analysed. The implementation of 1m DTM to simulate the ground surface allowed an accurate representation of the ground surface and the movement of superficial water in the areas analysed. The application of shallow water equations to the areas where runoff generated debris flows occurred, showed that the locations where cuttings failed corresponded to the locations where higher shear

stresses were obtained. This result indicated a clear correlation between the failures investigated and hydrodynamic forces developed in their surfaces during rainstorms.

As the critical shear stress for the soil analysed was already obtained in CFD-DEM, the proposed method consisted of comparing the critical shear stress and the actual shear stress under the rainfall conditions at the moment of failure. The novel method was called the discrete-based numerical method or DNM.

Although the method resulted successful in all the cases analysed, the calculation of the actual shear stress seemed a parameter not familiar for geotechnical engineers to be used in a routine basis. A second variant of the novel method called the Rapid Routine Method (RRM) was designed as a less accurate simplified version of DNM to serve as a filter of what cases needed further evaluation in DNM. The principles behind the RRM was the calculation of the flow rate reaching the crest of the cutting from the catchment area and then, the derivation of the actual shear stress from the flow rate.

Catchment areas for transportation cuttings were calculated using ArcGIS. The software allowed an accurate representation of the catchments following an unambiguous process that can be replicated by any user. Considering the low values of permeability in the soils investigated, several orders of magnitude lower than the intensities of rainfall at the time of failure, ignoring infiltration processes for the calculation of the flow rate seemed to be a reasonable and a conservative assumption and the flow rate reaching the crest of the cutting was calculated as the product of area of the catchment by the intensity of the rainfall.

The following challenge was the derivation of the shear stress at the cutting face from the flow rate at crest. A numerical experiment consisting of a 1m wide tilting slab representing the cutting face for different slope angles was numerically simulated using CFD. Different flow rates were imposed at the crest of the slab and the average shear stress at the surface was calculated. The same procedure was repeated for a number of flow rates and slopes angles, and a chart shear stress vs slope angle was generated for a range of plausible flow rates.

For the derivation of the shear stress, the slab surface was designed as a rough wall to simulate the mesoscale protuberances of the soil surface. To do this, a Nikuradse roughness coefficient used for the simulation of asperities was utilised. Limitations of CFD do not allow for the effect of vegetation at the cutting face, however, consideration of vegetation would result in diminishing the velocity of water and hence the developing

shear stresses, and the conservative assumption of bare soils was considered in the analysis.

The movement of surface water runoff flowing down the cutting face is irregular and the assumption of the cutting face as a planar surface in the tilting slab, was one of the limitations of the method. The shear stress applied in real cuttings is higher when as a result of irregularities in the cutting face, the water is funnelled and hence the velocity increased for the same flow rate. For the application of the method to the case studies, a 1m width was assumed and the results agreed relatively well with the shear stresses obtained using DNM.

The novel method proposed was generated from the combination of multiple disciplines in numerical analysis. The validity of DNM and RRM to assess the vulnerability against runoff generated debris flows was tested against 17 real cuttings and natural slopes: 6 cases at Watford, 5 at St Bees, 4 at Beaminster, 1 at Loch Treig and 1 at Hooley.

Both the DNM and the RRM showed good performance in assessing the vulnerability against runoff, although some differences between the FoS obtained by DNM and RRM were found. The differences are attributed to the simplifications of the RRM method and mostly the assumption of runoff width =1. However, RRM proved to be a valuable alternative as a first and rapid assessment.

The novel method in the two variants offers a valuable contribution to the asset management of cutting and it can be applied for several purposes. The method could be applied to calculate a threshold rainfall intensity that makes cuttings vulnerable to failures, evaluate cuttings where runoff drainage is needed and prioritise interventions considering FoS as a comparative parameter.

10.2 Recommendations for Practice

A series of recommendations are listed in order to reduce the vulnerability of cuttings to runoff generated debris flows:

- Maintenance of dense vegetation in cuttings

  Maintaining vegetation in cuttings lower the velocity of runoff and consequently the bed shear stress. Additionally, the soil strength is enhanced by roots and the risk of runoff generated debris flows is reduced.

- Use of DTMs to locate cuttings more at risk of runoff generated debris flows

The use of DTMs has been proved successful in the identification of low points where runoff is concentrated and can be used as a tool to locate the cuttings more at risk of runoff generated debris flows

- Construction and maintenance of crest drains

  Construction of crest drainages in cuttings located at low points would avoid funnelling of water at the crest and would reduce the vulnerability of cuttings to runoff generated debris flows.

- Regrading of steep cuttings

  Regrading of identified vulnerable cuttings would lead to a higher stability against runoff generated debris flows

10.3 Recommendations for Further Work

The novel method has been developed for chalk and clayey soils and verified for 17 real cases. The assumption of 10cm diameter particles that worked well for clayey soils and Grade D_c chalk should be analysed for other type of soils. Then, additional soils can be implemented using the same methodology so that to obtain a critical shear stress threshold chart for every soil of interest in the UK railway network.

The novel method was designed on the assumption that the ground surface is impermeable. This assumption worked well for high intensity-short duration rainstorms in relatively small catchment areas. For the expansion of the novel method to larger catchments, lower intensities with higher duration of rainfall could lead to high flow rates at the crest of the cutting and therefore shear stresses with the potential to trigger debris flows. Further investigation considering infiltration could be implemented in the DNM approach and checked against case studies with larger catchment areas.

The assumption of n=1 could be further investigated by analysing the case studies with different values of n to obtain the value that best approximate the DNM.

The UKCP18 Scientific Report (Murphy et al., 2018), foresees a future scenario where as a consequence of the climate change, wetter winters (December-January-February) with an increasing number of days of heavier precipitation will become more frequent. Particularly, UKCP18 predict increases in hourly precipitation extremes where by 2070 rainfall associated with an event that occurs typically once every 2 years will increase by 25%. As such, as an additional opportunity for further work, the novel method could be

utilised as a tool to assess the impact of climate change in the stability of transportation cuttings.

References

Aberg, B. (1993) Washout of grains from filtered sand and gravel materials. **Journal of Geotechnical Engineering**, 119 (1): 36–53

AECOM (2019) **Ground Investigation Report** [online]. West Berkshire. Available from: https://assets.publishing.service.gov.uk/government/uploads/system/uploads/attachment_data/file/871098/RFI2859_-_Annex_B_-_Part_1.pdf

Afkhami, M., Hassanpour, A., Fairweather, M., et al. (2015) Fully coupled les-dem of particle interaction and agglomeration in a turbulent channel flow. **Computers & Chemical Engineering**, 78: 24–38

Ahmadi, G. (2005) **Lift Force** [online]. Available from: https://webspace.clarkson.edu/projects/crcd/public_html/me637/notes/aerosols/aerosols_page11.html [Accessed 1 June 2019]

Aitken, J.F., Ball, D.. F., Gould, D., et al. (2003) "Ground stability and foundation conditions, Cainozoic of north-east Scotland." In **Cainozoic geology and landscape evolution of north-east Scotland. Memoir of the British Geological Survey, sheets 66E, 67, 76E, 77, 86E, 87W, 87E, 95, 96W, 96E and 97 (Scotland).**

Aktas, Y., Stocker, J., Carruthers, D., et al. (2017) A sensitivity study relating to neighbourhood-scale fast local urban climate modelling within the built environment. **Procedia Engineering**, 198: 589 – 599

Allen, R.G., Pereira, L.S., Raes, D., et al. (1998) Crop evapotranspiration - Guidelines for computing crop water requirements. **FAO Irrigation and drainage.Food and Agriculture Organization of the United Nations.**, 56

Aluwihare, S. and Watanabe, K. (2003) Measurement of evaporation on bare soil and estimating surface resistance. **Journal of Environmental Engineering**, 129 (12): 1157–1168

Amos, C.L., Feeney, T., Sutherland, T.F., et al. (1997) The stability of fine-grained sediment from the Frase River Delta. **Estuarine, Coastal and Shelf Science**, 45: 507–524

An, H.C., Ouyang, C.J., Zhao, C., et al. (2020) Landslide dynamic process and parameter sensitivity analysis by discrete element method: the case of Turnoff Creek rock avalanche. **Journal of Mountain Science**, 17 (7): 1581–1595

Andersson, T. (1969) Small-scale variations of the contamination of rain caused by washout from the low layers of the atmosphere. **Tellus**, 21 (5): 685–692

ANSYS Fluent (2011) **ANSYS FLUENT Theory Guide**

ANSYS Fluent (2013) **ANSYS Fluent User's Guide**

Armanini, A. and Gregoretti, C. (2005) Incipient sediment motion at high slopes in uniform flow condition. **Water Resources Research**, 41 (12): 1–8

Arnold, T. (2014) "Construction Camden Town to Cheddington." In **Notes and extracts on the history of the London and Birmingham railway**.

Ashcroft, D. (2014) **Council tree felling may have caused landslide which killed couple, inquest told** [online]. Available from: https://www.telegraph.co.uk/news/uknews/road-and-rail-transport/10660626/Council-tree-felling-may-have-caused-landslide-which-killed-couple-inquest-told.html [Accessed 19 June 2019]

Atkins (2012) **Stafford Area Improvements Norton Bridge Grade Separation GRIP 4 Design** [online]. Available from: https://infrastructure.planninginspectorate.gov.uk/wp-content/ipc/uploads/projects/TR040004/TR040004-000206-5.3 Norton Bridge Final DCO - ES Volume 3 Report 11 Part 2.pdf

Ayres, Q. (1936) **Soil Erosion and its Control**. MeGraw-Hill Book Company

Aysen, A. (2002) **Soil Mechanics: Basic Concepts and Engineering Applications**. CRC Press

Babtie Group (2003) **Development of the Soil Slope Hazard Index and Associated Algorithm**

Bagnold, R.A. (1938) The movement of desert sand. **A Mat**, 157: 594–620

Bah, A.R., Kravchuk, O. and Kirchhof, G. (2009) Sensitivity of drainage to rainfall, vegetation and soil characteristics. **Computers and electronics in agriculture**, 68 (1): 1–8

Bai, Y. and Bai, Q. (2005) **Subsea pipelines and risers**. Elsevier

Bam Ritchies (2010) **Hooley cutting. Geotechnical Report**.

Baran, O., Kodl, P. and Aglave, R.H. (2013) "DEM simulations of fluidized bed using a scaled particle approach." In **Particle Technology Forum**. **2013**. pp. 1–9

Barbour, S.L., Sladen, J. and Wright, I. (2006) The design and construction of a soil vapor barrier in Caerphilly, South Wales, UK. **Canadian Geotechnical Society Conference,**

Saskatoon, Saskatchewan.

Barry, R.G. and Chambers, R.E. (1966) A preliminary map of summer albedo over England and Wales. **Quarterly Journal of the Royal Meteorological Society**, 92 (394): 543–548

Batalha, M.S., Barbosa, M.C., Faybishenko, B., et al. (2018) Effect of temporal averaging of meteorological data on predictions of groundwater recharge. **Journal of Hydrology and Hydromechanics**, 66 (2): 143–152

Bates, P.D., Lane, S.N. and Ferguson, R.I. (2005) **Computational fluid dynamics: applications in environmental hydraulics**. John Wiley & Sons

Baum, R.L., Savage, W.Z. and Godt, J.W. (2008) TRIGRS — A Fortran Program for Transient Rainfall Infiltration and Grid-Based Regional Slope-Stability Analysis, Version 2.0. **U.S. Geological Survey Open-File Report**, (2008–1159): 75

Baum, R.L., Savage, W.Z. and Wasowski, J. (2003) Mechanics of earth flows. **Proceedings of the International Conference FLOWS, Sorrento, Italy.**

BBC News (2014) **Beaminster tunnel landslide warning ahead of deaths** [online]. Available from: https://www.bbc.co.uk/news/uk-england-dorset-26338593

BBC NEWS (2016) **Two hurt as train derailed in flood landslide near Watford Junction** [online]. Available from: https://www.bbc.co.uk/news/uk-england-beds-bucks-herts-37382635 [Accessed 22 July 2019]

Bear, J. and Corapcioglu, M.Y. (2012) **Fundamentals of transport phenomena in porous media**. Springer Science & Business Media

Bell, F.G. (1977) A note on the physical properties of the chalk. **Engineering Geology**, 11 (3): 217–225

Bell, F.G., Culshaw, M.G. and Cripps, J.C. (1999) A review of selected engineering geological characteristics of English Chalk. **Engineering Geology**, 54: 237–269

Bennett, H.H. (1939) **Soil conservation**. McGraw Hill, New York

Berti, M., Bernard, M., Gregoretti, C., et al. (2020) Physical interpretation of rainfall thresholds for runoff-generated debris flows. **Journal of Geophysical Research: Earth Surface**, 125 (6)

Berti, M. and Simoni, A. (2005) Experimental evidences and numerical modelling of debris flow initiated by channel runoff. **Landslides**, 2 (3): 171–182

BGS (2017) **Stob Coire Sgriodain landslide, Scottish Highlands** [online]. Available from: https://www.bgs.ac.uk/landslides/Tulloch.html [Accessed 30 August 2019]

Birch, G.P. and O'Donovan, A.J. (2015) Hooley cutting stabilisation Projet de stabilisation de la voie ferrée de Hooley. **Proceedings of the XVI ECSMGE Geotechnical Engineering for Infrastructure and Development** [online]. Available from: https://www.icevirtuallibrary.com/doi/pdf/10.1680/ecsmge.60678.vol4.240

Bishop, A.W. (1973) The stability of tips and spoil heaps. **Quarterly Journal of Engineering Geology and Hydrogeology** [online], 6 (3–4): 335–376. Available from: http://qjegh.lyellcollection.org/cgi/doi/10.1144/GSL.QJEG.1973.006.03.15

Bittelli, M., Ventura, F., Campbell, G.S., et al. (2008) Coupling of heat, water vapor, and liquid water fluxes to compute evaporation in bare soils. **Journal of Hydrology**, 362 (3–4): 191–205

Blijenberg, H.M., De Graaf, P.J., Hendriks, M.R., et al. (1996) Investigation of infiltration characteristics and debris flow initiation conditions in debris flow source areas using a rainfall simulator. **Hydrological Processes**, 10 (11): 1527–1543

Boon, D., Kirkham, M. and Scheib, A. (2014) **Physical properties of till deposits from Anglesey, north west Wales** [online]. Available from: http://nora.nerc.ac.uk/id/eprint/510871/1/OR14052.pdf

Borgomeo, E., Hebditch, K.V., Whittaker, A.C., et al. (2014) Characterising the spatial distribution, frequency and geomorphic controls on landslide occurrence, Molise, Italy. **Geomorphology**, 226: 148–161

Bouchemella, S., Ichola, I.A. and Séridi, A. (2016) "Estimation of the empirical model parameters of unsaturated soils." In **E3S Web of Conferences. Vol. 9**. **2016**

Boutrup, E. (1977) Computerized Slope Stability Analysis for Indiana Highways. **Joint Highway Research Project**. 1

BRD (2018) **Ground Investigation** [online]. Rainham. Available from: http://walterandrandall.co.uk/wp-content/uploads/2018/03/BRD3008-OR3-A-Rainham-SI.pdf

Brezgin, D.V., Aronson, K.E., Mazzelli, F., et al. (2017) The surface roughness effect on the performance of supersonic ejectors. **Thermophysics and Aeromechanics**, 24 (4): 553–561

Briggs, K. (2010) Charing Embankment : Climate change impacts on embankment hydrology. **Ground Engineering**, 43 (6): 28–31

Briggs, K., Smethurst, J. and Powrie, W. (2014) Modelling the influence of tree removal on embankment slope hydrology. **Landslide Science for a Safer Geoenvironment**, 1: 241–246

Briggs, K.M. (2011) **Impacts of climate and vegetation on railway embankment hydrology**. University of Southampton

Briggs, K.M., Smethurst, J.A., Powrie, W., et al. (2013) Wet winter pore pressures in railway embankments. **Proceedings of the institution of civil engineers – geotechnical engineering**, 166 (5): 451–465

Briggs, K.M., Smethurst, J.A., Powrie, W., et al. (2016) The influence of tree root water uptake on the long term hydrology of a clay fill railway embankment. **Transportation Geotechnics**, 9: 31–48

Brinson, H.F. and Brinson, L.C. (2015) **Polymer engineering science and viscoelasticity**. New York: Springer

Brooks, R.H. and Corey, a T. (1964) Hydraulic properties of porous media. **Hydrology Papers, Colorado State University. Fort Collins CO**, 3 (3): 27 pgs

Brownlie, W.R. (1981) **Prediction of Flow Depth and Sediment Discharge in Open Channels**

Buchanan, P. and Savigny, K.W. (1990) Factors controlling debris avalanche initiation. **Canadian Geotechnical Journal**, 27 (5): 659–675

Buffington, J.M. and Montgomery, D.R. (1998) A systematic analysis of eight decades of incipient motion studies, with special reference to gravel-bedded rivers. **Water Resources Research**, 33 (8): 1993–2029

Bundy, S. (2013) Geotechnical properties of chalk putties. **Doctoral dissertation, University of Portsmouth**

Burcharth, H.F. and Andersen, O.K. (1995) On the one-dimensional steady and unsteady porous flow equations. **Coastal engineering**, 24 (3–4): 233–257

Burland, J.B. and Lord, J.A. (1970) "The load deformation behaviour of the Middle Chalk at Mundford, Norfolk; A comparison between full scale performance and insitu and laboratory measurements." In **Proc. Cnnf. on Insitu Investigations in Soils and Rocks,**

B.G.S. London. **1970**

C.C.S. (2014) **Site Investigation Report. Dilke Street London**. [online]. Available from: https://www.rbkc.gov.uk/idoxWAM/doc/Other-1486184.pdf?extension=.pdf&id=1486184&location=volume2&contentType=application/pdf&pageCount=1

Cai, Z., Raymond, G.P. and Bathurst, R.J. (1994) Estimate of static track modulus using elastic foundation models. **Transportation Research Record**, 1470: 65

Camillo, P.J. and Gurney, R.J. (1986) A resistance parameter for bare-soil evaporation models. **Soil Science**, 141 (2): 95–105

Cammeraat, L.H. (2002) A review of two strongly contrasting geomorphological systems within the context of scale. **Earth Surface Processes and Landforms**, 27: 1201–1222

Cannon, S.H., Gartner, J.E., Parrett, C., et al. (2003) Wildfire-related debris flow generation through episodic progressive sediment bulking processes, western USA. **Proceedings of the Third International Conference on Debris-Flow Hazards Mitigation**, pp. 71–82

Casagli, N., Ermini, L. and Rosati, G. (2003) Determining grain size distribution of the material composing landslide dams in the Northern Apennines: sampling and processing methods. **Engineering geology**, 69 (1–2): 83–97

Cawsey, D.C. and Farrar, N.S. (1976) A simple sliding apparatus for the measurement of rock joint friction. **Géotechnique**, 26: 382–386

Cebeci, T. and Bradshaw, P. (1977) **Momentum transfer in boundary layers**. McGraw-Hill New York

Chang, Y.S. and Scotti, A. (2006) Turbulent convection of suspended sediments due to flow reversal. **J Geophys Res Oceans**, 111 (C7)

Chen, F. (2009) **Coupled flow discrete element method application in granular porous media using open source codes**. University of Tennessee

Chen, F., Drummb, E.C. and Guiochon, G. (2011) Coupled discrete element and finite volume solution of two classical soil mechanics problems. **Computers and Geotechnics**, 38 (5): 638–647

Chen, H., Zhang, X., Abla, M., et al. (2018) Effects of vegetation and rainfall types on surface runoff and soil erosion on steep slopes on the Loess Plateau, China. **Catena**, 170:

141–149

Chen, J. (2011) **Discrete element method (DEM) analyses for hot-mix asphalt (HMA) mixture compaction**. University of Tennessee

Chen, J., Wang, Y., Li, X., et al. (2015) Erosion prediction of liquid-particle two-phase flow in pipeline elbows via CFD–DEM coupling method. **Powder technology**, 282: 25–31

Chiew, Y.M. and Parker, G. (1994) Incipient Sediment Motion on Non-Horizontal Slopes. **J. Hydra. Res.**, 32 (5): 649–660

Cho, S.E. (2014) Probabilistic stability analysis of rainfall-induced landslides considering spatial variability of permeability. **Engineering Geology** [online], 171: 11–20. Available from: http://dx.doi.org/10.1016/j.enggeo.2013.12.015

Christensen, B.A. (1995) Incipient sediment motion on non horizontal slopes. **Discussion Journal of Hydraulics Research**, 33 (5): 725–728

Clarke, B.G. (2017) **Engineering of glacial deposits**. CRC Press

Clarke, B.G. (2018) The engineering properties of glacial tills. **Geotechnical Research**, 5 (4): 262–277

Clarke, B.G., Hughes, D.B. and Hashemi, S. (2008) Physical characteristics of subglacial tills. **Geotechnique**, 58 (1): 67–76

Clayton, C.R.I. (1977) "Some properties of remoulded chalk." In **Proc 9th Int Conf Soil Mech and Found Engg. Vol 1**. **Tokyo**. **1977**. pp. 65–68

Clayton, C.R.I. (1978) **Chalk as Fill**. University of Surrey

Climent, N., Arroyo, M., O'Sullivan, C., et al. (2014) Sand production simulation coupling DEM with CFD. **European Journal of Environmental and Civil Engineering**, 18 (9): 983–1008

Concept (2016) **Geotechnical and geochemical interpretative report**. [online]. Available from: planbuild.southwark.gov.uk

Coussot, P. and Meunier, M. (1996) Recognition, classification and mechanical description of debris flows. **Earth-Science Reviews**, 40: 209–227

Crabb, G.I. and Atkinson, J.H. (1991) "Determination of soil strength parameters for the analysis of highway slope failures." In **Slope stability engineering developments and applications: Proceedings of the international conference on slope stability organized**

by the Institution of Civil Engineers and held on the Isle of Wight. **1991**. pp. 13–18

Crapper, M., Fell, M. and Gammoh, I. (2014) Earthworks risk assessment on a heritage railway. **Proceedings of the Institution of Civil Engineers-Geotechnical Engineering**, 167 (4): 344–356

Croney, D. and Coleman, J.D. (1954) Soil structure in relation to soil suction (pF). **Journal of Soil Science**, 5 (1): 75–84

Crosta, G.B., Frattini, P. and Fusi, N. (2007) Fragmentation in the Val Pola rock avalanche, Italian alps. **Journal of Geophysical Research: Earth Surface**, 112 (F1)

Crow, P. (2005) The Influence of Soils and Species on Tree Root Depth. **Forestry Commission** [online]. Available from: https://www.forestry.gov.uk/pdf/FCIN078.pdf/$FILE/FCIN078.pdf

Cruden, D. and Varnes, D. (1996) Landslide Types and Processes. **Transportation Research Board, U.S. National Academy of Sciences, Special Report**, 247: 36–75

Culshaw, M.G., Entwisle, D.C., Giles, D.P., et al. (2017a) Chapter 6 Material properties and geohazards. **Geological Society, London, Engineering Geology Special Publications**, 28: 599–740

Culshaw, M.G., Entwisle, D.C., Giles, D.P., et al. (2017b) "Material properties and geohazards." In **Engineering geology and geomorphology of glaciated and periglaciated terrains**. London, UK: Geological Society of London. pp. 599–740

Cundall, P.A. (1971) "A computer model for simulating progressive large scale movements in blocky rock systems." In **Symposium of the International Society for Rock Mechanics**. **France**. **1971**

Cundall, P.A. and Strack, O.D.L. (1979) A discrete numerical model for granular assemblies. **Geotechnique**, 29 (1): 47–65

D'Apuzzo, M., Evangelisti, A. and Nicolosi, V. (2017) "Preliminary investigation on a numerical approach for the evaluation of road macrotexture." In **Computational Science and its Applications**. pp. 157–173

Degetto, M., Gregoretti, C. and Bernard, M. (2015) Comparative analysis of the differences between using LiDAR and contour-based DEMs for hydrological modeling of runoff generating debris flows in the Dolomites. **Frontiers in Earth Science**, 3: 21

Dey, S. and Debnath, K. (2000) Influence of StreamWise Bed Slope on Sediment

Threshold Under Stream Flow. **Irrig. and Drain. Engrg. ASCE.**, 126 (4): 255–263

Doherty, E., Kelly, P. and Crapper, M. (2013) Evaluation of a risk assessment system for heritage railway earthworks. **Railway Engineering 2013**, pp. 9–10

Donnez, P. (2012) **ssentials of Reservoir Engineering, vol. II.**

Dronkers, J.J. (1964) **Tidal computations in rivers and coastal waters**. Amsterdam

Dubina, R. and Eliáš, J. (2016) Effect of rolling resistance in DEM models with spherical bodies. **Transactions of the VŠB–Technical University of Ostrava, Civil Engineering Series**, 16 (2): 11–18

Duck, R. (2015) **On the Edge**. Edinburgh University Press

Duncan, J.M. and Wright, S.G. (1980) The accuracy of equilibrium methods of slope stability analysis. **Engineering geology**, 16 (1–2): 5–17

Dutykh, D. and Clamond, D. (2016) Modified Shallow Water Equations for significantly varying seabeds. **Applied Mathematical Modelling**, 40 (23–24): 9767–9787

Eckersley, D. (1990) Instrumented laboratory flowslides. **Geotechnique**, 40: 489–502

EDEM (2014) **EDEM 2.6 Theory Reference Guide**. [online]. Available from: https://www.edemsimulation.com/content/uploads/2016/08/EDEM2.6_theory_reference_guide.pdf

Engelund, F. and Fredsøe, J. (1976) A sediment transport model for straight alluvial channels. **Hydrology Research**, 7 (5): 293–306

Ergun, S. (1952) Fluid flow through packed columns. **Chem. Eng. Prog**, 48: 88–94

Escauriaza, C. and Sotiropoulos, F. (2011) Lagrangian model of bed-load transport in turbulent junction flows. **J Fluid Mech**, 666: 36–76

ESRI (2011) **Arc Hydro Tools - Tutorial**. [online]. Available from: http://downloads.esri.com/archydro/archydro/Tutorial/Doc/Arc Hydro Tools 2.0 - Tutorial.pdf

Estrada, N., Azema, E., Radjai, F., et al. (2011) Identification of rolling resistance as a shape parameter in sheared granular media. **Phys Rev E**, 84: 011306

Eyles, N. and Sladen, J.A. (1981) Stratigraphy and geotechnical properties of weathered lodgement till in Northumberland, England. **Quarterly Journal of Engineering Geology and Hydrogeology**, 14 (2): 129–141

Farrell, E.R. and Lawler, M.L. (2001) Estimating ground movements in a very stiff lodgement till. **Geotechnical Engineering: Meeting Society's Needs: Proceedings of the Fourteenth Southeast Asian Geotechnical Conference, Hong Kong**, 1 (10–14): 309

Feddes, R.A., Kabat, P., Van Bakel, P., et al. (1988) Modelling soil water dynamics in the unsaturated zone—state of the art. **Journal of Hydrology**, 100 (1–3): 69–111

Feddes, R.A., Kowalik, P.J. and Zaradny, H. (1978) **Simulation of Field Water Use and Crop Yield**. Wageningen, The Netherlands: Centre for Agricultural Publishing and Documentation.

Feddes, R.A. and Lenselink, K.J. (1994) Evapotranspiration. **Drainage principles and applications**, 16: 145–173

Di Felice, R. (1994) The voidage function for fluid-particle interaction systems. **Journal of Multiphase Flow**, 20 (1): 153–159

Fellenius, W. (1926) **Erdstatische Berechnungen mit Reibung und Kohasion**. Berlin

Ferdowsi, B., Ortiz, C.P. and Jerolmack, D.J. (2018) Glassy dynamics of landscape evolution. **Academy of Sciences**, 115 (19): 4827–4832

Ferley, S.J.J. (2013) **An examination of the effects of geological and glacigenic controls on the engineering properties of tills using a domain based approach** [online]. University of Birmingham. Available from: https://etheses.bham.ac.uk/id/eprint/5187/2/Ferley14PhD.pdf

Fernández-Pato, J., Caviedes-Voullième, D. and García-Navarro, P. (2016) Rainfall/runoff simulation with 2D full shallow water equations: Sensitivity analysis and calibration of infiltration parameters. **Journal of hydrology**, 536: 496–513

Fernandez Luque, R. and Van Beek, R. (1976) Erosion and transport of bed-load sediment. **Journal of hydraulic research**, 14 (2): 127–144

Ferrero, A.M., Segalini, A. and Umili, G. (2015) Experimental tests for the application of an analytical model for flexible debris flow barrier design. **Eng Geol**, 185 (33–42)

Fletcher, M.S. and Mizon, D.H. (1983) "Piles in chalk for Orwell Bridge." In **ICE symposium on advances in piling and ground treatment for foundations**. **London**. **1983**

FLOW 3D (2016) **FLOW 3D, Users Manual**. [online]. Available from: flow3d.com

Foster, J. (2010) **Holderness Case Study** [online]. Available from:

https://pt.slideshare.net/fozzie/holderness-case-study/7 [Accessed 28 September 2020]

Fournier, F. (1956) The effect of climatic factors on soil erosion estimates of solids transported in suspension in runoff. **Association Hydrologic Int**, 38

Fredlund, D., Rahardjo, H. and Fredlund, M. (2012) **Unsaturated Soil Mechanics in Engineering Practice**. p. 944

Fredlund, D.G. and Krahn, J. (1977) Comparison of slope stability methods of analysis. **Canadian Geotechnical Journal**, 14 (3): 429–439

Fredlund, D.G. and Rahardjo, H. (1993) **Soil Mechanics for Unsaturated Soils**. John Wiley & Sons.

Fredlund, D.G. and Xing, A. (1994) Equations for the soil-water characteristic curve. **Canadian Geotechnical Journal**, 31 (6): 1026–1026

Fugro (2016) **Ground Investigation** [online]. Hackney, London. Available from: http://planningdocs.hackney.gov.uk/NorthgatePublicDocs/00046396.pdf

Galliford-Costain-Atkins (2014) **Man Trunk UIDs – Eccles WWTW – Tunnels and Shafts**. [online]. Available from: http://www.hwa.uk.com/site/wp-content/uploads/2018/02/2a.-Parsons-Brinckerhoff-Ground-Investigation-Report-Sept-2014.pdf

van Genuchten, M.T. (1980) A closed-form equation for predicting the hydraulic conductivity of unsaturated soils. **Soil science society of America journal**, 44 (5): 892–898

Goudie, A. (2004) **Encyclopedia of geomorphology (Vol. 2)**., 2

Green, W.H. and Ampt, G. (1911a) Studies on soil physics: I. Flow of air and water throught soils. **Journal of Agricultural Science**, 4 (1973): 1–24

Green, W.H. and Ampt, G.A. (1911b) Studies on soil physics: I. flow of air and water through soils. **Journal of Agricultural Science**, 4 (1–24)

Greenwood, J.R., Morgan, R.P.C., Coppin, N.J., et al. (2001) **Bioengineering: The Longham Wood Cutting Field Trial**

Gregoretti, C. (2000) The initiation of debris flow at high slopes: Experimental results. **Journal of Hydraulic Research** [online], 38 (2): 83–88. Available from: http://www.tandfonline.com/doi/abs/10.1080/00221680009498343

van de Griend, A.A. and Owe, M. (1994) Bare soil surface resistance to evaporation by vapor diffusion under semiarid conditions. **Water Resources Research**, 30 (2): 181–188

Ground and Water (2015) **Ground investigation report at Victoria House, Victoria Road.** [online]. Winchester. Available from: https://groundandwater.co.uk/wp-content/uploads/2018/11/GWPR1361-Victoria-House-Victoria-Road-updated-Ground-Investigation-Report-FULL-FINAL.pdf

Gu, X. and Yang, J. (2013) A discrete element analysis of elastic properties of granular materials. **Granular Matter**, 15 (2): 139--147

Gu, Z. and Wang, H. (1991) Gravity waves over porous bottoms. **Coastal engineering**, 15 (5): 497–524

Guo, C.X., Zhou, J.W., Cui, P., et al. (2014) A theoretical model for the initiation of debris flow in unconsolidated soil under hydrodynamic conditions. **Hazards and Earth System Sciences Discussions**, 2 (6): 4487–4524

Guo, J. (2002) "Hunter Rouse and Shield's Diagram." In **Advances in Hydraulics and Water Engineering, Proc. 13th IAHR-APD Congress, vol.2, World Scientific, Singapore**. **2002**

Gupta, A. (2016) Relative Effectiveness of Trees and Shrubs on Slope Stability. **Electron. J. Geotech. Eng**, 21: 737–753

Gupta, P. (2015) **Verification and validation of a DEM-CFD model and multiscale modelling of cohesive fluidization regimes**. University of Edinburgh

Gyr, A. and Schmid, A. (1997) Turbulent flows over smooth erodible sand beds in flumes. **Journal of Hydraulics Research**, 35 (4): 525–544

Halcrow, W. (1979) Felixstowe–Weedon Trunk Road A45 Ipswich By Pass Southern Section Orwell Bridge. **Supplementary site investigation report**

Hall, K.R., Smith, G.M. and Turcke, D.J. (1995) Comparison of oscillatory and stationary flow through porous media. **Coastal Engineering**, 24: 217–232

Hamza, O. and Bellis, A. (2008) Assessment of a bridge pier pile foundation subjected to bearing replacement. **Atkinsglobal Technical Journal** [online], 6. Available from: https://www.atkinsglobal.com/~/media/Files/A/Atkins-Corporate/group/sectors-documents/roads/library-docs/technical-journal-6/087-assessment-of-a-bridge-pier-pile.pdf

Hansen, W.R. (1973) Effects of the May 5-6, 1973, Storm in the Greater Denver Area, Colorado. **US Geological Survey**, 689

Harries, W.J.R., Hollyer, S.E. and Hopson, P.M. (1982) The sand and gravel resources of the country around Hemel Hempstead, St Albans and Watford, Hertfordshire. **Institute of Geological Sciences, Natural Environment Research Council**

Hashemi, S., Hughes, D.B. and Clarke, B.G. (2006) The characteristics of glacial tills from Northern England derived from a relational database. **Geotechnical & Geological Engineering**, 24 (4): 973–984

Hergarten, S. and Robl, J. (2015) Modelling rapid mass movements using the shallow water equations in Cartesian coordinates. **Natural Hazards and Earth System Sciences**, 15 (3): 671–685

Heyerdahl, H. (2017) **Influence of extreme long-term rainfall and unsaturated soil properties on triggering of a landslide- A case study** [online]. Available from: https://www.nat-hazards-earth-syst-sci-discuss.net/nhess-2017-410/nhess-2017-410.pdf [Accessed 16 June 2019]

Hicks, M.A., Brinkgreve, R.B. and Rohe, A. (2014) **Numerical Methods in Geotechnical Engineering**. CRC press

Higgibottom (1965) The engineering geology of chalk. **Symposium on chalk in earthworks and foundations**

Highland, L.M. and Bobrowsky, P. (2008) **The Landslide Handbook — A Guide to Understanding Landslides**

Le Hir, P., Cann, P., Waeles, B., et al. (2008) Erodibility of natural sediments: experiments on sand/mud mixtures from laboratory and field erosion tests. **Proceedings in Marine Science**, 9: 137–153

Holmes, J.D. (2018) **Wind loading of structures**. CRC press

Honorio, H.T. and Maliska, C.R. (2014) “On the performance of coupled and segregated methods for solving two-dimensional incompressible flows employing unstructured grids.” In **15th Brazilian Congress of Thermal Sciences and Engineering**. **2014**

Horn, H.M. and Deere, D.U. (1962) Frictional characteristics of minerals. **Geotechnique**, 12 (4): 319–335

Horton, H.E. (1940a) An approach toward a physical interpretation of infiltration

capacity. **Soil Science Society of America Proceedings**, 5: 399–417

Horton, R. (1940b) An approach toward a physical interpretation of infiltration capacity. **Soil Science Society of America**, 5: 399–417

Houwing, E.J. and van Rijn, L.C. (1997) In Situ Erosion Flume (ISEF): determination of bed-shear stress and erosion of a kaolinite bed. **Journal of Sea Research**, 39: 243–253

Huang, J., da Silva, M.V. and Krabbenhoft, K. (2013) Three-dimensional granular contact dynamics with rolling resistance. **Computers and Geotechnics**, 49: 289–298

Hugget, R.J. (1997) **Environmental Change: The evolving ecosphere**. London: Routledge Kegan & Paul

Hung, C., Liu, C.H. and Chang, C.M. (2018) Numerical investigation of rainfall-induced landslide in mudstone using coupled finite and discrete element analysis. **Geofluids**, p. 15

Hungr, O., Evans, S.G., Bovis, M.J., et al. (2001) A review of the classification of landslides of the flow type. **Environmental and Engineering Geoscience**, 7 (3): 221–238

Hungr, O., Leroueil, S. and Picarelli, L. (2014) The Varnes classification of landslide types, an update. **Landslides**, 11 (2): 167–194

Hutchinson, J.N. (1970) A Coastal Mudflow on the London Clay Cliffs at Beltinge, North Kent. **Geotechnique**, 20 (4): 412–438

Hutchinson, J.N. (1988) General report: Morphologycal and geotechnical parameters of landslides in relation to geology and hydrogeology. **Proceedings, Fifth International Symposium on Landslides**, 1: 3–35

Ikeda, S. (1982) Incipient motion of sand particles on side slopes. **Journal of the Hydraulic division, ASCE**, 108 (HY1)

Independent (2016) **Watford junction crash: London train derails in landslide before being hit by another train** [online]. Available from: https://www.independent.co.uk/travel/news-and-advice/london-midland-train-derails-watford-junction-euston-injuries-delayed-news-latest-cause-a7310646.html [Accessed 22 July 2019]

Israr, J. and Indraratna, B. Rujikiatkamjorn, C. (2016) Laboratory investigation of the seepage induced response of granular soils under static and cyclic loading. **Geotechnical Testing Journal**, 39 (5): 795–812

Iverson, R.M. (1997) The physics of debris flows. **Reviews of Geophysics** [online], 35 (3): 245–296. Available from: http://dx.doi.org/10.1029/97rg00426%5Cnhttp://doi.wiley.com/10.1029/97RG00426

Iverson, R.M. (2000) Landslide triggering by rain infiltration. **Water Resources Research**, 36 (7): 1897

Iverson, R.M. and Major, J.J. (1986) Groundwater seepage vectors and the potential for hillslope failure and debris flow mobilization. **Water Resour. Res.**, 22: 1543–1548

Iverson, R.M. and Reid, M.E. (1992) Gravity-driven groundwater flow and slope failure potential: 1. Elastic Effective-Stress Model. **Water Resources Research**, 28 (3): 925–938

Iverson, R.M., Reid, M.E. and LaHusen, R.G. (1997) Debris-flow mobilization from landslides. **Ann. Rev. Earth Planet. Sci.**, 25: 85–138

Jaeger, J. (2005) **New Solutions in Contact Mechanics**. Germany: WITpress

Jain, R.K. and Kothyari, U.C. (2009) Cohesion influences on erosion and bed load transport. **Water resources research**, 45 (6)

Janbu, N. (1954) "Application of Composite Slip Surface for Stability Analysis." In **European Conference on Stability of Earth Slopes, Stockholm. 1954**

Jardine, R.J., Symes, M.J. and Burland, J.B. (1984) The measurement of soil stiffness in the triaxial apparatus. **Geotechnique**, 34 (3)

Jenner, H.N. and Burfitt, R.H. (1974) "Chalk: An engineering material." In **meeting of the Southern Area of the Institution of Civil Engineers**. **Brighton**. **1974**

Jennings, J.E.B. and Burland, J.B. (1962) Limitations to the use of effective stresses in partly saturated soils. **Géotechnique**, 12 (2): 125–144

Jing, L., Kwok, F.C., Zhao, T., et al. (2018) Effect of Particle Size Segregation in Debris Flow Deposition: A Preliminary Study. **Proceedings of GeoShanghai 2018 International Conference: Geoenvironment and Geohazard. GSIC**, pp. 73–80

Johnson, K.L. (1987) **Contact Mechanics**. Cambridge: Cambridge University Press

Joy, D., Wear, R. and Holmes, P. (2017) **An Introduction to Cumbrian Railways**. Cumbrian Railways Association

Kafui, D.K., Johnson, S., Thornton, C., et al. (2011) Parallelization of a Lagrangian–Eulerian DEM/CFD code for application to fluidized beds. **Powder Technology**, 207 (1–3): 270–278

Kawano, K., Shire, T. and O'Sullivan, C. (2017) Coupled DEM-CFD analysis of the initiation of internal instability in a gap-graded granular embankment filter. **EPJ Web of Conferences**, 140

Kawano, K., Shire, T. and O'Sullivan, C. (2018) Coupled particle-fluid simulations of the initiation of suffusion. **Soils and foundations**, 58 (4): 972–985

Keefer, D.K. (1999) Earthquake-induced landslides and their effects on alluvial fans. **Journal of Sedimentary Research**, 69 (1): 84–104

Khan, H. and Pittam, J.T. (2018) **Discrete Element Modelling of Lateral Earth Pressure** [online]. Available from: http://demlateralearthpressure.weebly.com/index.html [Accessed 11 August 2019]

Kim, D., Kim, G. and Baek, H. (2015) Relationship between thermal conductivity and soil–water characteristic curve of pure bentonite-based grout. **International Journal of Heat and Mass Transfer**, 84: 1049–1055

Kimei, M. and Khabongo, L. (2004) **School Certificate Geography 3**. East African Publishers

Kohnke, H. and Bertrand, A. (1959) **Soil Conservaiton**. McGraw-Hill

Kojan, E., Foggin III, G.T. and Rice, R.M. (1972) Prediction and analysis of debris slide incidence by photogrammetry, Santa Ynez-San Rafael Mountains, California. **In Twenty-fourth IGC (Int. Geol. Conf.**, pp. 124–131

Kozmenko, A.S. (1954) **Principles of anti-erosion land-improvement**. Moscow

Kruggel-Emden, H., Simsek, E., Rickelt, S., et al. (2007) Review and extension of normal force models for the discrete element method. **Powder Technology**, 171 (3): 157–173

Kumar, N., Suhr, B., Marschnig, S., et al. (2019) Micro-mechanical investigation of railway ballast behavior under cyclic loading in a box test using DEM: effects of elastic layers and ballast types. **Granular Matter**, 21 (4): 106

Kuriqi, A., Koçileri, G. and Ardıçlıoğlu, M. (2019) Recalling Meyer-Peter and Müller Approach for Assessment of Bed-Load Sediment Transport. **2019**

Kvočka, D., Ahmadian, R. and Falconer, R. (2017) Flood inundation modelling of flash floods in steep river basins and catchments. **Water**, 9 (9): 705

Lai, X., Liao, K., Feng, H., et al. (2016) Responses of soil water percolation to dynamic

interactions among rainfall, antecedent moisture and season in a forest site. **Journal of Hydrology**, 540: 565–573

Lake, L. (1975) **The engineering properties of chalk with special reference to foundation design and performance**. University of Surrey

Lambe, T.W. and Whitman, R.V. (1969) **Soil mechanics**. John Wiley & Sons, New York

Larcher, W. (1975) **Physiological Plant Ecology**. New York: Springer Verlag

Lee, S.H. (2010) **Numerical modelling of rapidly varied river flow**. University of Nottingham

Leong, E.C. and Rahardjo, H. (1997) A review of soil-water characteristic curve equations. **J. Geotech. Geoenviron. Eng.**, 123 (12): 1106–1117

Li, H. (2013) **Discrete element method (DEM) modelling of rock flow and breakage within a cone crusher**. University of Nottingham

Li, X. and Zhao, J. (2016) Numerical simulation of dam break by a coupled CFD-DEM approach. **Japanese Geotechnical Society Special Publication**, 2 (18): 691–696

Liang, D., Özgen, I., Hinkelmann, R., et al. (2015) Shallow water simulation of overland flows in idealised catchments. **Environmental Earth Sciences**, 74 (11): 7307–7318

Lick, W., Jin, L. and Gailani, J. (2004) Initiation of movement of quartz particles. **J. Hydraul. Eng.**, 130 (8): 755–761

Little, J.A. (1984) **Engineering properties of glacial tills in the Vale of St. Albans.** City University

Liu, C., Yu, Z. and Zhao, S. (2020a) Quantifying the impact of a debris avalanche against a flexible barrier by coupled DEM-FEM analyses. **Landslides** [online], 17 (1): 33–47. Available from: https://link.springer.com/article/10.1007/s10346-019-01267-8

Liu, C., Zhixiang, Y. and Qiang, W. (2020b) A unified SHP-DEM-FEM approach for modelling of debris flow impacts on protective structures. **16th Internaitonal LS-DYNA Users Conference**

Liu, M., Wen, Y., Liu, R., et al. (2015) Investigation of fluidization behaviour of high density particle in spouted bed using CFD-DEM coupling method. **Powder technology**, 280: 72–82

Liu, W. and He, S. (2020) Comprehensive modelling of runoff-generated debris flow from

formation to propagation in a catchment. **Landslides**, 9: 1–16

Lord, J.A., Clayton, C.R. and Mortimore, R.N. (2002) **Engineering in chalk**. CIRIA.

Lord, J.A., Twine, D. and Yeow, H. (1994) Foundations in chalk.CIRIA Project Report PR11. **Construction Industry Research and Information Association.**, 11

Loveridge, F.A., Spink, T.W., O'Brien, A.S., et al. (2010) The impact of climate and climate change on infrastructure slopes, with particular reference to southern England. **Quarterly Journal of Engineering Geology and Hydrogeology**, 43 (4): 461–472

Lu, N. and Likos, W.J. (2006) Suction Stress Characteristic Curve for Unsaturated Soil. **Journal of geotechnical and geoenvironmental engineering**, 132 (2): 131–142

Lupini, J.F. (1980) **The residual strength of soils**. Imperial College of Science and Technology

Lupini, J.F., Skinner, A.E. and Waughan, P.R. (1981) The drained residual strength of cohesive soils. **Geotechnique**, 31 (2): 181–213

Luque, R.F. and van Beek, R. (1976) Erosion and Transport of Bed-Load Sediment. **J. Hydra. Res**, 14 (2): 127–144

Lyubimova, T., Lepikhin, A., Parshakova, Y., et al. (2016) The risk of river pollution due to washout from contaminated floodplain water bodies during periods of high magnitude floods. **Journal of Hydrology**, 534: 579–589

Maidment, D.R. and Morehouse, S. (2002) "Drainage systems." In **Arc Hydro. Gis for water resources**.

MAINLINE Project (2013) "Deliverable 2.2: Degradation and intervention modelling techniques." In **MAINtenance, renewal and Improvement of rail transport iNfrastructure to reduce Economic and environmental impacts**.

Makse, H.A., Johnson, D.L. and Schwartz, L.M. (2000) Packing of compressible granular materials. **Physical review letters**, 84 (18): 4160

Mantz, P.A. (1973) Cohesionless, fine graded, flaked sediment transport by water. **Nat. Phys. Sci. (Lond.)**, 246: 14–16

Marsland, A. and Powell, J.J.M. (1991) Field and laboratory investigations of the clay tills at the test bed site at the Building Research Establishment, Garston, Hertfordshire. **Geological Society, London, Engineering Geology Special Publications**, 7 (1): 229–238

Matthews, M.C. and Clayton, C.R. (1993) Influence of intact porosity on the engineering properties of a weak rock. **A Anagnostopoulos, F Schlosser, N Kalteziotis and R Frank (eds), Geotechnical Engineering of hard soils – soft rocks**, 1: 693–702

Matthews, M.C. and Clayton, C.R.I. (2004) Large diameter plate tests on weathered in-situ Chalk. **Quarterly journal of engineering geology and hydrogeology**, 37 (1): 61–72

McColl, S.T. (2015) Landslide causes and triggers. **Landslide Hazards, Risks and Disasters**, pp. 17–42

McGown, A. (1975) **Genetic influences on the nature and properties of basal melt out tills**. University of Strathclyde

McKee, C.R. and Bumb, A.C. (1984) "The importance of unsaturated flow parameters in designing a monitoring system for hazardous wastes and environmental emergencies." In **Proceedings of the Hazardous Materials Control Research Institute, National Conference**. **1984**. pp. 50–58

McKee, C.R. and Bumb, A.C. (1987) Flow-testing coalbed methane production wells in the presence of water and gas. **SPE formation Evaluation**, 2 (4): 599–608

Mehta, A.J., Hayter, E.J., Parker, W.R., et al. (1989) Cohesive sediment tranport. Part 1: Process description. **Journal of hydraulic engineering**, 115: 1076–1093

Meigh, A.C. and Early, K.R. (1957) Some physical and engineering properties of chalk. **Proceedings of the 4th International Conference on Soil Mechanics and Foundation Engineering**, 1: 68–73

Melchiorre, C. and Frattini, P. (2012) Modelling probability of rainfall-induced shallow landslides in a changing climate, Otta, Central Norway. **Climatic change**, 113 (2): 413–436

Meng, X.M., Jia, Y.G., Shan, H.X., et al. (2012) An experimental study on erodibility of intertidal sediments in the Yellow River delta. **International Journal of Sediment Research**, 27: 240–249

Mergili, M. (2008) **Integrated modelling of debris flows with Open Source GIS dissertation by**., (July)

Merwade, V. (2019) **Stream Network and Watershed Delineation using Spatial Analyst Hydrology Tools** [online]. Available from: https://web.ics.purdue.edu/~vmerwade/education/lab3.pdf

Meyer-Peter, E. and Müller, R. (1948) "Formulas for bed-load transport." In **IAHSR 2nd**

meeting, Stockholm, appendix 2. IAHR. 1948

Mochtar, H.I.B. and Mochtar, N.E.B. (2018) The Effect of Cracks Propagation on Cohesion and Internal Friction Angle for High Plasticity Clay. **International Journal of Applied Engineering Research**, 13 (5): 2504–2507

Molz, F.J. and Remson, I. (1970) Extraction term models of soil moisture use by transpiring plants. **Water Resour. Res**, 6: 1346–1356

Mongan, C.E. (1985) Validity of Darcy's law under transient conditions. **USGS Numbered Series**. 1331 p. 16

Monteith, J.L. (1965) Evaporation and environment. **Symp. Soc. Exp. Biol.**, 19: 205–234

Mortimore, R.N. (2014) **Logging the Chalk**. Caithness, Scotland: Whittles Publishing

Mouchel (2011) **Ground Investigation Report Volume 9 Section 3H - Findings of the Investigation, Section 3H:Tullyvar – Aughnacloy**.

Mualem, Y. (1976) A new model for predicting the hydraulic conductivity of unsaturated porous media. **Water resources research**, 12 (3): 513–522

Murphy, J.M., Harris, G.R., Sexton, D.M.H., et al. (2018) **UKCP18 Land Projections: Science Report**

Nelder, L.M., Gunn, D.A. and Reeves, H. (2006) Investigation of the geotechnical properties of a Victorian Railway Embankment. **1st Int. Conf. Railway Foundations**, pp. 34–47

Network Rail (2014a) Annual report and accounts. **Delivering a better railway for a better Britain**

Network Rail (2014b) **Examination of earthworks, NR/L3/CIV/065**., 5

Network Rail (2015a) **CP5 Earthworks Asset Policy**. Milton Keynes

Network Rail (2015b) **The management of reports of safety related events on buildings and civil engineering infrastructure, NR/L3/CIV/028**., (5)

Network Rail (2017a) Definition of soil cutting hazard index. **Standards, Network Rail. NR/L3/CIV/065/mod2**

Network Rail (2017b) **Management of reports of safety related geotechnical incidents, NR/L3/CIV/185**., 1

Network Rail (2017c) **NR/L2/CIV/086 Module 12. Definition of Earthwork Criticality**.

Network Rail (2018) **Earthworks Technical Strategy** [online]. Available from: https://cdn.networkrail.co.uk/wp-content/uploads/2018/07/Earthworks-Technical-Strategy.pdf

Ng, C.W.W. and Shi, Q. (1998) A numerical investigation of the stability of unsaturated soil slopes subjected to transient seepage. **Computers and geotechnics**, 22 (1): 1–28

Ng, T.T. (2006) Input parameters of discrete element methods. **Journal of Engineering Mechanics**, 132 (7): 723–729

Nieber, J.L. and Walter, M.F. (1981) Two-dimensional soil moisture flow in a sloping rectangular region: Experimental and numerical studies. **Water Resources Research**, 17 (6): 1722–1730

Ning, Z. and Ghadiri, M. (2006) Distinct element analysis of attrition of granular solids under shear deformation. **Chemical Engineering Science**, 61 (18): 5991–6001

Niyogi, P., Chakrabartty, S.K. and Laha, M.K. (2006) **Introduction to computational fluid dynamics**. India: Pearson India

Norouzi, H.R., Zarghami, R., Sotudeh-Gharebagh, R., et al. (2016) **Coupled CFD-DEM modeling: formulation, implementation and application to multiphase flows**. John Wiley & Sons.

Norris, J.E., Stokes, A., Mickovski, S.B., et al. (2008) **Slope stability and erosion control: ecotechnological solutions**. Springer Science & Business Media

Nosewicz, S., Rojek, J., Chmielewski, M., et al. (2017) Application of the Hertz formulation in the discrete element model of pressure-assisted sintering. **Granular Matter**, 19 (1): 16

Novak, V. (1987) Estimation of soil-water extraction patterns by roots. **Agricultural Water Management**, 12 (4): 271–278

Novák, V. (2012) **Evapotranspiration in the Soil-plant-atmosphere System**. Springer, Dordrecht

Nuth, M. and Laloui, L. (2008) Effective stress concept in unsaturated soils: clarification and validation of a unified framework. **International journal for numerical and analytical methods in Geomechanics**, 32 (7): 771–801

Nyambayo, V.P. and Potts, D.M. (2010) Numerical simulation of evapotranspiration using

a root water uptake model. **Computers and Geotechnics**, 37 (1–2): 175–186

O'Brien, A.S. (2013) The assessment of old railway embankments: time for a change? **Partial Saturation in Compacted Soils: Géotechnique Symposium in Print 2011**, pp. 19–32

O'Donovan, A.J. (2014) "The Hooley Cutting Stabilisation Project." In **YGG – Geotechnics in the Rail Industry**. **2014** [online]. Available from: https://www.ice.org.uk/ICEDevelopmentWebPortal/media/Documents/Regions/UK Regions/12th-May-2015-YGG-Hooley-Cutting-Stabilisation-Project.pdf

O'Sullivan, C. and Bray, J.D. (2004) Selecting a suitable time step for discrete element simulations that use the central difference time integration scheme. **Engineering Computations**, 21 (2/3/4): 278–303

ORR (2017) "chapter 6b: Civil Engineering Assets." In **Strategy for regulation of health and safety risks** [online]. Available from: https://orr.gov.uk/__data/assets/pdf_file/0005/24647/safety-strategy-chapter-6b-civil-engineering-assets.pdf

Otsubo, K. and Muraoka, K. (1988) Critical shear stress of cohesive bottom sediments. **Journal of Hydraulic Engineering**, 114 (10): 1241–1256

Özgen, I., Teuber, K., Simons, F., et al. (2015) Upscaling the shallow water model with a novel roughness formulation. **Environmental Earth Sciences**, 74 (11): 7371–7386

Ozulu, İ.M. and Gökgöz, T. (2018) Examining the stream threshold approaches used in hydrologic analysis. **ISPRS International Journal of Geo-Information**, 7 (6): 201

PA Media (2016) **Landslip caused the train to be derailed** [online]. Available from: https://www.mirror.co.uk/news/uk-news/train-derailed-watford-junction-due-8846468 [Accessed 13 August 2020]

Parasnis, D.S. (1952) A study of rock densities in the English Midlands. **Geophysical Supplements to the Monthly Notices of the Royal Astronomical Society**, 6 (5): 252–271

Parker, C. (2012) Stabilising Hooley Cutting. **therailengineer**, (97): 6–10

Parker, G. (1990) Surface-based bedload transport relation for gravel rivers. **Journal of hydraulic research**, 28 (4): 417–436

Penman, H.L. (1948) "Natural evaporation from open water, bare soil and grass." In **Proceedings of the Royal Society of London. Series A. Mathematical and Physical**

Sciences, 193. 1948

Penman, H.L. and Schofield, R.K. (1951) Some physical aspects of assimilation and transpiration. **Symp. Soc. Exptl. Biol**, 5 (115)

Perrochet, P. (1987) Water uptake by plant roots. A simulation model. **Journal of hydrology**, 95 (1–2): 55–61

Philip, J.R. and De Vries, D.A. (1957) Moisture movement in porous materials under temperature gradients. **Transactions American Geophysical Union**, 38 (2): 222–232

Plenker, D. and Grabe, J. (2016) "Simulation of sand particle transport by coupled CFD-DEM: First investigations." In **8th Int. Conf. Scour and Erosion**. **2016**. pp. 109–118

Poulos, H. (1989) Pile behaviour-theory and application. **Geotechnique**, 39 (3): 365–415

Power, C., Mian, J., Spink, T., et al. (2016) Development of an Evidence-based Geotechnical Asset Management Policy for Network Rail, Great Britain. **Procedia Engineering**, 143: 726–733

Powrie, W. and Li, E.S.F. (1991) Finite element analyses for an in situ wall propped at formation level. **Geotechnique**, 41 (4): 499–514

Prasad, R. (1988) A linear root water uptake model. **Journal of Hydrology**, 99 (3–4): 297–306

Puig, J. (1973) Problemes des terrassement dans la Craie. **Bull. Liaison Lab. P. et eh, Special V**

Qian, Z., Hu, X., Huai, W., et al. (2009) Numerical simulation and analysis of water flow over stepped spillways. **Science in China Series E: Technological Sciences**, 52 (7): 1958–1965

Radcliffe, D., Hayden, T., Watson, K., et al. (1980) Simulation of Soil Water within the Root Zone of a Corn Crop. **Agronomy Journal**, 72 (1): 19–24

Rahardjo, H., Ong, T.H., Rezaur, R.B., et al. (2007) Factors Controlling Instability of Homogeneous Soil Slopes under Rainfall. **Journal of Geotechnical and Geoenvironmental Engineering**. 133 (12) pp. 1532–1543

RAIB (2008a) **Derailment in Hooley Cutting, near Merstham, Surrey 13 January 2007. Rail Accident Report**

RAIB (2008b) **Derailment of a passenger train near Kemble 15 January 2007. Rail**

Accident Report

RAIB (2010) **Derailment near Gillingham tunnel, Dorset 28 November 2009. Rail Accident Report**

RAIB (2012) **Derailment at Clarborough tunnel, near Retford, Nottinghamshire, 27 April 2012**.

RAIB (2018a) **Landslip and derailment at Loch Eilt, north-west Scotland**.

RAIB (2018b) **Landslip and derailment at Loch Treig, north-west Scotland 22 January 2018. Rail Accident Report**

RAIB, D. for T. (2014) **Class investigation into landslips affecting Network Rail infrastructure between June 2012 and February 2013** [online]. Derby UK. Available from: https://www.gov.uk/raibwww.raib.gov.uk

RAIB, D. of transport. (2017) **Derailment due to a landslip, and subsequent collision, Watford** [online]. Derby UK. Available from: www.gov.uk/raib

RAIB, R.A.I.B. (2008c) **Network Rail's Management of Existing Earthworks**., (December)

Rango, A., Tartowski, S.L., Laliberte, A., et al. (2006) Islands of hydrologically enhanced biotic productivity in natural and managed arid ecosystems. **Journal of Arid Environments**, 65: 235–252

Rankine, B. (2016) **Cooks Road. Geotechnical and Structural Design Report**.

Rapp, A. (1963) The Debris Slides at Ulvadal, Western Norway: An Example of Catastrophic Slope Processes in Scandinavia. **Nachrichten der Akademie der Wissenschaften Gottingen, Mathematisch-Physikalische Klass**, 13: 195–210

Rat, M. and Schaeffner, M. (1990) "Classification of chalk and conditions of use in embankments." In **Chalk Proceedings of the International Chalk Symposium**. **1990**. pp. 425–428

Razoaki, R.N. (2000) **Effect of ageing on mechanics of chalk slurries**. University of Portsmouth

Reddi, L.N. and Bonala, M.V.S. (1997) Critical shear stress and its relationship with cohesion for sand–kaolinite mixtures. **Canadian Geotechnical Journal**, 34: 26–33

Reid, M.E., LaHusen, R.G. and Iverson, R.M. (1997) Debris-Flow Initiation Experiments Using Diverse Hydrologic Triggers. **Debris-Flow Hazards Mitigation: Mechanics,**

Prediction and Assessment, pp. 1–11

Richards, L. a (1931) Capillary conduction of liquids throuhg porous media. **Physics 1 (1931)**, 1: 318–333

Risnes, R., Madland, M.V., Hole, M., et al. (2005) Water weakening of chalk—Mechanical effects of water–glycol mixtures. **Journal of Petroleum Science and Engineering**, 48 (1–2): 21–36

Ritchie, A.M. (1958) Recognition and identification of landslides. **Landslides and Engineering Practice, Highway Research Board Special Report**, 29: 48–68

Ritchie, J.T. (1972) Model for predicting evaporation from a row crop with incomplete cover. **Water resources research**, 8 (5): 1204–1213

Roberts, J., Jepsen, R., Gotthard, D., et al. (1998) Effects of particle size and bulk density on erosion of quartz particles. **Journal of Hydraulic Engineering**, 124 (12): 1261–1267

Román, M.O., Schaaf, C.B., Lewis, P., et al. (2010) Assessing the coupling between surface albedo derived from MODIS and the fraction of diffuse skylight over spatially-characterized landscapes. **Remote Sensing of Environment**, 114 (4): 738–760

De Roo, A.P.J. and Riezebos, H.T.H. (1992) Infiltration experiments on loess soils and their implications for modeling surface runoff and soil erosion. **Catena**, 19: 221–239

Rouainia, M., Davies, O., O'Brien, T., et al. (2009) Numerical modelling of climate effects on slope stability. **Proceedings of the Institution of Civil Engineers-Engineering Sustainability**, 162 (2): 81–89

Rvard Hoffman, G.J. and Van Genuchten, M.T. (1983) "Soil properties and efficient water use: Water management for salinity control." In **Limitations to efficient water use in crop production**. pp. 73–85

Sabbagh-Yazdi, S., Zounemat-Kermani, M. and Mastorakis, N.E. (2007) "Velocity profile over spillway by finite volume solution of slopping depth averaged flow." In **Proceedings of the 2nd IASME / WSEAS International Conference on Continuum Mechanics**. **2007**. pp. 99–106

Sabbagh-yazdi, S.R. and Mastorakis, N.E. (2007) Multi-Layer Computation of Coupled Finite Volume Solution of Depth-Averaged Flow in Steep Chute Spillways Considering Air Concentration Effects. **Journal of Fluid Mechanics**, 4: 244–249

Saffman, P.G.T. (1965) The lift on a small sphere in a slow shear flow. **Journal of fluid**

mechanics, 22 (2): 385–400

Santamarina, J.C., Klein, A. and Fam, M.A. (2001) Soils and waves: particulate materials behavior, characterization and process monitoring. **Journal of Soils and Sediments**, 1 (2): 130

Sassa, K. (1998) **Mechanisms of landslide triggered debris flows**. Springer Netherlands

Schaap, M.G. and van Genuchten, M.T. (2006) A modified Mualem–van Genuchten formulation for improved description of the hydraulic conductivity near saturation. **Vadose Zone Journal**, 5 (1): 27–34

Schilirò, L., Esposito, C. and Mugnozza, G.S. (2015) Evaluation of shallow landslide-triggering scenarios through a physically based approach: an example of application in the southern Messina area (northeastern Sicily, Italy). **Natural Hazards & Earth System Sciences**, 15: 2091–2109

Schmeeckle, M. (2015) The role of velocity, pressure, and bed stress fluctuations in bed load transport over bed forms: numerical simulation downstream of a backward-facing step. **Earth Surf Dyn**, 3: 105–112

Schmeeckle, M.W. (2014) Numerical simulation of turbulence and sediment transport of medium sand. **Journal of Geophysical Research: Earth Surface**, 119: 1240–1262

Schmeeckle, M.W., Nelson, J.M., Pitlick, J., et al. (2001) Interparticle collision of natural sediment grains in water. **Water Resources Research**, 37 (9): 2377–2391

Schwarzkopf, J.D., Sommerfeld, M., Crowe, C.T., et al. (2011) **Multiphase Flow with Droplets and Particles**. CRC Press Taylor & Francis Group

Science, L. (2010) **Ground Investigation Report**. [online]. Available from: https://www.landscience.co.uk/application/files/8614/2797/3546/geotechnical.pdf

SEEP/W (2014) **SEEP/W for finite element seepage analysis, user's guide.**

Shafipour, R. and Soroush, A. (2008) Fluid coupled-DEM modelling of undrained behavior of granular media. **Computers and Geotechnics**, 35 (5): 673–685

Shakoor, A. and Cook, B.D. (1990) The effect of stone content, size, and shape on the engineering properties of a compacted silty clay. **Bull. Assoc. Eng. Geologists**, 27 (2): 245–253

Shan, T. and Zhao, J. (2014) A coupled CFD-DEM analysis of granular flow impacting on a

water reservoir. **Acta Mechanica**, 225 (8): 2449–2470

Sharpe, C.F.. (1938) **Landslides and related phenomena**. First Edit. Johnson, D. (ed.). Columbia University Press

Shelley, T.L. and Daniel, D.E. (1993) Effect of gravel on hydraulic conductivity of compacted soil liners. **Journal of Geotechnical Engineering**, 119 (1): 54–68

Shiach, J.B., Mingham, C.G., Ingram, D.M., et al. (2004) The applicability of the shallow water equations for modelling violent wave overtopping. **Coastal Engineering**, 51 (1): 1–15

Shields, A. (1936) Application of Similarity Principles and Turbulence Research to Bed-Load Movement. **Mitt. Preuss. Versuchsanst. Wasserbau Schiffbau**, 26 (5–24): 47

Shuttleworth, W.J. and Wallace, J.S. (1985) Evaporation from sparse crops--An energy combination theory. **Q. J. R. Meteorol. Soc**, 111: 839–855

Shvidchenko, A.B. and Pender, G. (2000) Flume study of the effect of relative depth on the incipient motion of coarse uniform sediments. **Water Resources Research**, 36 (2): 619–628

Skaggs, T.H., van Genuchten, M.T., Shouse, P.J., et al. (2006) Macroscopic approaches to root water uptake as a function of water and salinity stress. **Agricultural water management**, 86 (1–2): 140–149

Skempton, A.W. (1964) Long-term stability of clay slopes: Fourth Rankine Lecture. **Geotechnique**, 14 (2): 77–102

Skempton, A.W. (1996) Embankments and Cuttings on the early Railways. **Construction History**, Vol. 11: 33–49

Skempton, A.W. and Brown, J.D. (1961) A landslide in boulder clay at Selset, Yorkshire. **Geotechnique**, 11 (4): 280–293

Skempton, A.W. and Hutchinson, J. (1969) “Stability of natural slopes and embankment foundations.” In **Soil Mech & Fdn Eng Conf Proc Mexico**. **1969**

SLH (2011) **Pressure drag** [online]. Available from: https://www.sciencelearn.org.nz/images/1654-pressure-drag

SLOPE/W (2018) **Stability Modelling with SLOPE/W**

Smethurst, J.A., Clarke, D. and Powrie, W. (2006) Seasonal changes in pore water

pressure in a grass covered cut slope in London Clay. **Géotechnique**, 56 (8): 523–537

Smith, C. (2013) **Solution validation: Software gave confidence in Beamister Tunnel slope remediation design** [online]. Available from: https://www.geplus.co.uk/features/solution-validation-software-gave-confidence-in-beamister-tunnel-slope-remediation-design-01-08-2013/ [Accessed 4 June 2020]

Smith, F. (1841) Merstham Tunnel Landslip. **Associated Society of Locomotive Engineers and Firemen** [online]. Available from: http://ignitingtheflameofunity.yolasite.com/1841-merstham-tunnel.php

Sobolev, S.S. (1948) **Development of Erosion Processes in the European USSR and their Control**. Moscow

Soe, T.M. and Khaing, S. (2017) Comparison of turbulence models for computational fluid dynamics simulation of wind flow on Cluster of Buildings in Mandalay. **International Journal of Scientific and Research Publications**, 7 (8): 337–350

Soltani, H., Muraleetharan, K.K., Bulut, R., et al. (2016) Prediction of soil suction using measured climatic data. **Environmental Geotechnics**

Southern Water (2017) **Geotechnical and Geo-environmental Interpretative Report**. [online]. Available from: https://apps.eastsussex.gov.uk/environment/planning/applications/register/documents/datawright saved documents/scannedinfo/planning/wd-833-cm/preliminary risk assessment appendix b.pdf

Spencer, E. (1967) A Method of analysis of the Stability of Embankments Assuming Parallel Inter-Slice Forces. **Géotechnique**, 17 (1): 11–26

Standards, N.R. (2017) **Examination of Earthworks Manual**

Stanley, O., Buchan, J. and Bressey, C.H. (1933) British Bridges: An Illustrated Technical and Historical Record. **London: Organising Committee of the Public Works, Roads and Transport Congress**, p. 79

STAR-CCM+ (2017) **STAR-CCM+ User Guide**

Steinbrenner, W. (1934) Tafeln zur Setzungsberechnung. **Die Strasse**, VI: 121–124

Stephenson, G.R. and Freeze, R.A. (1974) Mathematical simulation of subsurface flow contributions to snowmelt runoff, Reynolds Creek Watershed, Idaho. **Water Resources Research**, 10 (2): 284–294

Suzuki, K., Bardet, J.P., Oda, M., et al. (2007) Simulation of upward seepage flow in a single column of spheres using discrete-element method with fluid-particle interaction. **Journal of Geotechnical and Geoenvironmental Engineering**, 133 (1): 104–109

Takahashi, T. (1978) Mechanical Characteristics of Debris Flow. **Journal of Hydraulic Division. ASCE.**, 104: 1153–1169

Takahashi, T. (1991) **Debris Flow**. A.A. Balkema (Rotterdam)

Tan, T.S. (2003) **Characterisation and engineering properties of natural soils**. CRC press

Temple, P.H. and Rapp, A. (1972) Landslides in the Mget Area, Western Uluguru Mountains, Tanzania. **Geografiska Sciences, 1968, pp. 395-401. Annale**, 54 (3–4): 157–193

The Guardian (2012) **Beaminster tunnel landslip deaths: police force refers itself to IPCC** [online]. Available from: https://www.theguardian.com/uk/2012/jul/18/beaminster-tunnel-deaths-police-ipcc

The Guardian (2014) **Mudslide that killed two was "landslip waiting to happen", inquest hears** [online]. Available from: https://www.theguardian.com/world/2014/feb/25/mudslide-killed-two-dorset-landslip-waiting-happen-inquest-hears [Accessed 8 June 2020]

The Guardian (2016) **Train derailed in Watford as torrential rain hits UK** [online]. Available from: https://www.theguardian.com/uk-news/video/2016/sep/16/train-derailed-in-watford-as-torrential-rain-hits-uk-video

Thomasset, F. (2012) **Implementation of finite element methods for Navier-Stokes equations**. Springer Science & Business Media

Thornton, C. and Randall, C.W. (1988) Applications of theoretical contact mechanics to solid particle system simulation. **Studies in Applied Mechanics**, 20 (133–142)

Tognacca, C., Bezzola, G.R. and Minor, H.E. (2000) "Threshold criterion for debris-flow initiation due to channel-bed failure." In **Proc. of the 2nd Int. Conf. on Debris Flow, Hazards and Mitigation**. **Rotterdam, The Netherlands**. **2000**. pp. 89–97

Toro, E.F. (2013) **Riemann solvers and numerical methods for fluid dynamics: a practical introduction**. Springer Science & Business Media.

Townsend, P.J.A. (2018) **Numerical simulation of the shallow water equations coupled with a precipitation system driven by random forcing**. University of Sussex

Traoré, P., Laurentie, J.C. and Dascalescu, L. (2015) An efficient 4 way coupling CFD–DEM model for dense gas–solid particulate flows simulations. **Computers and Fluids**, 113: 65–76

Tratch, D.J. (1995) **A geotechnical engineering approach to plant transpiration and root water uptake**. University of Saskatchewan

Tratch, D.J., Wilson, G.W. and Fredlund, D.G. (1995) "An introduction to analytical modeling of plant transpiration for geotechnical engineers." In **48th Annual Canadian Geotechnical Conference**. **Vancouver BC**. **1995**. pp. 771–780

Trenter, N.A. (1999) **Engineering in glacial tills. CIRIA REPORT C504**

Tsaparas, I., Rahardjo, H., Toll, D.G., et al. (2002) Controlling parameters for rainfall-induced landslides. **Computers and Geotechnics**, 29 (1): 1–27

Turkeltaub, T., Dahan, O. and Kurtzman, D. (2014) Investigation of groundwater recharge under agricultural fields using transient deep vadose zone data. **Vadose Zone Journal**, 13 (4)

Turner, J.H. (1979) **The London, Brighton and South Coast Railway: Completion and Maturity, Vol 3.** 1st ed. HarperCollins Distribution Services

Twine, D. and Wright, R.H. (1991) "Farmers Avenue Road Crossing, Castle Mall development, Norwich." In **Proceedings 4th International Deep Foundation Conference Stresa**. **Rotterdam**. **1991**. pp. 147–155

UK Environmental Agency (2019) **Monthly water situation report** [online]. Available from: https://assets.publishing.service.gov.uk/government/uploads/system/uploads/attachment_data/file/807680/Hertfordshire_and_North_London_Water_Situation_Report_May_2019.pdf

USGS (2016) **Landslides Types and Processes** [online]. Available from: https://pubs.usgs.gov/fs/2004/3072/fs-2004-3072.html [Accessed 21 May 2020]

Usuki, N., Yoshino, K. and Mizumaya, T. (2019) "Soil characteristics of long-traveling landslides and a hybrid model to predict travel distance." In **7th International Conference on Debris-Flow Hazards Mitigation**. **Golden, Colorado, USA**. **2019**

Utili, S., Zhao, T. and Houlsby, G. (2015) 3D DEM investigation of granular column collapse: evaluation of debris motion and its destructive power. **Engineering geology**,

186: 3–16

Vallejo, L.E. and Morris, R.N. (1979) **An explanation for mudflows**., (3)

Vandervaere, J.P., Peugeot, C., Jaramillo, R.A., et al. (1997) Estimating hydraulic conductivity of crusted soils by using disc infiltrometers and micro-tensiometers. **J. Hydrol**, 188–189: 203–223

Vanoni, V.A. (1975) Sedimentation Engineering. **American Society of Civil Engineers, Manuals and Reports on Engineering Practice**, 54: 745

Varado, N., Braud, I. and Ross, P.J. (2006) Development and assessment of an efficient vadose zone module solving the 1D Richards' equation and including root extraction by plants. **Journal of Hydrology**, 323 (1–4): 258–275

Varnes, D. (1958) Landslide Types and Processes. **Landslides and Engineering Practice**, 29: 20–47

Varnes, D.J. (1978) Slope Movement Types and Processes. **Transportation Research Board Special Report**, (176): 11–33

Vásquez-Méndez, R., Ventura-Ramos, E., Oleschko, K., et al. (2010) Soil erosion and runoff in different vegetation patches from semiarid Central Mexico. **Catena**, 80 (3): 162–169

Versteeg, H.K. and Malalasekera, W. (2007) **An introduction to computational fluid dynamics: the finite volume method**. Second Edi. Pearson education

Wallace, J.S., Roberts, J.M. and Sivakumar, M.V.K. (1990) The estimation of transpiration from sparse dryland millet using stomatal conductance and vegetation area indicies. **Agric. For. Meteorol**, 51: 35–49

Ward, W.H., Burland, J.B. and Gallois, R.W. (1968) Geotechnical assessment of a site at Mundford, Norfolk, for a large proton accelerator. **Geotechnique**, 18 (4): 399–431

Wasserman, S. (2016) **Choosing the Right Turbulence Model for Your CFD Simulation** [online]. Available from: https://www.engineering.com [Accessed 19 May 2019]

Wen, C.Y. and Yu, Y.H. (1966) A generalized method for predicting the minimum fluidization velocity. **AIChE Journal**, 12 (3): 610–612

Wiberg, P.L. and Smith, J.D. (1987) Calculations of the critical shear stress for motion of uniform and heterogeneous sediments. **Water Resources Research**, 23 (8): 1471–1480

Wilcock, P., Pitlick, J. and Cui, Y. (2009) Sediment transport primer estimating bed-material transport in gravel-bed rivers. **United States Department of Agriculture**, General Te

Wilcock, P.R. and Crowe, J.C. (2003) Surface-based transport model for mixed-size sediment. **Journal of Hydraulic Engineering**, 129 (2): 120–128

Wilkes, P.F. (1974) **A geotechnical study of a trial embankment on alluvial deposits at King's Lynn.** University o f Surrey

Williams, J., Prebble, R.E., Williams, W.T., et al. (1983) The influence of texture, structure and clay mineralogy on the soil moisture characteristic. **Soil Research**, 21 (1): 15–32

Wilson, G.W. (1990) **Soil evaporative fluxes for geotechnical engineering problems**. University of Saskatchewan

Wilson, G.W., Fredlund, D.G. and Barbour, S.L. (1994) Coupled soil-atmosphere modelling for soil evaporation. **Canadian Geotechnical Journal**, 31 (2): 151–161

Wood, R.F. and Nimmo, M. (1962) Chalk Downland Afforestation. **Forestry Commission**, 34

WSP (2014a) **A45 Daventry Link Road, Interpretative Geotechnical Report**. [online]. Available from: https://www.northamptonshire.gov.uk/councilservices/environment-and-planning/planning/planning-applications/documents/PDF Documents/Road Scheme Applications/14.00086.CCDFUL-ESV2-Appendix16.4.pdf

WSP (2014b) **A45 Daventry Link Road Ground Investigation Report Northamptonshire County Council**. [online]. Available from: https://www.northamptonshire.gov.uk/councilservices/environment-and-planning/planning/planning-applications/documents/PDF Documents/Road Scheme Applications/14.00086.CCDFUL-ESV2-Appendix16.3Part1.pdf

Xia, X. and Liang, Q. (2018) A new depth-averaged model for flow-like landslides over complex terrains with curvatures and steep slopes. **Engineering Geology**, 234: 174–191

Yalin, M.S. and Karahan, E. (1979) Inception of sediment transport. **J. Hydraul. Div.**, 105 (11): 1433–1443

Yan, Y. (2011) **Development of a coupled CFD system code capability (with a modified porous media model) and its applications to simulate current and next generation reactors**. University of Illinois. USA.

Yan, Y. and Ji, S. (2010) Discrete element modeling of direct shear tests for a granular material. **International journal for numerical and analytical methods in geomechanics**, 34 (9): 978–990

Yan, Z., Wilkinson, S.K., Stitt, E.H., et al. (2015) Discrete element modelling (DEM) input parameters: understanding their impact on model predictions using statistical analysis. **Computational Particle Mechanics**, 2 (3): 283–299

Yang, W.C. (2003) **Handbook of fluidization and fluid-particle systems**. First Edit. CRC Press

Yoo, C., Ku, J.M., Jun, C., et al. (2016) Simulation of infiltration facilities using the SEEP/W model and quantification of flood runoff reduction effect by the decrease in CN. **Water Science and Technology**, 74 (1): 118–129

Yu, H.S., Salgado, R., Sloan, S.W., et al. (1998) Limit analysis versus limit equilibrium for slope stability. **Journal of Geotechnical and Geoenvironmental Engineering**, 124 (1): 1–11

Zanke, U.C. (2001) Zum Einfluss der Turbulenz auf den Beginn der Sedimentbewegung. **Mitteilungen des Instituts fur Wasserbau und Wasserwirtschaft der TU Darmstadt**, (120)

Zanke, U.C. (2003) On the influence of turbulence on the initiation of sediment motion. **International Journal of Sediment Research**, 18 (1): 17–31

Zeghal, M. and El Shamy, U. (2004) A continuum-discrete hydromechanical analysis of granular deposit liquefaction. **International Journal for Numerical and Analytical Methods in Geomechanics**, 28 (14): 1361–1383

Zhang, H.J., Zhou, J.Z., Bi, S., et al. (2014) A well-balanced numerical scheme for shallow water simulation on adaptive grids. **Journal of Physics: Conference Series**, 495 (1)

Zhao, J. and Shan, T. (2013) Coupled CFD--DEM simulation of fluid--particle interaction in geomechanics. **Powder technology**, 239: 248--258

Zhao, T. (2014) **Investigation of Landslide-Induced Debris Flows by the DEM and CFD**. University of Oxford

Zhao, T. (2017) **Coupled DEM-CFD Analyses of Landslide-Induced Debris Flows.** Springer Singapore

Zhao, T., Dai, F. and Xu, N. (2017) Coupled DEM-CFD investigation on the formation of

landslide dams in narrow rivers. **Landslides**, 14 (1): 189--201

Zheng, Q. (2012) **Finite Element Study of Particle Contact Mechanics and Stockpiling Process**. The University of New South Wales

Zhou, J.G. and Stansby, P.K. (1998) ALES Shallow-Water Flow Solver with Non-Hydrostatic Pressure: Wave Applications. **Coastal Engineering Proceedings**, 1 (26)

Zhou, Y.C., Wright, B.D., Yang, R.Y., et al. (1999) Rolling friction in the dynamic simulation of sandpile formation. **Physica A: Statistical Mechanics and its Applications**, 269 (2–4): 536–553

APPENDIX A

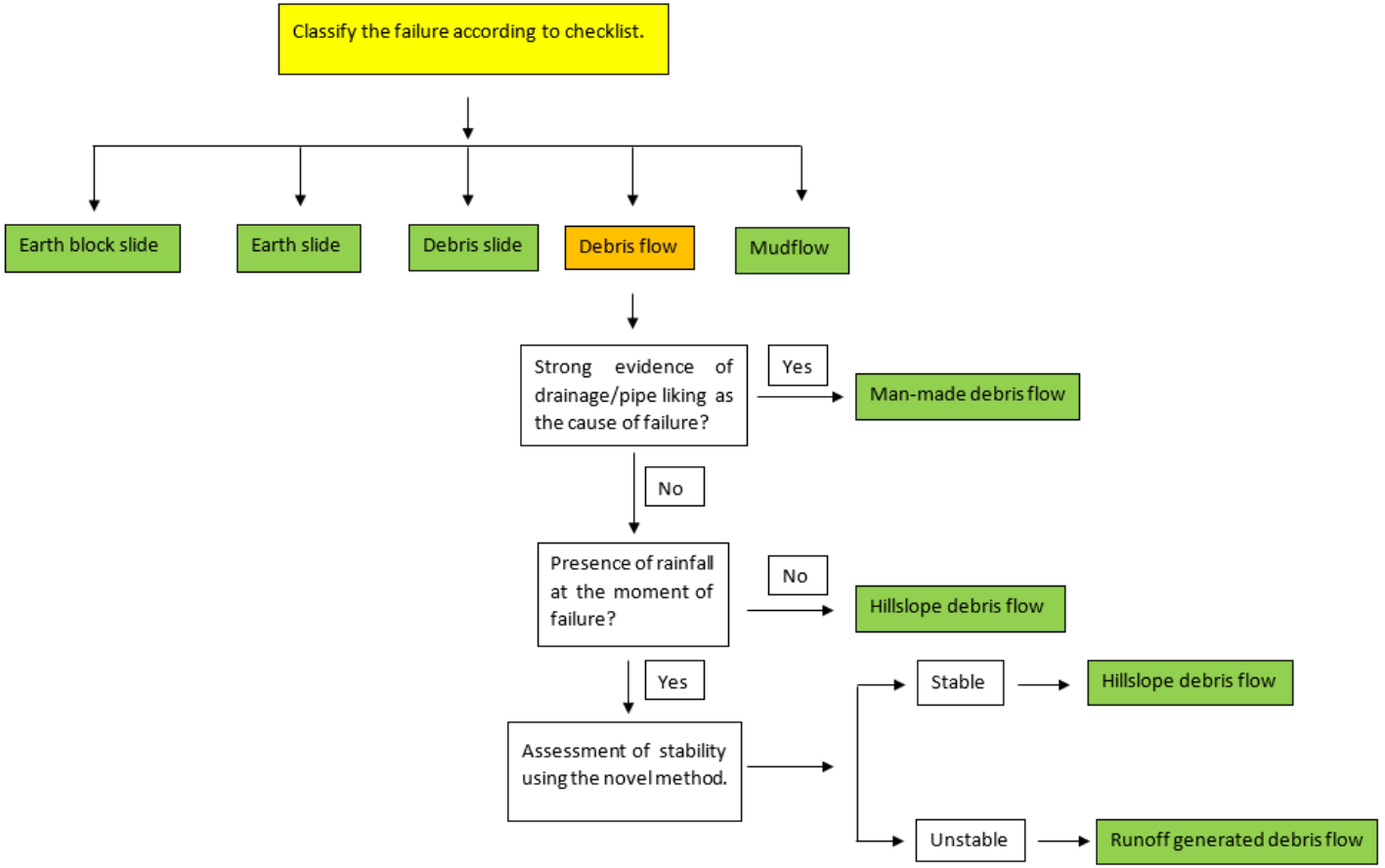

Figure A 1 Process to Classify Shallow Failures

Table A 1 Check-list table

Visual Features	Cutting Features	Earth Block Slide	Earth slides	Debris slides	Debris flow	Mudflows
		Scores	Scores	Scores	Scores	Scores
Sliding along a roughly planar surface		🟢	🟢	🟢	🟢	🟢
Low deformation		🟢	🔴	🔴	🔴	🔴
Greatly deformed		🔴	🟢	🟢	🟡	🟡
Extremely deformed		🔴	🔴	🔴	🟢	🟢
Material fails predominantly as a unit		🟢	🟢	🟢	🔴	🔴
Material fails as a flow		🔴	🔴	🔴	🟢	🟢
Undulating surface with ripple like structures		🟡	🟢	🟢	🔴	🔴
Short runout distances		🟢	🟡	🟡	🔴	🔴
Long runout distances		🔴	🟢	🟢	🟡	🟡
Extreme runout distances		🔴	🔴	🔴	🟢	🟢
Presence of abundant water		🟡	🟡	🟡	🟡	🟢
Mostly Cohesive		🟢	🟢	🔴	🟡	🟢
Distinct slicken sided surface and slicken sided lateral margins		🟢	🟢	🟢	🟡	🟡
Distinct Lobate toe		🟡	🟢	🟢	🔴	🔴
Total Scores						

The first column of the table contains the visual features used for the classification. The second column corresponds to the visual features presented in the cutting.

- When the visual feature in the first column is detected in the cutting, a ✔ symbol is marked in the second column.
- When the feature is not clearly detected, a ✱ symbol is marked in the second column
- When the feature is missing, a ✘ symbol is used.

Columns 3 to 7 corresponds to the different categories of failure: Earth Block Slide, Earth slides, Debris slides, Debris flow and Mudflows. The symbol 🟢 has been pre-marked when the feature in column 1 is strongly associated to the category. The symbol 🔴 has been pre-marked when the feature in column 1 is strongly NOT associated to the category. The symbol 🟡 has been pre-marked when the feature may or may not be present for the corresponding category.

When a cutting is to be classified a procedure is to be followed row by row:

* if the symbol in column 2 is ✔, cells with the symbol 🟢 will be marked as 1.
* if the symbol in column 2 is ✔, cells with the symbol 🔴 will be marked as 0.
* if the symbol in column 2 is ✘, cells with the symbol 🔴 will be marked as 1.
* if the symbol in column 2 is ✘, cells with the symbol 🟢 will be marked as 0.
* if the symbol in column 2 is ✱ all cells in the corresponding row will be marked as 0.
* cells with the symbol 🟡 will be marked as 0.

The scores will be added for each category and the one with the higher score will represent the category associated to the cutting. In case that 2 or more categories present the same score, the category with more 🟡 is prevalent.

The proposed classification system has been applied to five cases obtained from rapid response reports filed by Amey (Table A 2) and the scouring results are presented in Table A 3, Table A 4, Table A 5, Table A 6 and Table A 7. Table A 2 shows photographs of the cutting failures with a list of the features observed. The results from the scoring system show that the check-list is a valuable tool that assists in the classification of mass failures.

Table A 2 Case studies for the classification of failures in the proposed system

CASE 1: Earth Block Slide	**Visual Features**
	* **Distinct slicken sided surface and slicken sided lateral margins** * **Low deformation** * **Material fails predominantly as a unit** * **Short runout distances** * **Mostly cohesive soil** * **No distinct lobate toe** * **No ripple like structures**
CASE 2: Earth Slide	**Visual Features**
	* **Greatly deformed** * **Material fails predominantly as a unit** * **Long runout distances** * **Cohesive Soil** * **Distinct Lobate toe**
CASE 3: Debris Slide	**Visual Features**
	* **Greatly deformed** * **Material fails predominantly as a unit** * **Long runout distances** * **Distinct Lobate toe** * **Distinct slicken sided surface and slicken sided lateral margins** * **Mostly Coarse Soil**
Case 4: Debris flow	**Visual Features**
	* **Extremely deformed** * **Material does NOT fail predominantly as a unit** * **Extreme runout distances** * **Distinct slicken sided surface and slicken sided lateral margins** * **No Distinct Lobate toe** * **No Low points at the crest of the cutting** * **No high water content**

CASE 5: Mudflow	**Visual Features**
	* **Extremely deformed** * **Material does NOT fail predominantly as a unit** * **Extreme runout distances** * **Cohesive Soil** * **Abundant Water** * **No distinct lobate Toe** * **High Plsticity** * **No soil peds from aggregation**

Table A 3 CASE 1 check list: Earth Block Slide

Visual Features	Cutting Features	Earth Block Slide		Earth slides		Debris slides		Debris flow		Mudflows	
			Scores		Scores		Scores		Scores		Scores
Low deformation	✓	🟢	1	🔴	0	🔴	0	🔴	0	🔴	0
Greatly deformed	☒	🔴	1	🟢	0	🟢	0	🟡	0	🟡	0
Extremely deformed	☒	🔴	1	🔴	1	🔴	1	🟢	0	🟢	0
Material fails predominantly as a unit	✓	🟢	1	🟢	1	🟢	1	🔴	0	🔴	0
Material fails as a flow	☒	🔴	1	🔴	1	🔴	1	🟢	0	🟢	0
Undulating surface with ripple like structures	☒	🟡	0	🟢	0	🟢	0	🔴	1	🔴	1
Short runout distances	✓	🟢	1	🟡	0	🟡	0	🔴	0	🔴	0
Long runout distances	☒	🔴	1	🟢	0	🟢	0	🟡	0	🟡	0
Extreme runout distances	☒	🔴	1	🔴	1	🔴	1	🟢	0	🟢	0
Presence of abundant water	☒	🟡	0	🟡	0	🟡	0	🟡	0	🟢	0
Mostly Cohesive	✓	🟢	1	🟢	1	🔴	0	🟡	0	🟢	1
Distinct slicken sided surface and slicken sided lateral margins	✓	🟢	1	🟢	1	🟢	1	🟡	0	🟡	0
Distinct Lobate toe	☒	🟡	0	🟢	0	🟢	0	🔴	1	🔴	1
Total Scores		11		7		6		3		4	

Table A 4 CASE 2 check list: Earth Slide

Visual Features	Cutting Features	Earth Block Slide		Earth slides		Debris slides		Debris flow		Mudflows	
			Scores		Scores		Scores		Scores		Scores
Low deformation	☒	🟢	0	🔴	1	🔴	1	🔴	1	🔴	1
Greatly deformed	✓	🔴	0	🟢	1	🟢	1	🟡	0	🟡	0
Extremely deformed	☒	🔴	1	🔴	1	🔴	1	🟢	0	🟢	0
Material fails predominantly as a unit	✓	🟢	1	🟢	1	🟢	1	🔴	0	🔴	0
Material fails as a flow	☒	🔴	1	🔴	1	🔴	1	🟢	0	🟢	0
Undulating surface with ripple like structures	✱	🟡	0	🟢	0	🟢	0	🔴	0	🔴	0
Short runout distances	☒	🟢	0	🟡	0	🟡	0	🔴	1	🔴	1
Long runout distances	✓	🔴	0	🟢	1	🟢	1	🟡	0	🟡	0
Extreme runout distances	☒	🔴	1	🔴	1	🔴	1	🟢	0	🟢	0
Presence of abundant water	☒	🟡	0	🟡	0	🟡	0	🟡	0	🟢	0
Mostly Cohesive	✓	🟢	1	🟢	1	🔴	0	🟡	0	🟢	1
Distinct slicken sided surface and slicken sided lateral margins	☒	🟢	0	🟢	0	🟢	0	🟡	0	🟡	0
Distinct Lobate toe	✓	🟡	0	🟢	1	🟢	1	🔴	0	🔴	0
Total Scores		5		9		8		2		3	

Table A 5 CASE 3 check list: Debris Slide

Visual Features	Cutting Features	Earth Block Slide	Scores	Earth slides	Scores	Debris slides	Scores	Debris flow	Scores	Mudflows	Scores
Low deformation	☒	🟢	0	🔴	1	🔴	1	🔴	1	🔴	1
Greatly deformed	✓	🔴	0	🟢	1	🟢	1	🟡	0	🟡	0
Extremely deformed	☒	🔴	1	🔴	1	🔴	1	🟢	0	🟢	0
Material fails predominantly as a unit	✓	🟢	1	🟢	1	🟢	1	🔴	0	🔴	0
Material fails as a flow	☒	🔴	1	🔴	1	🔴	1	🟢	0	🟢	0
Undulating surface with ripple like structures	✱	🟡	0	🟢	0	🟢	0	🔴	0	🔴	0
Short runout distances	☒	🟢	0	🟡	0	🟡	0	🔴	1	🔴	1
Long runout distances	✓	🔴	0	🟢	1	🟢	1	🟡	0	🟡	0
Extreme runout distances	☒	🔴	1	🔴	1	🔴	1	🟢	0	🟢	0
Presence of abundant water	✓	🟡	0	🟡	0	🟡	0	🟡	0	🟢	1
Mostly Cohesive	☒	🟢	0	🟢	0	🔴	1	🟡	0	🟢	0
Distinct slicken sided surface and slicken sided lateral margins	✓	🟢	1	🟢	1	🟢	1	🟡	0	🟡	0
Distinct Lobate toe	✓	🟡	0	🟢	1	🟢	1	🔴	0	🔴	0
Total Scores			5		9		10		2		3

Table A 6 Case 4 check list: Debris flow

Visual Features	Cutting Features	Earth Block Slide	Scores	Earth slides	Scores	Debris slides	Scores	Debris flow	Scores	Mudflows	Scores
Low deformation	☒	🟢	0	🔴	1	🔴	1	🔴	1	🔴	1
Greatly deformed	☒	🔴	1	🟢	0	🟢	0	🟡	0	🟡	0
Extremely deformed	✓	🔴	0	🔴	0	🔴	0	🟢	1	🟢	1
Material fails predominantly as a unit	☒	🟢	0	🟢	0	🟢	0	🔴	1	🔴	1
Material fails as a flow	✓	🔴	0	🔴	0	🔴	0	🟢	1	🟢	1
Undulating surface with ripple like structures	☒	🟡	0	🟢	0	🟢	0	🔴	1	🔴	1
Short runout distances	☒	🟢	0	🟡	0	🟡	0	🔴	1	🔴	1
Long runout distances	☒	🔴	1	🟢	0	🟢	0	🟡	0	🟡	0
Extreme runout distances	✓	🔴	0	🔴	0	🔴	0	🟢	1	🟢	1
Presence of abundant water	☒	🟡	0	🟡	0	🟡	0	🟡	0	🟢	0
Mostly Cohesive	☒	🟢	0	🟢	0	🔴	1	🟡	0	🟢	0
Distinct slicken sided surface and slicken sided lateral margins	✓	🟢	1	🟢	1	🟢	1	🟡	0	🟡	0
Distinct Lobate toe	☒	🟡	0	🟢	0	🟢	0	🔴	1	🔴	1
Total Scores			2		2		3		*8		8

*Debris flows is prevalent over mudflow by the number of 🟡.

Table A 7 CASE 5 check list: Mudflow

Visual Features	Cutting Features	Earth Block Slide	Scores	Earth slides	Scores	Debris slides	Scores	Debris flow	Scores	Mudflows	Scores
Low deformation	☒	🟢	0	🔴	1	🔴	1	🔴	1	🔴	1
Greatly deformed	☒	🔴	1	🟢	0	🟢	0	🟡	0	🟡	0
Extremely deformed	✓	🔴	0	🔴	0	🔴	0	🟢	1	🟢	1
Material fails predominantly as a unit	☒	🟢	0	🟢	0	🟢	0	🔴	1	🔴	1
Material fails as a flow	✓	🔴	0	🔴	0	🔴	0	🟢	1	🟢	1
Undulating surface with ripple like structures	☒	🟡	0	🟢	0	🟢	0	🔴	1	🔴	1
Short runout distances	☒	🟢	0	🟡	0	🟡	0	🔴	1	🔴	1
Long runout distances	☒	🔴	1	🟢	0	🟢	0	🟡	0	🟡	0
Extreme runout distances	✓	🔴	0	🔴	0	🔴	0	🟢	1	🟢	1
Presence of abundant water	✓	🟡	0	🟡	0	🟡	0	🟡	0	🟢	1
Mostly Cohesive	✓	🟢	1	🟢	1	🔴	0	🟡	0	🟢	1
Distinct slicken sided surface and slicken sided lateral margins	☒	🟢	0	🟢	0	🟢	0	🟡	0	🟡	0
Total Scores			3		2		1		7		9